



Synthesis and Characterisation of Chiral Metal Phosphonates with Applications in Magnetism, Catalysis and Luminescence

PhD Thesis Submitted by
Graeme W. Bowling

Supervisor: Dr Lee J. Higham

School of Chemistry
Newcastle University
Newcastle upon Tyne
United Kingdom

Abstract

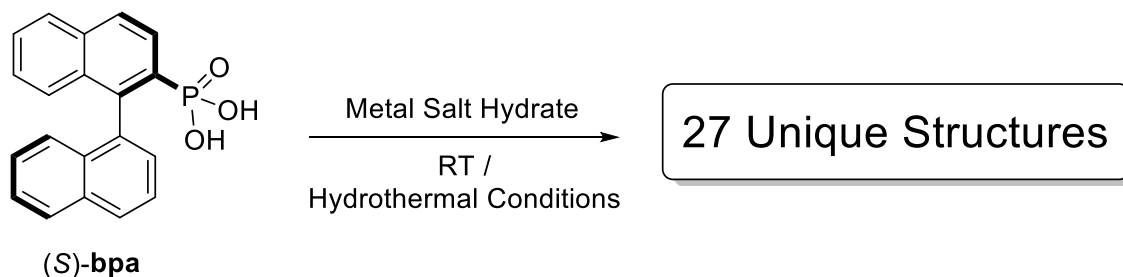
This thesis details an improved synthesis and full characterisation of a chiral phosphonic acid, (*S*)-[1,1'-binaphthalen]-2-ylphosphonic acid, (*S*)-**bpa**, derived from the commercially-available (*R*)-binol. From this sterically encumbered phosphonic acid ligand, a total of 27 new chiral metal phosphonates (11 first-row transition metal, 2 second-row transition metal and 14 lanthanide) have been prepared and characterised by single-crystal X-ray diffraction.

Chapter 1 discusses the history of metal phosphonate chemistry and how reagents and conditions can be controlled in order to determine certain metal phosphonate structures. It also explains the nomenclature of phosphonate binding which will be used throughout the thesis.

Chapter 2 discusses the synthesis of (*S*)-**bpa** and how it was optimised from the parent (*R*)-binol. The ligand was then reacted with Co(II) under different conditions in order to prepare three cobalt(II) phosphonates of remarkably different morphologies. Furthermore, (*R*)-**bpa** was synthesised and used to prepare the corresponding (*R*)- derivatives of the aforementioned three cobalt(II) phosphonates. One by-product of these reactions, the mononuclear Co(II) complex $[\text{Co}(\text{OAc})_2(\text{Py})_2(\text{H}_2\text{O})_2]$ (Py = pyridine) was found to exhibit slow relaxation after magnetic susceptibility measurements were conducted on it ($U_{\text{eff}} = 25 \text{ cm}^{-1}$ (36 K)). The magnetic susceptibility data for the other cobalt(II) phosphonates is pending.

Chapter 3 further explores the versatility of (*S*)-**bpa** and details the preparation of nine transition metal phosphonates – seven first-row (Sc, two Mn, Fe, Ni, Cu and Zn) and two second-row (Y and Cd).

In Chapter 4, we turn our attention to the lanthanides and the successful preparation and full characterisation of 14 (*S*)-**bpa**-lanthanide phosphonates (all except for promethium) is detailed. The structures adopt three different forms throughout the series – the first from La to Sm, the second from Eu to Tm and the third include Yb and Lu. Photophysical studies were conducted on the europium phosphonate and it was found to be fluorescent.



Acknowledgements

Firstly, I would like to thank Dr Lee J Higham, my supervisor and mentor for giving me the opportunity to work on this fascinating area of phosphorus chemistry and nurturing not only my laboratory skills, but also my academic writing. I think it's fair to say that in some regards this has been a learning curve for the both of us, but we got there in the end. I wish you (and Liverpool FC of course) all the best in your future endeavours.

Secondly, I would like to thank Dr Ana Cioran and Dr Connor Sibbald, the former members of the Higham group who first delved into metal phosphonate chemistry. Your support in helping me find my feet in this unfamiliar area has been invaluable and I cannot be grateful enough. I only hope that I did you proud in giving this a proper home in this thesis and (with any luck) future publications.

Of course, thanks should be given to the Higham group, Dr James Fleming, Dr Jennifer Wallis, Dr Antonio Sánchez-Cid, Charlotte Hepples and Roger Mallett for helping me with my day-to-day problems and generally making our group a pleasant place to work for all. A special mention goes to Dr Manuel Abelairas-Edesa for turning an incredibly green chemist just starting his MChem into the person I am today. Thank you for your time and patience. I still remember your cardinal rule *"El jefe dice, el mono hace."*

I must give thanks the countless MChem, summer and Erasmus students who have worked with me in this project, in particular, Penélope da Vila Gorrita, Kelsey Cairns, Adam Lowery and Stepen Kirvan. I hope someday you will get a chance to read this thesis and see your hard work immortalised.

My unending gratitude goes to the crystallographers of Newcastle University, Dr Paul Waddell, Dr Mike Probert and Professor William Clegg, without whom, this thesis would not exist. Thank you for your hard work and patience. I think if you ever see another lanthanide cluster again it will be too soon.

Finally, my thanks go to my family, whose support and patience with me throughout my PhD (and indeed all throughout my education) has been invaluable.

List of Publications

1. J. P. S. Walsh, G. W. Bowling, A. Ariciu, N. F. M. Jailani, N. F. Chilton, P. G. Waddell, D. Collison, F. Tuna and L. J. Higham, *Magnetochemistry*, 2016, **2**, 23.
2. G. W. Bowling, J. T. Fleming, A. Ficks and L. J. Higham, *Organomet. Chem.*, 2017, **41**, 48 – 92.

Contents

Abstract	I
Acknowledgements	II
List of Publications.....	III
List of Structures	VIII
Chapter 1 – Background and Introduction	13
1.1 Phosphonic Acids and Metal Phosphonates	13
1.2 Applications of Metal Phosphonates	15
1.2.1 Magnetism.....	16
1.2.2 Catalysis.....	19
1.2.3 Luminescence	22
1.2.4 Absorption and Separation.....	26
1.2.5 Medicinal	27
1.3 Nomenclature of Metal Phosphonate Binding	28
1.3.1 Zirconium Phosphonates.....	30
1.3.2 Iron Phosphonates	31
1.3.3 Lanthanide Phosphonates	33
1.4 Controlling the Morphology/Topology of Metal Phosphonates	36
1.4.1 Employing Phosphonic Acids with Steric Encumbrance.....	36
1.4.2 Co-Ligand or Ancillary-Ligand Method	37
1.4.3 Hydrothermal/Solvothermal Method	38
1.5 Scope of Work	41
1.5.1 An Atropisomeric, Sterically Encumbered Phosphonic Acid	41
1.5.2 Rationalising the Choice of Ligand	42
1.5.3 Methods of Analysis.....	44
Chapter 2 – Control over 0-D, 1-D and 2-D Morphology / Topology – Dictating the Structure and Properties of Chiral Cobalt Phosphonates.....	45
2.1 Ligand Synthesis	45

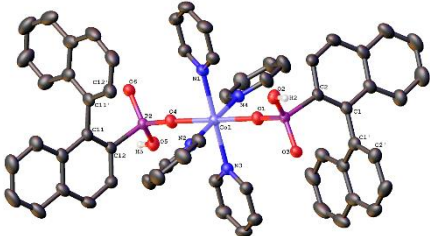
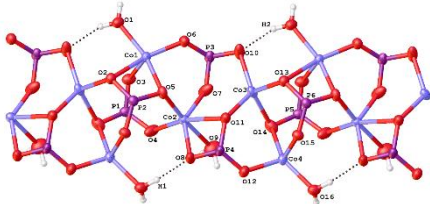
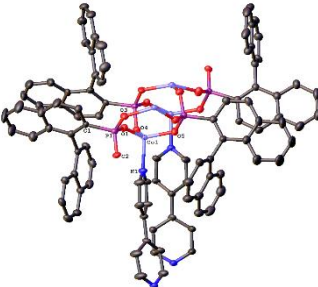
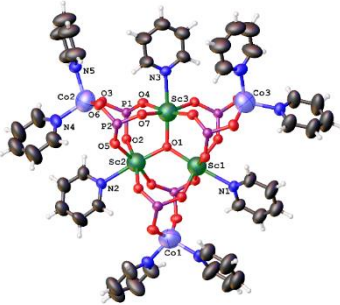
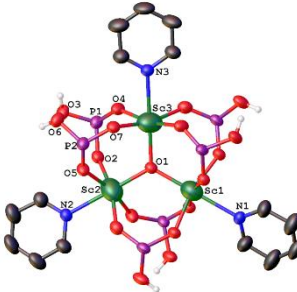
2.1.1 Preparation of (<i>R</i>)- 31	45
2.1.2 Preparation of (<i>S</i>)- 32	46
2.1.3 Preparation of (<i>S</i>)- 33 and (<i>S</i>)- 34	47
2.1.4 Preparation of (<i>S</i>)- bpa	48
2.2 [Co(OAc) ₂ (Py) ₂ (H ₂ O) ₂], 36 Synthesis and Characterisation	49
2.3 [Co((<i>S</i>)-bpa) ₂ (Py) ₄], (<i>S</i>)- 37 Synthesis and Characterisation	55
2.4 Higher-Order Co-(<i>S</i>)-bpa Phosphonates	58
2.4.1 One-Dimensional Co Polymeric Chain, (<i>S</i>)- 38	58
2.4.2 Two-Dimensional Co-4,4'-Bipy Polymeric Sheet, (<i>S</i>)- 42	60
2.5 Preparation of (<i>R</i>)- 37 , (<i>R</i>)- 38 and (<i>R</i>)- 42	63
2.6 Preparation of a Mixed Co-Sc Cluster, (<i>S</i>)- 43	64
2.7 Testing the Catalytic Properties of (<i>S</i>)- 38 and (<i>S</i>)- 42	67
2.8 Conclusion	69
Chapter 3 – Coordination of (<i>S</i>)-bpa to Other Transition Metals	71
3.1 Introduction	71
3.2 First-Row Transition Metal Phosphonates	72
3.2.1 Scandium Phosphonate, (<i>S</i>)- 44	72
3.2.2 Manganese Phosphonates, (<i>S</i>)- 45 and (<i>S</i>)- 46	76
3.2.3 Iron Phosphonate, (<i>S</i>)- 48	81
3.2.4 Nickel and Copper Phosphonates, (<i>S</i>)- 49 and (<i>S</i>)- 50	83
3.2.5 Zinc Phosphonate, (<i>S</i>)- 51	86
3.3 Second-Row Transition Metal Phosphonates	89
3.3.1 Yttrium Phosphonate, (<i>S</i>)- 52	89
3.3.2 Cadmium Phosphonate, (<i>S</i>)- 53	93
3.4 Conclusion	94
Chapter 4 – Coordination of (<i>S</i>)-bpa to Lanthanides	97
4.1 Introduction	97
4.2 Coordination to Early Lanthanides, La – Sm, (<i>S</i>)- 54 – (<i>S</i>)- 58	98

4.3 Coordination to Later Lanthanides, Eu – Tm, (S)- 59 – (S)- 65	102
4.4 Coordination to Final Lanthanides, Yb and Lu, (S)- 66 and (S)- 67	105
4.5 Photophysical Properties of Eu Phosphonate, (S)- 51	110
4.6 Conclusion	112
Conclusion and Future Work	113
Experimental	115
General Procedure.....	115
Synthesis of (R)- 31	117
Synthesis of (S)- 32	118
Alternative Synthesis of (S)- 32	119
Synthesis of (S)- 33	119
Synthesis of (S)- 34	120
Synthesis of (S)- bpa	121
Synthesis of 36	123
Synthesis of (S)/(R)- 38	124
Synthesis of (S)/(R)- 42	125
Synthesis of (S)- 43	126
Synthesis of Monometallic Co, Mn, Ni, Cu, Cd Phosphonates (S)- 37, 45, 49, 50, 53 General Procedure.....	127
Synthesis of (S)- 44	129
Synthesis of (S)- 46	130
Synthesis of (S)- 48	131
Synthesis of (S)- 51	132
Synthesis of (S)- 52	133
Synthesis of La, Ce, Pr, Nd, Sm Phosphonates (S)- 54, 55, 56, 57, 58 , General Procedure ...	134
Synthesis of Eu, Gd, Tb, Dy, Ho, Er, Tm Phosphonates (S)- 59, 60, 61, 62, 63, 64, 65 , General Procedure.....	136
Synthesis of Yb and Lu Phosphonates (S)- 66, 67 , General Procedure.....	138

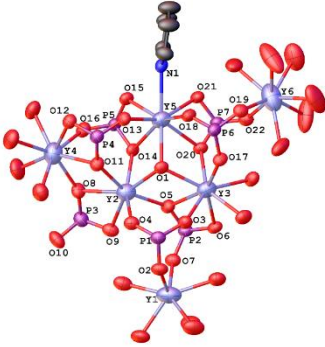
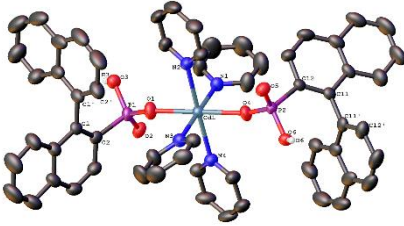
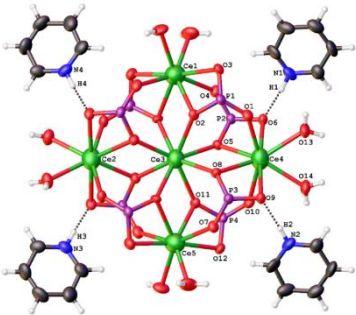
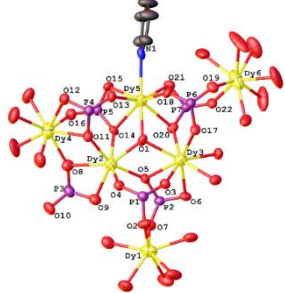
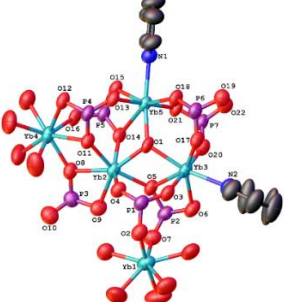
References	139
Appendix.....	146
Table of Screenings for the Layering, Stirring and Hydrothermal Synthesis	146
Bond Valence Sum Calculations.....	149
Co 1-D Chain, (S)- 38	149
Mn ₆ Cluster, (S)- 46	150
Crystallographic Information Tables	151

List of Structures

Below is a list of all novel metal phosphonates mentioned in this thesis with their corresponding systematic name and crystal structure.

Name	Systematic Name	Crystal Structure
(S)-37	$[\text{Co}((S)\text{-bpa})_2(\text{Py})_4]$	
(S)-38	$[\text{Co}_4((S)\text{-bpa})_4]_n$	
(S)-42	$[\text{Co}_2((S)\text{-bpa})_2(\text{bipy})]_n$	
(S)-43	$[\text{Sc}_3\text{Co}_3((S)\text{-bpa})_6\text{O}(\text{Py})_9]$	
(S)-44	$[\text{Sc}_3((S)\text{-bpa})_6\text{O}(\text{Py})_3]$	

Name	Systematic Name	Crystal Structure
(S)-45	$[\text{Mn}((S)\text{-bpa})_2(\text{Py})_4]$	
(S)-46	$[\text{Mn}_6((S)\text{-bpa})_6\text{O}(\text{Py})_3(\text{H}_2\text{O})_6]$	
(S)-48	$[\text{Fe}_3((S)\text{-bpa})_6\text{O}(\text{Py})_3]$	
(S)-49	$[\text{Ni}((S)\text{-bpa})_2(\text{Py})_4]$	
(S)-50	$[\text{Cu}((S)\text{-bpa})_2(\text{Py})_4]$	
(S)-51	$[\text{Zn}_4((S)\text{-bpa})_4(\text{Py})_4]$	

Name	Systematic Name	Crystal Structure
(S)-52	$[\text{Y}_6((S)\text{-bpa})_7\text{O}(\text{Py})(\text{H}_2\text{O})_{17}]$	
(S)-53	$[\text{Cd}((S)\text{-bpa})_2(\text{Py})_4]$	
(S)-54 – (S)-58	$[\text{Ln}_5((S)\text{-bpa})_8(\text{H}_2\text{O})_8]$ (Ln = La, Ce, Pr, Nd, Sm)	
(S)-59 – (S)-65	$[\text{Ln}_6((S)\text{-bpa})_7\text{O}(\text{Py})(\text{H}_2\text{O})_{17}]$ (Ln = Eu, Gd, Tb, Dy, Ho, Er, Tm)	
(S)-66 – (S)-67	$[\text{Ln}_5((S)\text{-bpa})_7\text{O}(\text{Py})_2(\text{H}_2\text{O})_9]$ (Ln = Yb, Lu)	

Chapter 1 – Background and Introduction

1.1 Phosphonic Acids and Metal Phosphonates

An organophosphonic acid with regards to organic chemistry is a term describing a class of phosphorus (V) compounds with the general formula RPO_3H_2 . These range from the simple phenylphosphonic acid **1** (Figure 1.1) – a well-studied ligand in metal phosphonate complexes¹ – to more complex, commercially important derivatives, examples of which would include the antiviral agent phosphonoformic acid² (Foscavir®) **2** and the herbicide *N*-(Phosphonomethyl)glycine³ (Roundup®) **3**.

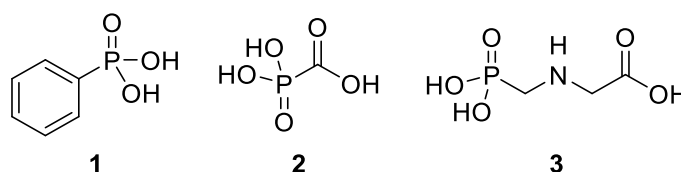


Figure 1.1 Phenylphosphonic acid **1**,¹ phosphonoformic acid **2**² and *N*-(Phosphonomethyl)glycine **3**.³

The phosphonic acid moiety, RPO_3H_2 exists in equilibrium with its two deprotonated forms – usually referred to as the mono- and di-anionic phosphonates, RPO_3H^- and RPO_3^{2-} (the exact position of equilibrium is dependent principally on the pH, see Figure 1.2). Usually, the first proton is strongly acidic while the second is several orders of magnitude less so.⁴

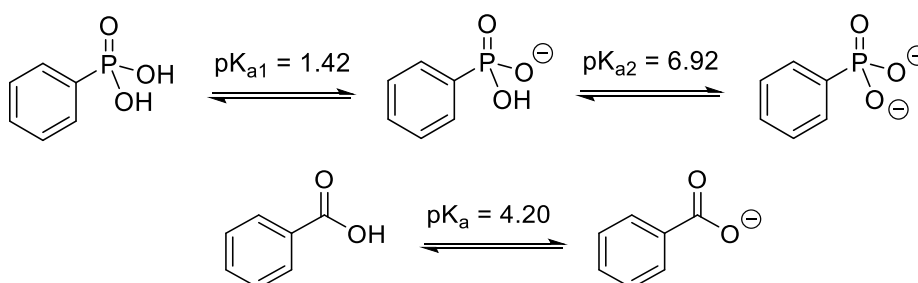


Figure 1.2 Top: Phenylphosphonic acid with its mono- and doubly deprotonated forms. Acid dissociation constants (H_2O at 25 °C) are given for each deprotonation.⁴ Bottom: Benzoic acid and its pK_a .

As Figure 1.2 shows, phenylphosphonic acid is roughly 1000 times more acidic than benzoic acid, due to the greater delocalisation present in the PO_3H^- anion compared the CO_2^- anion. Like carboxylates, phosphonates are known to be hard Lewis bases,⁵ and thus generally form strong bonds with hard metal cations M^{n+} ($n = 2$ or greater). Hard cations tend to have a small ionic radius and a high oxidation state. Hard-soft acid-base (HSAB) theory would dictate hard metal ions such as first-row transition metals and the lanthanides would be the most suited electron acceptors,⁶ and indeed, a plethora of such complexes exist in the literature, although they are

by no means the only metals which can bind phosphonates.⁷ A search of the Cambridge Crystallographic Database Centre (CCDC) reveals many first- and second-row transition metal (TM) phosphonates have had their crystal structures elucidated.⁸ Table 1 shows this.

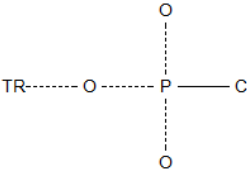
Search Function (TR = Transition Metal)	TM Phosphonate (First-row)	Published Crystal Structures	TM Phosphonate (Second-row)	Published Crystal Structures
	Sc	4	Y	36
	Ti	110	Zr	52
	V	296	Nb	5
	Cr	17	Mo	274
	Mn	229	Tc	1
	Fe	129	Ru	32
	Co	417	Rh	3
	Ni	189	Pd	20
	Cu	661	Ag	77
	Zn	458	Cd	160

Table 1 Published crystal structures of various first- and second-row transition metal phosphonates. Data accessed from the CCDC's Conquest® program on 16/07/2018.

Copper phosphonates are the most numerous, with 661 crystal structures published as of 2018. Surprisingly, there are a relatively large number of molybdenum phosphonate crystal structures published in the literature at 274 – more than many first-row transition metal phosphonates such as Cr, Mn, Fe and Ni. Perhaps the relative success of molybdenum phosphonate chemistry lies in its maturity. The archetypal ammonium phosphomolybdate – the first polyoxometalate (POM) – was discovered in 1826.⁹ POMs exist in a variety of sizes but generally consist of two principle components – a polyanionic cluster and cations to balance this large negative charge.¹⁰ Here, the oxometallic polyhedral MO_x ($x = 5$ or 6) is the basic building block. POMs have attracted attention as potential candidates for a variety of applications including water-splitting,¹¹ antiviral drugs¹² and catalysis.¹³

It is often pertinent to discuss metal phosphonates in terms of their crystal structures, in order to understand their solid-state behaviour. Solution-based studies such as NMR spectroscopy are limited in their applications here since the vast majority of metal phosphonates have unpaired electrons and thus significant line-broadening will occur.¹⁴ However, some phosphonates such as yttrium or lanthanum exist in the d^0 or f^0 states, and therefore NMR-based studies may also be used in conjunction with crystal data.

1.2 Applications of Metal Phosphonates

Metal phosphonates have garnered increasing attention in the past few years, owing to their potential applications in areas including 1) catalysis,¹⁵ such as when Clearfield and co-workers demonstrated tin phenylphosphonate functioned as an exceptional catalyst in Baeyer-Villiger oxidations.¹⁶ 2) absorption and separations,¹⁷ such as when Bein and co-workers demonstrated that a mixed NaLa phenylphosphonate **4** exhibited high selectivity towards monovalent alkali cations.¹⁸ 3) the treatment of some cancers with metal phosphonates has also been investigated – bisphosphonate ligands, such as zoledronic acid **5**, have been shown to possess efficacy against early breast cancer development.¹⁹ 4) magnetism²⁰ is another application, such as when Christou *et al.* prepared an SMM Mn_3 cluster **7** from diphenyl phosphonic acid **6**²¹ and 5) luminescence is also an attractive opportunity,²² such as when Parker *et al.* prepared specific europium phosphonates **8** that have been proposed as organelle stains for live cell imaging.²³ Figure 1.3 illustrates some of these compounds.

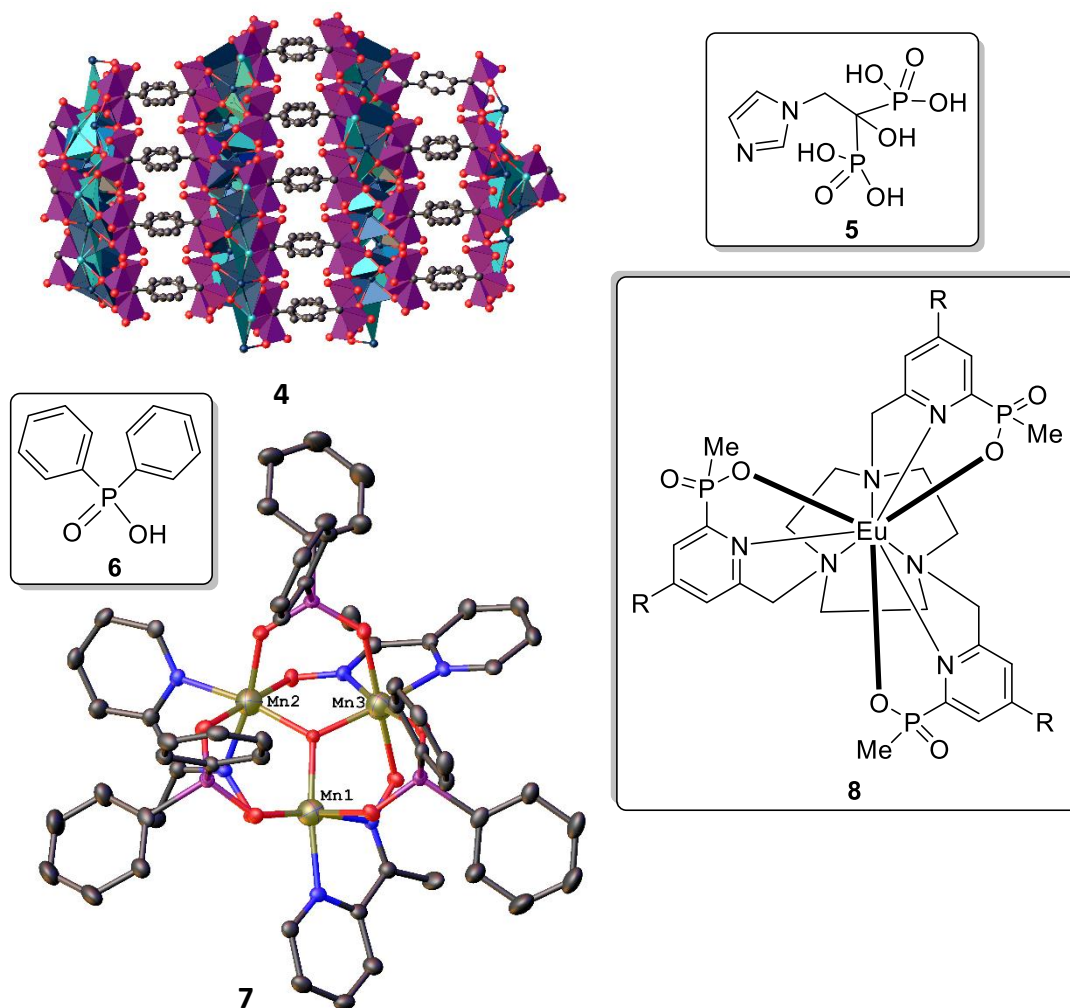


Figure 1.3 Top left: Structure of the NaLa phosphonate MOF **4** prepared by Bein and co-workers.¹⁸ Bottom left: Structure of the diphenylphosphonic acid **6** used by the Christou group to prepare the Mn_3 SMM **7**.²¹ Top right: structure of NE-58051 **5** which demonstrated high efficacy against breast cancer.¹⁹ Bottom right: Core structure of the Eu phosphonate **8** which was prepared by Parker *et al.* and demonstrated effectiveness at organelle staining.²³

As can be seen, phosphonic acids and metal phosphonates find a wide range of applications in several fields of chemistry, biology and materials science. These will be examined in greater detail in the following sections.

1.2.1 Magnetism

In the early 1990s it was discovered that a manganese acetate cluster (Figure 1.4) could retain its magnetisation in the absence of an externally-applied magnetic field at liquid helium temperatures.²⁴ The dodecametallic manganese acetate cage, $[\text{Mn}_{12}\text{O}_{12}(\text{OAc})_{16}(\text{H}_2\text{O})_4]$ (or Mn_{12}Ac in shorthand) **9** became the progenitor in a long line of so-called single-molecule magnets (SMMs). SMMs display magnetic hysteresis on the molecular scale. Hysteresis refers to the aligning of the dipoles of the molecule with an external magnetic field, which is retained even after the field is shut off. The intrinsic properties of SMMs include a high spin ground state, S , and for that spin to have easy-axis type anisotropy (deviation of the electron density from a perfect sphere, resulting in directional dependence of an external magnetic field along an energetically favourable axis – the easy axis). A large negative zero-field splitting (removal of spin microstate degeneracy for systems with $S > \frac{1}{2}$ in the absence of an external magnetic field) is also required. As attempts to synthesise more effective SMMs were undertaken, it was soon observed that control of both spin and anisotropy were essential – very high spin compounds with no spin anisotropy are not SMMs.²⁵ compound **9** was found to have an anisotropy barrier of 51 cm^{-1} , while the largest anisotropy barrier recorded in a transition metal cluster (at the date of writing this thesis) was found to be 1277 cm^{-1} . This belonged to a dysprosium metallocene species, $[(\text{Cp}^{\text{ttt}})_2\text{Dy}]^+$ ($\text{Cp}^{\text{ttt}} = 1,2,4\text{-tri(tert-butyl)cyclopentadiene}$) prepared by Layfield and co-workers.²⁶

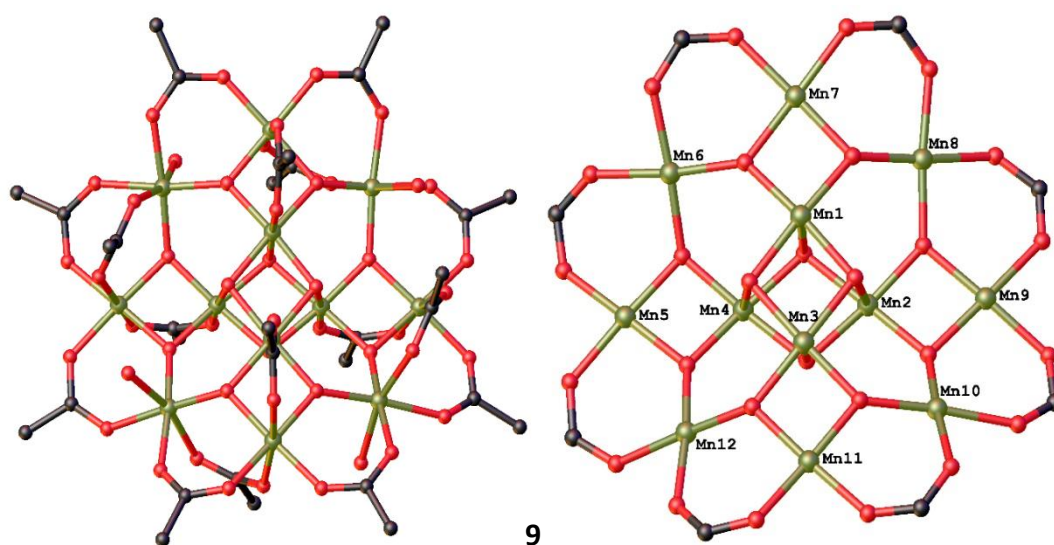


Figure 1.4 Left: Structure of Mn_{12}Ac **9** in the crystal. Right: **9** with peripheral CH_3 groups removed and Mn atoms labelled. The cube-like core with Mn(IV) atoms 1-4 can be visible.²⁴

Notwithstanding the interesting intrinsic properties of SMMs, it was soon realised they could in principle be used in new technological applications. Magnetic data storage, such as that found in common hard disk drives, is one such avenue. These store data by magnetising a thin strip of ferromagnetic material coated onto a disc (called a platter). The actual information is stored in domains – grains in the material which have different magnetic alignments to their neighbours (Figure 1.5). Multiple grains comprise a single bit.

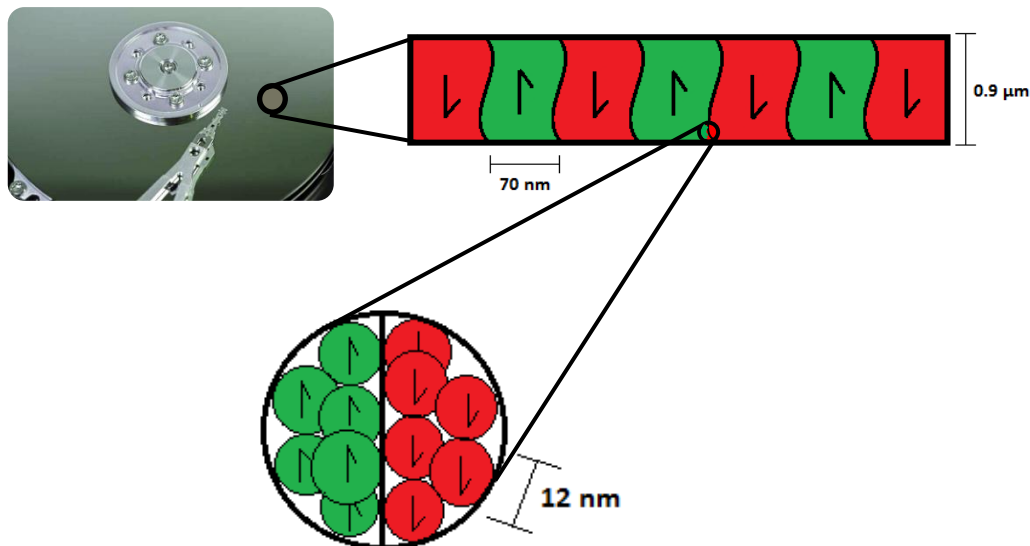


Figure 1.5 Diagrammatic representation of the domains found in the ferromagnetic material coated onto a hard-disk drive platter. Shown below is a single grain which exists at the boundary between two domains. In this example, red denotes a 0 in binary while green denotes a 1.

Current efforts in data-storage technology are focused mainly on reducing the number of grains per bit.²⁷ It is postulated that the theoretical limit in storage with contemporary ferromagnetic materials is 20 Tbit/inch².²⁸ If greater storage density can be realised (and indeed, with the advent of quantum computing, may become a necessity²⁹) then it is necessary to consider bit storage with regards to individual molecules. This is where SMMs could play a vital role.

Despite this, the true potential of SMMs can only be realised when two major obstacles are overcome. The first hurdle, as mentioned previously, is that their tendency to retain magnetisation in the absence of external magnetic fields only occurs at liquid helium temperatures. Raising the temperature even a few degrees K higher results in complete loss of magnetisation and the molecules revert back to simple paramagnets. Thus, the operating temperatures need to be somehow increased – liquid nitrogen temperatures would be a logical first milestone due to liquid nitrogen’s greater availability and ease of handling when compared to liquid helium. The second problem is successfully depositing the potential SMM material onto

a surface where the individual molecules can be addressed. Currently only a few examples of this avenue being explored exist in the literature.³⁰

It may then, beg the question, where do metal phosphonates fit into this? Well, as discussed in the previous section, by careful fine-tuning of the steric bulk on the phosphonic acid and by careful choice of co-ligand, discrete clusters could be prepared. Thus, by applying the same principles, it was reasoned that anisotropic clusters could be prepared. And indeed, this was found to be the case – there are multitudes of SMM metal phosphonates in the literature.³¹ One such example is a $\text{Cu}_{24}\text{Dy}_8$ cage **11** prepared by Winpenny and co-workers,³² from the reaction between tritylphosphonic acid **10** (Figure 1.6), $\text{Cu}(\text{OAc})_2 \cdot 4\text{H}_2\text{O}$ and $\text{Dy}(\text{NO}_3)_3 \cdot 6\text{H}_2\text{O}$ in a 1:2:1 ratio. A somewhat unwieldy structure to represent in conventional ball-and-stick format – the framework consists of an inner cube of 12 Cu(II) centres connected to an outer cube of another 12 Cu(II) centres, with eight Dy(III) centres capping each vertex of the cube (Figure 1.6).

Variable AC susceptibility measurements were performed which indicated **11** possessed frequency-dependence – characteristic of slow magnetic relaxation. Single-crystal measurements of **11** were performed using micro-SQUID analysis, and the observed hysteresis loops showed increased coercivity (resistance to an external magnetic field) as the temperature decreased (Figure 1.6). The blocking temperature was calculated to be 4.6 K.³²

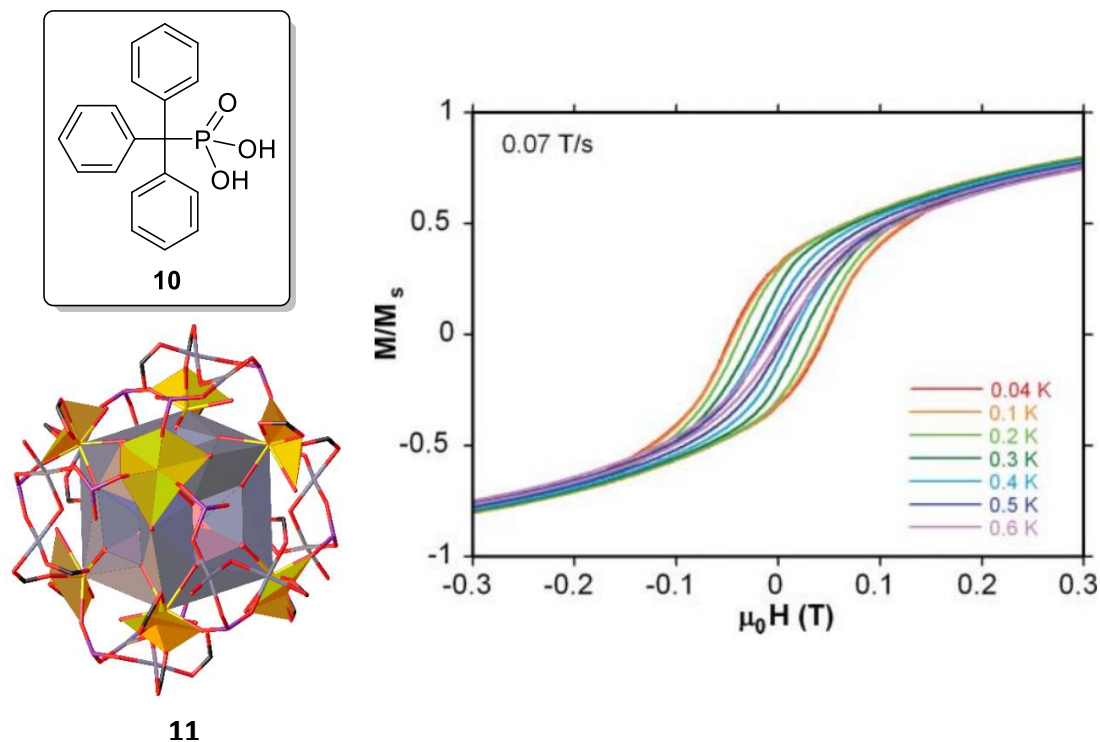


Figure 1.6 Top left: Structure of the tritylphosphonic acid ligand **10** used to prepare the $\text{Cu}_{24}\text{Dy}_8$ SMM below. Bottom left: Structure of the $\text{Cu}_{24}\text{Dy}_8$ cage **11** in the crystal (grey areas indicate Cu atoms while the yellow polyhedra capping the vertices represent Dy atoms). Right: Hysteresis loops for **11** at various temperatures. It can be seen that coercivity (the distance between the widest point of the loop) increases as the temperature decreases.³²

1.2.2 Catalysis

Metal phosphonates have demonstrated efficacy in certain catalytic transformations – almost all of which are oxidations – with a few exceptions.³³ It should be stressed the emphasis here is less on achieving optimal conversions or *ees* to complicated transformations, rather a demonstration of how standard oxidants used in common oxidation reactions such as peracids or chromium(VI)-based reagents can be avoided. Peracids are expensive, hazardous and ecologically undesirable due to the generation of carboxylic by-products, while chromium(VI) salts are known carcinogens.³⁴

In 2001, Corma *et al.* prepared a Sn β -zeolite which was found to be an efficient catalyst for Baeyer-Villiger oxidations of both saturated and unsaturated ketones with hydrogen peroxide as the oxidant.³⁵ The Baeyer-Villiger (BV) reaction is the oxidative cleavage of a carbon-carbon bond adjacent to a carbonyl, which converts ketones to esters and aldehydes to phenols, the latter *via* an ester intermediate (Figure 1.7). Traditionally, peracids such as *m*-CPBA were used as the oxidants, however these have the drawbacks of producing unwanted carboxylic acids as by-products, as well as the disadvantages listed above.³⁶ The high activity was attributed to direct activation of the ketone group, as opposed to other catalysts, which first activate the hydrogen peroxide. In 2008, Clearfield *et al.* prepared a layered Sn(IV) phenylphosphonate by reaction of tin(IV) chloride pentahydrate and phenylphosphonic acid *via* hydrothermal synthesis.¹⁶ This was found to improve conversions and selectivity for the BV oxidation of 4-methoxybenzaldehyde when compared to the Sn β -Zeolite (Table 2). Further to this, it was found that the oxidation with their phosphonates performed best when no solvent was used – the presence of any organic solvent actually decreased the performance of the catalyst.

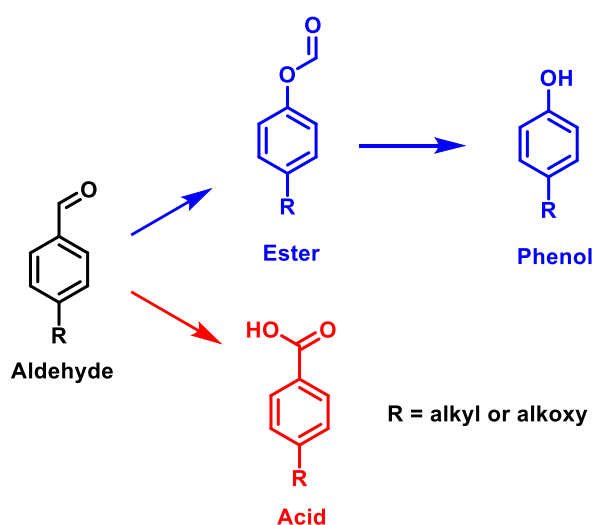


Figure 1.7 Generic reaction scheme showing the two possible pathways of the BV oxidation of an aryl aldehyde. The preferred pathway (blue) leads to the formation of an ester, which can then be converted into a phenol while the undesired pathway (red) forms the corresponding carboxylic acid.

Catalyst	Sn Content / % Wt.	Conversion / %	Selectivity for Phenol / %	Conditions
SnO ₂ β-zeolite	2	56	46	Acetonitrile solvent
Sn β-zeolite	2	79	79	Acetonitrile / 50% H ₂ O ₂
Sn Phenylphosphonate	24.5	98	100	No solvent / 30% H ₂ O ₂

Table 2 Tin content, conversion and selectivity for the BV oxidation of 4-methoxybenzaldehyde for a SnO₂ β-zeolite, the Sn β-zeolite prepared by Corma et al., and the Sn phenylphosphonate prepared by Clearfield et al.¹⁶

The postulated reasons for this marked increase in efficacy were two-fold. Firstly, the phosphonates contain ~20% Sn by weight, compared to the ~2% Sn in the zeolites. This suggests a higher density of Sn(IV) active sites on the surface of the phosphonate, leading to increased conversions. The second reason was deduced from an inspection of the scanning electron microscopy (SEM) images of the phosphonates – it was found that the layered structure contained an abundance of defects in the lattices – a stark contrast to the almost perfectly ordered Sn β-zeolite structure. It was these defect sites where a molecule of H₂O₂ could form a complex with the Sn.¹⁶

Sullivan and co-workers have developed a range of silica-supported alkyl phosphonates **12** which when coordinated to various metals (Figure 1.8), proved to be effective catalysts for allylic and benzylic oxidations,³⁷ as well as epoxidations³⁸ and conversions of sulfides to sulfoxides.³⁹ The traditional reagents for these transformations are chromium-based salts, manganese oxide or permanganate coupled with a strong peracid such as *meta*-chloroperoxybenzoic acid. As well as the aforementioned difficulties when handling these compounds such as their inherent toxicity, stoichiometric quantities of the oxidising agent are often required, making the process uneconomical – especially if performed on an industrial scale. In contrast, the alkyl phosphonates are used in typical loadings of ~0.5-5 mol% (based on the metal) and can be re-used without any evidence of metal leaching.^{37,38,39} Cheap oxidants such as tert-butylhydroperoxide and sodium bromate are employed as the oxidising agents.

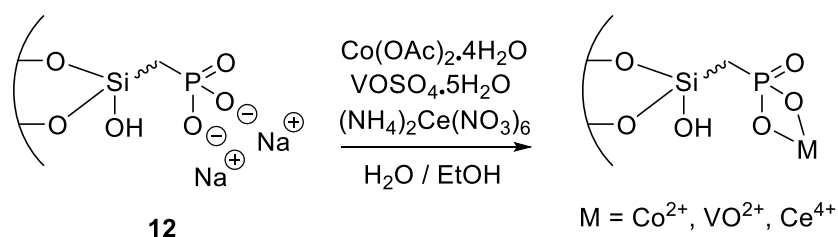


Figure 1.8 Formation of the active catalysts by reaction of the sodium phosphonate precursor with various metal salts. The chain length can either be two methylenes (ethyl) or four (butyl) methylenes long.

One important transformation is the modification of steroid derivatives. Thus, the cobalt complex of **12** was investigated in the allylic oxidation of the unsaturated steroid derivatives **13** – **16** (Figure 1.9).^{37a} The results are summarised in Table 3.

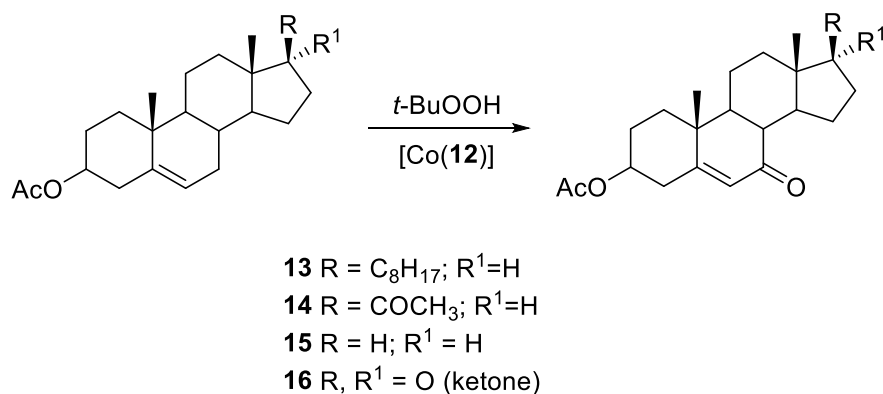


Figure 1.9 Oxidation of steroid derivatives **13** – **16** using *tert*-butylhydroperoxide and catalysed by the cobalt analogue of **12**.

Substrate	Mmol. Co	Time / h	Temperature / °C	Isolated Yield / %
13	0.096	20	55	80
13	0	24	70	0
14	0.096	24	50	97
15	0.096	24	50	70
16	0.096	24	50	86

Table 3 Results of the allylic oxidations of substrates **13** – **16**, catalysed by [Co(**12**)]. All reactions were conducted in acetonitrile on a 1 mmol scale (9.6% catalyst loading). Conversions were determined by filtration followed by washing with aq. sodium sulfite (10%) and reduction in vacuo.^{37a}

In actual fact, these silica-supported alkyl phosphonates are available commercially from Strem Chemicals Inc. as the VO(II), Mn(II), Co(II) or Ce(IV) analogues.⁴⁰ Since these are simple oxidation reactions which can be monitored by ¹H NMR spectroscopy, it would be interesting to see how our TM phosphonates compare with these derivatives already on the market. We will look at the oxidation of simpler analogues such as substituted cyclohexenes rather than the steroid derivatives.

1.2.3 Luminescence

Luminescence is a rather umbrella term which in its simplest definition refers to the emission of visible light by a material after some form of excitation. If one wishes to convey the method of excitation with a little more specificity, a prefix may be added to the term. Taking some examples of common luminescence:

Photoluminescence refers to a compound which is excited by photons (visible or UV illumination being the most common means).

Chemiluminescence refers to a compound which is excited by a chemical reaction.

Electroluminescence refers to a compound which is excited by an electrical current.

Cathodoluminescence refers to a compound which is excited by a beam of electrons or cathode rays.

Furthermore, the term “luminescence” confers no indication as to the method (or competing methods) of the actual emission process. It is often used interchangeably with the more specific methods of decay, leading to some confusion. The two most commonly encountered processes of emission are:

Fluorescence which is usually characterised by a short lifetime of the excited state (~100 ns or less).

Phosphorescence which is usually characterised by a longer lifetime of the excited state (on the order of milliseconds to seconds).

A tangible effect of these differing processes is that a material that exclusively fluoresces will immediately cease after the source of excitation (such as a UV lamp) is removed; a material that phosphoresces, on the other hand, will continue to emit an “afterglow” even after the excitation source is removed. The processes can be visually summarised in a Jabłoński diagram (Figure 1.10).

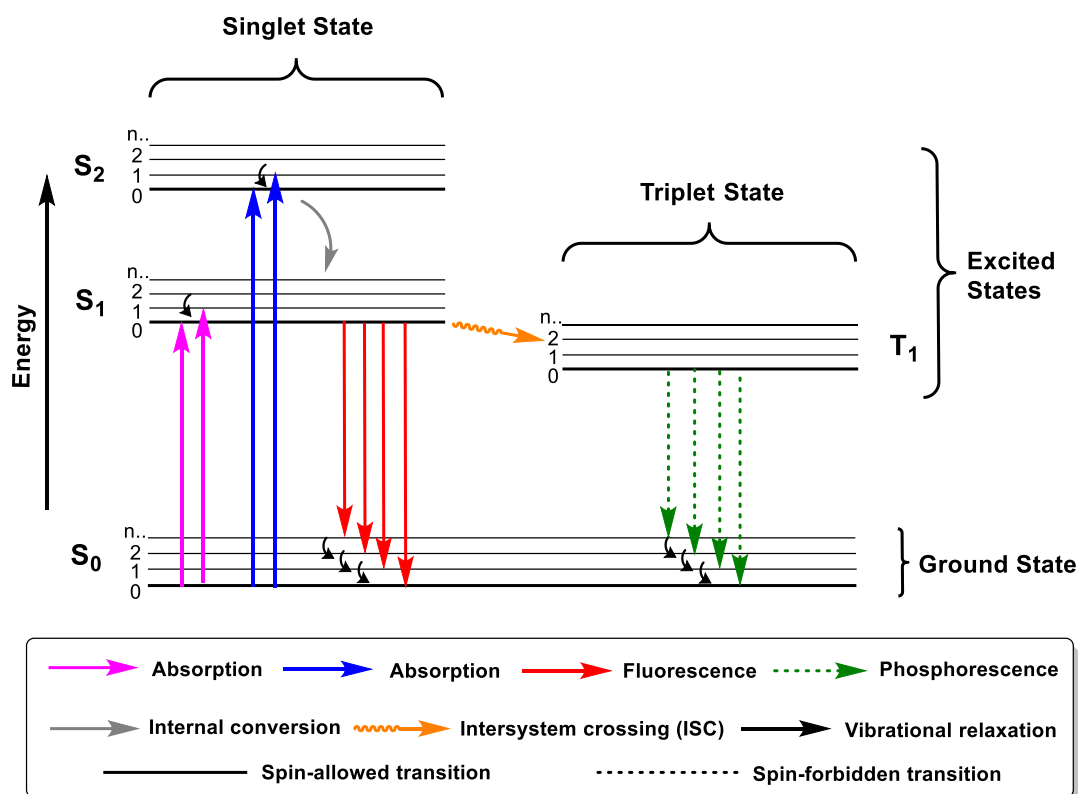


Figure 1.10 Simplified Jablonski diagram illustrating various electronic transitions. For the sake of simplicity, the energy levels of $n = 0, 1, 2$ etc. are shown with equal spacing, but in reality, the spacings converge at higher values of n . Moreover, the ground and excited states are drawn as a level plane, when in reality, they exist as potential wells.

The number of distinct materials used in commercial phosphors (species which fluoresce or phosphoresce) is rather limited – usually they consist of ceramic oxides. For instance, the phosphors in cathode-ray tube (CRT) monitors are typically based around Y_2O_3S doped with either Eu or Tb, and ZnS doped with AgCl (giving rise to red, green and blue respectively). Organic-inorganic hybrid compounds such as metal phosphonates provide the opportunity to bridge the gap between the high tunability of the organic moieties and the metal atoms which provide the mechanism for the actual luminescence. The metals alone will emit at specific wavelengths, but when bound to the metals, the ligands allow these wavelengths to be shifted to different frequencies, or can suppress or accentuate certain emissions, leading to different colours and intensities.

A significant number of lanthanide phosphonates exhibiting attractive luminescent properties have been published in the literature over the last few decades, many of which are described along with their luminescence properties in the review by Mao.²² Many lanthanide compounds fluoresce when exposed to UV light, with the majority of the electronic transitions being governed by rearrangement of the f -electrons, commonly known as the $f \rightarrow f$ transitions.

Chen *et al.* prepared a number of chiral one-dimensional lanthanide phosphonate chains (Ln = Eu, Gd, Tb, Dy) *via* the hydrothermal method.⁴¹ The phosphonic acid utilised was (*S*)-(phosphonomethyl)-L-proline ((*S*)-**17**, Figure 1.11), which itself was prepared from L-Proline. Enantiopure proline was chosen as the precursor since chiral organic-inorganic frameworks are potentially applicable in asymmetric catalysis and enantioselective separations.⁴² After hydrothermal treatment, colourless block crystals of each of the four lanthanide phosphonates were isolated – all of which were found to be isostructural with each other. Solid state photoluminescence studies were conducted on the Eu and Tb derivatives, both of which were found to be intensely fluorescent. Figure 1.11 shows the structure of the Eu derivative (*S*)-**22** in the crystal, as well as its emission spectrum.

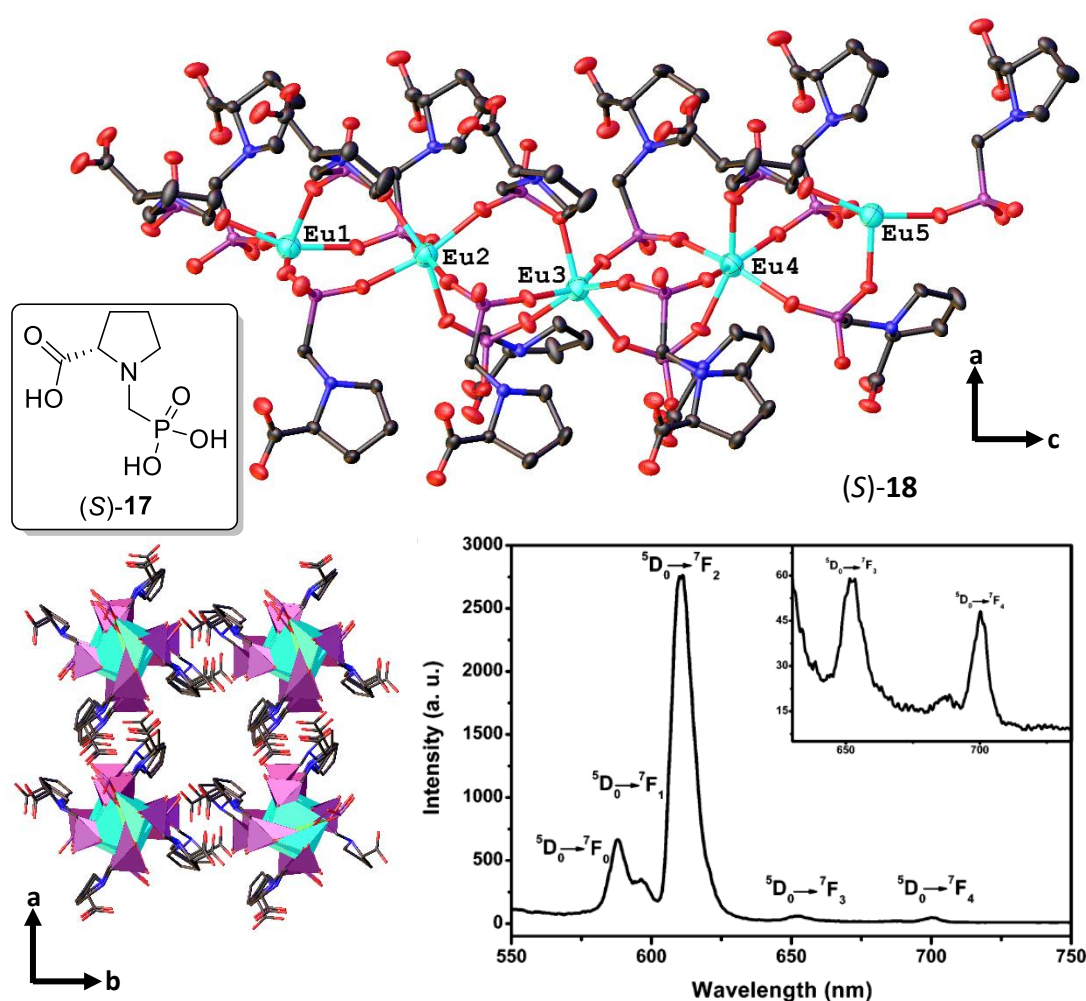


Figure 1.11 Top: Structure of (*S*)-(phosphonomethyl)-L-proline (**17**) and structure of the helical europium phosphonate chain (**18**) in the crystal (hydrogen atoms omitted). Bottom left: View of (**18**) down the *c*-axis with europium and phosphorus atoms depicted as polyhedra, with the channel forming between four separate chains. Bottom right: Solid-state emission spectrum of (**18**) ($\lambda_{\text{ex}} = 249$ nm) with all major *f* \rightarrow *f* transitions shown.⁴¹

The result is an infinite helical chain (by virtue of the chirality in (S)-**17**) extending down the *c*-axis. One important property of these chains are the complete lack of water molecules coordinated to the lanthanide atoms – these are known to quench the fluorescence properties of lanthanide complexes.⁴³ A lack of bound aqua ligands implies complete encapsulation of the europium ions by the ligand has occurred – this is an essential attribute for strong emission *via* fluorescence, since interaction with solvent molecules is known to facilitate the undesired non-radiative decay processes.⁴³ The Tb analogue, (S)-**19** also produced strong solid-state emission when excited by UV light. Its emission spectrum is shown in Figure 1.12.

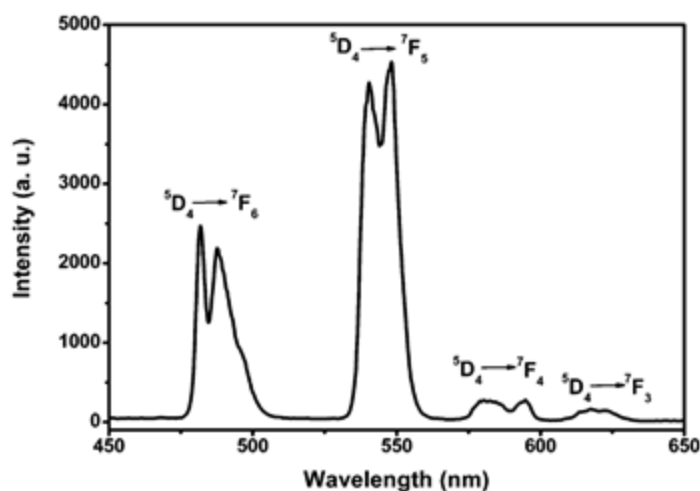


Figure 1.12 Solid-state emission spectrum of the terbium(III) phosphonate analogue (S)-**19** ($\lambda_{ex} = 248$ nm) with all major $f \rightarrow f$ transitions shown.⁴¹

Therefore, by careful fine-tuning of the ligand, a Eu or Tb fluorescent marker with highly specific intensities in its emission bands could be synthesised. Lanthanide phosphonates can, and have fulfilled this role.⁴⁴ With regards to security tagging, the advantages of a lanthanide-based marker as opposed to organic or transition-metal based markers would be that any fake organic fluorescent marker which glows red or green could still be identified as counterfeit, since the relative intensities of the sharp emission lines produced by the lanthanide complex can be easily identified, and are distinctive for each complex. On the other hand, the broad emission bands of a genuine and counterfeit transition metal complex would be almost impossible to distinguish with UV-vis spectroscopy.

In conclusion, we would also like to examine the photoluminescence properties of any europium and terbium phosphonates which we will prepare. Since the interaction between lanthanide cations and anionic ligands is coulombic, the phosphonate moiety would be an ideal candidate for a strongly binding ligand. Having seen that the photophysical properties of Eu(III) and Tb(III) complexes are desirable, we will attempt to prepare analogous compounds using chiral phosphonic acids in order to establish their properties for comparison.

1.2.4 Absorption and Separation

The successful selective absorption, and by inference, separation of specific metals, liquids and gases is of critical importance in the modern world and finds applications in a multitude of industrial processes including water treatment,⁴⁵ metal recycling,⁴⁶ ion exchange separations⁴⁷ and gas sensing.⁴⁸ Zeolites and metal-organic frameworks (MOFs) such as POMs can generally fulfil these roles with varying degrees of success,⁴⁹ although one feature that remains constant is the rigidity of the framework. It was believed that this was an essential structural feature since flexibility would lead to a collapse of the structure.⁵⁰ This perspective has since been fundamentally changed with the discovery of flexible porous frameworks capable of expanding their unit cell volumes (some up to 170%⁵¹) with the connections between the inorganic and organic moieties remaining intact.⁵² Further to this, some of these MOFs have been shown to adapt their pore sizes to accommodate guest molecules of varying sizes, leading to high specificity for certain guest atoms or molecules.⁵³

In 2009, Bein and co-workers developed a flexible phosphonate MOF based on the 1,4-phenylenebis(methyldiylne)-tetrakis(phosphonic acid) ligand **20** (Figure 1.13).¹⁸ Reaction of this ligand with lanthanum(III) nitrate hexahydrate and sodium hydroxide in deionised water *via* hydrothermal synthesis yielded the sodium lanthanum phosphonate NaLa[(**20**)]·4H₂O, **4**. The Na⁺ ions that resided in the framework's cavities were found to completely exchange with other monovalent cations (Li⁺, K⁺ and Rb⁺ but not Cs⁺) when the phosphonate was stirred in a saturated solutions of LiCl, KCl and RbCl. This was achieved by the structure expanding and contracting its pore sizes to accommodate the various monovalent cations, from 0.76 Å (Li⁺) to 1.52 Å (Rb⁺). Remarkably, divalent alkali earth cations (Mg²⁺, Ca²⁺, Sr²⁺, Ba²⁺) and some divalent transition metal cations (Mn²⁺, Ni²⁺, Cu²⁺) were completely rejected by **4** (Figure 1.13). This phosphonate therefore provided the means to separate mono and divalent cations in a cheap and facile manner – the insoluble phosphonate is simply added to a solution containing the mixture, stirred under ambient conditions for 72 hours and filtered.

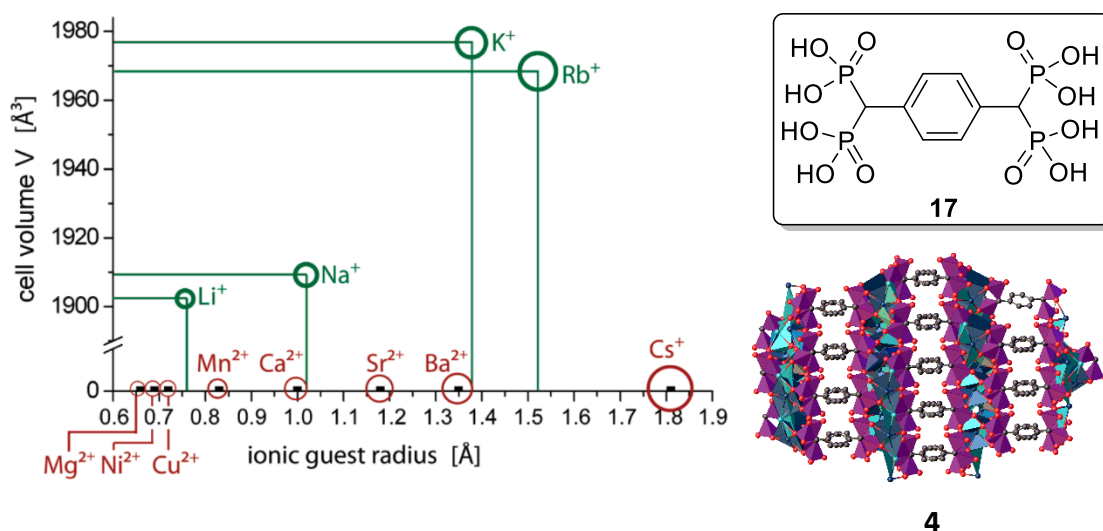


Figure 1.13 Left: Graphical representation of how the cell volume of **4** expands or contracts to accommodate the various monovalent cations (excluding Cs^+). As can be seen, divalent cations are completely rejected. Top right: Structure of the tetrakis-phosphonic acid ligand **17** used to prepare the NaLa phosphonate. Bottom right: Structure of the NaLa phosphonate **4** in the solid-state with phosphonates represented by polyhedra.¹⁸

1.2.5 Medicinal

Nitrogen-containing bisphosphonates (NBPs) have proven to be effective at strengthening bones and preventing osteoporosis.⁵⁴ Risedronic acid **21** (often sold commercially as its sodium salt) is one such example of an established bisphosphonate drug (Figure 1.14). Zoledronic acid **5** is another example (Figure 1.211). These drugs function by inhibiting the function of osteoclasts (specialised bone cells that break down other bone tissue). Since osteoporosis is caused by these tissue destroying cells being more active than the tissue-forming cells, the NBPs help to restore the equilibrium of the two.

Furthermore, NBPs such as the aforementioned have demonstrated utility in treating osteolytic bone metastasis (secondary tumour growth in the bones). They exhibit anti-tumour activity *in vitro* and can reduce skeletal tumour burden and reduce metastases *in vivo*.¹⁹

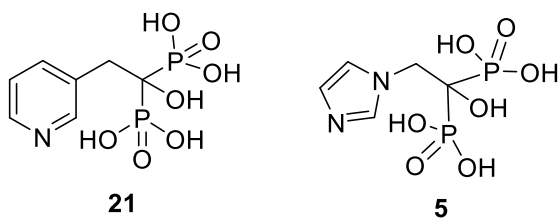


Figure 1.14 Risedronic acid **21** and zoledronic acid **5**.⁵⁴

1.3 Nomenclature of Metal Phosphonate Binding

The doubly deprotonated form of the phosphonic acid molecule, RPO_3^{2-} contains three identical oxygen donor atoms and, in principle, can bind up to nine metal ions *via* the nine lone pairs of the three oxygen atoms. In order to convey the coordination of such potentially high denticity ligands in the most succinct manner possible, Harris notation is used.⁵⁵ Harris notation describes the binding mode in the general form $[\text{X.Y}_1\text{Y}_2...\text{Y}_n]$ where X is the total number of metal ions in the whole system, and each value of Y refers to the number of metal atoms bound to the donor atoms. The ordering of Y is dictated by the Cahn-Ingold-Prelog priority rules – donor atoms of higher atomic number are listed first (although for phosphonates this rule is nullified as all atoms are oxygen). Figure 1.15 illustrates some common binding combinations with their respective Harris notation.

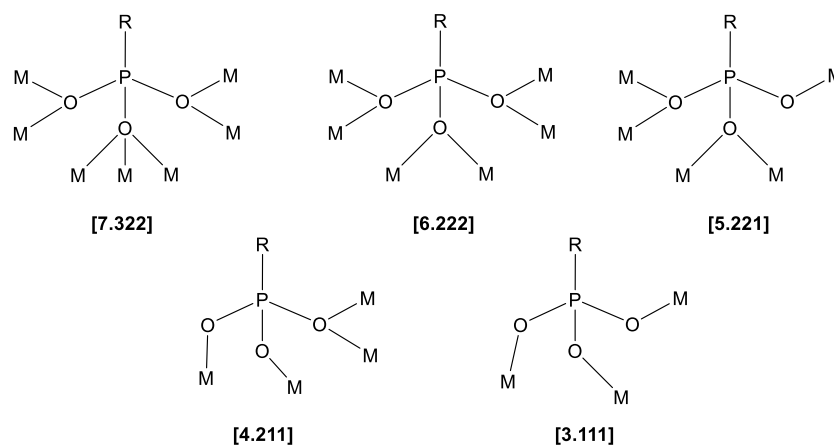


Figure 1.15 Examples of some common binding modes with their respective Harris notations.

For instance, if we consider the hexametallic cobalt phosphonate **22**, prepared by the Winpenny group (Figure 1.16),⁵⁶ we can deduce that the binding mode for the sole phosphonate ligand in **22** is [6.222] – six cobalt atoms are bound to the phosphonate, with each oxygen binding to two cobalts.

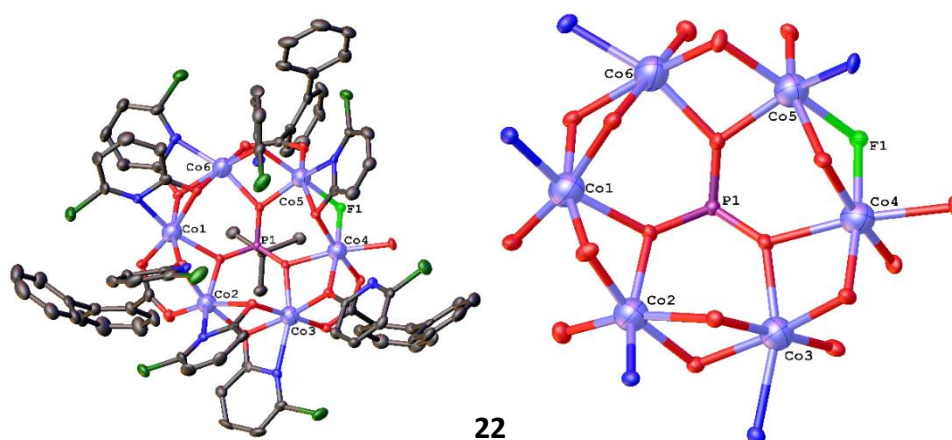


Figure 1.16 Left: Crystal structure of the hexametallic cobalt phosphonate cluster **22** prepared by the Winpenny group.⁵⁶ Right: Core of the structure with peripheral ligands omitted. This will be discussed in the following section as an example of the ancillary ligand method of preparing molecular metal phosphonates.

So far, we have not considered the possibility of more than one oxygen atom of the phosphonate binding to the same metal. Should this be the case, there is an additional layer to the notation which must be incorporated. Consider the following binding modes in Figure 1.17.

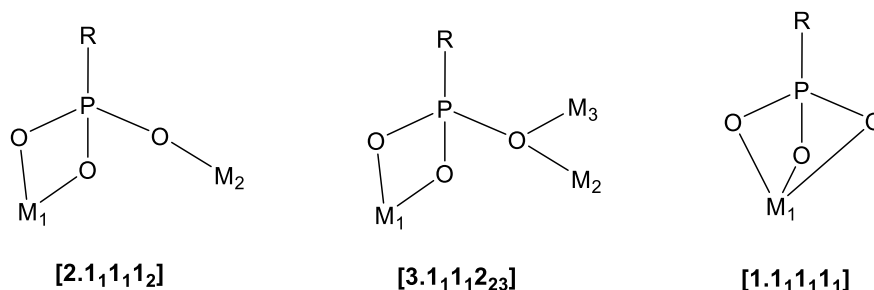


Figure 1.17 Further examples of common binding modes with their respective Harris notations.

Again, the leading X-value – which determines the total number of metals bound by the ligand – remains the same as before. However, a subscript is introduced for the Y-values – this distinguishes the different metals in the system – which now becomes a necessity, since it is now required to know which metal is chelated and which binds individually. The subscript number indicates the arbitrarily assigned metal number, which is usually labelled beforehand in the crystal structure (see Figure 1.31). To take the second binding configuration as example, there are three metal ions in total bound by the phosphonate, so the X value is 3. Two oxygen atoms chelate to M_1 , therefore both the first two Y values contain the subscript 1. The final oxygen binds to M_2 and M_3 , therefore its value is 2. However, it must also contain the two individual subscripts for M_2 and M_3 (as it does not chelate to these). The Harris notation is therefore $[3.1_11_12_{23}]$. Figure 1.18 illustrates this.

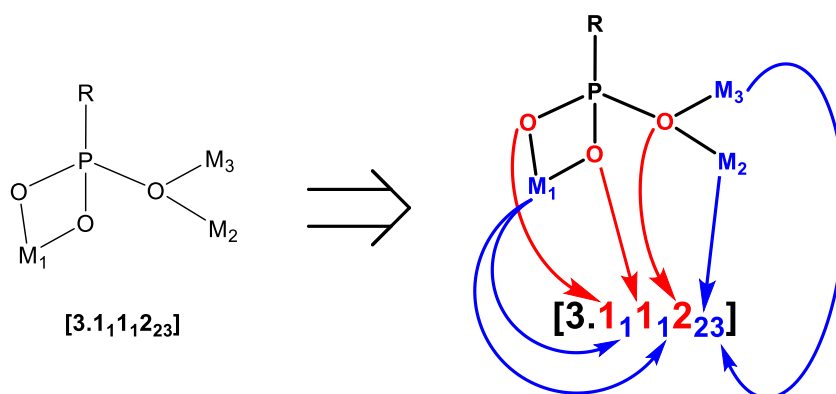


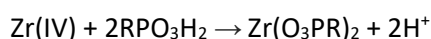
Figure 1.18 Visual interpretation of how the Harris notation is derived for chelating ligands.

Thus, with some practice, Harris notation allows for almost instant recognition of which metals bind to which atom, and how many chelate (if any). Henceforth, we shall describe the binding modes of the phosphonate clusters presented in this thesis using this notation.

At this juncture it would be prudent to briefly summarise the history of metal phosphonate chemistry while applying the Harris notation to these examples. Should wider reading on the topic be deemed necessary, there exist several excellent reviews on metal phosphonate chemistry. Clearfield and Demadis' *Metal Phosphonate Chemistry: From Synthesis to Applications* provides a comprehensive synopsis of how this interdisciplinary field has developed over the last 25-30 years.⁵⁷ The summary which will be described here will be mostly limited to the reaction of phenylphosphonic acid with metals, as it will be shown that this phosphonic acid is the most sensible benchmark for our studies. Phenylphosphonic acid is a well-studied ligand in coordination chemistry – it is cheap, commercially available and soluble in a wide range of non-polar and polar solvents such as simple alcohols and even water. This allows its coordination behaviour to be directly compared in both aqueous and organic media.¹

1.3.1 Zirconium Phosphonates

In 1978, Alberti *et al.* directly reacted various phosphonic acids with a source of Zr(IV), producing the first zirconium phosphonates.⁵⁸ In general,



It was known that zirconium diphenylphosphonate $\text{Zr}(\text{O}_3\text{PPh})_2$ **23** (Figure 1.19) formed an extended layered structure – each layer consisted of an infinitely-long $\text{Zr}(\text{O}_3\text{PPh})_2$ chain, and these chains were stacked on top of each other. Ascertaining the exact structure from single crystal X-ray diffraction proved difficult due to its virtually insoluble nature. It was not until 1993 that Poojary *et al.* solved the structure by X-ray powder diffraction.⁵⁹ The structure is indeed layered – virtually identical to that of zirconium phosphate.⁶⁰ The phenyl rings are tilted 30° relative to the grain of the chains. The interlayer Ph...Ph spacings are 13.7 – 14.7 Å.

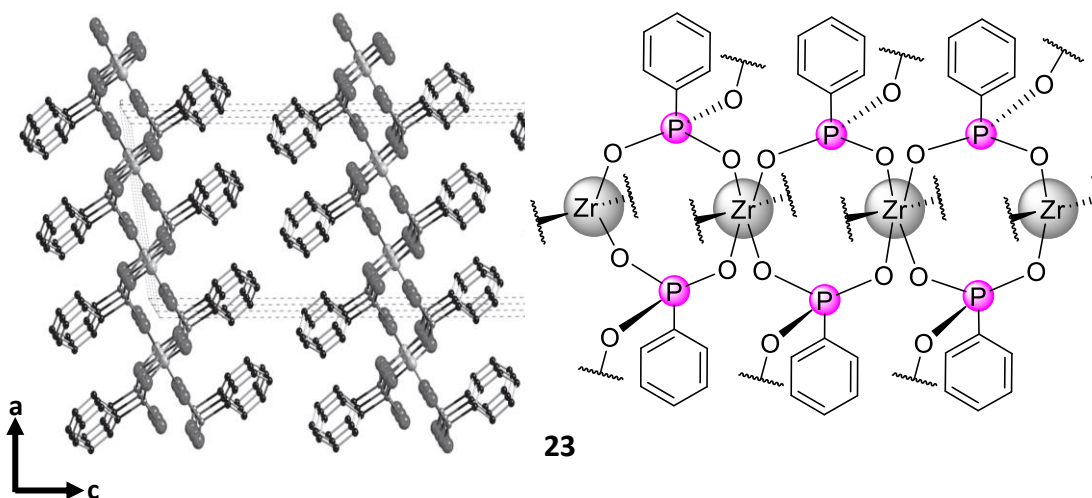


Figure 1.19 Left: α -Zirconium phenylphosphonate, $\text{Zr}(\text{O}_3\text{PPh})_2$ **5**, as viewed down the *b*-axis.⁵⁸ Right: Representation of the connectivity of the Zr atoms to the phosphonates in one of the layers.

Relating back to the earlier discussion on nomenclature, the phosphonates in **23** bind in a [3.111] configuration (the third oxygen in the phosphonate shown in Figure 1.19 binds to another layer of Zr atoms).

1.3.2 Iron Phosphonates

In 1990, Rouxel *et al.* prepared the iron(III) phosphonate species $\text{HFe}(\text{PhPO}_3\text{H})_4$ **24** in dichloromethane from iron oxychloride and an excess of phenylphosphonic acid.⁶¹ Again, the compound is layered in structure (similar to the α -ZrP type motif) with each of the Fe^{3+} atoms octahedrally coordinated by oxygen atoms from six different phosphonate groups. Two of these phosphonate groups bind in a monodentate [2.110] manner while the other four bridge in a [2.110] manner (Figure 1.20).

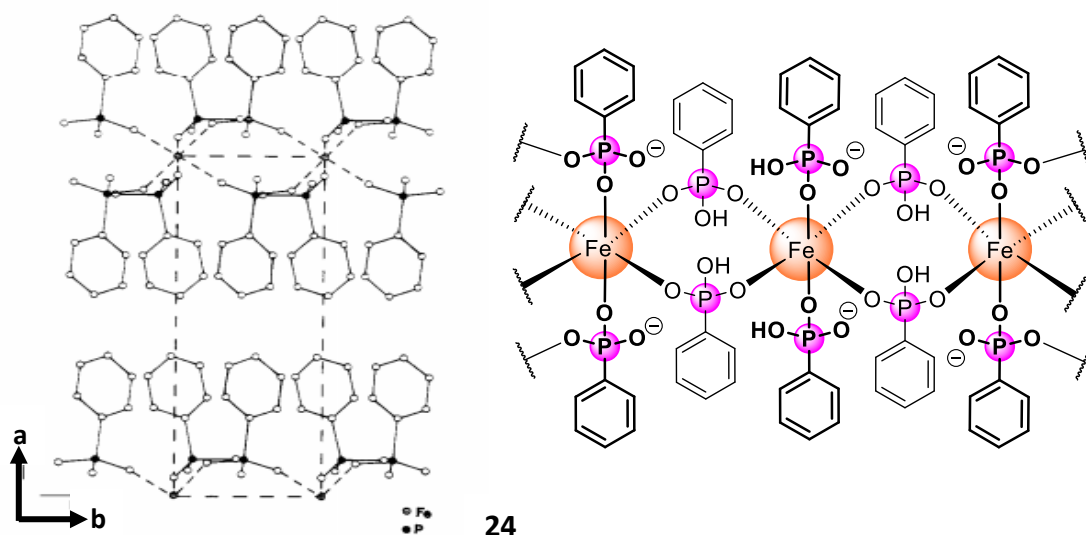


Figure 1.20 Left: Structure of $\text{HFe}(\text{PhPO}_3\text{H})_4$ **6** in the crystal as viewed down the c-axis.⁶¹ Right: Representation of the connectivity of the Fe atoms to the phenylphosphonic acid ligands.

It was noted that when the solvent was switched from dichloromethane to acetone, the rate of consumption of FeOCl was impeded i.e. the rate of reaction to form the layered phosphonate was slowing. The reaction rate was further reduced when water was used as the solvent. This was attributed to decreased association of phenylphosphonic acid with the solvent when performed in dichloromethane, as opposed to acetone and water, which through hydrogen bonding, would hinder the interactions of the active oxygen atoms in phenylphosphonic acid with the $\text{Fe}(\text{III})$ ions. This illustrates the importance of solvent choice in phosphonate chemistry. In the case of **24**, the solvent choice only affected the rate of reaction – the product remained the same. However, as we shall see later, different solvents can sometimes lead to different products entirely, or even determine if a product forms at all.

Another group of common iron(III) phosphonate motifs are the oxo-centred tri-iron clusters, $[\text{Fe}^{\text{III}}_3(\mu_3\text{-O})]$. Figure 1.21 is a typical example from Winpenny *et al.* – $[\text{Fe}^{\text{III}}_4(\mu_3\text{-O})(\text{Cl})(\text{O}_3\text{P-Ph})_3(\text{O}_2\text{C-Ph})_3(\text{py})_5]$, **25** – formed from the reaction of PhPO_3H_2 with $[\text{Fe}^{\text{III}}_3(\mu_3\text{-O})(\text{O}_2\text{CMe})_6(\text{OH}_2)_3](\text{NO}_3)$ in pyridine.⁶² The Fe1-O1-Fe2, Fe1-O1-Fe3 and Fe2-O1-Fe3 angles are almost exactly 120° apart and the N1, N2 and N3 atoms are virtually coplanar, giving the appearance of a central propeller-like structure with the phosphonates and final Fe centre lying out of plane. Each of the three phosphonate ligands bind in a [3.111] manner. Furthermore, there is a lone chloro ligand bound to Fe3.

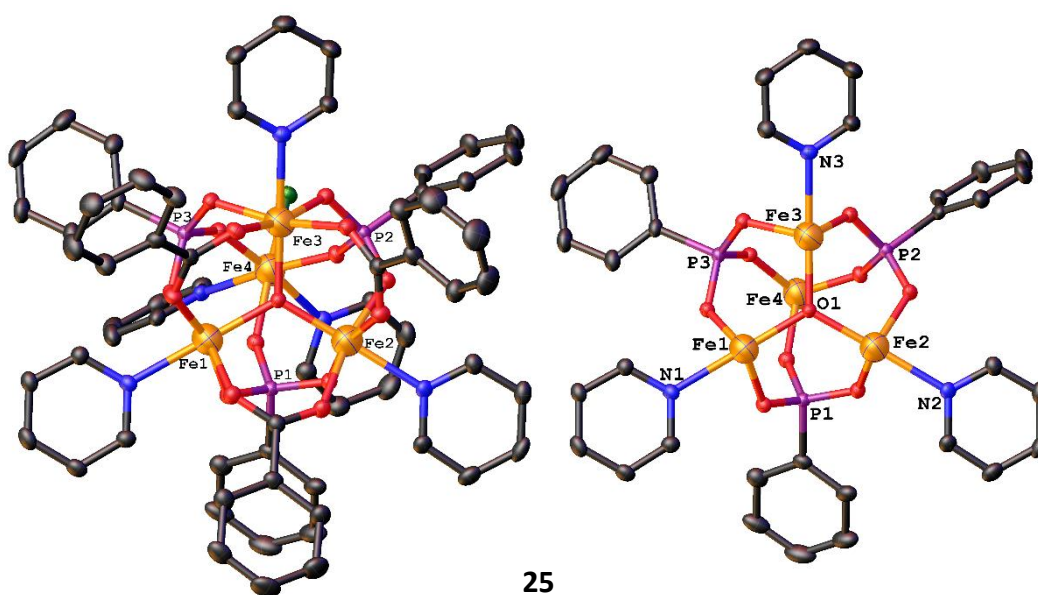


Figure 1.21 Left: Structure of $[\text{Fe}^{\text{III}}_4(\mu_3\text{-O})(\text{Cl})(\text{O}_3\text{P-Ph})_3(\text{O}_2\text{C-Ph})_3(\text{py})_5]$ **25** in the crystal. Right: Structure of $[\text{Fe}^{\text{III}}_4(\mu_3\text{-O})(\text{Cl})(\text{O}_3\text{P-Ph})_3(\text{O}_2\text{C-Ph})_3(\text{py})_5]$ core with peripheral ligands omitted.⁶² This will be discussed in the following section as an example of the ancillary ligand method of preparing molecular metal phosphonates.

Unlike the previous examples, this metal phenylphosphonate does not form a layered structure, but instead forms discrete Fe_4 clusters. As will be explained in the following section, this was achieved by starting with an iron carboxylate cage rather than an iron salt. The carboxylate ligands were substituted for phenylphosphonate ligands in the subsequent reaction, leading to the formation of **25**. Pyridine was added as a secondary ligand and has also incorporated itself onto the structure of **25**.

1.3.3 Lanthanide Phosphonates

Lanthanide phosphonate chemistry could still be considered a fledgling field when compared to that of its transition metal phosphonate counterpart. An inspection of the CCDC for lanthanide phosphonates using the same search parameters as for first- and second-row transition metals (Table 1) reveals that there are, in general, fewer total structures published (Table 4).

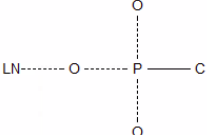
Search Function (LN = Lanthanide)	Ln Phosphonate	Published Crystal Structures	Ln Phosphonate	Published Crystal Structures
	La	104	Tb	65
	Ce	49	Dy	66
	Pr	55	Ho	27
	Nd	76	Er	44
	Pm	0	Tm	4
	Sm	45	Yb	20
	Eu	83	Lu	10
	Gd	114		

Table 4 Published crystal structures of various lanthanide phosphonates. Data accessed from the CCDC's Conquest® program on 16/07/2018.

Indeed, the most interesting area of lanthanide phosphonate chemistry – at least in terms of magnetism – are the mixed Ln-TM clusters.⁶³ However, we shall restrict ourselves in this section to discussing only phosphonates of homometallic origin. In 1992 Clearfield and co-workers successfully prepared lanthanum phenylphosphonate, $[\text{La}(\text{O}_3\text{PPh})(\text{HO}_3\text{PPh})]$ **26** and solved its structure (Figure 1.37).⁶⁴ The crystal system is triclinic with a layered structure. Each lanthanum atom is 8-coordinate – one oxygen atom chelates to a lanthanum, with the remaining two oxygens bridging to an adjacent lanthanum each (Figure 1.22).

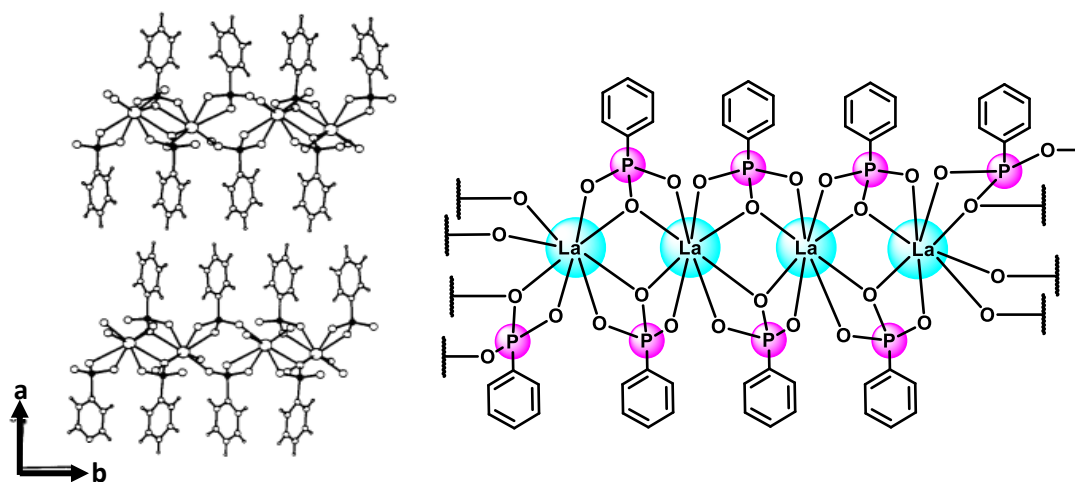


Figure 1.22 Left: Structure of $[\text{La}(\text{O}_3\text{PPh})(\text{HO}_3\text{PPh})]$ in the crystal, as viewed down the c -axis.⁶⁴ Right: Representation of the connectivity of the La atoms to the phosphonates.

Assigning the binding of the phosphonates in Harris notation here becomes somewhat tricky, due to the nature of the species and presence of chelating oxygens, which requires distinguishing between metals. However, **26** is polymeric, with all lanthanum atoms being equivalent. Therefore, to differentiate between these, we arbitrarily number the lanthanum atoms in an alternating fashion: La₁, La₂, La₁, La₂... Now it is possible to describe the binding of each phosphonate as [2.1₁2₂1₂] (remembering that the ordering of the Y-values is inconsequential here since all atoms are oxygen). Although it is not pertinent for phosphonates, if the ligand were to contain different atoms capable of binding (such as nitrogen or sulfur), then the ordering of the Y-values would become a necessity. The ligand 6-(diethylamino)-2-hydroxy-4-sulfanyl-1,3,5-triazine **27** (Figure 1.23) prepared by the Winpenny group is one such example.⁶⁵ It contains three heteroatoms (nitrogen, oxygen and sulfur) and exhibited a multitude of possible binding modes when bound to cobalt. These are represented in Figure 1.38.

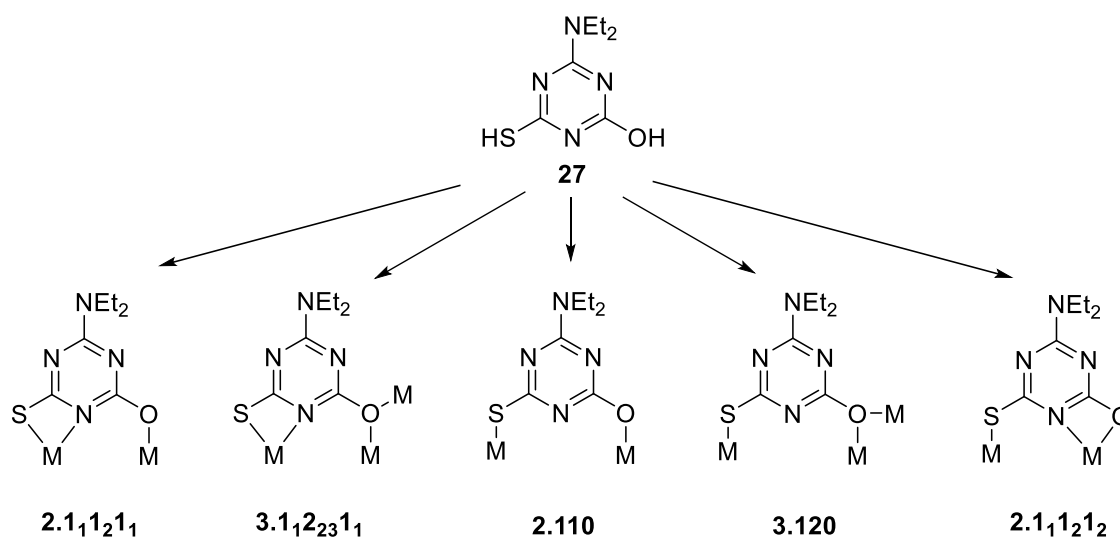


Figure 1.23 Structure of the ligand 6-(diethylamino)-2-hydroxy-4-sulfanyl-1,3,5-triazine **27** and its five experimentally found methods of binding to cobalt. The Harris notations for each binding configuration are shown below.

Since the Cahn-Ingold-Prelog priority rules use atomic number as the parameter for assigning priority,⁶⁶ in this instance it would be S > O > N. This would be the order of the corresponding Y-values. Taking the leftmost binding configuration from Figure 1.23 as an example, it can be seen that the sulfur and nitrogen atoms chelate the first cobalt, while the second cobalt binds in a monodentate fashion to the oxygen. The X value is therefore 2, from the two cobalt atoms binding in total. The first Y value (which corresponds to the sulfur atom) is bound to one cobalt, so its value is 1, and since it chelates, its subscript value is 1 – to represent the arbitrarily

assigned first cobalt. The second Y value corresponds to the oxygen. This binds to one cobalt, so its value is 1. It binds to the second cobalt making its subscript value 2.

Finally, the third Y value corresponds to the nitrogen atom. It binds to one cobalt, giving it a value of 1. Furthermore, it binds to the same cobalt that the sulfur does, so its subscript value is the same as that for sulfur, which is the first cobalt atom.

As seen with all but one example, it is evident that the simple reaction between a metal salt and phenylphosphonic acid in the presence of a solvent results in the formation of infinite polymeric chains, which usually manifests itself as waxy precipitates. The literature of the early days of metal phosphonates is dominated with analogous structures to the ones shown here⁵⁷ – chemists did not fully understand how to control the coordination environments in order to prevent polymerisation.⁵⁷

Nowadays, there are several methods which can be employed in order to inhibit polymerisation and bias the chemical system towards producing discrete clusters (as in Figure 1.32) or even monometallic metal phosphonates. By carefully controlling the solvent system and incorporating secondary ligands (in this case pyridine and benzoic acid), a distinction between forming polymeric species and forming discrete clusters can be achieved. Controlling this distinction is important, since polymeric phosphonate species such as the aforementioned NaLa phosphonate **4** and the Sn(IV) phenylphosphonate excel at absorptions / separations and catalysis. The presence of pores in their lattices allows for a high frequency of guest-host interactions which are necessary for these processes to occur. Consequently, if one intends to prepare an SMM with a phosphonic acid then this requires the formation of discrete phosphonate clusters such as **7** or **11**, since these species must be molecular and not polymeric.

1.4 Controlling the Morphology/Topology of Metal Phosphonates

As we have seen in Section 1.3, the early days of metal phosphonate chemistry contained almost exclusively layered polymeric structures incorporating simple phosphonic acids such as phenylphosphonic acid. As this field of chemistry developed, it became possible to modify the experimental conditions in order to prevent polymerisation. While the formation of polymeric phosphonate species would almost certainly (and indeed does) find many applications as we have seen in Section 1.2, forming discrete clusters makes it amenable to study these species by other analytical techniques. The polymers are usually insoluble and non-crystalline, which prevents most conventional methods of analytical chemistry (solution-based NMR, UV-vis absorption/emission, single crystal X-ray diffraction) from applying. As a fitting testament to this, if one considers the aforementioned zirconium phenylphosphonate, it took 15 years from when it was first prepared to unambiguously assign its structure. Before this time, the structure could only be inferred to be similar to zirconium phosphate, whose structure was known.

There are three main methods⁶⁷ which can be employed (either individually or in tandem) to disfavour the formation of polymers and favour the formation of discrete clusters or monomeric phosphonates, or vice versa.

1.4.1 Employing Phosphonic Acids with Steric Encumbrance

An inherent feature of early metal phosphonates that quickly becomes apparent is that the phosphonic acid precursors used often contained small and unhindered R groups such as methyl-, ethyl-, or as we have seen, phenylphosphonic acid. However, if the steric bulk of the organic group bound to the phosphonic acid moiety is increased, the vacant coordination sites of metals which would otherwise accommodate another phosphonic acid (and thus lead to polymerisation) start to become blocked. This has the effect of only allowing a metal to bind to usually one or two phosphonic acids before its inner sphere of coordination becomes completely obstructed, and, unless the metal forms small clusters *via* bridging phosphonates, no further coordination occurs. The result is a discrete complex or cluster which is now, more often than not, soluble in a variety of solvents and possible to crystallise.^{67a,67b}

In 2007, Winpenny *et al.* synthesised tetrametallic Mn₄, Co₄ and Cu₄ clusters of the form [M₄(O)(Ph₃CPO₃)₄Py₄] (M = Mn, Co, Cu) using the aforementioned bulky tritylphosphonic acid **10** (Figure 1.40) in the presence of pyridine.⁶⁸ Here, the trityl groups were postulated to discourage unwanted polymerisation, and this indeed was the case. Figure 1.24 illustrates the Mn₄ core of the manganese analogue, **28**.

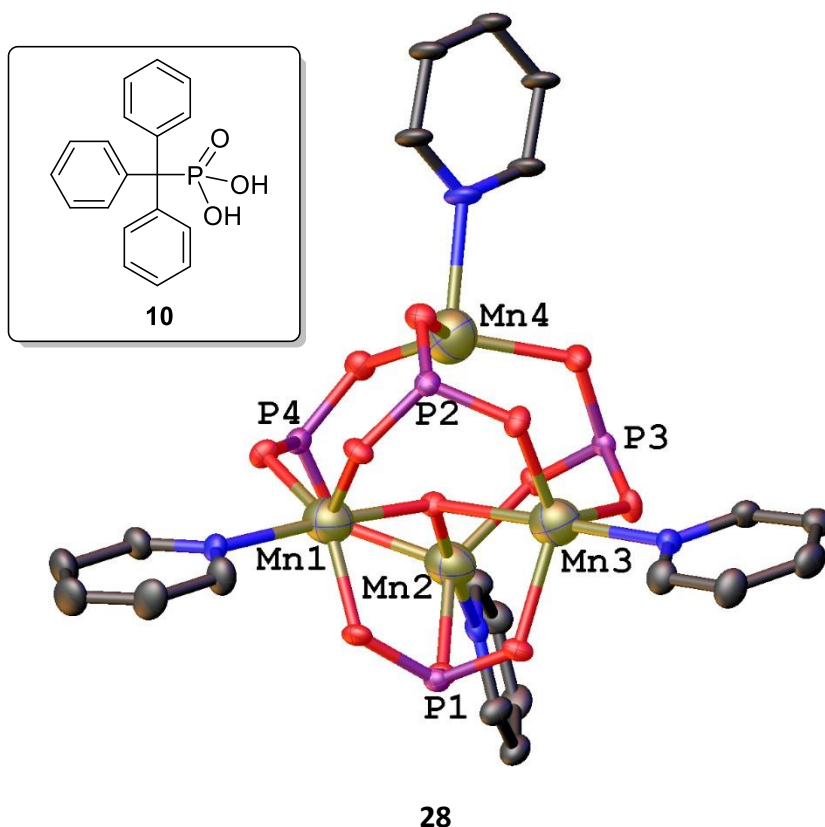


Figure 1.24 Inset: Structure of tritylphosphonic acid **10**. Right: Structure of $[\text{Mn}_4(\text{O})(\text{Ph}_3\text{CPO}_3)_4\text{Py}_4]$ core **28** with trityl groups omitted.⁶⁸ This will be discussed as an example of the ancillary ligand method of preparing molecular metal phosphonates.

The Mn_4 , Co_4 and Cu_4 cages are all isostructural with one another, and in each case, all contain four tritylphosphonate ligands bound in a [3.111] fashion.

1.4.2 Co-Ligand or Ancillary-Ligand Method

This method was first reported by Chandrasekhar and co-workers^{67c} and, in principle, functions in a similar manner as the bulky phosphonic acid method, with the primary aim of blocking vacant coordination sites on the metal. In this instance however, a secondary, or even a secondary and tertiary ligand (often called the co-ligand or ancillary ligand) is used to achieve this function. The phosphonic acid itself can either be bulky or relatively unencumbered. Frequently used co-ligands in metal phosphonate chemistry include pyridine,⁶⁹ pyrazoles,⁷⁰ bipyridines⁷¹ and carboxylic acids.⁷²

We have already seen this method employed in **28** (Figure 1.24), which used pyridine as the co-ligand. Also, in the previous sections, **22** used 6-chloro-2-hydroxypyridine and 1-naphthalenecarboxylic acid as the primary and secondary co-ligands (Figure 1.16) while **25** used pyridine and benzoic acid (Figure 1.21).

1.4.3 Hydrothermal/Solvothermal Method

One important procedure used to favour the formation of polymeric metal phosphonates that shall be discussed here is that which uses hydrothermal or solvothermal synthesis. Although in the literature both of these words are used interchangeably, there is technically a difference. Hydrothermal refers to the synthesis being performed in aqueous solvents (since “hydro” means water), while solvothermal implies an organic-based solvent is used in the synthesis. Figure 1.25 illustrates a typical autoclave which has been fully disassembled.

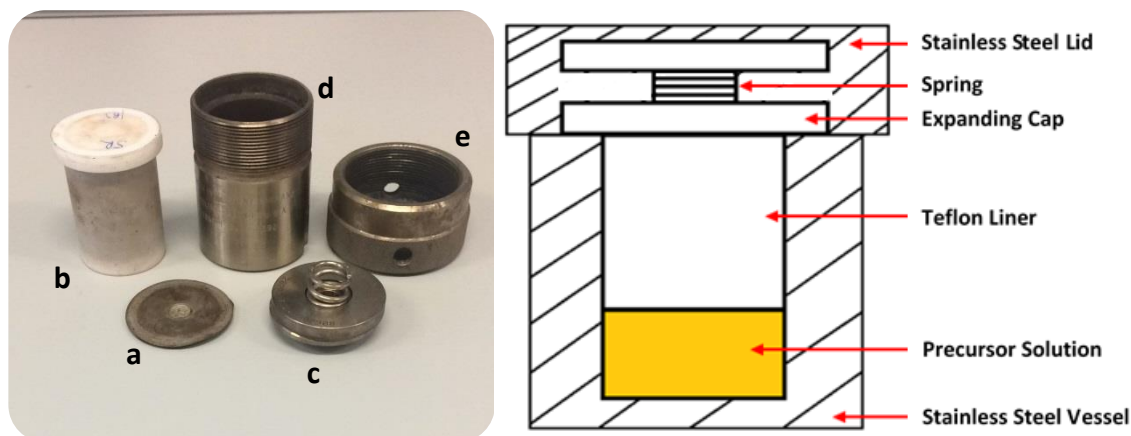


Figure 1.25 Left: Disassembled hydrothermal / solvothermal autoclave which will be used in this project. Right: Schematic showing the cross-section of the autoclave shown on the left.

A typical procedure would involve adding the precursor compounds (the metal salt, the phosphonic acid and if desired, a co-ligand) with a small amount of solvent to a PTFE-lined vessel – often called the “liner” (b), and sealing the contents with a PTFE lid. The liner is then placed inside a stainless-steel autoclave (d), and on top is placed an expanding cap (c) and sealing cap (a). The expanding cap contains a recess where a spring can fit between this and the sealing cap. If any gases are generated in the reaction, they will force the spring to contract which allows the PTFE liner to expand in volume slightly to accommodate. This is a safety feature which prevents any potential build-up of pressurised gases from rupturing the autoclave during heating. Finally, the lid of the autoclave (e) is screwed on to the vessel by hand. If desired, a locking rod can be inserted into the hole in the lid and used to tighten the vessel further by providing torque. The vessel is then placed inside an oven reactor and heated for the desired period of time.

Because they are being heated in a sealed and pressurised compartment (at 160 °C with the liner filled to roughly a third of its capacity the pressure would be around 5 bar⁷³), the reaction contents can be heated to a significantly higher temperature than they would otherwise normally be, since the solvent cannot boil off. After a set period of time (typically greater than

24 h) of heating (at typically 100 – 200 °C) the vessel is cooled at an exceedingly slow rate. This should have the effect of causing the newly formed compound to slowly precipitate out of solution, which in theory, leads to the formation of crystals. Because the cooling required is significantly slower than if the oven were to be simply switched off, the ovens used typically contain a programmable thermostat which allows for precise control of the rate of cooling and heating.⁷³ A typical procedure might involve a ramp (increase) in temperature from ambient (around 20 °C) to 160 °C at a rate of 5 °C / min. The ramp up temperature can be relatively fast – only the ramp down (cooling) must be slow. This would be followed by holding the temperature at 160 °C for 72 hours (three days) before ramping down the temperature by 0.1 °C / min back to ambient. The oven could then be switched off and the contents of the autoclave inspected.

Hydrothermal syntheses typically produce polymeric species, especially in the case of metal phosphonates. An example of such a species prepared in this manner would be the uranyl phosphonate $[(\text{UO}_2)_3(\text{MPDP})_2]$ **30** (MPDPH_4 = (5-methyl-1,3-phenylene)bis(phosphonic acid) **29**) synthesised by Sun and co-workers (Figure 1.26).⁷⁴

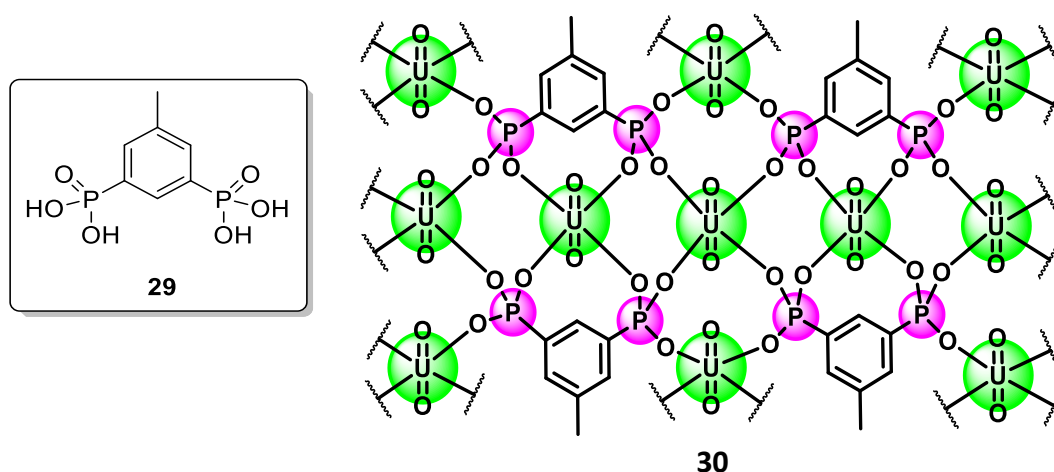


Figure 1.26 Inset: Structure of 5-methyl-1,3-phenylene)bis(phosphonic acid), MPDPH_4 **29**.⁷⁴ Right: Representation of the connectivity of the uranyl groups to the phosphonates in **30**.

A somewhat exotic reaction by virtue of the limited availability of uranium compounds, uranyl phosphonates are generally prepared from either the parent uranyl acetate or uranyl nitrate,⁷⁵ and, in the interests of safety for the chemist performing the reactions, contain only depleted uranium i.e. the ^{238}U isotope. While safer than its enriched ^{235}U counterpart, depleted uranium salts still carry health risks associated with being a heavy metal. They tend to accumulate in the kidneys.⁷⁶ In **30**, each uranyl (UO_2^{2+}) ion binds to four oxygens and thus exists in an octahedral arrangement. Each phosphonate binds in a [3.111] manner, although if the entire ligand is

considered then the configuration would be [5.11211]. There is no rule in Harris notation as to whether just the phosphonate moiety should be considered, or the entire ligand if, say, it contains more than one phosphonate functionality as is the case with **30**. The only important fact is that the binding moiety is clearly specified in the Harris notation. In this thesis, it is preferred that the phosphonates be treated individually, and thus the [3.111] convention is preferred in order to describe the binding of **30**, since the latter method can quickly cause the Harris notation to become unwieldy.

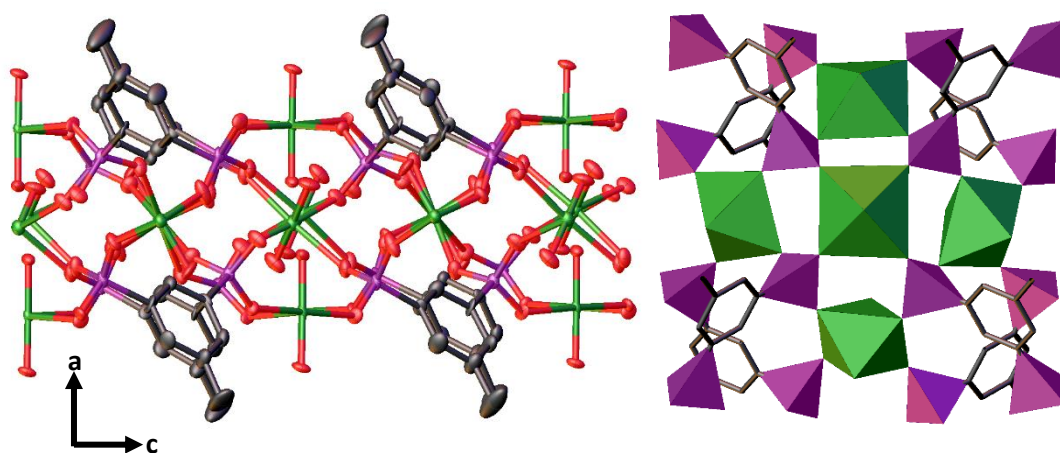


Figure 1.27 Left: Structure of $[(\text{UO}_2)_3(\text{MPDP})_2]$ **30** in the solid-state, as viewed down the *b*-axis of the crystal structure. Right: Polyhedra representation of the coordination environment of the uranyl groups.

In Figure 1.27 a polyhedra style was chosen. Polyhedra are a useful tool for representing the coordination environment of the metals and the phosphonates in a macro-structure. In this example, it can be seen that the uranyl moieties exist in an octahedral state, since the polyhedra are octahedra. Moreover, it allows for the quick determination which areas are the alkyl or aryl backbone, and which are the phosphonate.

The disadvantages of hydrothermal synthesis include being unable to monitor the growth of crystals (if any) until the autoclave has completely cooled to room temperature, and the inability to add any additional reagents to the mixture during heating. Nevertheless, the hydrothermal method remains a critical tool in the assembly of metal phosphonates – its use can allow for the access to motifs which would otherwise be impossible to achieve under ambient conditions, or by conventional heating.⁷³

1.5 Scope of Work

1.5.1 An Atropisomeric, Sterically Encumbered Phosphonic Acid

The chiral phosphonic acid ligand chosen for this work is (*S*)-[1,1'-Binaphthalen]-2-ylphosphonic acid, (*S*)-**bpa**, which is derived from the commercially available (*R*)-1,1'-Bi-2-naphthol, or (*R*)-binol in shorthand (Figure 1.29).⁷⁷ Binol and (*S*)-**bpa** exhibit a type of chirality known as atropisomerism. Unlike the more common cause of chirality – the presence of a stereocentre – atropisomerism is the result of a stereoaxis. The spatial arrangement of substituents on either side of this axis coupled with restricted rotation about the C-C bond results in two non-superimposable mirror images, giving rise to chirality.⁷⁸ Figure 1.28 illustrates how absolute configuration can be interpreted from the intermediates (*R*)-**31** and (*S*)-**32** (see Figure 1.30).

To assign the absolute configuration to each compound, the Cahn-Ingold-Prelog priority rules are invoked.⁶⁶ These rules consider the atomic number of the atoms concerned and accordingly give priority to the higher atomic number, which in turn will result in an (*R*)- or (*S*)- configuration depending on whether going from highest to lowest priority results in a clockwise or anti-clockwise motion (Figure 1.50).

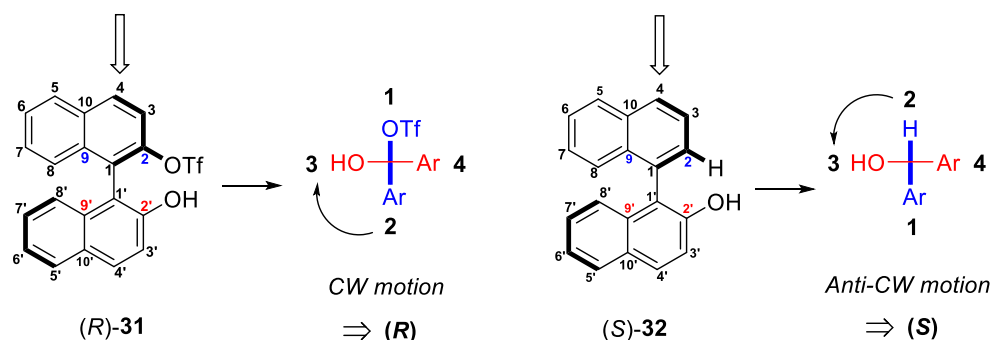


Figure 1.28 Structure of (*R*)-**31** and (*S*)-**32** with their respective Newman projections. The Newman projection is necessary in order to derive the absolute configuration and thus explain the change of (*R*) to (*S*) in the first step of the synthesis. This is on account of replacing the triflate (OTf) group with a hydrogen.

In this case, looking down the stereoaxis (broad arrow), the group with the highest priority is the triflate group (both contain oxygen and so the next atom is inspected, and sulfur has a higher atomic number than hydrogen). This is assigned the top position, 1 in the Newman projection. The group with the subordinate priority on this ring is carbon 9 so this is assigned to position 2 (Figure 1.50). Moving down to the bottom naphthyl ring, the group with the highest priority in this assignment is the hydroxyl group on C2', so this is assigned as position 3. This carbon 9', to be assigned the last-most position, 4.

Finally, with consideration being given to the relative positions of the groups assigned to 2 and 3, the direction of motion from 2 \rightarrow 3 is examined. If this follows a clockwise motion, the molecule is assigned the (*R*)- configuration – as is the case with (*R*)-**31**. Consequently, the change in priority resulting from the substitution of OH for H in (*S*)-**32** leads to the change in absolute configuration to (*S*), because the hydrogen attached to C2' is of lower priority than C9'.

1.5.2 Rationalising the Choice of Ligand

Previously, the Higham group demonstrated how (*R*)-binol could be converted into the first air-stable, chiral primary phosphine,⁷⁹ which could then be functionalised by a variety of methods.⁸⁰ During the course of this work, different modifications to this original synthesis will be investigated.

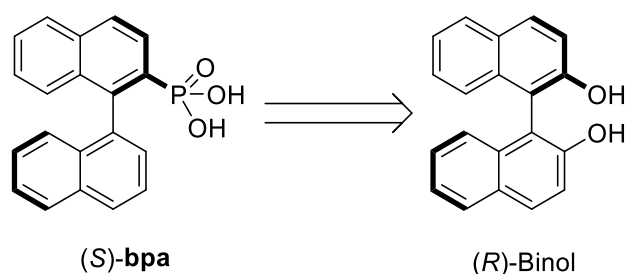


Figure 1.29 Structure of (*S*)-**bpa**, which is derived from the parent (*R*)-binol.

Preliminary studies on (*S*)-**bpa** by previous members of the Higham group indicated that this ligand was ideally suited for the synthesis of chiral metal phosphonates.⁸¹ It is a completely air-stable, free-flowing powder which is soluble in a wide range of organic solvents (although it is not water-soluble). More importantly, the steric bulk provided by the binaphthyl rings limits the aforementioned unwanted oligomerisation – a property not shared by the phenylphosphonic acid derivatives. Furthermore, the synthetic route to (*S*)-**bpa** is achievable in five high-yielding steps (Figure 1.30).

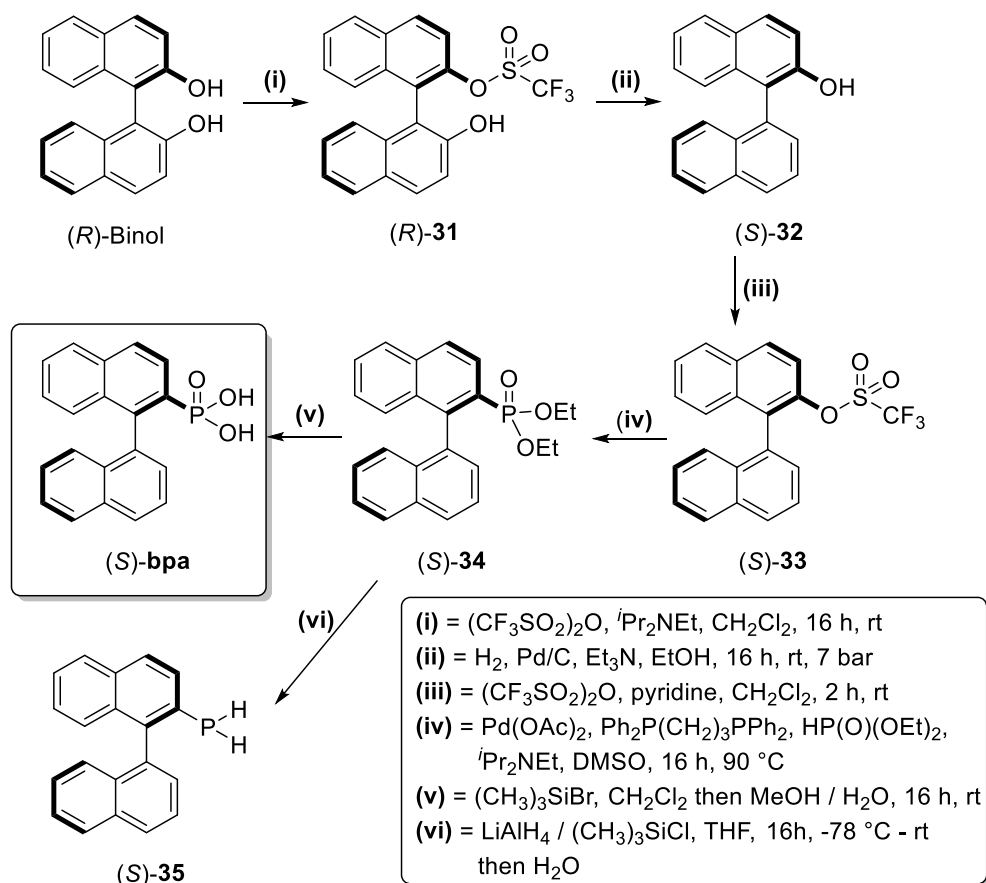


Figure 1.30 Original Higham group synthesis of (S)-bpa starting from (R)-binol. The phosphonate intermediate (S)-34 can either be hydrolysed into the phosphonic acid, (S)-bpa or reduced to the primary phosphine, (S)-35.

It is prudent to ask why we should go to the trouble of synthesising an optically pure enantiomer of **bpa** when racemic binol is a significantly cheaper starting compound.⁷⁷ The reason is two-fold – first, and most importantly, it is clear that the nature of the phosphonic acid determines the nature of the metal phosphonate structure. By starting with an optically pure precursor and comparing them to the racemic analogues, the effect of enantiocontrol on the resultant structure will be able to be determined, much in the same way that enantiopure amino acids help to determine protein structure.⁸²

Secondly, as discussed, one important application of TM phosphonates is in oxidative catalysis. Chiral phosphonates could be used to promote catalytic asymmetric oxidations.

1.5.3 Methods of Analysis

The characterisation of the (*S*)-**bpa** ligand as well as the intermediate compounds will be performed by ^1H , ^{13}C and ^{31}P and ^{19}F NMR spectroscopy, infrared spectroscopy and high-resolution mass spectrometry. If possible, suitable crystals of (*S*)-**bpa** will be grown in order for the structure to be characterised by single-crystal X-ray diffraction. The optical purity of each intermediate and (*S*)-**bpa** will be ascertained by optical rotation analysis.

Characterisation of the metal phosphonates will primarily involve single-crystal X-ray diffraction to unambiguously assign a structure – hence the importance of growing single crystals of sufficient quality. Since most of these clusters will be paramagnetic, they will be unsuitable for NMR spectroscopy due to the likely line broadening.¹⁴ In these instances, Electron Paramagnetic Resonance (EPR) spectroscopy will be employed. However, there will be a number of d^0 and f^0 metal phosphonates which will be prepared. Since these species will contain no unpaired electrons, NMR spectroscopy will be used here. In conclusion, this project aims to:

- Synthesise the novel chiral phosphonic acid ligand, (*S*)-[1,1'-Binaphthalen]-2-ylphosphonic acid, (*S*)-**bpa**, on a multi-gram scale.
- Attempt to coordinate (*S*)-**bpa** onto a variety of first-row transition metals and lanthanide hydrate salts.
- Attempt a range of crystallisation techniques such as slow evaporation, layering and the hydrothermal method, in order to obtain chiral crystals of M-(*S*)-**bpa** clusters (M = transition metal / lanthanide). If successful, this will be extended to second- and third-row TMs and main-group elements.
- Successfully characterise any novel complexes or clusters using a combination of X-ray Crystallography, Elemental Analysis, High-Resolution Mass Spectrometry and Infrared Spectroscopy.
- Investigate any potentially interesting magnetic properties of M-(*S*)-**bpa** complexes, where appropriate, using Electron Paramagnetic Resonance (EPR) Spectroscopy and variable-temperature Magnetic Susceptibility analysis (to determine any SMM-like behaviour).
- Investigate any potential catalytic activity in allylic and benzylic oxidations of TM-(*S*)-**bpa** complexes and compare their performances to that of commercially available phosphonates.
- Investigate the luminescence properties of Ln-(*S*)-**bpa** complexes, specifically Eu(III) and Tb(III).

Chapter 2 – Control over 0-D, 1-D and 2-D Morphology / Topology – Dictating the Structure and Properties of Chiral Cobalt Phosphonates

2.1 Ligand Synthesis

This chapter outlines the synthesis of three new cobalt phosphonates, each possessing vastly different morphologies. Furthermore, a mixed Co_3Sc_3 cluster has been successfully prepared. However, before we delve into this, it would behoove us to first discuss the synthesis of the ligand. As mentioned in the previous chapter, the ligand can be prepared in five steps. These will be described in detail in the subsequent sections.

2.1.1 Preparation of (*R*)-**31**

The first step of the ligand synthesis required mono-triflation of (*R*)-binol. It was found that by adding only one equivalent of triflic anhydride, and by slowly introducing it into a vigorously stirred dilute solution of (*R*)-binol, the mono-triflated product, (*R*)-**31** was almost exclusively made, with a small amount of *bis*-triflated by-product. The reaction proceeded in excellent yield (92%) and required only an aqueous work-up. A single peak at -74.4 ppm in the ^{19}F NMR spectrum confirmed the presence of (*R*)-**31**, as well as a significantly smaller peak at -78.3 ppm, which was attributed to the *bis*-triflated side product.

In the preparation described by the Higham group, it was reported that (*R*)-**31** – which exists as an oil in ambient conditions – was used without further purification. However, it was found that the oil still contained a noticeable amount of the *bis*-triflated impurity. We therefore set about trying to crystallise it, and since triethylamine is employed in the subsequent hydrogenation step, crystallising it as its triethylamine salt seemed logical. Thus, by dissolving (*R*)-**31** in dichloromethane and adding excess triethylamine, yellow crystals of $[\text{HNEt}_3]^+(\text{R})\text{-}\mathbf{31}^-$ formed after 24 h. These were carefully washed with cold acetone and dried. The stable, free-flowing powder proved to be significantly easier to handle and store. Moreover, ^1H and ^{19}F NMR spectroscopy indicated the small amount of *bis*-triflated side product was no longer present – presumably it was still in the filtrate after failing to crystallise. Figure 2.1 illustrates the process of preparing $[\text{HNEt}_3]^+(\text{R})\text{-}\mathbf{31}^-$.

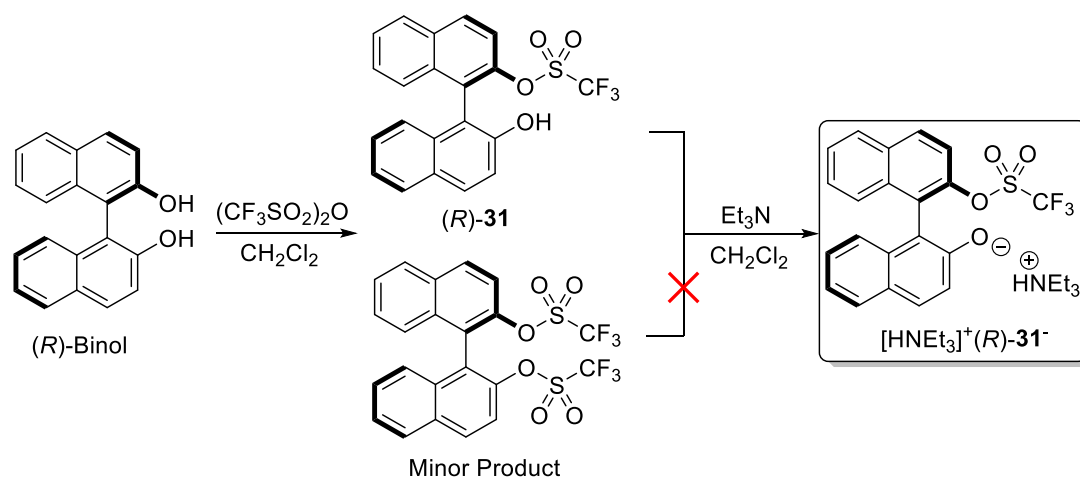


Figure 2.1 Reaction of (*R*)-binol with trifluoromethanesulfonic anhydride to form (*R*)-31 and the bis-triflated minor product. The latter is removed by filtration since it does not crystallise with triethylamine, leaving the pure product [HNEt₃]⁺(*R*)-31⁻.

2.1.2 Preparation of (*S*)-32

The second step involved the hydrogenation of (*R*)-31 in a steel autoclave to afford (*S*)-32. In the original synthesis published by the Higham group, this hydrogenation required stirring at 48 hours and 5 bar of pressure.⁷⁹ However, it was found that by increasing the pressure to 7 bar, complete conversion of (*R*)-31 was achieved in 24 hours. After filtration (to remove the Pd/C residues) and aqueous work-up, a white-yellow solid was obtained in excellent yield (80%). ¹H NMR spectroscopy indicated the product was sufficiently pure to react in the next step.

We wished to investigate whether this step could be performed without the use of hydrogen, due to the risks and inconveniences that are associated with such a reagent. A search of the literature revealed that a myriad of syntheses for the reductive cleavage of an aryl triflate existed. One particular method described by Sajiki and co-workers involved the use of palladium on carbon, elemental magnesium and ammonium acetate to achieve the reduction. The hydrogen which would replace the triflate group on the aryl ring was provided by methanol, which was the solvent used.⁸³ Furthermore, the reduction was shown to proceed to completion in ambient temperatures for a range of aryl triflate substrates. The reaction times themselves were also very short – most reductions were complete after one hour.

Thus, [HNEt₃]⁺(*R*)-31⁻ was converted back to its pure form by treatment with water and aqueous 1M HCl, before being dried under vacuum to yield a white-yellow solid of the pure (*R*)-31. It was believed that this was necessary, since the authors specifically stated triethylamine suppressed the yields of the reaction. Since this reaction had never before been tested on a substrate like (*R*)-31, we established a screening to investigate which conditions led to the most optimal yields.

The results are summarised in Table 5.

Entry	Temperature / °C	Duration / h	NH ₄ OAc used?	Methanol Grade	Form of (R)-31	Isolated Yield ^c / %
1	20	2	No	Reagent ^a	Salt	20
2	65	2	No	Anhydrous ^b	Pure	25
3	20	24	No	Anhydrous ^b	Pure	10
4	65	24	Yes	Reagent ^a	Pure	25
5	65	24	Yes	Anhydrous ^b	Pure	40
6	65	48	Yes	Anhydrous ^b	Pure	65
7	65	72	Yes	Reagent ^a	Pure	50
8	65	72	Yes	Anhydrous ^b	Pure	85

Table 5 Results of the screening for the reduction of (R)-31 to (S)-32. *a* = 99% grade; *b* = 99.9% anhydrous grade; *c* = after work-up. For reference, the yield for the hydrogenation was 80%.

Unfortunately, we were unable to achieve satisfactory yields at ambient temperatures and short reaction times (Entries 1 and 3). The optimum conditions were determined to be running the reaction at reflux for 72 hours using anhydrous methanol and one equivalent of NH₄OAc additive (Entry 8). While this method of reduction did not completely supersede hydrogenation, it did provide a useful alternative whenever hydrogen gas was unavailable, and thus, both methods were used in tandem whenever possible.

2.1.3 Preparation of (S)-33 and (S)-34

Subsequent triflation was performed on (S)-32 to afford (S)-33 in good yield (80%). Again, after aqueous work-up, the pale orange powder could be reacted directly in the phosphonylation step. This step involved a palladium-catalysed substitution of the triflate moiety for a diethyl phosphonate. It was soon realised that this reaction suffered from a loss of yield if scaled up (at substrate masses exceeding ca. 3 g). Therefore, the triflate was separated into several batches and reacted separately before being combined in the work-up phase. An unfortunate side-product in this reaction was the unsubstituted 1,1'-binaphthalene, as ascertained by ¹H NMR spectroscopy. The crude product was therefore purified by column chromatography to yield colourless crystals of (S)-34 (65% yield). A single peak at 17.9 ppm in the {¹H}³¹P NMR spectrum confirmed the presence of (S)-34. Also present was a small peak at 7.4 ppm which was attributed to residual diethyl phosphite. This was removed by heating (S)-34 under vacuum at 50 °C for 3 hours.

2.1.4 Preparation of (S)-bpa

The final step involved conversion of the phosphonate ester into the corresponding phosphonic acid. This was achieved by reaction of (S)-**34** with bromotrimethylsilane to form a silyl ether intermediate. Subsequent hydrolysis afforded (S)-**bpa** in a quantitative yield. We initially performed the hydrolysis of the phosphonate ester with concentrated HCl; however, it soon became apparent that this method led to incomplete hydrolysis and cumbersome work-ups. We therefore opted for a rather esoteric approach for the hydrolysis – that is, the use of bromotrimethylsilane, first described by McKenna.⁸⁴ The mechanism for the ester cleavage is provided in Figure 2.2. To our delight, this reagent afforded clean and quantitative cleavage of the phosphonate ester with a simple work-up. $\{^1\text{H}\}^{31}\text{P}$ NMR spectroscopy indicated a change in chemical shift from 17.9 ppm to 12.9 ppm, which confirmed successful hydrolysis had occurred. Crystals suitable for single-crystal X-ray diffraction were grown from the slow evaporation of a dichloromethane solution. The X-ray crystal structure of (S)-**bpa** is shown in Figure 2.2.

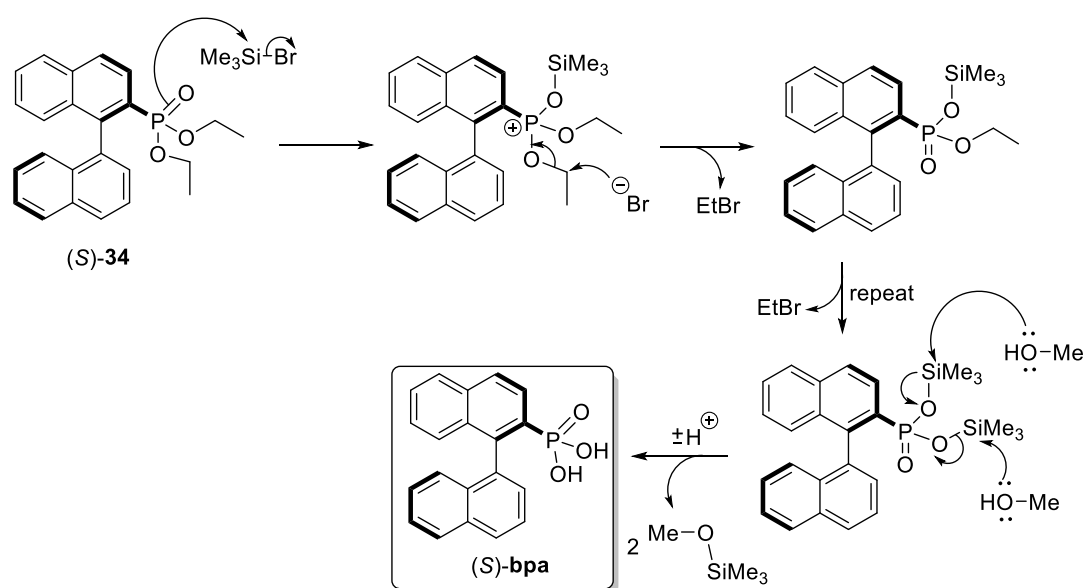


Figure 2.2 Mechanism for the double silylation of (S)-**34** followed by hydrolysis with methanol. Since the toxic gas ethylbromide is liberated in the first step, this reaction was performed under Schlenk-line conditions at all times.

(S)-**bpa** exists as a fine, free-flowing powder that is soluble in all organic solvents, but not water. This former attribute was advantageous when performing crystallisations, since it allowed us to perform screenings in a wide range of solvents without fear of their incompatibility with the ligand. The presence of water in the asymmetric unit of the crystal structure (Figure 2.3) was expected, as the strongly polar phosphonate group forms strong hydrogen bonds, and water was used in excess in the ligand's work-up.

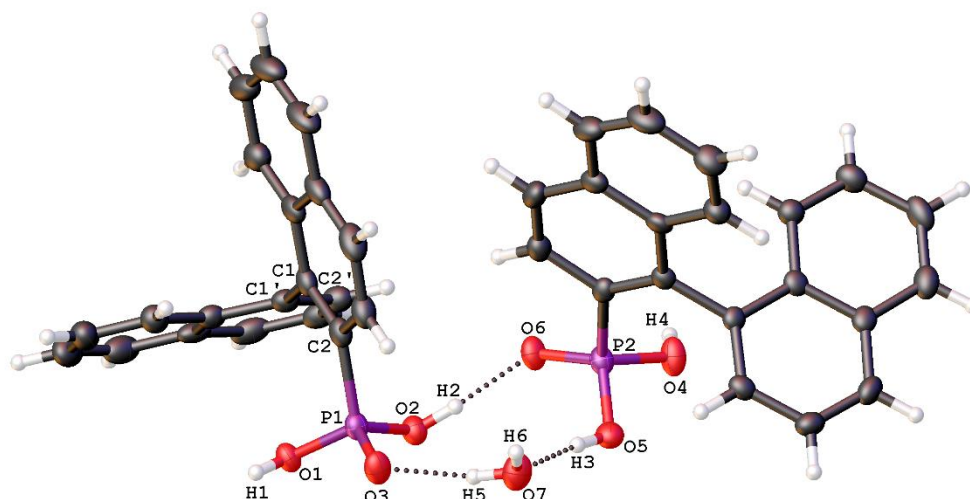


Figure 2.3 Structure of an (*S*)-**bpa** dimer in the crystal, with a bound molecule of water. Selected bond lengths and angles; C2-P1, 1.800 Å; P1-O1, 1.544 Å; P1-O2, 1.548 Å; P1-O3, 1.495 Å; O3...H5, 1.844 Å; O6...H2, 1.752 Å; O7...H3, 1.714 Å; C2-C1-C1'-C2' = 80.430°.

2.2 [Co(OAc)₂(Py)₂(H₂O)₂], **36** Synthesis and Characterisation

We first turned to cobalt as the transition metal with which to perform coordination reactions with (*S*)-**bpa**. There were a multitude of reasons for choosing cobalt as the first metal to study – one is the simple fact that Co(II) salts such as the acetate or nitrate are commercially cheap. Therefore, a large number of coordination reactions could be conducted with emphasis on optimising the metal to ligand ratio, or solvent choices, in order to grow the highest quality crystals without the need to worry about wasting copious amounts of metal salt precursor. As to why we did not investigate Co(III) salts, few are commercially available due to their intrinsically high reduction potential. Consider the half-cell equation; $\text{Co(III)} + \text{e}^- \rightarrow \text{Co(II)}$, $E = +1.92 \text{ V}$ (c.f. chlorine to chloride, $E = +1.36 \text{ V}$, meaning chloride would reduce Co(III) to Co(II)). Fluoride is one of the few simple anions capable of stabilising Co(III).⁸⁵

The main reason for choosing cobalt was down to the actual chemistry of the Co(II) ion. Octahedrally-coordinated Co(II) possesses the $^4\text{T}_{1\text{g}}$ ground state, which, due to spin-orbit coupling (the interaction between a particle's spin and its motion),⁸⁶ is magnetically highly anisotropic.⁸⁷ Since anisotropy is a highly desired characteristic in the search for new SMMs, we reasoned that attempting to prepare octahedrally-coordinated Co(II)-(*S*)-**bpa** complexes would be a solid foundation with which to start. Pyridine was chosen as a base since it not only assists in solubilising (*S*)-**bpa**, but also acts as a co-ligand – preventing any unwanted polymerisation. To this end, pyridine has been used to great effect in the literature.^{62,68}

Therefore, a methanol-acetonitrile (1:1) solution of cobalt acetate tetrahydrate and a pyridine solution of (*S*)-**bpa** were mixed together and stirred for five minutes before being left in air. After two days, large pink rhombohedral crystals had formed (Figure 2.4), which at this point were assumed to be a Co(II) complex of (*S*)-**bpa**. However, single-crystal X-ray diffraction indicated that these crystals were not of the desired aforementioned complex, but rather the complex $[\text{Co}(\text{OAc})_2(\text{Py})_2(\text{H}_2\text{O})_2]$ **36**, which had previously been reported by Williams and co-workers.⁸⁸ Figure 2.4 shows **36** in the crystal.

36 can best be described as a centrosymmetric diaceto diaqua dipyridine octahedral high-spin Co(II) complex crystallising in the *Pcba* space group and possessing the *C_i* point group. Each of the ligand pairs occupy a coordination position *trans* to each other. The Co-OAc bond lengths are shorter (2.076(2) Å) when compared to the Co-N (2.159(3) Å) and Co-OH₂ (2.121(2) Å) bond lengths. Intramolecular hydrogen bonding occurs between the hydrogens of the aqua ligands and the acetate oxygens, forming a pseudo six-membered ring. There is virtually no distortion in the axial Co-N1 and Co-N2 bond lengths which indicates **36** is a high-spin Co(II) complex, due to weak Jahn-Teller effects.⁸⁹ The H1...O6 and H2...O5 hydrogen bond lengths are both 1.833(0) Å. The N1-Co-O1, N1-Co-O3 and O1-Co-O3 bond angles all fall with the narrow range of 88.78(8) – 92.69(10)°. Intermolecular hydrogen bonding is present in the acetate and aqua ligands of neighbouring molecules of **36**, creating sheets that extended infinitely down the *b*-axis (Figure 2.5).

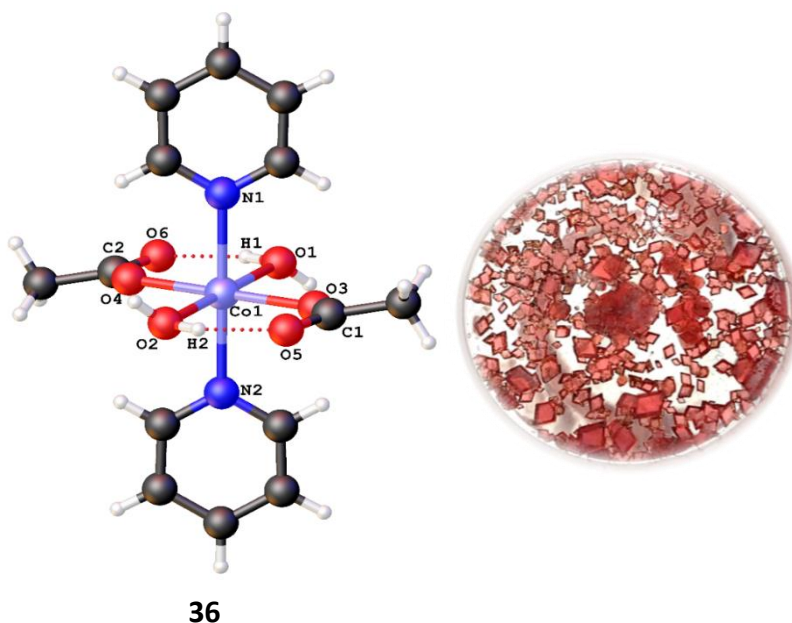


Figure 2.4 Left: Structure of **36** in the crystal. Due to the spatial orientation of the aqua ligands, the only symmetry present in **36** is the inversion centre at Co1. Right: Physical form of **36**, as viewed under a standard laboratory microscope (10x zoom).

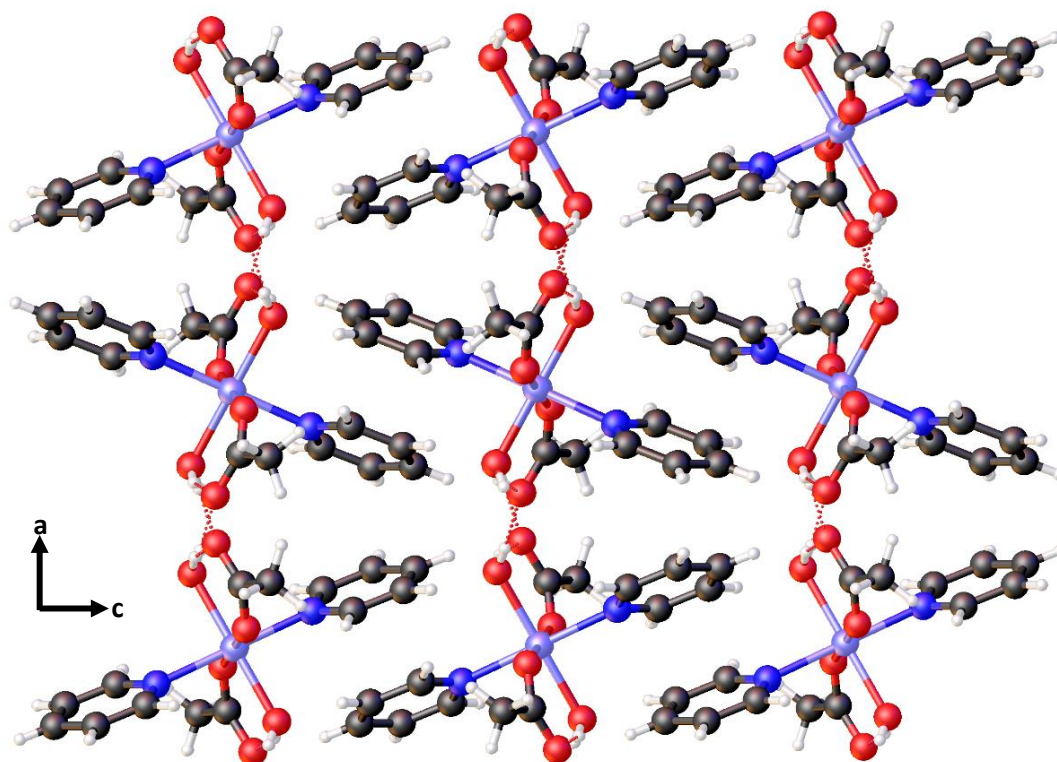


Figure 2.5 Packing diagram of **36** as seen down the *b*-axis. The molecules adopt a Herringbone-type arrangement with intermolecular hydrogen bonding forming between the molecules in each layer.

36 appears to be a somewhat unassuming complex that already exists in the literature and whose inclusion into this thesis seems somewhat redundant. However, when a dried and triturated sample was sent to the National EPR Facility and Service at the University of Manchester, variable temperature ac magnetic susceptibility studies indicated that **36** exhibited slow magnetic relaxation – a property unknown in the original paper it was published in. We have since published these findings.⁹⁰

The magnetic susceptibility plot of $\chi_M T(T)$ for **36** is shown in Figure 2.6. Applying the spin-only formula here is inadequate, since the form of the trace (red line) is typical for a monometallic Co(II) species influenced by an orbital contribution to its magnetic moment. Moreover, the room temperature $\chi_M T$ value was found to be $3.04 \text{ cm}^3 \text{ K mol}^{-1}$, which is significantly higher than the calculated spin-only value ($1.875 \text{ cm}^3 \text{ K mol}^{-1}$) for an $S = 3/2$ ion with $g = 2$, although is within the range expected for octahedral Co(II) complexes.⁹¹ As the temperature was decreased, the $\chi_M T$ fell to $1.44 \text{ cm}^3 \text{ K mol}^{-1}$ at 2 K. Ac susceptibility measurements were then performed on a powder sample of **36**. It was observed that the range of the field strength at which **36** exhibited frequency dependence of the out-of-phase component was between 0 and 5000 Oe at 1.8 K. A peak in the out-of-phase (imaginary) susceptibility manifested under applied external fields and

reached a maximum shift to low frequencies for 1500 Oe, which was considered as the optimal field strength in which slow magnetic relaxation could be observed for **36** (Figure 2.7).

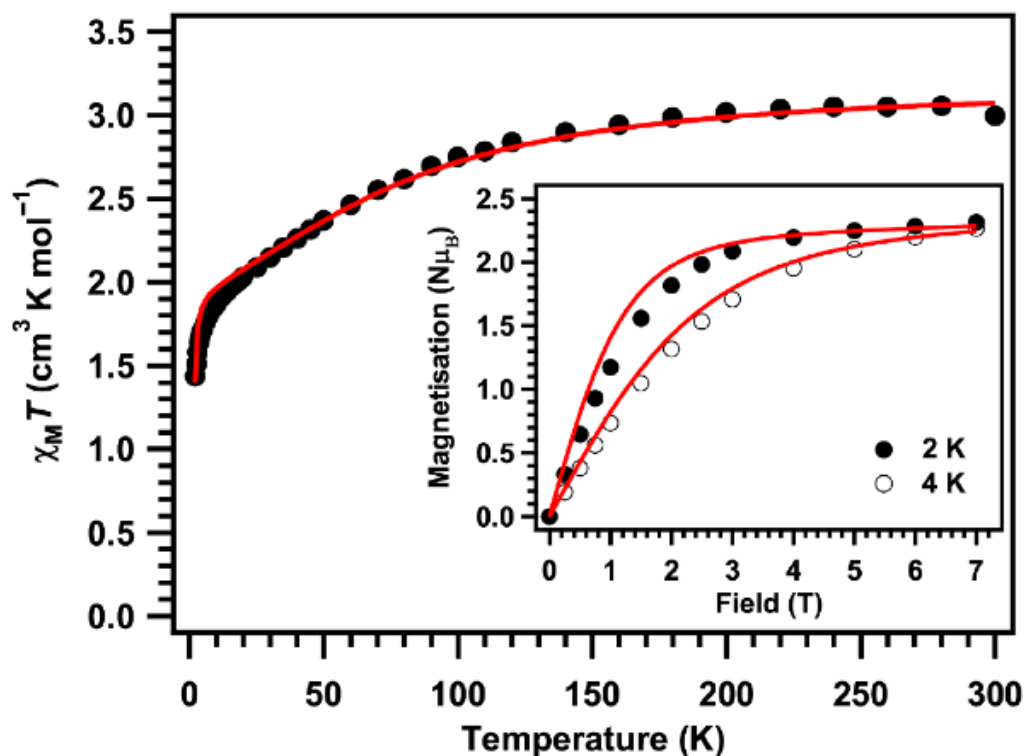


Figure 2.6 Main: Variable temperature magnetic susceptibility plot of **36** measured under a static field of 0.1 T. Inset: Field-dependent magnetisation at 2 and 4 K. The red traces are simulations.⁹⁰

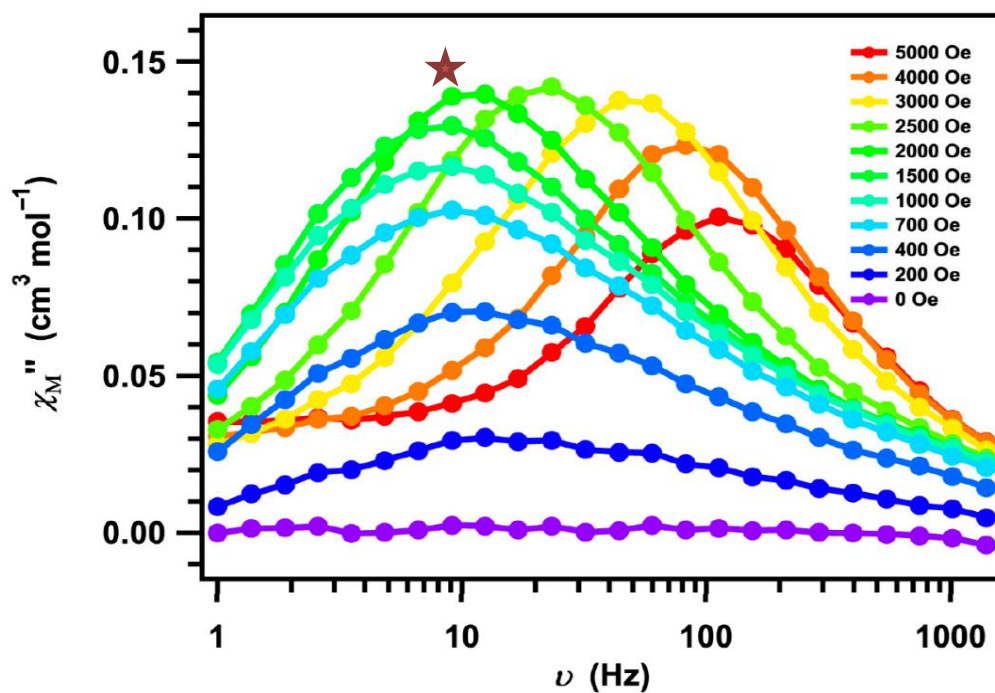


Figure 2.7 Frequency-dependence of the imaginary ac susceptibility of **36** measured under several applied fields at 1.8 K. The solid lines are guides for the eye. The trace marked with a red star (1500 Oe) was determined as the optimal field strength to perform further measurements.⁹⁰

Further to this, additional ac susceptibility measurements were conducted at this field strength over a range of temperatures (1.8 – 10 K) and oscillation frequencies (1 – 1400 Hz). Figure 2.8 illustrates this.

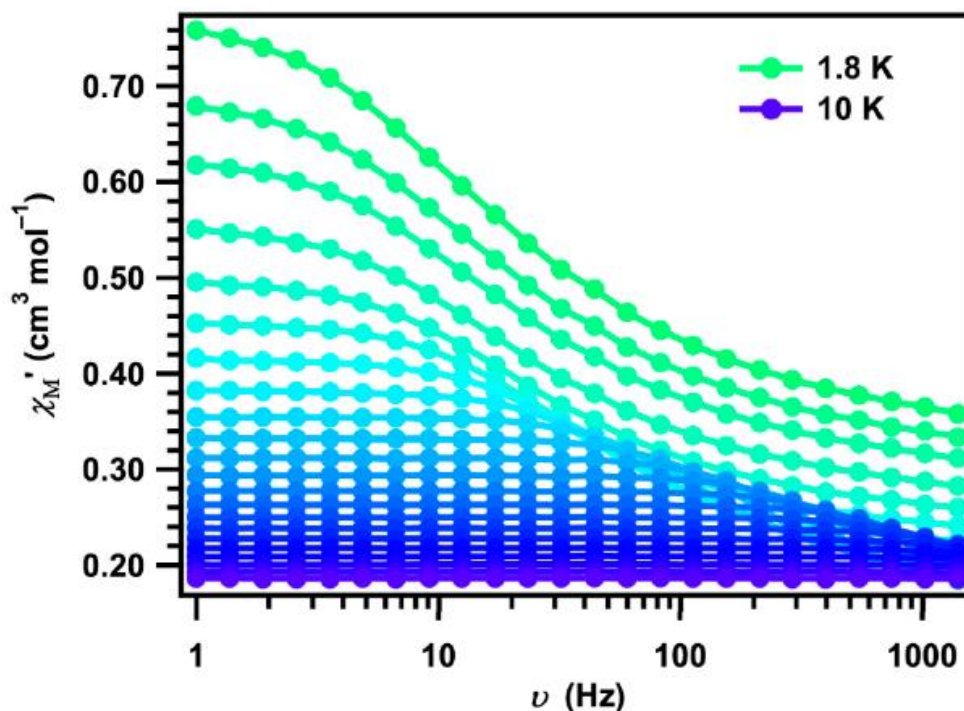


Figure 2.8 Frequency dependence of the ac susceptibilities of **36** measured under a static field of 1500 Oe and temperatures ranging from 1.8 – 10 K. The solid lines are guides for the eye.⁹⁰

The relaxation times were modelled with *ab initio* techniques in order to determine the mechanism (or mechanisms) of magnetic relaxation. The model returned a calculated U_{eff} of 25 cm^{-1} (36 K). However, when this value was compared to experimental data at high temperatures (5 – 10 K), there was a large discrepancy in the energy separations of the ground and excited states. While the model assumed a separation of 25 cm^{-1} , the experimental separation which was derived from Figure 2.8 returned a calculated energy gap of $\sim 264 \text{ cm}^{-1}$, which implies a two-phonon Raman relaxation. A phonon is a quantum of mechanical or vibrational energy (much like how a photon is a quantum of light or electromagnetic energy), while a two-phonon Raman process refers to **36** relaxing slowly by emitting phonons through the crystal lattice. Assigning the mechanism of relaxation at low temperatures was significantly easier – at low temperatures (< 5 K), Figure 2.8 shows magnetic susceptibilities that vary according to the frequency of the applied field, with high temperatures almost completely quenching this process. This indicates that at low temperatures, **36** relaxes *via* quantum-tunnelling of magnetisation (QTM).

Furthermore, the low-temperature (< 20 K) solid-state EPR spectrum of **36** was ran (Figure 2.9) and confirmed that the electronic structure of the complex was rhombic i.e. its g -values (g_x , g_y and g_z) are all unequal due to the C_i symmetry of the molecule. As previously mentioned, contributions by the orbital angular momentum to the total spin means that consideration of only the spin-angular momentum of Co(II) as $S = 3/2$ is wholly inadequate. This manifests itself as a significantly more complicated EPR spectrum – the analysis of which is beyond the scope of this thesis. As such, it will not be discussed further here. What can be seen, however, are the individual g -values (shown in Figure 2.9) and the corresponding easy-, intermediate- and hard-axes for **36** derived from these values. The experimental g -values compare well with the simulated g -values (Table 6). These were obtained by modelling **36** as an effective $S = 1/2$ spin-state due to the aforementioned large energy gap to the first excited energy state as a result of spin-orbit coupling.

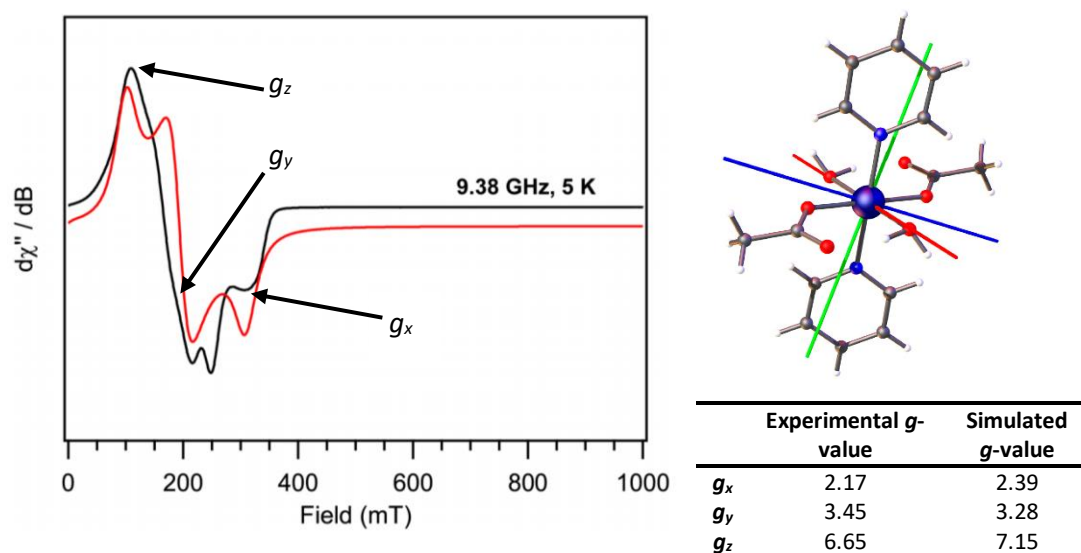


Figure 2.9 Left: Powder EPR spectrum of **36** (X-band) performed at 5 K. The red line is the simulated EPR spectrum. The three g -values are labelled onto the real spectrum (black line). Right: Structure of **36** with derived easy- (blue, g_z), intermediate- (green, g_y) and hard- (red, g_x) axes. Bottom right: **Table 6** Experimental and simulated g -values for **36**.⁹⁰

In conclusion, **36** exhibits slow relaxation but not in a process that is comparable to how an SMM slowly relaxes i.e. with a measurable effective barrier to reversal of magnetisation (U_{eff}). Rather, **36** relaxes by two different methods, depending on the temperature. At high temperature, slow relaxation by a two-phonon Raman process dominates, while at low temperatures, it occurs *via* quantum tunnelling of magnetisation (QTM). Thus, by definition **36** is not an SMM. It is however, an excellent example of a *pseudo*-octahedral Co(II) complex with a rhombic electronic structure and whose slow magnetic relaxation is a combination of two competing processes.

2.3 [Co((*S*)-bpa)₂(Py)₄], (*S*)-**37** Synthesis and Characterisation

While the unexpected synthesis and discovery of the slow magnetic relaxation in **36** was indeed an interesting endeavour, we were eager to prepare Co(II) complexes that would contain (*S*)-**bpa**. We opted for the continual use of pyridine as the base since crystallisation screenings indicated it not only helped solubilise the metal salts and ligand better than other bases such as hydroxide, but also did not crystallise as the protonated salt like other nitrogen-containing bases normally do, such as triethylamine. This led to fewer unwanted by-products crystallising as the mother liquor evaporated.

However, it was evident that certain reaction conditions would have to be modified to favour the formation of a Co-(*S*)-**bpa** complex over **36**. To this end, we focused on changing two factors – the solvent system, and the method of which the metal salt and ligand were allowed to interact. To prepare **36**, methanol and acetonitrile were employed as the primary solvents, and it was noted that the stirred solution was not completely clear – that is to say not all substituents were fully dissolved. Therefore, to ensure full dissolution, a small amount of distilled water would be added to the solvent mixture.

Next, the method of mixing the substituents was addressed. In the case of **36**, the cobalt(II) acetate and (*S*)-**bpa** were added together and stirred in solution for 24 hours before being left to evaporate. A literature search revealed that in some cases, layering two solvents could prove fruitful, such as when Winpenny and co-workers prepared a Co(II) phosphonate cage by layering hexane onto an acetonitrile solution of the cobalt phenylphosphonate,⁹² or when Zheng and co-workers prepared mixed Mn(II)/Mn(III) clusters by layering diethyl ether onto a pyridine solution of the manganese cyclohexylphosphonate.^{72a} An optimal solvent system and layering technique was established after a myriad of screenings (see Appendix). These screenings involved dissolving both species first in ethanol and then acetonitrile, and then combinations of the two. A small amount of water was added later to assist the dissolution of the metal salt hydrate. The cobalt(II) acetate was dissolved in a mixture of three solvents – water, ethanol and acetonitrile, while the ligand was dissolved in pyridine. The solutions were stirred in separate vials for five minutes to achieve full dissolution, before the vial containing (*S*)-**bpa** dissolved in pyridine was loaded into a syringe and carefully layered on top of the cobalt acetate solution. Upon completion of the layering, Parafilm was placed over the vial and three holes were perforated into the film so that slow evaporation – and in theory, better quality crystals – could be obtained. Figure 2.10 illustrates this process.

After sitting for 24 hours, colourless parallelepipedal crystals were observed in the solution. Single-crystal X-ray diffraction revealed them to be a Co(II) complex which contained two *trans*-molecules of (*S*)-**bpa** and four equatorial pyridine ligands. Figure 2.11 shows the structure of $[\text{Co}((\text{S})\text{-bpa})_2(\text{Py})_4]$, (*S*)-**37** in the solid-state.

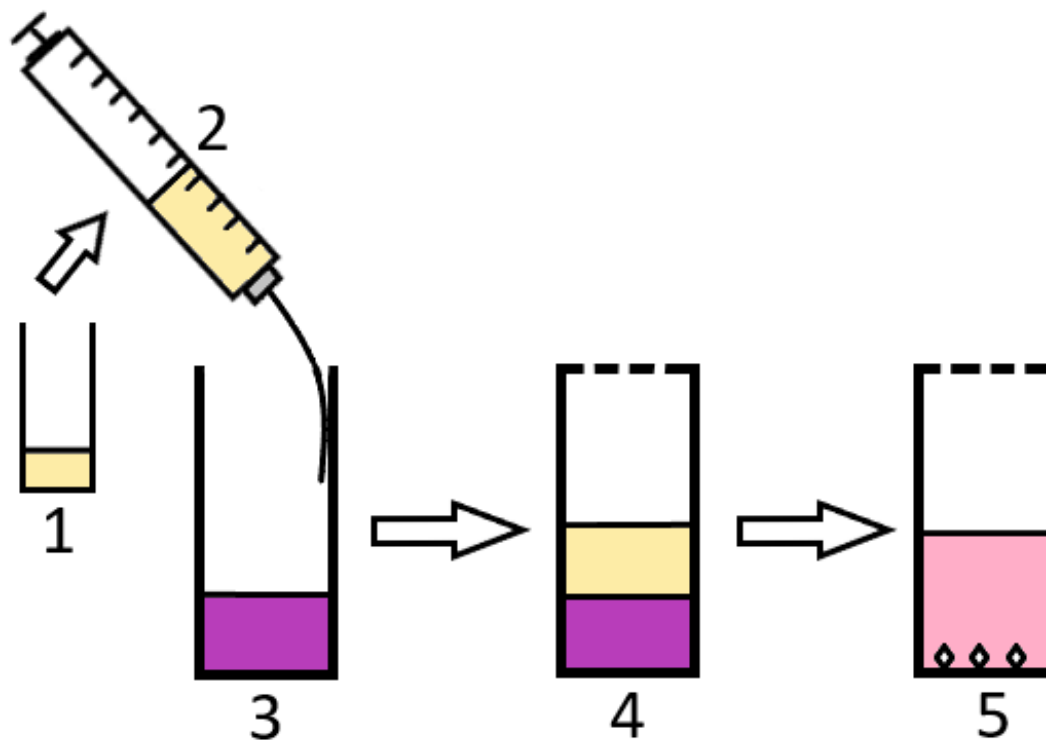
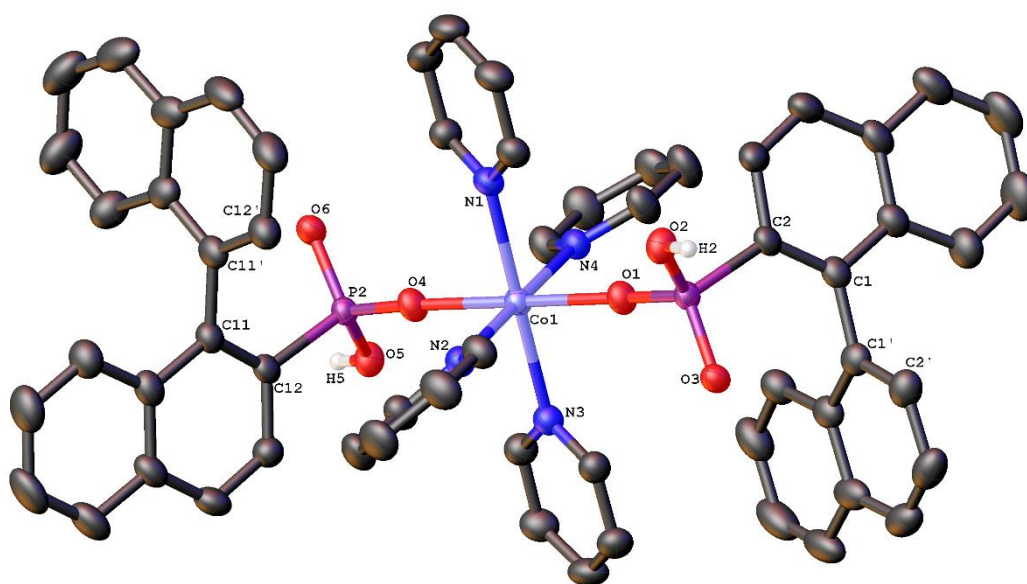


Figure 2.10 Schematic of the layering process used to prepare (*S*)-**37**. A solution of (*S*)-**bpa** in pyridine **1** is drawn up into a syringe **2** before being carefully layered on top of a solution of $\text{Co}(\text{OAc})_2 \cdot 4\text{H}_2\text{O}$ in H_2O / EtOH / MeCN **3**. After completion of the layering, Parafilm is placed over the top of the vial and three holes are made **4**. After ca. 24 hours, crystals of (*S*)-**37** can be observed, **5**.



(S)-37

Figure 2.11 Structure of (*S*)-**37** in the crystal, with hydrogen atoms on both the pyridine and binaphthyl rings omitted.

(*S*)-**37** crystallises in the monoclinic space group $P2_1$ and, being chiral by virtue of the (*S*)-**bpa** ligands, possesses the C_1 point group. Like **36**, it is an axially-distorted octahedral Co(II) complex, with bond angles falling within the ranges of $86.58(13)^\circ$ (N2-Co1-N3) to $94.66(13)^\circ$ (N1-Co1-N2). The complex contains four pyridine ligands occupying the equatorial position and two axially-bound molecules of (*S*)-**bpa** which bind in a monodentate fashion *via* the oxygen atoms on the phosphonate. This therefore leaves the phosphonate ligand itself mono-deprotonated in order to balance the charges (+2 from the Co(II) and (-1×2) from each phosphonate ligand). The Co1-O1 and Co1-O4 bond lengths are 2.030(3) and 2.029(3) Å respectively, while the Co1-N1, Co1-N2, Co1-N3 and Co1-N4 bond lengths are 2.183(3), 2.235(4), 2.170(3) and 2.240(3) Å respectively. The P1-C2 and P2-C12 bond lengths are 1.815(4) and 1.817(4) Å respectively. These values are consistent with previously reported monometallic cobalt phosphonates.⁹³

The packing diagram of (*S*)-**37** is shown in Figure 2.12. It can be seen that intermolecular hydrogen bonding forms between the two layers – specifically between the phosphonate hydrogen that is not deprotonated and the unbound phosphonate oxygen from an opposing molecule of (*S*)-**37**.

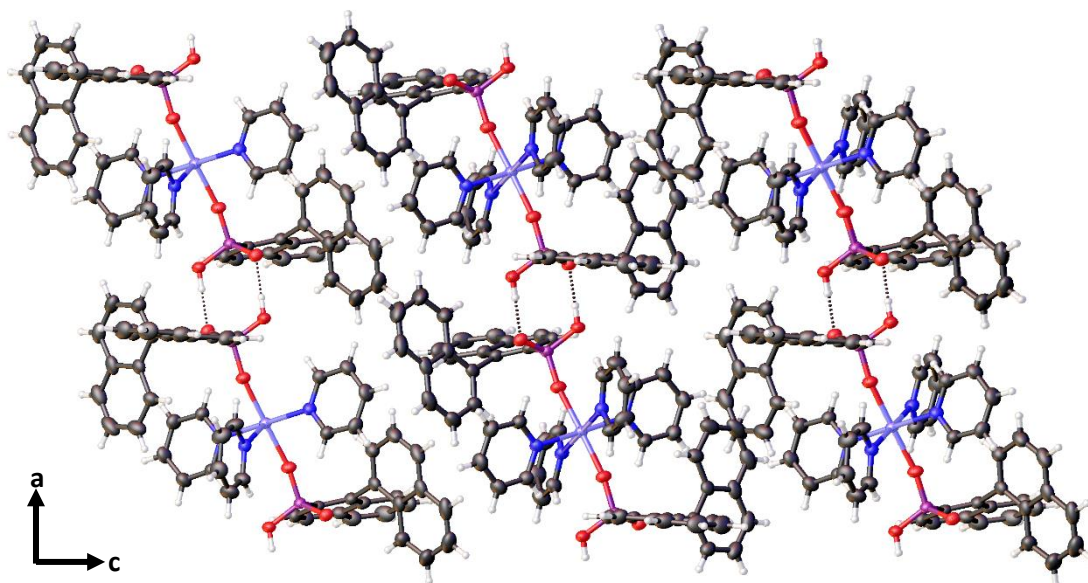


Figure 2.12 Packing diagram of (*S*)-**37** as viewed down the *b*-axis. The interlayer hydrogen bond lengths are 1.685 – 1.687 Å.

2.4 Higher-Order Co-(*S*)-**bpa** Phosphonates

The successful formation of the mononuclear Co(II) phosphonate in (*S*)-**37** under ambient conditions gave rise to the question as to whether higher-order cobalt phosphonates could be prepared, if the reaction conditions were altered. Indeed, as we have seen in Chapter 1, the hydrothermal method has been used to great effect – producing a plethora of layered, pillared and other higher dimensionality phosphonates. Thus, (*S*)-**bpa** and a cobalt(II) source were reacted with various co-ligands, bases and solvents. The temperatures and reaction times chosen were 160 °C and 72 hours respectively, with a cooling rate of 0.1 °C / min upon completion of the 72 hours of heating. The temperature was believed to be a good compromise of effective heating over ligand degradation – enough to allow for the formation of polymeric species, but not too high as to cause unwanted racemisation of the (*S*)-**bpa**. Furthermore, the duration of 72 hours (three days) was chosen in order to give the maximum possible time for the Co(II)-(*S*)-**bpa** polymers to form. It was also noted that 72 hours was a popular choice for other chemists in the preparation of metal phosphonates in the literature.^{74,94}

2.4.1 One-Dimensional Co Polymeric Chain, (*S*)-**38**

As a starting point, we first experimented with the hydrothermal route by reacting (*S*)-**bpa** with cobalt(II) acetate in the presence of pyridine (essentially the same reagents, equivalents and solvent system used to prepare (*S*)-**37**). Inspection of the Teflon liner revealed the presence of some crystals whose quality was too poor to refine the complete structure. However, one interesting caveat from what data could be acquired, was that pyridine was not incorporated into the structure – that is, the polymer contained only cobalt, oxygen and phosphonate ligands. Thus, after considerable experimentation with the equivalents, bases and solvent systems, we were able to isolate high quality crystals of (*S*)-**38** (Figure 2.13). This was achieved by employing one equivalent of (*S*)-**bpa** and one equivalent of cobalt(II) nitrate hexahydrate (the acetate form did not produce crystals of high quality). Furthermore, two equivalents of sodium hydroxide were used as the base (which in theory would allow for the double deprotonation of the ligand) and a 1:1 mixture of ethanol / water provided the solvent system.

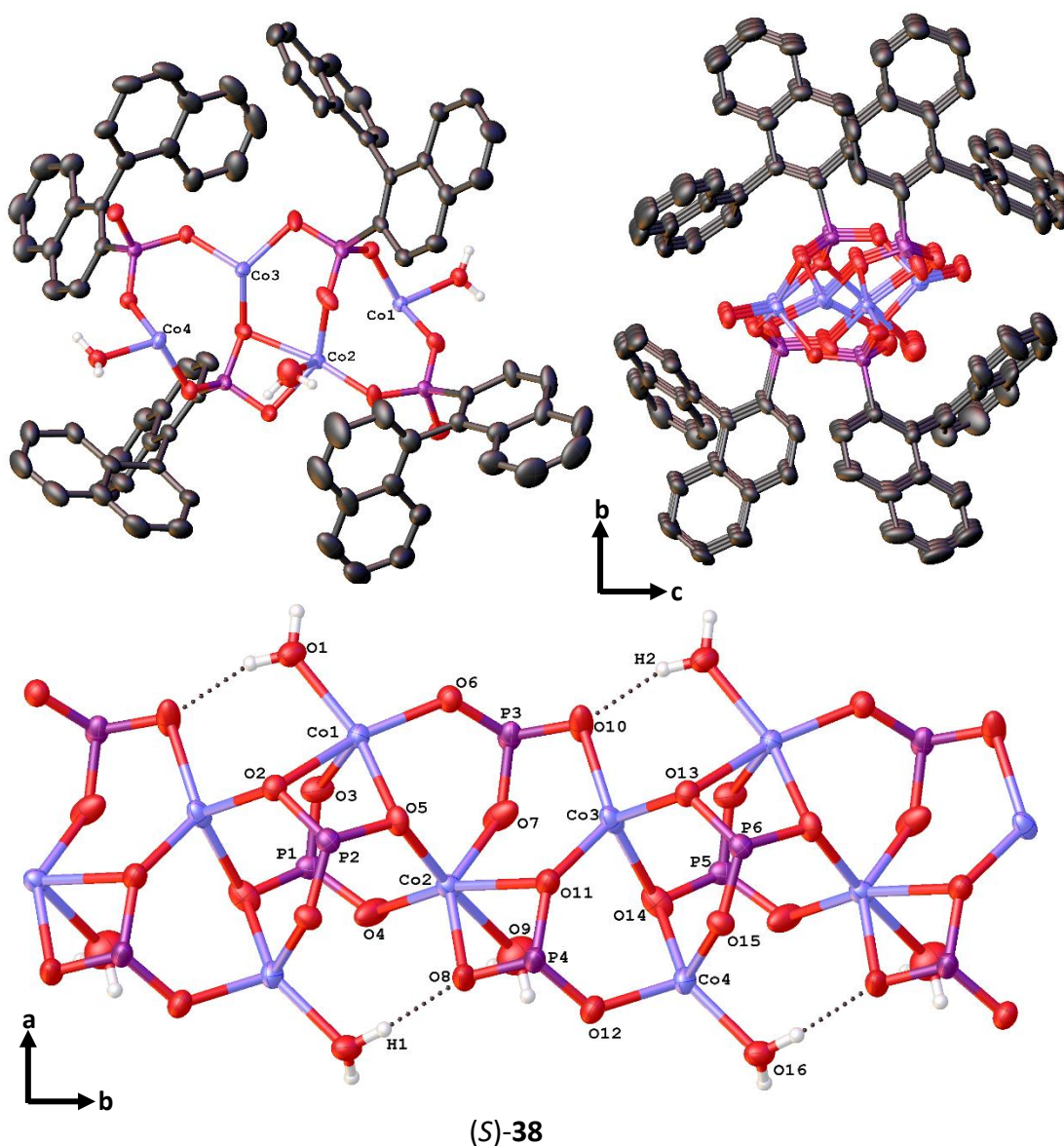


Figure 2.13 Top left: Structure of the asymmetric unit of (S)-38 in the crystal (hydrogen atoms on binaphthyls omitted). Top right: Structure of (S)-38 down the *a*-axis. Bottom: Structure of the (S)-38 core as viewed down the *c*-axis, with binaphthyls omitted.

(S)-38 crystallises in the monoclinic space group $P2_1$ and consists of a one-dimensional chain extending infinitely down the *a*-axis (Figure 2.33). The core is comprised of the cobalt phosphonate and is surrounded by a sheath of binaphthyl rings. There are a total of four different cobalt environments – two are four-coordinate, one is five-coordinate and another six-coordinate.

In order to confirm that all cobalt atoms still existed in the +2 oxidation state, we conducted BVS (Bond Valence Sum) analysis on all Co centres (see Appendix). This is an empirical method of calculating the oxidation states of metals by comparing the experimental bond lengths to donor atoms with tabulated bond lengths. While a useful tool, care should be taken when

applying it in order to calculate oxidation states where delocalisation is present, or any situation where a localised electron density is not a satisfactory model.⁹⁵ The calculations indicated all four cobalt atoms exist in the +2 oxidation state (see Appendix). The Harris notations for each of the four different phosphonate groups are as follows; P1 = [4.1₁1₂2₃4], P2 = [4.2₁2₂1₃1₄], P3 = [3.1₁1₂1₃], P4 = [3.1₂2₂1₄]. Thus, P2 and P4 bind in a bidentate manner while P1 and P3 bind in a monodentate manner and bridge four and three Co atoms respectively. Co1 and Co4 contain bound aqua ligands which form intramolecular hydrogen bonds to adjacent phosphonate oxygens. Inspection of the five-coordinate cobalt atom Co1 reveals the following bond lengths; Co1-O1 2.007(4), Co1-O2 2.262(4), Co1-O3 2.020(4), Co1-O5 2.095(4) and Co1-O6 1.939(4) Å while inspection of the phosphorus atom P3 reveals the following bond lengths; P3-O6 1.512(4), P3-O7 1.519(4) and P3-O10 1.533(4) Å. The H1...O8 and H2...O10 hydrogen bond lengths are 1.81(4) Å and 1.92(4) Å respectively. Comparison with previously reported Co(II) phosphonate polymers indicate a consistency in the bond lengths.^{1a,96}

2.4.2 Two-Dimensional Co-4,4'-Bipy Polymeric Sheet, (S)-**42**

The successful preparation of (S)-**38** was a promising result – it demonstrated (S)-**bpa** could form very different structures in both ambient and hydrothermal syntheses. Our attention then turned to whether this ligand would be able to be used in conjunction with a bridging ancillary ligand in order to prepare even higher dimensionality phosphonates than (S)-**38**. The use of linker molecules to generate complex architectures in hydrothermal synthesis is well-established in the literature.⁹⁷ These linkers are typically small organic compounds with a functionalisable group at two more positions on the molecule (in order to generate a repeat unit). Dicarboxylic acids,⁹⁸ diamines,⁹⁹ diazoles¹⁰⁰ and bipyridyls¹⁰¹ are some examples of commonly used linkers.

Owing to our success with pyridine, we turned to the most logical linker molecule, pyrazine (Figure 2.40). However, when pyrazine, (S)-**bpa** and Co(NO)₃·6H₂O were reacted under the same conditions and solvents as for (S)-**38**, it was found that (S)-**38** was also produced in this instance. Even after considerable alterations to the equivalents, (S)-**38** formed every time. Clearly pyrazine was merely deprotonating the ligand and was not incorporating itself into the structure. We postulated that sterically, the linker may have been too small to form these frameworks, since it would be competing for what little space there was with the already bulky binaphthyl rings of the ligand. Therefore, we substituted pyrazine for 4,4'-bipyridine – which can be thought of as an elongated form of pyrazine (Figure 2.14).

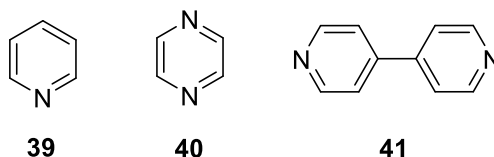


Figure 2.14 Structures of pyridine **39**, pyrazine **40** and 4,4'-bipyridine **41**. Pyridine exists as a liquid under ambient conditions while the latter two exist as crystalline solids.

When cobalt nitrate hexahydrate (1 mmol) and (*S*)-**bpa** (1 mmol) were reacted with 4,4'-bipyridine (0.5 mmol) in the presence of ethanol (2 mL) and water (2 mL), blue acicular crystals formed after 72 hours. These were immediately differentiated from the crystals of (*S*)-**38**, as these crystals were darker and possessed a lustre which was not present in the aforementioned crystals of (*S*)-**38**. The crystal structure of (*S*)-**42** was determined by single-crystal X-ray diffraction and its asymmetric unit is shown in Figure 2.15.

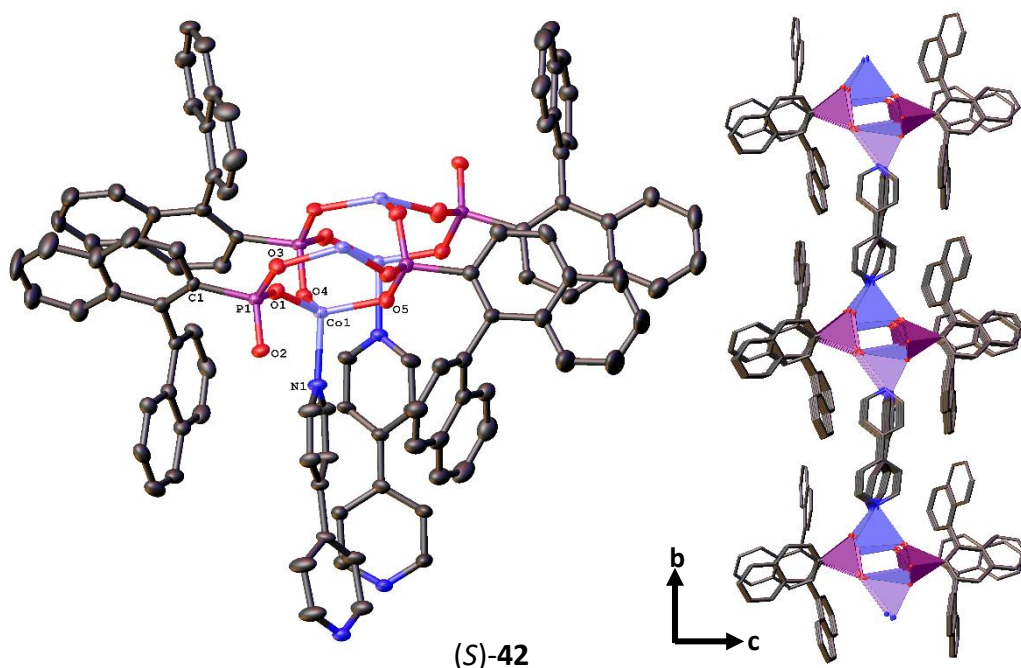


Figure 2.15 Left: Structure of the (*S*)-**42** asymmetric unit with hydrogen atoms omitted. Right: View of (*S*)-**42** down the *a*-axis (Co, P and O atoms represented by polyhedra).

Upon close inspection, (*S*)-**42** appears to be a layered structure crystallising in the triclinic space group *P*1. The macrostructure consists of two-dimensional sheets which extend infinitely parallel to the crystallographic [001] plane, while the cobalt phosphonate core is flanked by the binaphthyl groups in the [001] direction and the 4,4'-bipyridine groups in the [010] direction. (*S*)-**42** differs to (*S*)-**38** in that there is only one cobalt environment in the former – a tetrahedral Co(II) which is bound by three oxygen atoms from three separate phosphonate groups

([3.1₁1₂1₃] in Harris notation). The final coordination site is occupied by the nitrogen of the 4,4'-bipyridine ligand. Figure 2.16 illustrates this, and also shows the ladder-like framework which separates the layers of 4,4'-bipyridine molecules (right).

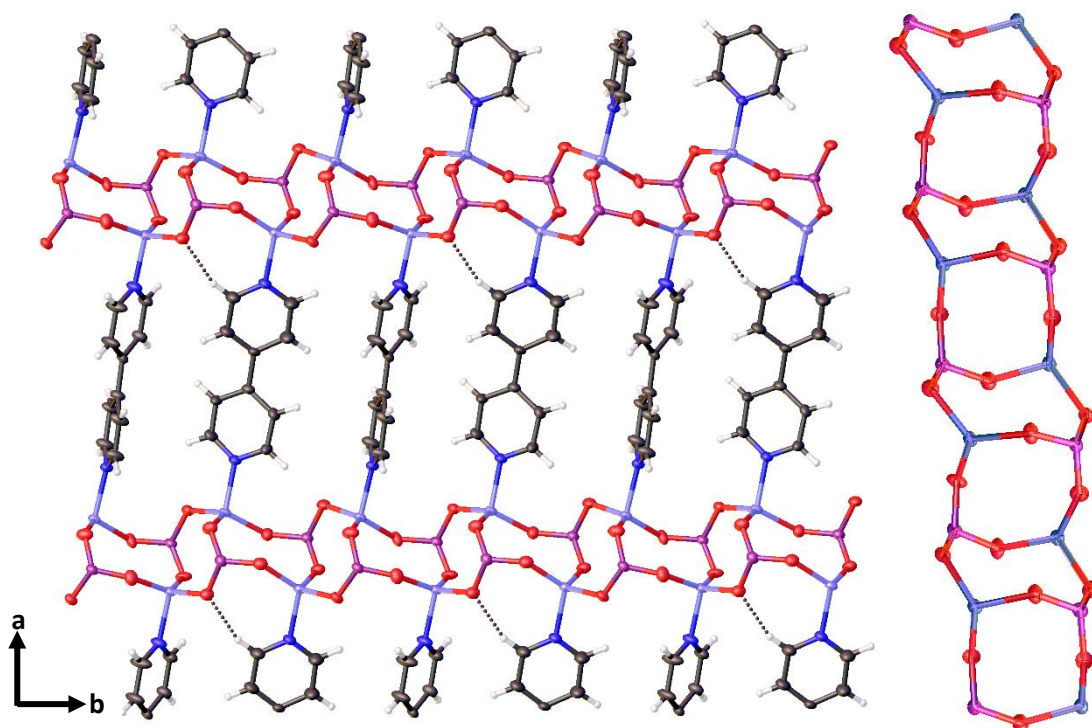


Figure 2.16 Left: Structure of (*S*)-**42** down the *c*-axis with binaphthyls omitted. Right: The ladder-like cobalt phosphonate core down the *b*-axis with binaphthyls and 4,4'-bipyridines omitted.

The Co-N bond lengths are 2.046(5)-2.066(5) Å, while the Co-O bond lengths were found to vary systematically depending on location; those in ladder rungs are 1.930(5)-1.949(5) Å, while those in ladder rails alternate along the chain in the two ranges 1.914(5)-1.917(5) and 1.934(5)-1.954(5) Å. The P-O bond lengths are 1.503(5)-1.538(5) Å and the P-C bond lengths are 1.809(6)-1.831(7) Å. Comparison of (*S*)-**42** with previously reported Co(II) phosphonate polymers indicated a consistency in the bond lengths.^{71b,102}

One interesting phenomenon we observed was that each alternate 4,4'-bipyridine group is twisted at an angle of around 90° relative to the *a*-axis, which we postulated was a physical manifestation of the scaffold trying to minimise steric repulsion that would arise if these groups were co-planar. This is in contrast to previously reported phosphonates in the literature in which the 4,4'-bipyridine linkers were found to be all co-planar.¹⁰³ For the intermittent 4,4'-bipyridine groups that are twisted, intramolecular hydrogen bonding arises between the ortho-hydrogen atoms of the 4,4'-bipyridines and the oxygen atoms of the adjacent phosphonate groups. We were eager to see if this characteristic manifested itself in other cobalt phosphonates in the

literature, and a search revealed this effect occurred in one other cobalt phosphonate – a diphosphonate, *N*-cyclohexylaminomethanediphosphonic acid described by Zheng.¹⁰⁴

With regards to the phosphonate core in (*S*)-**42**, the structure consists of a ladder-like framework of fused 8-membered rings adopting a boat-chair conformation. The rings consist of two cobalt atoms, two phosphorus atoms and four oxygen atoms. While a Co-O-P 8-membered ring is a common motif in many metal phosphonates,¹⁰⁵ to our knowledge this is the first occurrence of the Co-O-P ring forming a linear polymeric chain. The closest example is a layered fluoroaluminophosphate prepared by Xu *et al.*¹⁰⁶ However, in their case, the Al-O-P ladder was not linear – instead it contorted to form larger macrocyclic pores.

2.5 Preparation of (*R*)-**37**, (*R*)-**38** and (*R*)-**42**

In Chapter 1 we discussed briefly that when racemic **bpa** was employed, crystals failed to form for all crystallisations attempted. This was probably a consequence of the lack of stereoregularity in the binaphthyl rings, which would make crystalline packing difficult due to their bulk. However, we wished to demonstrate that if one were to start with (*S*)-binol in the synthesis, and therefore arrive at (*R*)-**bpa**, suitable crystals could still form, albeit with the opposite absolute configuration to the structures we have discussed hitherto.

Thus, we repeated the synthetic procedure described at the beginning of this Chapter, starting with (*S*)-binol, and prepared a batch of (*R*)-**bpa**. We then repeated the same crystallisations and isolated crystals of the corresponding (*R*)-**37**, (*R*)-**38** and (*R*)-**42**. After acquiring the crystal structures of these phosphonates, we determined that these were indeed the opposite absolute configuration of the aforementioned structures, due to the differing spatial orientations of the binaphthyl rings. Figure 2.17 illustrates this in the case of (*R*)-**37** and (*S*)-**37**.

This reproducibility is an important facet. Not only is it proof of concept that no matter which enantiomer of **bpa** is used, the same structure can be prepared, but it is also necessary if these phosphonates were to be tested in asymmetric catalysis where it would be preferable to have one enantiomer of each phosphonate.

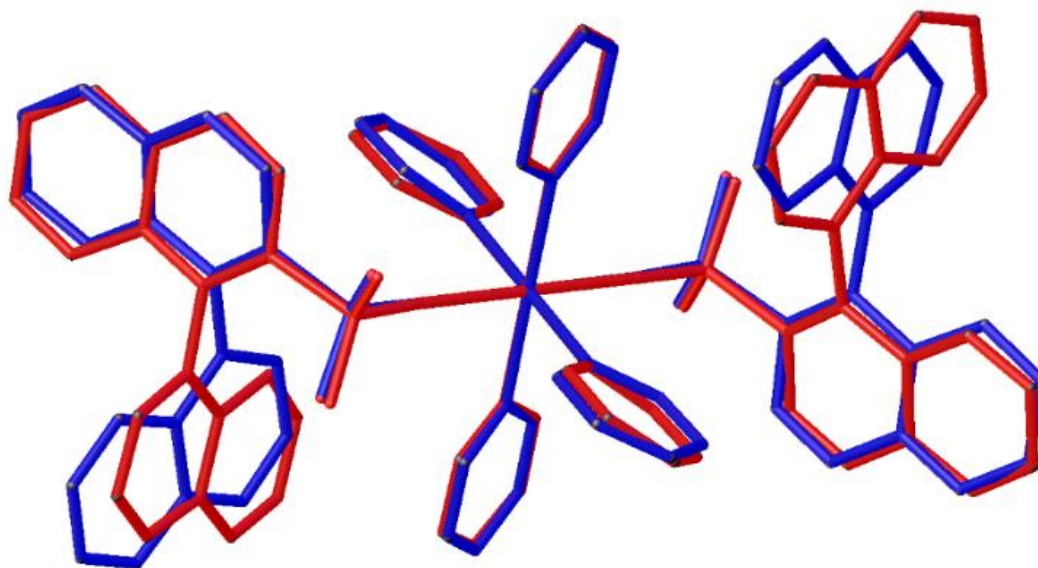


Figure 2.17 Overlapped wire structures of (*S*)-**37** (red) and (*R*)-**37** (blue). It can be seen that the lower binaphthyl rings (lower meaning the rings which do not contain the phosphonic acid moiety) are spatially oriented in opposing directions, which provided confirmation that these were opposite enantiomers.

2.6 Preparation of a Mixed Co-Sc Cluster, (*S*)-**43**

After successfully preparing a cohort of Co(II) phosphonates with varying complexities we were eager to see if (*S*)-**bpa** could be used to prepare mixed transition metal or mixed transition metal-lanthanide phosphonates. Indeed, many SMMs themselves consist of a transition metal component and a lanthanide component,¹⁰⁷ making these species a worthwhile avenue to explore.

The first attempts at preparing these mixed clusters involved simply stirring solutions of the ligand, cobalt acetate tetrahydrate and various lanthanide chloride hydrate salts in a myriad (see Appendix) of solvents such as ethanol, methanol, acetonitrile and combinations of these along with pyridine. Slow evaporation of the solvent or slow diffusion proved unsuccessful at preparing adequate crystals – most of the potentially suitable crystals were instead found to be globular when examined with plane-polarised light.

We then turned to our layering technique (see above) using the same pyridine solution of (*S*)-**bpa**, a mixed solution of cobalt acetate tetrahydrate and various lanthanide chloride hydrate salts from a good range in the series including lanthanum, europium, holmium and ytterbium. Unfortunately, no suitable crystals could be prepared by this method either. We also attempted a crystallisation with scandium and yttrium since these elements behave very similarly to lanthanides – both predominantly exist in the +3 oxidation state and also because scandium and yttrium are grouped into the rare earths with the rest of the lanthanides. The Co-Y layered

crystallisation failed, with a precipitate forming after 24 hours. However, the Co-Sc layered crystallisation (starting with 0.5 equivalents of both $\text{Sc}(\text{OTf})_3$ and $\text{Co}(\text{OAc})_2 \cdot 4\text{H}_2\text{O}$) yielded dark blue dendritic crystals after 48 hours (Figure 2.60). Single-crystal X-ray diffraction revealed these crystals to be of a mixed $\text{Co}(\text{II})$ - $\text{Sc}(\text{III})$ cluster, (*S*)-**43**. Figure 2.18 shows the structure of (*S*)-**43** in the crystal.

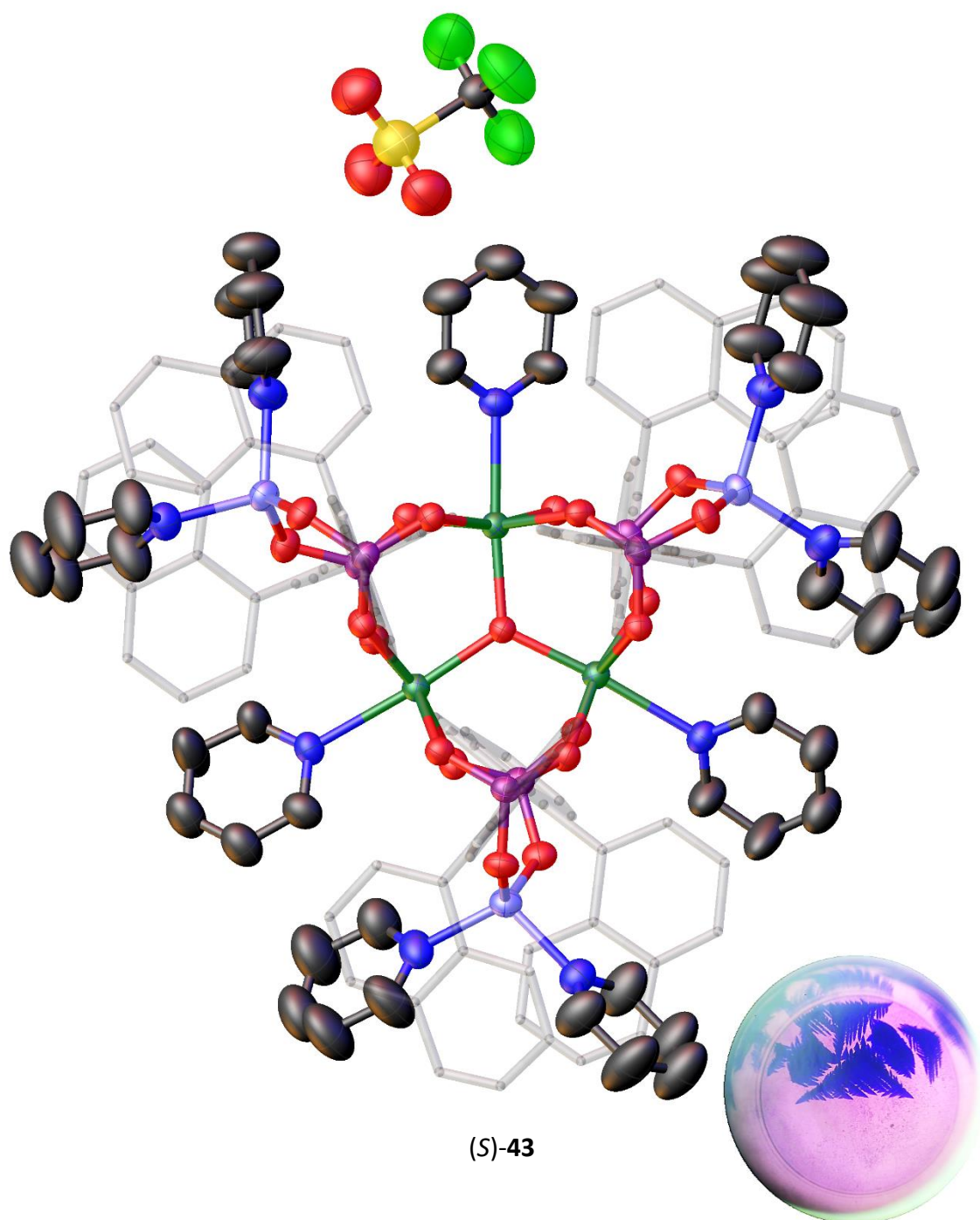


Figure 2.18 Structure of (*S*)-**43** in the crystal, with binaphthyl groups represented as translucent sticks and hydrogen atoms omitted. Also shown is the triflate (CF_3SO_3^-) counter-anion which balances the charge of the cluster. Bottom right: Physical form of (*S*)-**43**, as viewed under a standard laboratory microscope (10x zoom).

(*S*)-**43** is a mixed Co_3Sc_3 cluster crystallising in the space group $P2_13$ and in which all three scandium atoms exist in the +3 oxidation state, while all three cobalt atoms exist in the +2 state. The three octahedral Sc(III) atoms are bridged by a central μ_3 -oxygen and each bind to three pyridine ligands, forming a paddlewheel-type motif lying in the plane of the page. Emerging from, and going into the plane, are the six (*S*)-**bpa** groups, each binding in a [3.111] configuration (with two oxygens binding to two scandium ions while the third bridges to a cobalt ion). On the periphery of the cluster are the three Co(II) atoms, each adopting a tetrahedral arrangement. Two coordination sites are occupied by the phosphonate groups from two molecules of (*S*)-**bpa**, while two capping pyridine groups complete the coordination sphere. Figure 2.19 highlights the core of (*S*)-**43**.

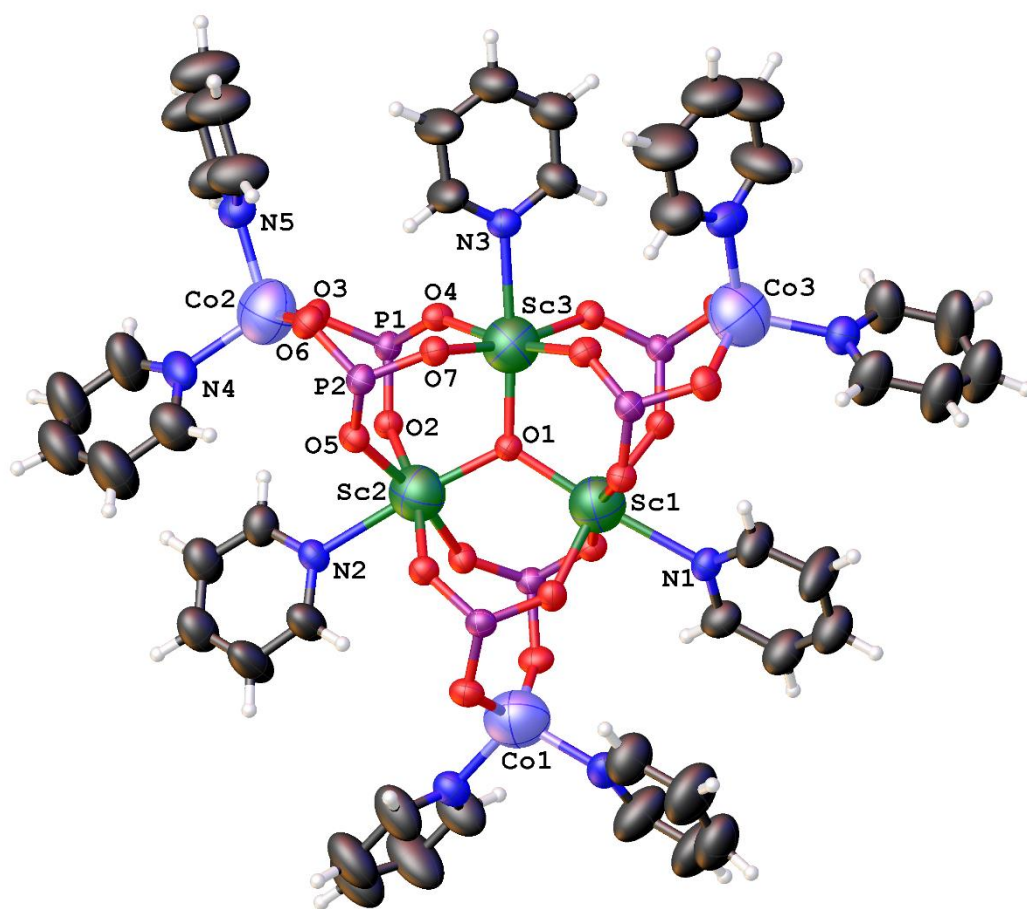


Figure 2.19 Structure of the (*S*)-**43** core in the crystal, with binaphthyl groups omitted. The large ellipsoids on the pyridine carbons are due to the relatively high rotational degrees of freedom possessed by the pyridines. The Co and Sc ellipsoids have been increased in size for ease of viewing.

With regards to Figure 2.19, The Sc1-O1, Sc2-O1 and Sc3-O1 bond lengths are all 2.0388(14) Å while the Sc1-N1, Sc2-N2 and Sc3-N3 bond lengths are all 2.406(7) Å. With regards to the phosphorus atoms, the P1-O2 and P1-O4 bond lengths are both 1.513(5) Å and the P1-O3 bond length is 1.524(6) Å. In comparison, the P2-O5, P2-O7 and P2-O6 bond lengths are 1.517(5), 1.521(5) and 1.532(6) Å respectively. The oxygen to cobalt bond lengths are shorter than the

oxygen to scandium – the Co2-O3 and Co2-O6 bond lengths fall short of 2 Å at 1.914(6) and 1.921(6) Å respectively. The oxygen to scandium bonds fall slightly over 2 Å however. The Sc2-O2, Sc2-O5, Sc3-O4 and Sc3-O7 bond lengths are 2.101(5), 2.107(5), 2.094(5) and 2.077(5) Å respectively. While it was initially assumed that the oxygen to scandium bond lengths would be shorter than oxygen to cobalt due to the higher charge density possessed by scandium (Sc(III) versus Co(II)), we postulated the shorter bond lengths to cobalt arose due to the tetrahedral arrangement of the cobalt atoms. Since the scandium centres adopted an octahedral arrangement, these would be much more sterically hindered, and would inevitably lead to longer bond lengths than the significantly less encumbered tetrahedral cobalt centres.

Interestingly, a search of mixed Co-Sc phosphonates in the literature revealed that no such structure exists. The only other example of a Co-Sc coordination complex we could find was a Cp*ScOC(CH₃)Co(CO)Cp species (Cp = cyclopentadienyl; Cp* = pentamethylcyclopentadienyl) prepared by Bercaw and co-workers.¹⁰⁸

The preparation of (S)-**43** was indeed an encouraging result and certainly gives impetus for any potential future researcher working with (S)-**bpa** to explore the avenue of mixed metal clusters, since as we have seen, it is certainly feasible to easily and reliably prepare these architectures in the case of scandium and cobalt. Moreover, if successful lanthanide-Co clusters could be reliably prepared, these would very likely possess SMM properties as mentioned above.

2.7 Testing the Catalytic Properties of (S)-**38** and (S)-**42**

In Chapter 1 we discussed how a commercially available silica-supported alkyl phosphonate – when coordinated to cobalt(II) – could catalyse allylic and benzylic oxidations to alkenes.³⁷ We wished to examine whether our polymeric phosphonates (S)-**38** and (S)-**42** were capable of producing similar results. These two phosphonates were chosen as they were the only polymeric cobalt phosphonates we had prepared and were insoluble. Thus, they would act as heterogeneous catalysts – much in the same way that the cobalt alkyl phosphonate **12** did.

In the original paper by Sullivan and co-workers, a number of alkene substrates were tested using *tert*-butyl hydroperoxide as the oxidant. These included terpenes, substituted cyclohexenes and steroid derivatives.³⁷ In order to save resources, we opted to first test the efficacy of (S)-**38** and (S)-**42** on cyclohexene itself (Figure 2.20). Since this is a simple, unhindered alkene, it would provide a good benchmark to gauge the catalytic properties of our phosphonates. Furthermore, the presence of any cyclohexenone product would be easily identifiable by ¹H NMR spectroscopy. The carbonyl group causes the two allylic protons to

become inequivalent, leading to two peaks at 5.50 and 6.57 ppm (cyclohexene only contains a single peak in this region at 5.69 ppm). After a catalysis run had finished, the crude material was filtered from the cobalt phosphonate and dried under vacuum. A ^1H NMR spectrum of the crude material was then recorded and the region around 6.57 ppm was carefully inspected for the peak which would indicate the presence of cyclohexenone product. If any peak was present here, the product would be purified by column chromatography in order to ascertain the yield. The reagents and equivalents were kept the same as those reported by Sullivan *et al.*, and the reactions were performed at varying times. Since (S)-**38** and (S)-**42** are polymeric species, we chose to use the same mass as the alkyl phosphonate (60 mg). Table 8 summarises the results of the catalytic screening.

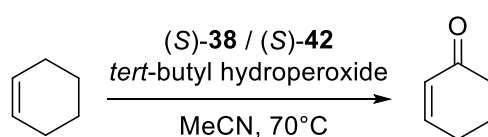


Figure 2.20 Reaction scheme for the attempted oxidation of cyclohexene to cyclohexenone using (S)-**38** and (S)-**42**.

Entry	Phosphonate	Reaction Time / h	Yield / %
1	None	48	0
2	(S)- 38	24	0
3	(S)- 38	36	0
4	(S)- 38	48	0
5	(S)- 42	24	0
6	(S)- 42	36	0
7	(S)- 42	48	0

Table 8 Results of the oxidation of cyclohexenone using (S)-**38** and (S)-**42** at various reaction times. Entry 1 uses only *tert*-butyl hydroperoxide. For reference, under the same conditions, Sullivan *et al.* reported a 90% yield.³⁷

Unfortunately, neither (S)-**38** nor (S)-**42** were able to catalyse the oxidation of cyclohexene to cyclohexenone. No peaks pertaining to the vinyl protons in cyclohexenone were seen whatsoever in the ^1H NMR spectrum of the crude filtered reaction. We speculated that due to the complete encapsulation of the Co(II) centres by the binaphthyl rings of the phosphonate groups, there was no area for the cobalt atoms to interact with the alkene substrate and the *tert*-butyl hydroperoxide. This was determined by inspection of the crystal structures of (S)-**38** and (S)-**42** with all atoms represented by their maximum van der Waals radii (Figure 2.21). This is in contrast to the alkyl cobalt phosphonate prepared by Sullivan and co-workers. Although there is no crystal structure or electron micrographs of their catalyst, it is known that the basic structure consisted of an alkyl phosphonate chain bound to a solid silica support. The cobalt

atoms bound to the phosphonates at the end of the chains were thus completely exposed, providing a large surface area of cobalt atoms to interact with the substrates and oxidants.

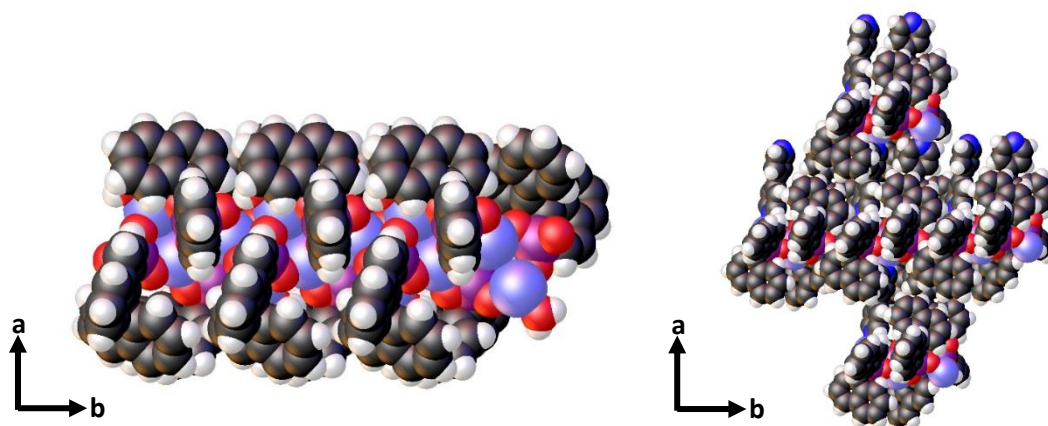


Figure 2.21 Left: Structure of (*S*)-**38** and right: (*S*)-**42** in the crystal with atoms represented as spheres with their maximum van der Waals radii. It can be seen that in both cases, as a consequence of the bulky nature of the binaphthyl rings, the cobalt atoms (light blue) are almost completely encapsulated and therefore unable to catalyse the allylic oxidation reaction.

Due to the unsuccessful results we obtained, (*S*)-**38** and (*S*)-**42** were not utilised in any further catalytic studies.

2.8 Conclusion

To conclude, we have demonstrated (*S*)-**bpa** to be a highly versatile ligand in cobalt chemistry, capable of generating a zero-dimensional, one-dimensional and two-dimensional Co(II) phosphonate depending on the reaction conditions and presence of co-ligands. Furthermore, the corresponding (*R*)- phosphonates were also prepared and the opposite absolute configuration unambiguously assigned by X-ray crystallography. We were also able to expand the scope of the coordination reactions by demonstrating that (*S*)-**bpa** could also bind to scandium and cobalt *in situ* to form a mixed Co-Sc cluster, which after a literature search, was revealed to be the first example of a mixed Co-Sc phosphonate. Figure 2.22 summarises the possible structures which can be obtained from (*R*)/(*S*)-**bpa** and a Co(II) source.

With regards to the catalytic properties, our polymeric phosphonates (*S*)-**38** and (*S*)-**42** proved unsuccessful at allylic oxidations, probably by virtue of the sterically demanding binaphthyl groups blocking the cobalt atoms from interacting with the substrate and oxidant. As such, any potential future chemist working with these structures should be advised to explore other avenues of catalysis. Perhaps gas-phase catalysis would prove to be a fruitful endeavour if there are any suitably sized channels or pores in these phosphonates.

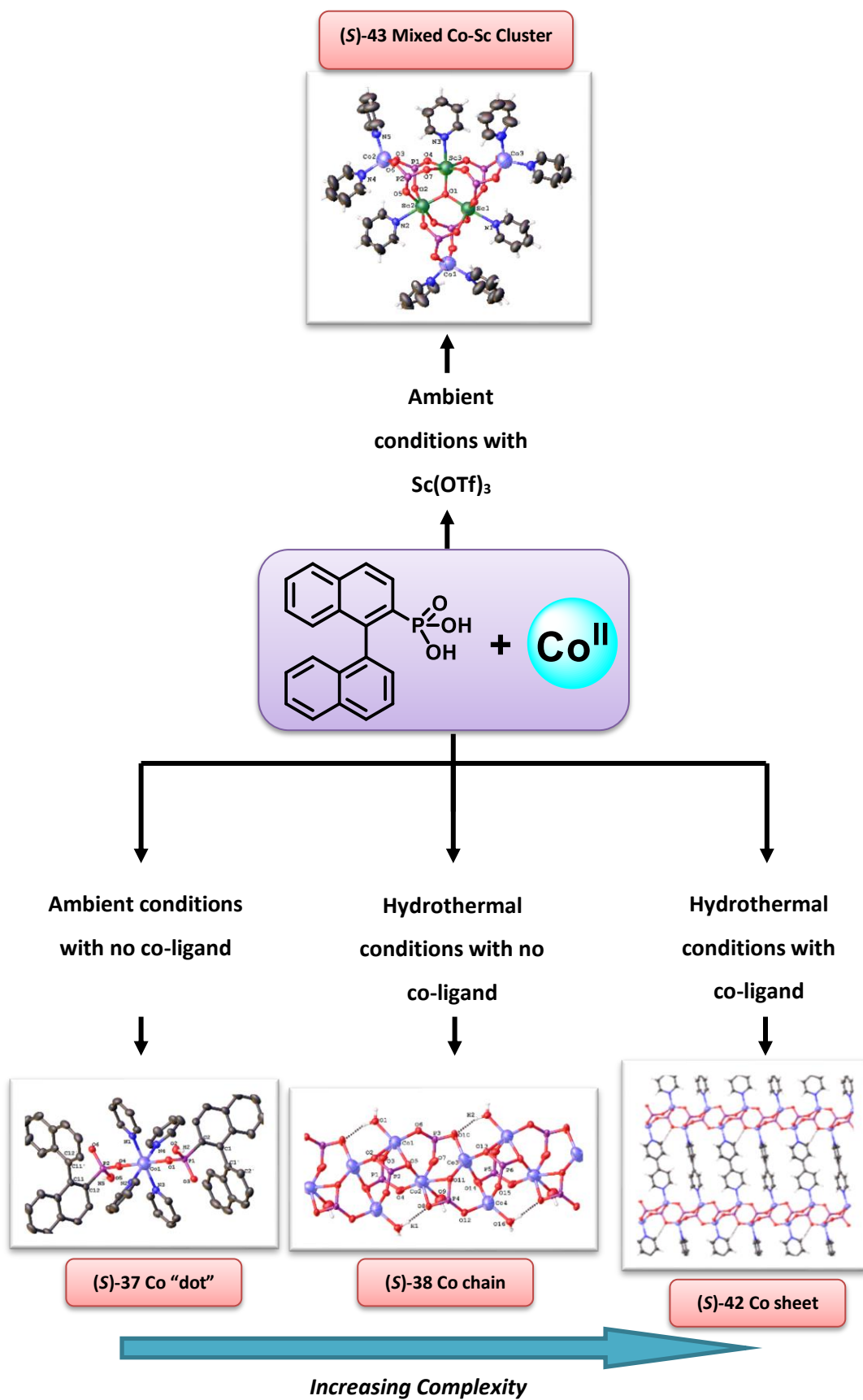


Figure 2.22 Scheme showing general route to the various Co(II) phosphonates discussed in this Chapter.

Chapter 3 – Coordination of (*S*)-**bpa** to Other Transition Metals

3.1 Introduction

After our success with cobalt, we were eager to expand the scope of this project by attempting to crystallise other transition metal phosphonates. Initially, there was no limit to what d-block metals were reacted with (*S*)-**bpa** in principle. Of course, a larger focus was placed on elements whose electronic profiles were suitable for SMM behaviour, such as most of the first-row transition row metals including manganese, iron, nickel and copper. Elements whose corresponding phosphonate complexes had proven effective at certain catalytic transformations (see Chapter 1) were also considered to be of interest. Finally, we were also keen to investigate whether main group and lanthanide metal phosphonates could also be prepared (see Chapter 4), but in this Chapter we will focus on non-cobalt transition metal systems.

One of the first phenomena we noticed was that the noble metals in their chloride salts (ruthenium, rhodium, palladium, silver, iridium, platinum and gold) did not react at all with (*S*)-**bpa**. Any crystals that were obtained were almost universally the pyridine complexes, such as $[\text{Au}(\text{Cl})_2(\text{Py})_4]\text{Cl}$. We attributed this to the incompatible hardness and softness between the metal centre (the Lewis acid) and the phosphonate oxygens of (*S*)-**bpa** (the Lewis base). Since phosphonates will always bind through their oxygen atoms, this makes them hard Lewis bases. They will therefore prefer to bind to hard Lewis acids such as Group 1 and 2 metals, first-row transition metals and lanthanides. In order to understand this principle more clearly, it is necessary to define the terms *hard* and *soft*. Hard Lewis acids and bases are generally characterised by their small ionic radii, low polarisability (the ability to form instantaneous dipoles) and high oxidation states. Consequently, soft Lewis acids and bases are characterised by their large and diffuse ionic radii, high polarisability and low oxidation states. The noble metals are soft Lewis acids and will therefore favour complex formation with soft Lewis bases such as phosphines, carbenes and to a lesser extent, sulfides.

Figure 3.1 shows a cut-down periodic table highlighting the hardness and softness of important elements in coordination chemistry.

whether a monometallic Sc-(*S*)-**bpa** complex or cluster could form, since it was already determined that it was feasible to form a mixed Co-Sc cluster in (*S*)-**43**.

Thus, scandium triflate was layered with (*S*)-**bpa** with the same method and equivalents outlined in Chapter 2. However, upon completion of the layering, a viscous precipitate formed, and no crystals could be obtained. After a crystallisation screening with various solvents, it was found that the 0.5 mL of water was causing this aggregation, but despite omitting water from the layering, no crystals were obtained. Thus, a change of tactic was adopted, and the ideal solvent was determined to be neat pyridine. The presence of any other organic solvent – regardless of amount – would cause precipitation. The optimised conditions were (*S*)-**bpa** (0.1 mmol), Sc(OTf)₃ (0.5 mmol – scaled to half equivalents due to the large molecular weight of scandium(III) triflate) and 3 mL of pyridine. These were stirred for 24 hours before being left to slowly evaporate. Parafilm was also placed over the top of the vials in order to inhibit the rate of evaporation.

After two weeks, colourless plates were observed. These were analysed by single-crystal X-ray diffraction and were found to be crystals of a Sc₃ cluster (*S*)-**44**. Figure 3.2 shows the structure of (*S*)-**44** and the (*S*)-**44** core in the crystal.

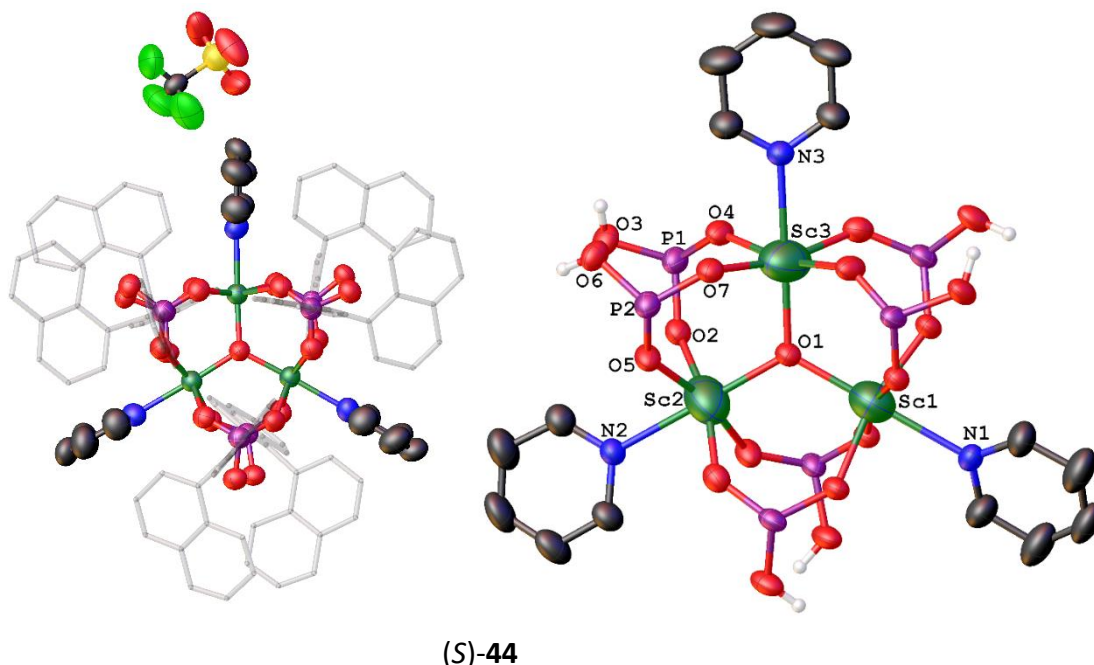


Figure 3.2 Left: Structure of (*S*)-**44** in the crystal, with binaphthyl groups represented as translucent sticks and hydrogen atoms omitted. Also shown is the triflate (CF₃SO₃⁻) counter-anion which balances the charge of the cluster. Right: Structure of the (*S*)-**44** core in the crystal with hydrogen atoms on pyridine groups omitted. The Sc ellipsoids have been increased in size for ease of viewing.

As can be seen, (*S*)-**44** is essentially a cut-down version of (*S*)-**43** with the three peripheral Co(py)₂ groups removed. In their place are six protonated OH groups from the phosphonates. This had the unforeseen effect of granting us some insight into how these structures might form. We theorise that in the case of (*S*)-**43**, the structure of (*S*)-**44** forms first, and the cobalt atoms in solution then “clip” onto the ends, along with six capping pyridine ligands, forming (*S*)-**43** (Figure 3.3). This is a well-established phenomenon in the literature and is known as cluster expansion. This generally involves a known cluster being crystallised, purified and re-dissolved in solution before having further equivalents of metal salt or ligand added. These bind to the periphery of the cluster and expand it in size, and in so doing, confer altered physical and chemical properties to the cluster. The only difference in our case was that this entire process was done in a one-pot, one-step process. Cluster expansion has been used to great effect by various research groups.^{62,111} Usually, a carboxylate ligand with its two oxygen donor atoms is substituted for a phosphonate with its three oxygen donor atoms. The extra oxygen atoms allow the cluster to bind to further metals, which in theory can allow for mixed-metal systems.

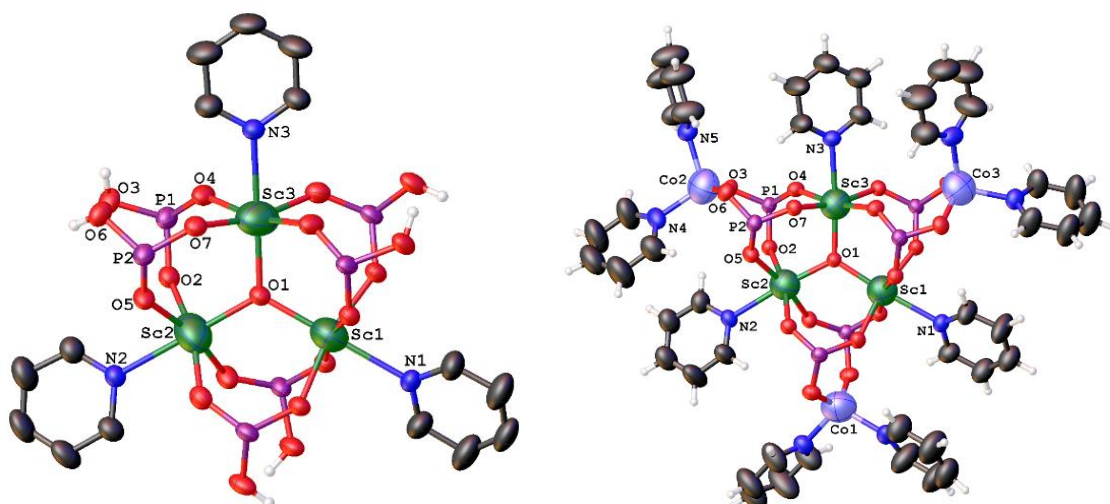


Figure 3.3 Comparison of (*S*)-**44** (left) and (*S*)-**43** (right) with binaphthyl groups omitted. It can be seen how the latter can be thought of as being an expanded cluster of the former.

(*S*)-**44** is a trimetallic Sc₃ cluster crystallising in the *P*3₁2 1 space group. The Sc1-O1 and Sc2-O1 bond lengths are both 2.050 Å while the Sc3-O1 bond length is 2.027 Å. The Sc1-N1 and Sc2-N2 bond lengths are both 2.357 Å while the Sc3-N3 bond length is 2.383 Å. Each phosphonate ligand binds in a [2.110] manner, and the P1-O2, P1-O3 and P1-O4 bond lengths are 1.504, 1.534 and 1.510 Å respectively, while the P2-O5, P2-O6 and P2-O7 bond lengths are 1.508, 1.546 and 1.512 Å respectively. The Sc2-O2, Sc2-O5, Sc3-O4 and Sc3-O7 bond lengths are 2.083, 2.093, 2.091 and

2.090 Å respectively. These values are consistent with the few Sc phosphonates that are already in the literature.¹¹²

We were also able to characterise (S)-**44** by NMR spectroscopy. This was previously inaccessible with (S)-**43** due to the paramagnetic nature of Co(II), which led to broad and indecipherable spectra. Sc(III) on the other hand, has an electronic d^0 configuration, and was therefore compatible with analysis by NMR spectroscopy. Thus, we prepared suitable NMR samples of (S)-**44** by dissolving the cluster in d_6 -dmso, which incidentally was the only organic solvent able to dissolve it. The ^1H NMR spectrum was somewhat broadened, and the multitude of aromatic peaks which comprise the signals of the binaphthyl rings had merged together. However, the $\{^1\text{H}\}^{31}\text{P}$ NMR spectrum was more promising, showing three distinct phosphorus environments (Figure 3.4). This was unexpected, as inspection of the crystal structure would imply that all phosphorus environments are the same, since each molecule of (S)-**bpa** binds in exactly the same manner. We speculated that these three peaks arose due to some of the phosphonate groups being deprotonated in solution, while some were protonated. In order to ascertain whether this was the case, two drops of 2 M HCl were added to the NMR tube containing the solution of (S)-**44**. The tube was shaken to encourage reaction and the same ^{31}P NMR experiment was reran. As expected, the three peaks collapsed into one single peak at 11.66 ppm (Figure 3.4). This was at a different chemical shift to the other three peaks and was close to the chemical shift of uncoordinated (S)-**bpa** in this solvent (12.40 ppm). This implies two possible outcomes – either the chemical shift of completely protonated (S)-**44** lies at 11.66 ppm, or the acid has caused the structure to break down, releasing unbound (but still protonated) (S)-**bpa** with a slightly altered chemical shift due to the presence of Sc^{3+} ions in the solution. Further studies would have to be conducted on the stability of (S)-**44** towards acidic media in solution.

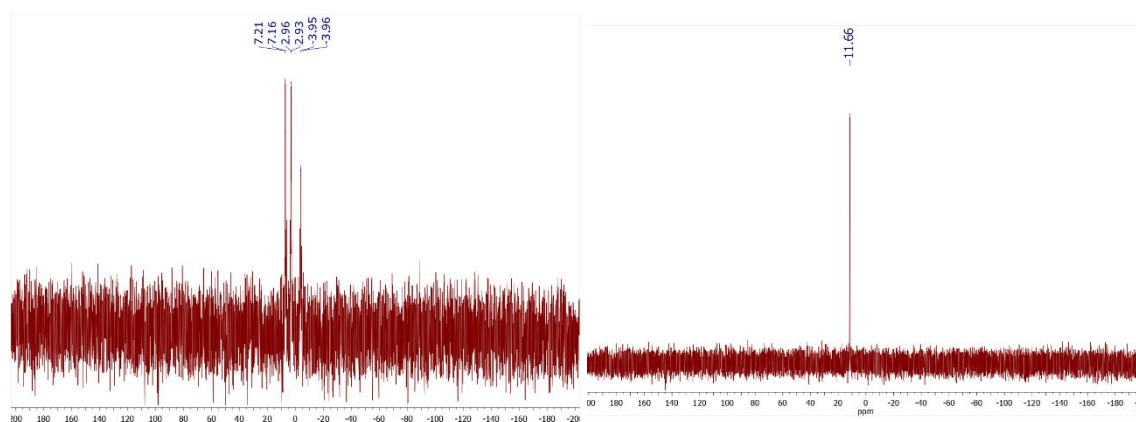


Figure 3.4 Left main: $\{^1\text{H}\}^{31}\text{P}$ NMR spectrum of (S)-**44** (recorded in non-deuterated dmso). The three regions fall within the chemical shift range of 7.19, 2.95 and -3.96 ppm. Inset: Expansion of the pertinent region. Right: $\{^1\text{H}\}^{31}\text{P}$ NMR spectrum of (S)-**44** after the addition of two drops of 2 M HCl. There is a single peak at 11.66 ppm. For reference, uncoordinated (S)-**bpa** has a chemical shift of 12.40 ppm in this solvent.

In conclusion, we have successfully prepared the first chiral scandium phosphonate (*S*)-**44**, which can be thought of as a precursor to the mixed Co-Sc cluster, (*S*)-**43**. Moreover, we obtained NMR information to a class of compounds which are normally NMR-incompatible due to the absence of the paramagnetic Co(II). While these were promising results, we did not perform any further studies to (*S*)-**44**, since scandium is a rather niche element and has no interesting magnetic properties (by virtue of the complete absence of d-electrons). Instead, we moved onto further coordination reactions of (*S*)-**bpa** with other transition metals.

3.2.2 Manganese Phosphonates, (*S*)-**45** and (*S*)-**46**

The next transition metal investigated was manganese. This was an important metal, namely since the first ever SMM prepared was a mixed valence manganese cluster (see Chapter 1). Manganese compounds exhibit oxidation states ranging from Mn(0) to Mn(VII). The most common oxidation states of manganese are +2, +4 and +7, although the most commonly observed oxidation state out of these three is +2 – any higher oxidation state Mn compounds are highly oxidising.¹¹³ Moreover, Mn(III) is prone to disproportionation in solution, forming Mn(II) and Mn(IV). With this in mind, we opted to use only Mn(II) salts in our crystallisations.

Thus, when a solution of (*S*)-**bpa** in pyridine was layered onto a solution of MnCl₂ in water, ethanol and acetonitrile, colourless parallelepipedal crystals formed after 24 hours. Single-crystal X-ray diffraction revealed these crystals to be of a monometallic Mn(II) complex, (*S*)-**45**. Figure 3.5 shows the structure of (*S*)-**45** in the crystal.

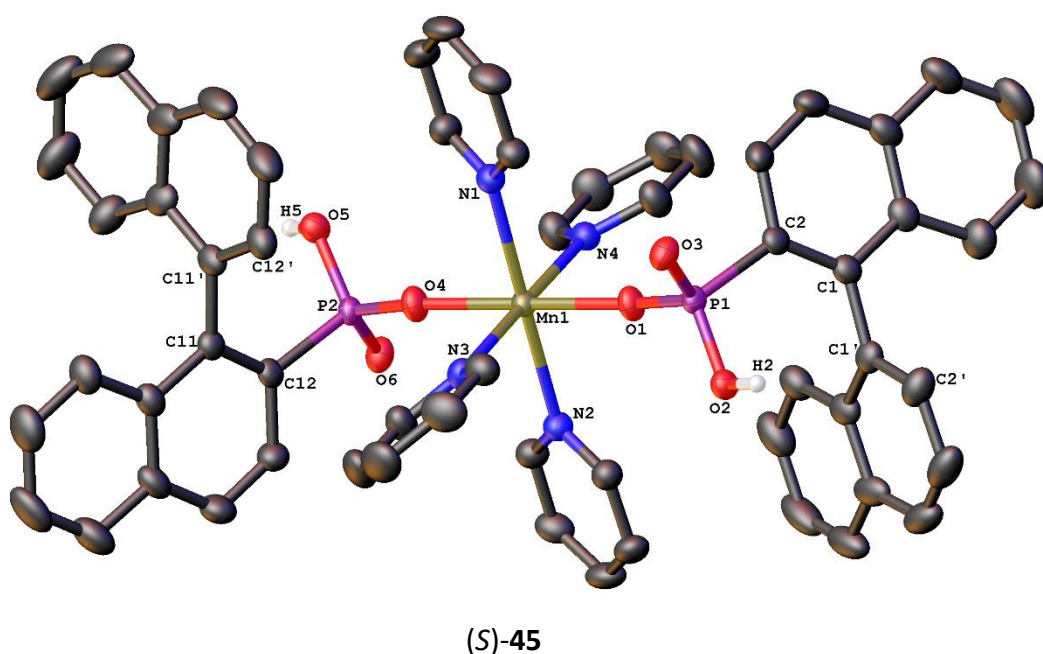


Figure 3.5 Left: Structure of (*S*)-**45** in the crystal with hydrogen atoms on binaphthyls and pyridines omitted.

It can be seen that (*S*)-**45** is completely isostructural to (*S*)-**37** (Chapter 2), with the Co(II) centre substituted for Mn(II). This is probably a manifestation of not only the bulky nature of (*S*)-**bpa**, in which two molecules would preferentially bind in an axial configuration to avoid steric repulsion, but also the exact same layering conditions which were used to prepare (*S*)-**37**. The pyridine base would occupy the four vacant coordination sites. The steric bulk of (*S*)-**bpa** appears to be able to dictate the size of the complex or cluster, depending on which conditions are employed. Therefore, despite the size of (*S*)-**bpa**, it is possible to prepare monometallic metal phosphonates using this ligand.

(*S*)-**45** is an octahedral, axially-distorted Mn(II) complex crystallising in the $P2_1$ space group and as mentioned previously, is completely isostructural with (*S*)-**37**, with four equatorial pyridine ligands and two axial-bound, mono-deprotonated (*S*)-**bpa** molecules which bind *via* the deprotonated oxygens on the phosphonate. The Mn1-N1, Mn1-N2, Mn1-N3 and Mn1-N4 bond lengths are 2.276(3), 2.350(3), 2.289(3) and 2.354(3) Å respectively. The Mn1-O1 and Mn1-O4 bond lengths are 2.0726(18) and 2.0739(17) Å respectively. The P1-C2 bond length is 1.815(3) Å while the P2-C12 bond length is 1.819(3) Å. The C2-C1-C1'-C2' torsion angle is 79.826° while the C12-C11-C11'-C12' torsion angle is 95.983°. These values are consistent with similar phosphonates in the literature.¹¹⁴ The packing diagram of (*S*)-**45** is shown in Figure 3.6.

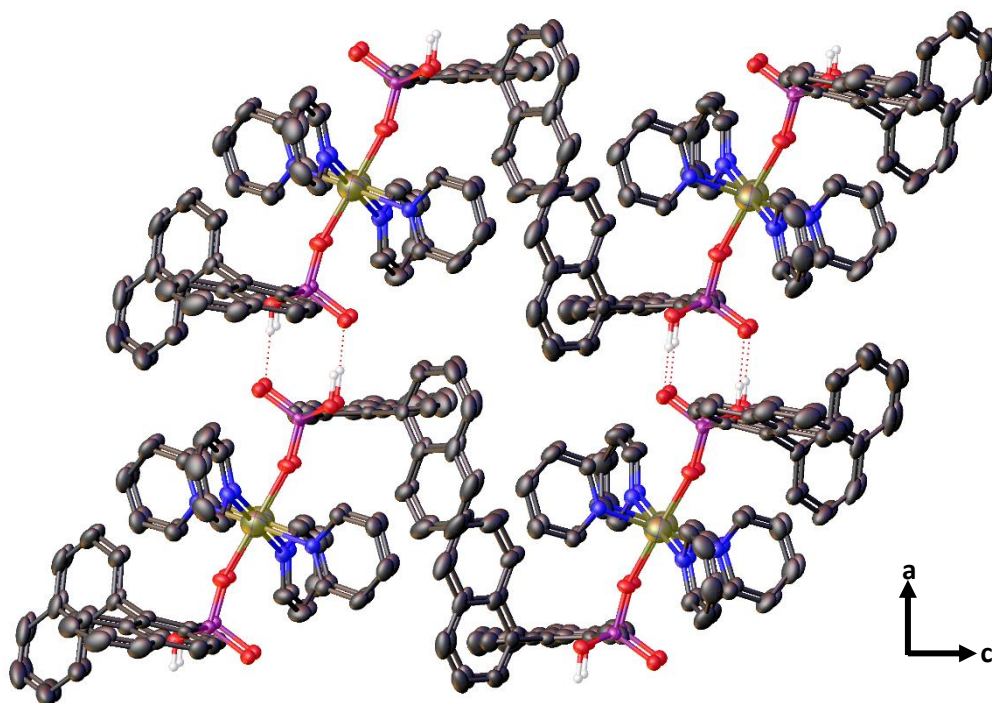


Figure 3.6 Packing diagram of (*S*)-**45** as viewed down the *b*-axis. The interlayer hydrogen bond lengths are 1.554 – 1.716 Å.

We also attempted to prepare higher order Mn(II) architectures *via* the hydrothermal method but unfortunately no reaction yielded crystalline material. However, when manganese acetate tetrahydrate and (*S*)-**bpa** (both 1 mmol) were stirred in a mixture of acetonitrile and pyridine for 24 hours before being left to evaporate, a rather different product began to crystallise. These were certainly not the colourless crystals of (*S*)-**45**, but instead were dark-red plates. Analysis by single-crystal X-ray diffraction revealed these crystals to be of a Mn₆ cluster, (*S*)-**46**. Figure 3.7 shows this cluster in the crystal and the (*S*)-**46** core.

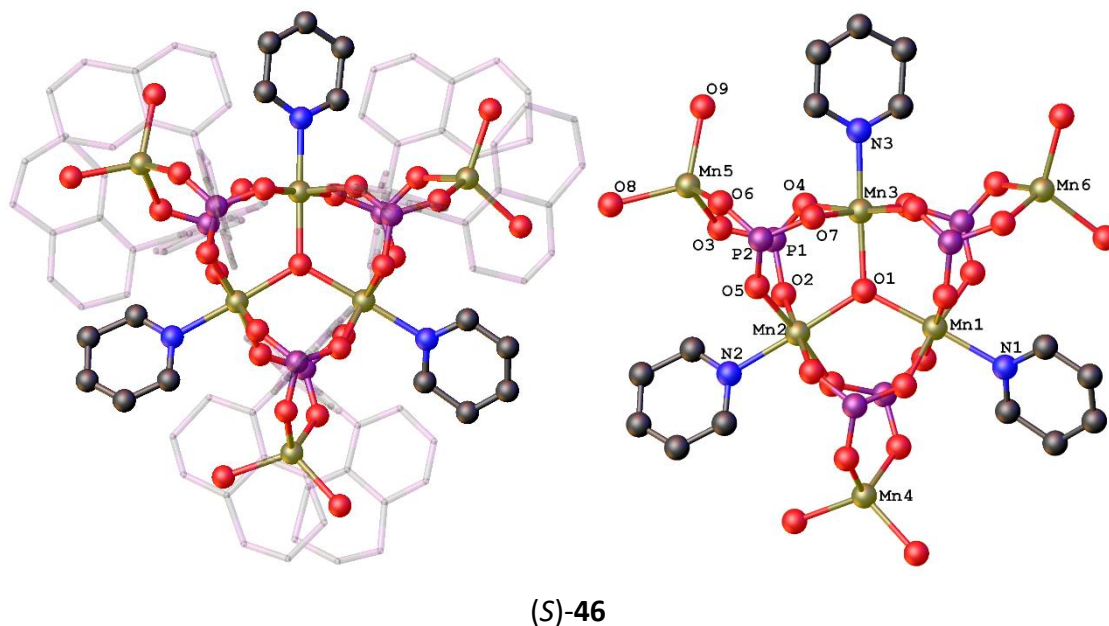


Figure 3.7 Left: Structure of (*S*)-**46** in the crystal, with binaphthyl groups represented as translucent sticks and hydrogen atoms omitted. It can be seen by the distorted appearance of the binaphthyls that this structure is unrefined. Right: Structure of the (*S*)-**46** core in the crystal with hydrogen atoms on pyridine groups omitted. The atoms are represented as hard spheres rather than typical ellipsoids due to the lack of refinement.

It should be noted that the crystal structure of (*S*)-**46** is unrefined at this point in time. High disorder in the crystal packing led to poor, high-angle diffraction. Thus, the bond lengths in the core of the structure can be quoted to a satisfactory degree of accuracy but the bond lengths at the periphery of the cluster (such as the binaphthyl rings and to a lesser extent the pyridine C-C bonds) cannot. Furthermore, the calculations for the positions of the hydrogen atoms has not been performed, and so some rationale must be applied. For instance, the six oxygen atoms that cap the Mn₄, Mn₅ and Mn₆ centres are almost certainly aqua ligands, since they realistically cannot be O²⁻ atoms as this would make no chemical sense – the overall charge of the cluster would be too negative to be feasibly possible. They also cannot be hydroxyl ligands since this would also lead to a significant and unstable overall negative charge for the cluster (see below).

Structurally, (S)-**46** bears some resemblance to (S)-**44**, retaining the same oxo-metal-pyridine paddlewheel motif. It crystallises in the $P2_13$ space group and the phosphonates bind in the typical [3.111] configuration. The P1-O2, P1-O3 and P1-O4 bond lengths are 1.526, 1.492 and 1.542 Å respectively, while the P2-O5, P2-O6 and P2-O7 are 1.525, 1.502 and 1.526 Å respectively. The Mn2-O2 Mn2-O5, Mn3-O4 and Mn3-O7 bond lengths are 1.894, 1.996, 2.018 and 1.921 Å respectively, which are significantly shorter than the axial Mn-O and Mn-N bond lengths (2.158 and 2.176 Å respectively). This implies some Jahn-Teller distortions are present in the inner, octahedral Mn atoms. With regards to the outer Mn centres, the Mn5-O3, Mn5-O6, Mn5-O8 and Mn5-O9 bond lengths are 2.027, 2.029, 2.145 and 2.189 respectively. These are consistent with Mn phosphonates in the literature.¹¹⁴

Originally, we assumed that all manganese centres in (S)-**46** existed in the +2 oxidation state, which was the oxidation state of the $\text{Mn}(\text{OAc})_2 \cdot 4\text{H}_2\text{O}$ precursor. However, when assuming a uniform +2 state for the Mn centres, the overall charge for the cluster could not be realistically reconciled. The total positive charge of the cluster would be $(6 \times 2+) = 12+$. Naturally, this would require a total negative charge of 12^- to balance the charges. However, we already obtain 12^- from the six phosphonate groups ($6 \times 2^-$) and are still left with the μ_3 -oxo bridge (a further 2^-). Furthermore, there are no realistic anions in solutions to balance this charge; acetate is negative and uncoordinated Mn^{2+} is unlikely.

In light of this, we propose that the inner manganese atoms, Mn1-Mn3 exist in the formal Mn(III) oxidation state, while the outer three manganese atoms Mn4-Mn6 exist in the Mn(II) state. Our reasoning behind this is three-fold. Firstly, balancing the charges is significantly more logical – now the total positive charge is $15+ ((3 \times 3+) + (3 \times 2+))$, which can be satisfactorily balanced by the six phosphonate groups (12^-) and the μ_3 -oxo bridge (2^-). This leaves an overall charge of $1+$, and we postulate that an acetate counter-anion exists somewhere in the asymmetric unit, albeit due to the lack of refinement in (S)-**46**, locating this counter-anion has proven somewhat difficult. For reference, if we assume the six periphery oxygen atoms were hydroxyl groups rather than aqua ligands, the overall charge of the cluster would be 11^- , which seems unlikely.

The second reason was that our BVS calculations (see Appendix) more closely modelled Mn1-Mn3 as being in the +3 state rather than +2. As an addendum, they also agreed very well with our assumption that Mn4-Mn6 were in the +2 state. Finally, some reading into the area revealed that Mn(III) ions commonly adopt an octahedral structure and have significant Jahn-Teller distortions, which is observed in (S)-**46**.¹¹⁵ The archetypal example of this is manganese(III) acetate **47**, which adopts the structure shown in Figure 3.8.

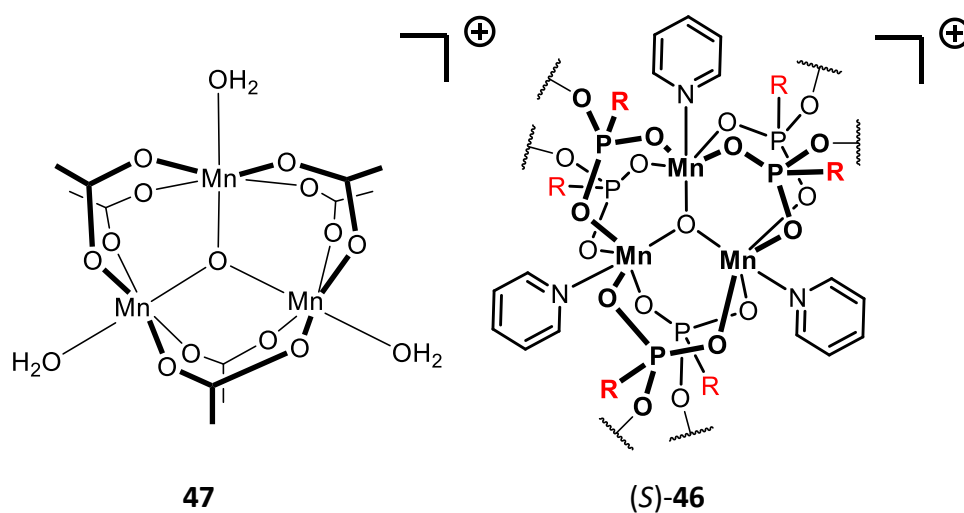


Figure 3.8 Left: Structure of manganese(III) acetate **47** in the solid-state. Right: Structure of the (S)-**46** core. While the ligands are different, the two structures share the same architecture and distorted axial bond lengths on the manganese centres.

Thus, (S)-**46** is a mixed-valence $\text{Mn}^{\text{II}}_3\text{Mn}^{\text{III}}_3$ cluster. We were eager to probe the magnetic properties of this phosphonate since mixed-valence manganese clusters have proven to be viable candidates for SMMs (notwithstanding the first SMM which was a mixed Mn(III)-Mn(IV) cluster. These results are pending.

3.2.3 Iron Phosphonate, (S)-48

Iron phosphonates are well-established in the literature as we have seen in Chapter 1, and we were eager to see how (S)-**bpa** would react with a source of the metal. Choosing a suitable oxidation state of iron to perform coordination reactions upon was straightforward in this case. The two most common oxidation states of iron are +2 and +3, and since Fe(II) readily oxidises to Fe(III) in water under ambient conditions (from $\text{Fe(III)} + \text{e}^- \rightarrow \text{Fe(II)}$, $E = +0.77 \text{ V}$ and $\text{O}_2 + 2\text{H}_2\text{O} + 4\text{e}^- \rightarrow 4\text{OH}^-$, $E = +1.19 \text{ V}$)¹¹⁶ this left iron(III) as the only suitable candidate for the preparation of a stable phosphonate.

We therefore set about attempting to crystallise (S)-**bpa** with an iron(III) source. However, when a pyridine solution of the ligand was layered with a solution of iron(III) chloride hexahydrate, a yellow precipitate immediately formed. After numerous attempts with a variety of solvents, yellow plates suitable for single-crystal X-ray diffraction were grown from a 3:1 ethanol / pyridine mixture. The crystals were revealed to be of a Fe_3 cluster, (S)-**48**. Figure 3.9 shows the structure of (S)-**48** in the crystal and the (S)-**48** core.

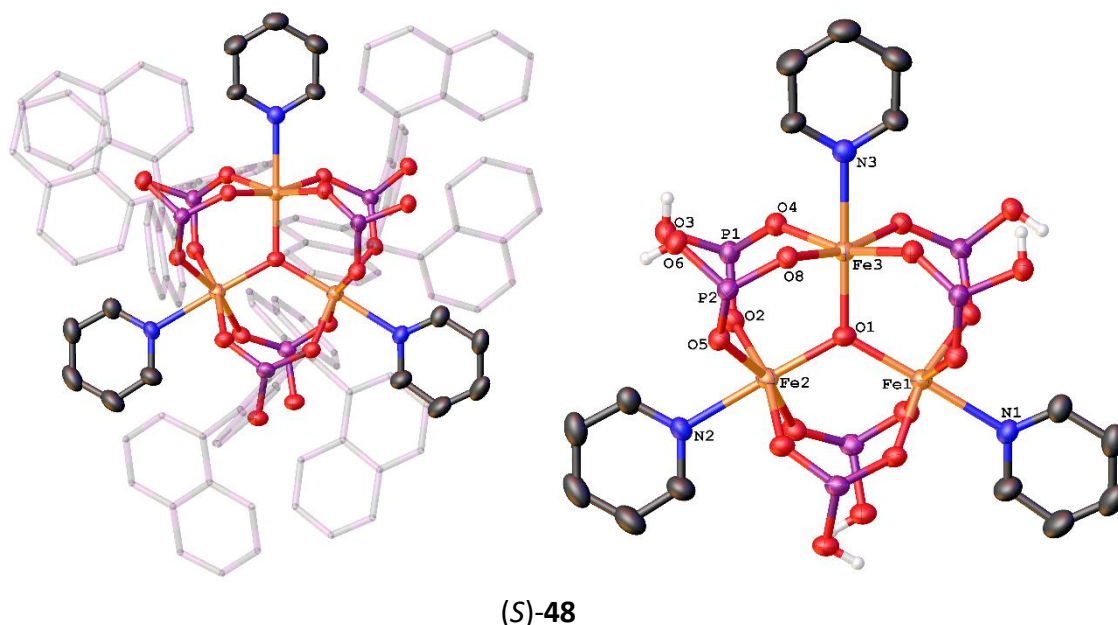


Figure 3.9 Left: Structure of (S)-**48** in the crystal, with binaphthyl groups represented as translucent sticks and hydrogen atoms omitted. Not shown is the lone chloride counter-anion which balances the cluster charge. Right: Structure of the (S)-**48** core in the crystal with hydrogen atoms on pyridine ligands omitted.

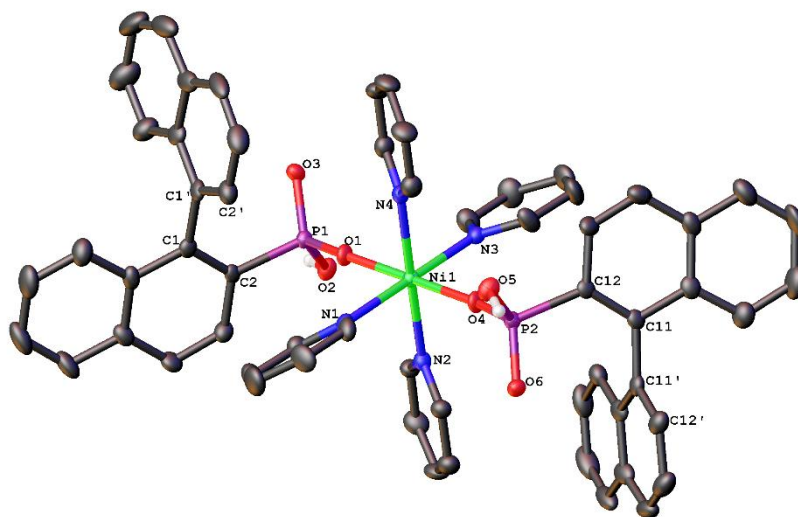
As can be seen from Figures 3.2 and 3.9, (S)-**48** is completely isostructural with the Sc_3 cluster, (S)-**44**, and retains the same O-M-N paddlewheel motif that we have seen in (S)-**46**, (S)-**44** and (S)-**43**. However, it crystallises in the trigonal space group $P3_121$, unlike (S)-**44**, which crystallises in the $P2_13$ space group. The Fe1-O1 and Fe2-O1 bond lengths are both 1.982(3) Å while the Fe3-O1 bond length is 1.949(6) Å. The Fe1-N1 and Fe2-N2 bond lengths are both 2.251(6) Å, while the Fe3-N3 bond length is 2.285(8) Å. The phosphonates bind in a [2.110] manner, and the P1-O2, P1-O3 and P1-O4 bond lengths are 1.511(5), 1.542(5) and 1.508(5) Å respectively, while the P2-O5, P2-O6 and P2-O7 bond lengths are 1.500(5), 1.555(5) and 1.505(5) Å respectively. The P1-O3 bond lengths are noticeably longer than the P1-O2 and P1-O4 bond lengths. This is probably due to the fact that the O3 oxygen atom does not bind to any iron centre while the O2 and O4 oxygen atoms do. The Fe2-O2 and Fe2-O5 bond lengths are 2.001(5) and 2.005(5) Å, while the Fe3-O4 and Fe3-O7 bond lengths are 2.001(5) and 2.026(4) Å respectively. These are consistent with iron(III) phosphonates already in the literature.¹¹⁷

Again, it can be seen that there are unbound oxygens on the phosphonate groups which potentially can be used to bind to a secondary metal *via* the cluster expansion method. We attempted to prepare such a cluster by employing both methods of cluster expansion. Thus, (S)-**48** was redissolved in a 1:1 mixture of ethanol and dichloromethane, and a second equivalent of $\text{FeCl}_3 \cdot 6\text{H}_2\text{O}$ or $\text{Mn}(\text{OAc})_2 \cdot 4\text{H}_2\text{O}$ were added to the solution. Adding a second equivalent of lanthanide salts including cerium, dysprosium, gadolinium and ytterbium chloride hexahydrates was also attempted. Further to this, (S)-**bpa** and 0.5 equivalents of both the $\text{FeCl}_3 \cdot 6\text{H}_2\text{O}$ and all aforementioned salts were stirred in pyridine and left to crystallise. Unfortunately, all of these methods proved unsuccessful, although we are certain this can be achieved by further experimentation with solvent systems and equivalents. (S)-**40** bears some resemblance to the iron(III) phosphonate $[\text{Fe}^{\text{III}}_4(\mu_3\text{-O})(\text{Cl})(\text{O}_3\text{P-Ph})_3(\text{O}_2\text{C-Ph})_3(\text{py})_5]$ **25** prepared by Winpenny and co-workers (Chapter 1). In their case however, an additional iron atom was bound to the phosphonate ligand.

3.2.4 Nickel and Copper Phosphonates, (S)-**49** and (S)-**50**

After having prepared Group 7 and 8 metal phosphonates in (S)-**45**, (S)-**46** and (S)-**48**, we wanted to explore the later first-row transition metals in Groups 10, 11, 12. These include nickel, copper and zinc. The reason these two phosphonates have been amalgamated into one sub-section is two-fold. Firstly, they are isostructural to one another, and secondly, the magnetic properties of these two phosphonates we have prepared have hitherto not been studied. Nickel and copper SMMs are somewhat rare compared to other transition metal elements such as cobalt, manganese or iron, although there are a few examples.^{32,118} These SMMs are clusters however, while the nickel and copper phosphonates we have prepared are monometallic.

For nickel, we opted to use the metal in its +2 state, as this is its most common oxidation state. Thus, when a pyridine solution of (S)-**bpa** was layered on top of a 0.5:1:1 water/ethanol/acetonitrile solution of nickel(II) chloride hexahydrate, pale blue parallelepipedal crystals were observed after 24 h. Single-crystal X-ray diffraction revealed these to be of a monometallic nickel phosphonate (S)-**49**. Figure 3.10 is the structure of (S)-**49** in the solid state.



(S)-**49**

Figure 3.10 Structure of (S)-**49** in the crystal with hydrogen atoms on binaphthyls and pyridines omitted.

(S)-**49** is an axially-distorted Ni(II) octahedral phosphonate complex and is isostructural with (S)-**37** and (S)-**45**. It crystallises in the $P2_1$ space group. The Ni1-O1 and N1-O4 bond lengths are 2.042(2) and 2.041(2) Å respectively. The Ni1-N1, Ni1-N2, Ni1-N3 and Ni1-N4 bond lengths are 2.168(4), 2.104(4), 2.170(4) and 2.127(4) Å respectively. The P1-O1, P1-O2 and P1-O3 bond lengths are 1.488(2), 1.544(3) and 1.520(3) Å respectively, while the P2-O4, P2-O5 and P2-O6 bond lengths are 1.496(2), 1.550(3) and 1.523(3) Å respectively. The P1-C2 and P2-C12 bond lengths are 1.818(4) and 1.818(5) Å respectively. The C2-C1-C1'-C2' torsion angle is 78.203°

while the C12-C11-C11'-C12' torsion angle is 96.593°. These values are consistent with similar nickel phosphonates in the literature.¹¹⁹

Interestingly, when we attempted to prepare a nickel phosphonate by adding all of the reagents simultaneously and stirring, we isolated crystals of the complex [NiCl₂(Py)₄] which were also pale blue in colour.

We then turned our attention to preparing a copper phosphonate. With this metal there were two realistic choices as to which oxidation state to use – both Cu(I) and Cu(II) have stable salts and widely available. Due to its reduced charge density, Cu(I) is significantly softer than Cu(II),¹²⁰ which may have led to incompatibility issues with the hard Lewis base of the phosphonate oxygens. A search of the literature indicates the overwhelming majority of copper phosphonates prepared employ a Cu(II) precursor, although one notable exception is a copper(I) phosphonate catalyst.^{15b} To this end, we restricted ourselves to working with Cu(II) exclusively.

When a pyridine solution of (S)-**bpa** was layered on top of a copper(II) acetate tetrahydrate solution of water/ethanol/acetonitrile, dark blue columnar crystals were obtained after 24 hours. Single-crystal X-ray diffraction revealed these to be of a mononuclear Cu(II) phosphonate, (S)-**50**. Figure 3.11 is the structure of (S)-**50** in the crystalline state.

(S)-**50** is isostructural with (S)-**37**, (S)-**45** and (S)-**49**. Interestingly, (S)-**50** crystallises in the *P*1 space group, as opposed to the other monometallic phosphonates that crystallise in the *P*2₁ space group. Nevertheless, (S)-**50** still retains its axial distortion with one major distinction – in all of the other cases, the M-O bonds were shorter than the M-N bonds. In the case of (S)-**50** however, the Cu-O bond lengths are significantly longer than the Cu-N bond lengths, and longer than the Co-O, Mn-O and Ni-O bond lengths by an average of around 0.4 Å. We attribute this to the significant Jahn-Teller distortion present in (S)-**50**. Cu(II) has the d⁹ configuration, and Jahn-Teller elongations are well documented for octahedral Cu(II) complexes.¹²¹ The Cu1-O1 and Cu1-O4 bond lengths are 2.338(2) and 2.460(2) Å respectively. The Cu1-N1, Cu1-N2, Cu1-N3 and Cu1-N4 bond lengths are 2.021(3), 2.071(3), 2.022(3) and 2.068(3) Å respectively. The P1-O1, P1-O2 and P1-O3 bond lengths are 1.496(3), 1.503(3) and 1.581(3) Å respectively, while the P2-O4, P2-O5 and P2-O6 bond lengths are 1.500(3), 1.501(3) and 1.576(3) Å respectively. The P1-C2 and P2-C12 bond lengths are 1.826(4) and 1.823(4) Å respectively. The C2-C1-C1'-C2' torsion angle is 102.473° while the C12-C11-C11'-C12' torsion angle is 88.484°.

As previously mentioned, the space group possessed by (S)-**50** differs to that of (S)-**49**, (S)-**45** and (S)-**37**. This manifests itself as a different packing arrangement in the crystal (Figure 3.12).

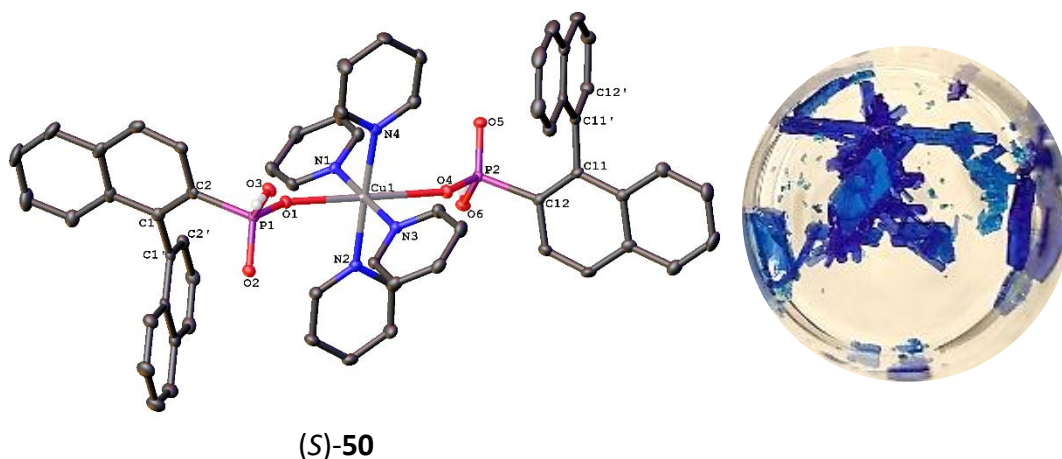


Figure 3.11 Left: Structure of (S)-50 in the crystal, with hydrogen atoms on binaphthyls and pyridines omitted. Right: A photograph of the crystals of (S)-50.

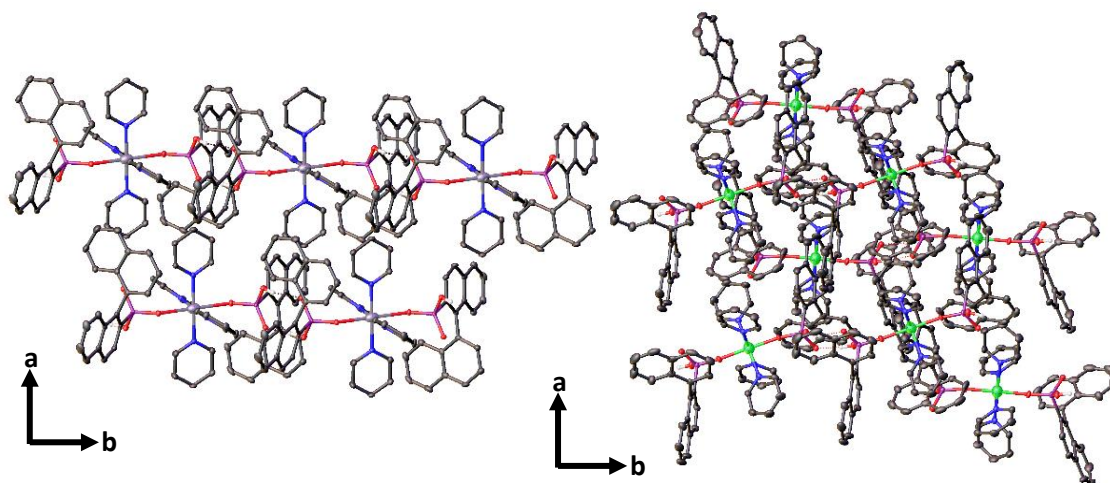


Figure 3.12 Left: Packing of the copper phosphonate (S)-50 in the crystal, with hydrogen atoms on binaphthyls and pyridines omitted. Right: Packing diagram of the nickel phosphonate (S)-49 in the crystal, with same hydrogens omitted. Both of these images are from the perspective of the *c*-axis. It can be seen by the different packing nature that these two isostructural species crystallise in different space groups.

A literature search on existing octahedral Cu(II) phosphonates revealed a consistency in these bond lengths to our copper phosphonate.¹²² One particular copper(II) phosphonate, prepared by Convery and co-workers, shares almost the exact same morphology as (S)-50.^{122c} Their work involved investigations into the oxidation of phenylphosphinic acid to phenylphosphonic acid using a solution of copper(I) acetate dihydrate in pyridine. It was found that after the oxidation had occurred, the species $[\text{Cu}(\text{O}_3\text{HPC}_6\text{H}_5)_2(\text{Py})_4]$ had crystallised from the solution. This is essentially the phenylphosphonic acid analogue of (S)-50. Some wider reading into the CCDC revealed that no other monometallic complexes analogous to $[\text{Cu}(\text{O}_3\text{HPC}_6\text{H}_5)_2(\text{Py})_4]$, or with any other phosphonic acid, had been prepared – copper was the only example.

3.2.5 Zinc Phosphonate, (S)-51

The final first-row transition metal phosphonates with which we successfully prepared crystals of with (S)-**bpa** was zinc. Only titanium, vanadium and chromium failed to yield crystalline material. The choice of oxidation state was obvious in this instance – zinc has one common oxidation state, +2 (the +1 state is accessible but is unstable unless it is protected by extremely bulky ligands).⁸⁹ Thus, we opted for zinc(II) in all cases.

However, when a solution of (S)-**bpa** in pyridine was layered on top of a water/ethanol/acetonitrile solution of zinc(II) acetate tetrahydrate, crystals did not form. Neither did they form when these reactants were stirred together under ambient conditions in pyridine, ethanol/pyridine or acetonitrile/pyridine. In all instances, a white precipitate immediately formed. As a final test to ascertain whether zinc would form crystals with (S)-**bpa**, we reacted zinc(II) acetate tetrahydrate (1 mmol), (S)-**bpa** (1mmol), pyridine (0.25 mL), ethanol (1 mL) and water (1 mL) *via* the hydrothermal method. Surprisingly, after three days colourless needles were observed. Single-crystal X-ray diffraction revealed these to be of a polymeric Zn(II) phosphonate, (S)-**51**. Figure 3.13 shows the structure of the (S)-**51** asymmetric unit in the crystal.

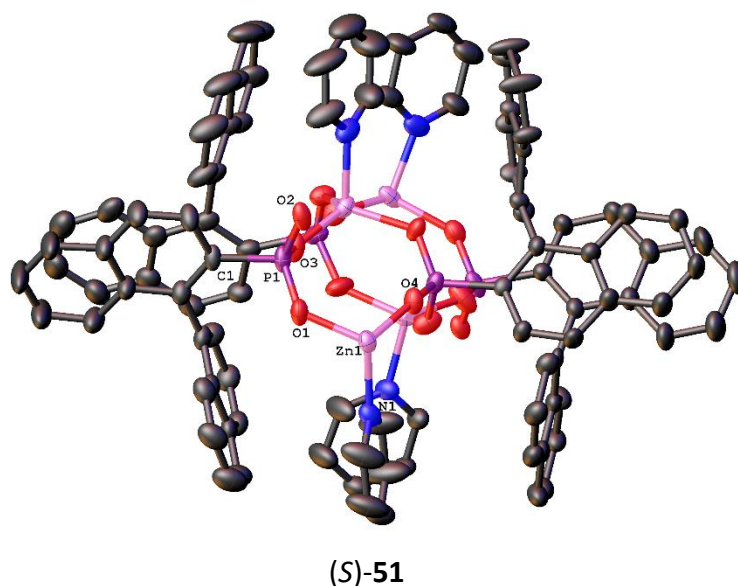


Figure 3.13 Structure of the (S)-**51** asymmetric unit in the crystal viewed down the *a*-axis with hydrogen atoms on binaphthyls and pyridines omitted.

(S)-**51** bears a striking resemblance to (S)-**42** (Chapter 2) in that the phosphonate groups bind in a [3.111] configuration, the binaphthyl rings protrude from the sides and the pyridines protrude at the top and bottom (when viewed down the *a*-axis). Furthermore, (S)-**51** crystallises in the same space group as (S)-**42** ($P2_1$). The Zn1-O1 bond lengths vary between 1.879 and 1.909 Å across the chain while the Zn1-O4 bond lengths vary between 1.914 and 1.937 Å. The Zn1-N1

bond lengths vary between 2.057 and 2.141 Å across the chain. The P1-O1 bond lengths vary between 1.519 and 1.520 Å, the P1-O2 bond lengths vary between 1.514 and 1.523 Å and the P1-O3 bond lengths vary between 1.515 and 1.518 Å. The P1-C1 bond lengths vary between 1.761 and 1.818 Å across the chain. Figure 3.14 shows the packing diagram of (*S*)-**51** as well as an individual chain. These values are consistent with similar zinc phosphonates in the literature.^{71,123}

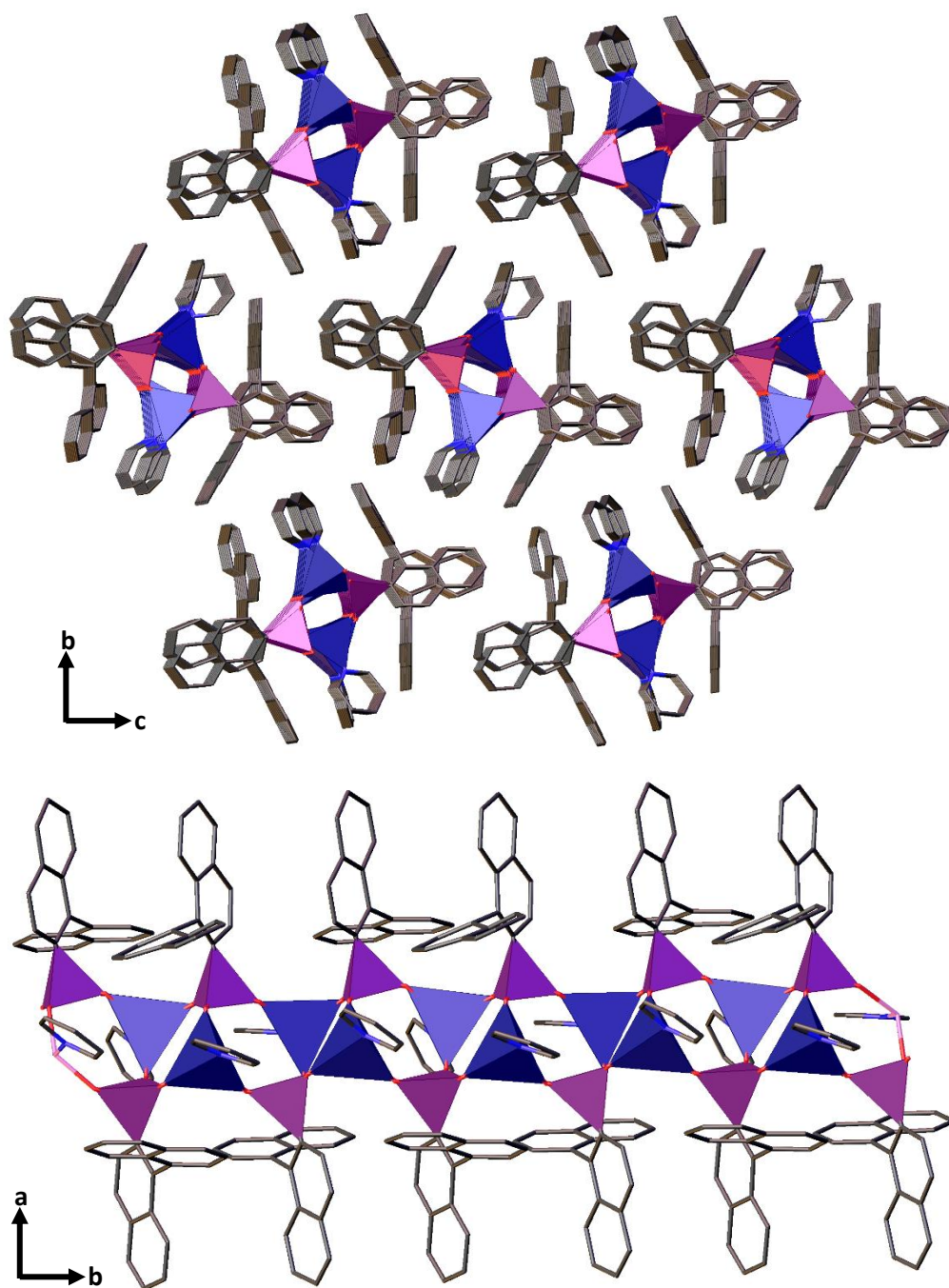


Figure 3.14 Top: Packing diagram of (*S*)-**51** as viewed down the *a*-axis with binaphthyls represented as wires and the zinc, oxygen and phosphorus atoms represented as polyhedra. Bottom: An individual chain of (*S*)-**51** viewed down the *c*-axis.

(S)-**51** consists of a one-dimension zinc phosphonate chain that extends infinitely down the *a*-axis. It can be viewed as a species that is halfway between the one-dimensional cobalt chain (S)-**38** and the two-dimensional cobalt sheet (S)-**42**, in that it is a one-dimensional metal phosphonate, similar to (S)-**38**, but also possesses exactly the same binding configurations as (S)-**42**. Unfortunately, when the analogous hydrothermal synthesis with 4,4'-bipyridine was attempted, no crystals were observed, even after considerable modifications to the equivalents and solvents. Likewise, as mentioned in Chapter 2, when pyridine was used with cobalt in the hydrothermal method, (S)-**38** was prepared instead.

To conclude, we have successfully prepared metal phosphonates of all first-row transition metals with (S)-**bpa**, excluding titanium, vanadium and chromium. For titanium, its chemistry is dominated by the +4 oxidation state, and due to the high oxidation state of Ti(IV), its compounds tend to have significant covalent character – TiCl₄ exists as a closed-shell structure, much like CCl₄. And much like CCl₄, it is a liquid under standard ambient conditions. Ti(IV) compounds also tend to react violently with water, forming the hydrated adduct [TiCl₄(OH₂)₂]. For this reason, it would be unsuitable to react with a phosphonate such as (S)-**bpa**, as all of the previous coordination reactions have been performed in aqueous media and open to air. For vanadium, we started with a vanadium (III) source in VCl₃ but no crystals formed from any of the crystallisation methods (stirring, layering and hydrothermal method). It was noted that the solution underwent several colour changes, due to the sequential oxidation of V(III) to V(V). Perhaps a future chemist doing further work on this project could utilise the vanadyl ion [VO]²⁺ as a vanadium source, as these are stable V(IV) ions that are known to form a wide variety of complexes.¹²⁴ Finally, for chromium the same problem as for vanadium was encountered – no crystals formed from any crystallisation method employed. In this instance, we started with chromium(III) chloride hexahydrate – a Cr(III) source. It is speculated that further modifications to equivalents or solvents will eventually yield a sufficient medium to prepare crystals.

Nevertheless, the versatility of (S)-**bpa** in the successful preparation of seven first-row transition metal phosphonates has been demonstrated. A particularly noteworthy observation was that the type of complex prepared depended heavily on the method used, with the layering method in all cases yielding monometallic octahedral metal phosphonates in (S)-**37**, (S)-**45**, (S)-**49** and (S)-**50**. Further to this, mechanical stirring yielded tri- and hexametallic clusters in (S)-**44**, (S)-**46** and (S)-**48**. Finally, the hydrothermal method yielded polymeric species in (S)-**38**, (S)-**46** and (S)-**51**. Thus, by adapting the crystallisation method accordingly, some degree of control can be exerted upon the size and dimensionality of the resulting metal phosphonate.

3.3 Second-Row Transition Metal Phosphonates

As mentioned at the beginning of this Chapter, the second-row transition metals are significantly softer in nature than their first-row counterparts. Furthermore, the late second-row transition metal elements contain the aforementioned noble metals ruthenium, rhodium, palladium and silver. Forming a phosphonate complex with these metals is disfavoured since these metals are soft Lewis acids and the oxygen of the phosphonate is a hard Lewis base. However, a literature search revealed that 32 ruthenium, 3 rhodium, 20 palladium and 77 silver phosphonate crystal structures exist in the literature (at the time of writing this thesis), which proves that these reactions are not impossible, although the difference is certainly noticeable when these are compared to the number equivalent iron, cobalt, nickel and copper phosphonates (129, 417, 189 and 661 respectively, see Chapter 1).

Although not all of the second-row transition metals were explored, coordination attempts using layering, stirring and the hydrothermal method were attempted on $\text{YCl}_3 \cdot 6\text{H}_2\text{O}$, RuCl_3 , RhCl_3 , $\text{Pd}(\text{OAc})_2$, $\text{Ag}(\text{NO}_3)_2$ and $\text{Cd}(\text{NO}_3)_2 \cdot 4\text{H}_2\text{O}$. We were able to isolate two crystalline second-row transition metal phosphonate complexes. The first was yttrium, which may come as little surprise since yttrium is regarded as a *pseudo*-lanthanide, and therefore is a hard Lewis acid. The second was the Group 12 metal, cadmium.

3.3.1 Yttrium Phosphonate, (*S*)-**52**

Yttrium is an almost exclusively trivalent transition metal and as such, with its chemistry being dominated by the +3 oxidation state. Its chemistry closely resembles that of the lanthanides, and this is apparent in nature – lanthanide-containing minerals such as monazite and bastnaesite often contain yttrium in varying quantities. We therefore expected that the coordination tendencies of any yttrium phosphonate that we were successful in making might give a clue as to the possibility of preparing related lanthanide phosphonates, which will be described in the following Chapter.

The yttrium source used was yttrium(III) chloride hexahydrate, which readily dissolved into the water/ethanol/acetonitrile mixture. However, when a solution of (*S*)-**bpa** in pyridine was layered on top of this solution, a white precipitate immediately formed. A change in tactic was clearly necessary, and this led to the eventual optimised conditions of simply stirring the yttrium chloride salt and (*S*)-**bpa** in pyridine for 24 hours before setting the solution aside for slow evaporation. After two weeks, colourless plates could be observed. These were analysed by single-crystal X-ray diffraction and found to be a hexametalllic yttrium cluster, (*S*)-**52**. Figure 3.15 shows (*S*)-**52** in the crystalline state and also the (*S*)-**52** core.

Since yttrium is below scandium in Group 3, we expected that a similar structure to the Sc_3 cluster, (S)-**44** would be observed. However, this was not the case. (S)-**52** is a highly irregular Y_6 cluster crystallising in the $P2_1$ space group and contains a central μ_3 -oxygen atom, as previously seen in (S)-**43**, (S)-**44**, (S)-**46** and (S)-**48**. Moreover, it contains seven bound molecules of (S)-**bpa**, with the phosphonate binding configurations shown in Table 8. The outer yttrium atoms – Y1, Y4 and Y6 – contain numerous aqua ligands (five, four and six respectively), although Y3 also contains two aqua ligands. Further to this, Y5 contains a single axially-bound pyridine ligand. Y2 contains no bound aqua ligands.

The overall charge for the cluster was determined to be 3+ and was calculated as follows; (6 x $\text{Y}^{3+} = 18+$ total positive charge) and ((7 x $\text{PO}_3^{2-} = 14-$) + ($\mu_3\text{-OH}^- = 1-$) = 15– total negative charge). This bridging oxygen was determined to be a hydroxyl, as opposed to an O^{2-} anion. There was significant evidence from the electron densities of the crystal structure to suggest that a hydrogen was present. Furthermore, it would allow the three chloride counter-anions to balance the charge of the cluster (Figure 3.30).

The bond lengths for all labelled atoms in Figure 3.15 are compiled in Table 9. These were found to be consistent with previously reported yttrium phosphonates in the literature.¹²⁵

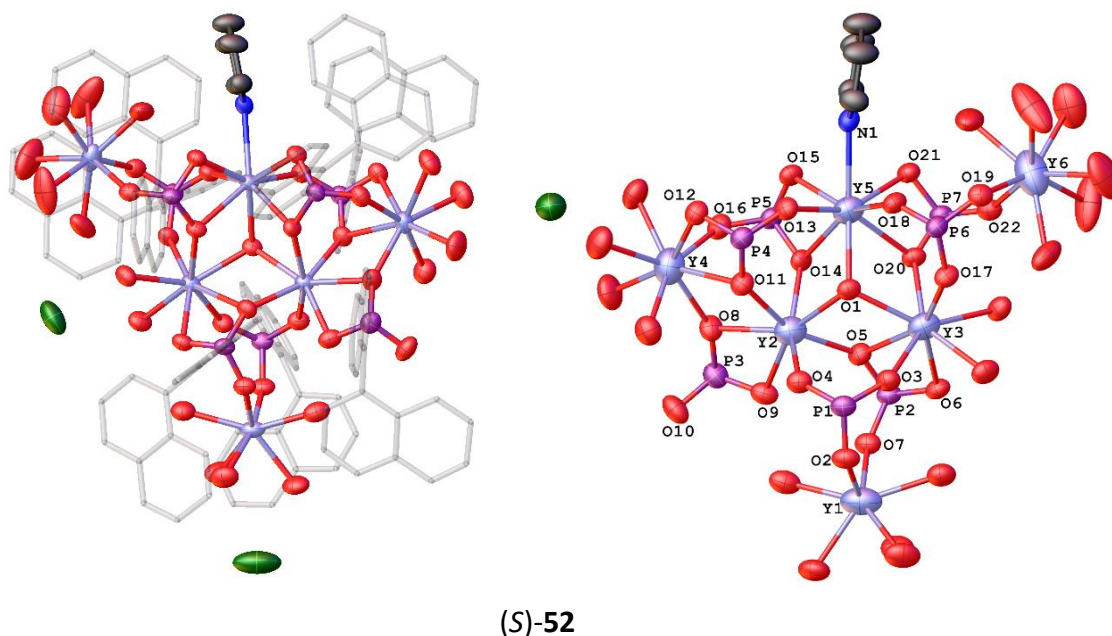


Figure 3.15 Left: Structure of (S)-**52** in the crystal, with binaphthyl groups represented as translucent sticks and hydrogen atoms omitted. Also shown are the three chloride counter-anions which balance the +3 charge of the cluster. Right: Structure of the (S)-**52** core in the crystal with hydrogen atoms and chloride counter-anions omitted. The yttrium ellipsoids have been enlarged for ease of viewing.

Phosphorus Atom	Binding Configuration	Binding Mode
P1	[3.1 ₁ 1 ₂ 1 ₃]	Monodentate
P2	[3.1 ₁ 2 ₂₃ 1 ₃]	Bidentate
P3	[2.1 ₂ 2 ₂₄]	Bidentate
P4	[3.2 ₂₄ 1 ₄ 1 ₅]	Bidentate
P5	[3.2 ₂₅ 1 ₄ 1 ₅]	Bidentate
P6	[3.1 ₃ 1 ₅ 1 ₆]	Monodentate
P7	[3.2 ₃₅ 1 ₅ 1 ₆]	Bidentate

Table 8 Binding configurations and corresponding binding modes of each phosphorus atom in (S)-52.

Bond	Length / Å	Bond	Length / Å	Bond	Length / Å
Y1-O2	2.177(7)	Y4-O12	2.363(7)	P2-O7	1.517(7)
Y1-O7	2.211(6)	Y4-O16	2.297(7)	P3-O8	1.540(7)
Y2-O1	2.321(6)	Y5-O1	2.358(6)	P3-O9	1.526(8)
Y2-O4	2.276(6)	Y5-O13	2.306(6)	P3-O10	1.501(7)
Y2-O5	2.255(6)	Y5-O14	2.469(6)	P4-O11	1.521(7)
Y2-O8	2.443(7)	Y5-O15	2.319(6)	P4-O12	1.526(7)
Y2-O9	2.321(6)	Y5-O18	2.207(7)	P4-O13	1.514(7)
Y2-O11	2.292(6)	Y5-O20	2.491(6)	P5-O14	1.548(6)
Y2-O14	2.287(6)	Y5-O21	2.389(6)	P5-O15	1.504(7)
Y3-O1	2.405(6)	Y5-N1	2.572(8)	P5-O16	1.496(7)
Y3-O3	2.246(6)	Y6-O19	2.244(7)	P6-O17	1.519(6)
Y3-O5	2.507(7)	Y6-O22	2.285(7)	P6-O18	1.513(7)
Y3-O6	2.381(6)	P1-O2	1.521(7)	P6-O19	1.515(7)
Y3-O17	2.263(6)	P1-O3	1.500(7)	P7-O20	1.518(6)
Y3-O20	2.324(6)	P1-O4	1.530(7)	P7-O21	1.519(6)
Y4-O8	2.321(7)	P2-O5	1.532(6)	P7-O22	1.522(7)
Y4-O11	2.468(6)	P2-O6	1.514(7)		

Table 9 Selected bond lengths in (S)-52 between all atoms labelled in Figure 3.31.

With Y(III) being a d^0 transition metal like Sc(III), we were also able to record the $\{^1\text{H}\}^{31}\text{P}$ NMR spectrum of (S)-**52** (Figure 3.16). The spectrum shows two distinct regions, one at 11.07 ppm and the other at 3.77 ppm. We postulate that these two regions are a result of the two binding modes of the phosphonates present in (S)-**52**. The larger peak at 11.07 ppm we assign to the phosphonates that bind in a bidentate manner, while the smaller peak at 3.77 ppm we assign to the phosphonates that bind in a monodentate manner. The reason for this is attributed to the relative intensities of both peaks. By consideration of Table 8, two phosphonates bind in a monodentate configuration while the other five bind in a bidentate configuration. This ratio of 5:2 is closely mirrored by the intensities of the two peaks.

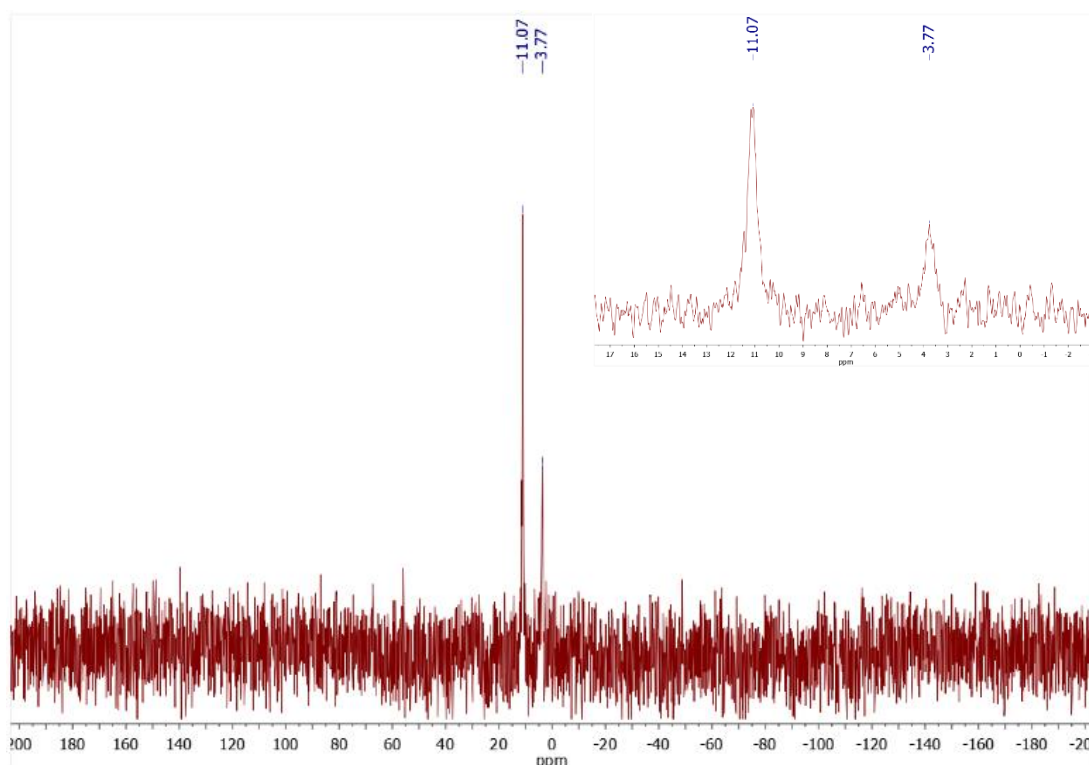


Figure 3.16 Main: $\{^1\text{H}\}^{31}\text{P}$ NMR spectrum of (S)-**52** (ran in standard dmsd). The two regions fall within the chemical shift range of 11.07 and 3.77 ppm. Inset: Expansion of the pertinent region. For reference, uncoordinated (S)-**bpa** has a chemical shift of 12.40 ppm in this solvent.

3.3.2 Cadmium Phosphonate, (S)-53

The final transition metal phosphonate we were able to isolate crystals of was a cadmium phosphonate. This may seem theoretically counter-intuitive, since cadmium is a soft metal if we consider Figure 3.1 at the beginning of this Chapter, and would therefore disfavour binding to hard donors such as oxygen. However, this does not reveal the full picture since there are many well-known inorganic compounds containing cadmium and oxygen such as cadmium(II) oxide (CdO), $[\text{Cd}(\text{H}_2\text{O})_6]^{2+}$ and $[\text{Cd}(\text{OH})_4]^{2-}$. Furthermore, a literature search of cadmium phosphonates revealed that (at the time of writing this thesis) there were 160 cadmium phosphonate crystal structures published, which even outstrips the number of iron phosphonates published. Therefore, a simple consideration of hardness and softness to determine viability of coordination is wholly inadequate in this instance. Many of these cadmium phosphonates were prepared in order to examine their luminescence properties,^{126a-c} with some demonstrating exceptional detection of various ions in solution such as $\text{Cr}_2\text{O}_7^{2-}$ and CrO_4^{2-} ions^{126d} and amino acids.^{126e}

While the +1 state is known for cadmium, the most common oxidation state is the +2 state, and thus we opted to employ cadmium(II) nitrate hexahydrate. When a solution of (S)-**bpa** in pyridine was layered on top of a solution of this cadmium(II) salt, colourless parallelepipedal crystals were observed after 24 hours. These crystals were revealed to be of a mononuclear Cd(II) phosphonate, (S)-**53**. Figure 3.17 shows (S)-**53** in the crystal.

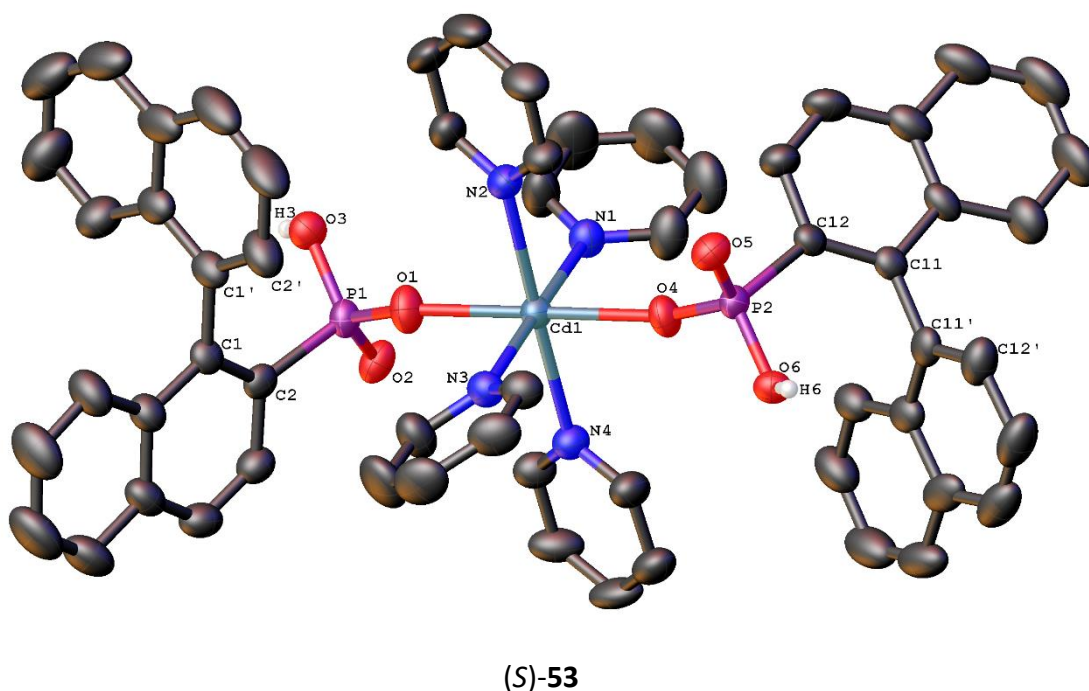


Figure 3.17 Structure of (S)-**53** in the crystal with hydrogen atoms on binaphthyls and pyridines omitted.

The final addition to the cohort of mononuclear M-(*S*)-**bpa** phosphonates, (*S*)-**53** is completely isostructural with (*S*)-**50**, (*S*)-**49**, (*S*)-**45** and (*S*)-**37**. Much like the copper phosphonate (*S*)-**50**, (*S*)-**53** possesses the *P1* space group. All oxygen and nitrogen to cadmium bond lengths are longer than the previous structures we have seen which reflects the significantly larger size of cadmium when compared to the first-row transition metals. The Cd1-O1 and Cd1-O4 bond lengths are 2.208(4) and 2.225(4) Å respectively which are incidentally shorter than the M-O bond lengths in the copper phosphonate, (*S*)-**50**. The Cd1-N1, Cd1-N2, Cd1-N3 and Cd1-N4 bond lengths are 2.404(5), 2.374(5), 2.402(5) and 2.357(5) Å respectively. The P1-O1, P1-O2 and P1-O3 bond lengths are 1.502(4), 1.506(4) and 1.568(5) Å respectively, while the P2-O4, P2-O5 and P2-O6 bond lengths are 1.491(4), 1.503(4) and 1.542(5) Å respectively. The P1-C2 and P2-C12 bond lengths are 1.818(5) and 1.817(5) Å respectively. The C2-C1-C1'-C2' torsion angle is 86.932°, while the C12-C11-C11'-C12' torsion angle is 101.149°. These values are consistent with similar cadmium phosphonates in the literature.¹²⁶

Since cadmium is below zinc in the periodic table, we had hoped to prepare the analogous cadmium polymer of (*S*)-**51**. Unfortunately, when (*S*)-**bpa** (1 mmol), Cd(NO₃)₂·6H₂O (1 mmol), pyridine (0.25 mL), ethanol (1 mL) and water (1 mL) were reacted *via* the hydrothermal method, no crystalline material was observed.

3.4 Conclusion

To conclude, we have prepared a total of 9 transition metal phosphonates (excluding cobalt). These were prepared by the three methods previously described – layering, stirring at room temperature and hydrothermal synthesis. The layering method prepared exclusively monometallic manganese, nickel, copper and cadmium phosphonates, (*S*)-**45**, (*S*)-**49**, (*S*)-**50** and (*S*)-**53** respectively. Stirring (*S*)-**bpa** with scandium(III) triflate and iron(III) chloride hexahydrate under ambient conditions resulted in the formation of two isostructural trimetallic clusters, (*S*)-**44** and (*S*)-**48**. Stirring (*S*)-**bpa** with manganese(II) acetate tetrahydrate under ambient conditions led to the formation of a hexametallc mixed-valence Mn(II)-Mn(III) cluster (*S*)-**46**, while the same approach with yttrium(III) chloride hexahydrate under ambient conditions led to the formation of a highly irregular hexametallc yttrium cluster, (*S*)-**52**. Finally, reacting (*S*)-**bpa**, zinc(II) acetate tetrahydrate and pyridine (as the co-ligand) *via* the hydrothermal method resulted in the formation of a two-dimensional zinc phosphonate chain, (*S*)-**51**. This is summarised in Figure 3.18.

We were successful in expanding the scope of the coordination reactions between (*S*)-**bpa** and transition metals other than cobalt. Furthermore, we have demonstrated further evidence of

control over morphology of the resulting phosphonates by simply altering the method of crystallisation. Although not successful with all first- and second-row transition metals, the layering method exclusively forms mononuclear metal phosphonates, while stirring at room temperature leads to clusters. The hydrothermal method, as with (S)-**38** and (S)-**42**, produces polymeric species.

Unfortunately, we were unable to isolate mixed TM-Ln clusters with any of the crystallisation techniques. However, the success with the mixed Co_3Sc_3 cluster (S)-**43** should provide impetus for preparing crystals of mixed clusters by further modification with solvent systems and reagent equivalents.

Overall, (S)-**bpa** has demonstrated flexibility in its mode of reactivity with transition metals, reacting with a wide range of metals and producing predictable structures based on the method in which we introduce it to a metal. This allows for the size of the clusters can be controlled to a certain degree.

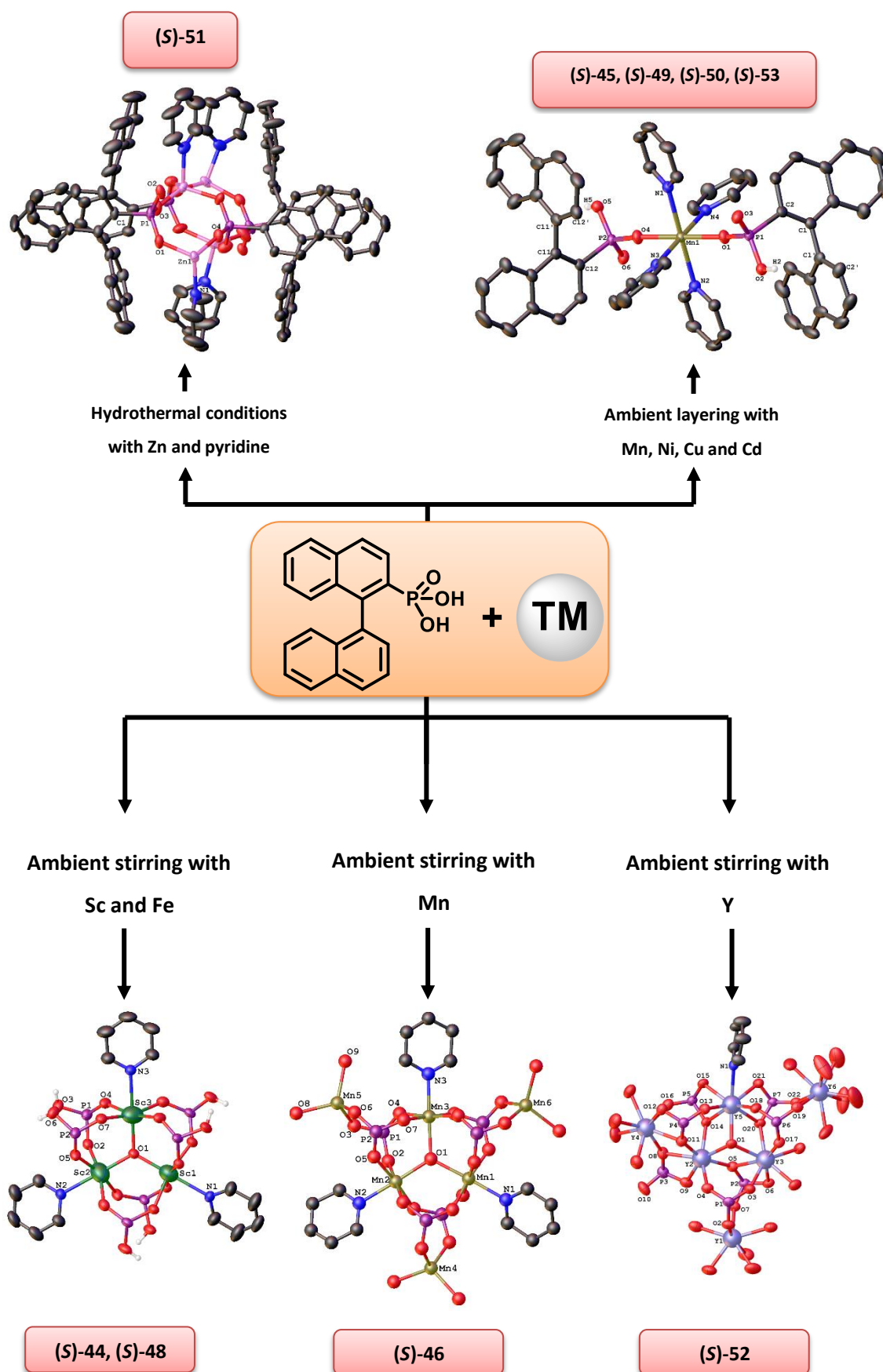


Figure 3.18 Scheme showing general route to the various transition metal phosphonates discussed in this Chapter.

Chapter 4 – Coordination of (S)-bpa to Lanthanides

4.1 Introduction

The lanthanides, from the Greek *λανθανειν* (lanthanein, *to lie hidden*), comprise of the fifteen elements starting from lanthanum ($Z = 57$) and ending in lutetium ($Z = 71$). All are primordial in nature except for promethium, which has no stable isotopes. The most stable isotope of promethium is ^{147}Pm which has a half-life of 17.7 years. Historically, scandium and yttrium were grouped together with the other lanthanides and these were collectively known as the *rare earths*. However, this name is somewhat of a misnomer, since they are not rare in the sense of their scarcity (thulium, the least abundant lanthanide is still more abundant than iodine). Rare in this context could be interpreted as *hard to get at* and refers to the long and cumbersome processes required to purify them, since the lanthanides are physically and chemically similar to each other.

Lanthanide chemistry is dominated by the +3 oxidation state, although the +2 and +4 oxidation states have been observed for some lanthanides such as Ce(IV) and Eu(II). However, these species are highly oxidising or reducing, so we shall restrict ourselves to the +3 chemistry. With regards to the orbitals, the 4f-electrons are very poor at shielding a nuclear charge, and as a consequence, as the atomic number increases, the stability of the 4f-orbitals also increases. In other words, they experience a greater nuclear charge as one goes across the series. Therefore, the ionic radii of the lanthanides decreases across the series. This is known as the lanthanide contraction (an approximate 0.2 Å decrease in ionic radius from La^{3+} to Lu^{3+}) and among other things, is the main reason for the similar ionic radii, and hence chemistry, of the second- and third-row transition metals. Figure 4.1 illustrates the decrease in ionic radii of Ln^{3+} ions.

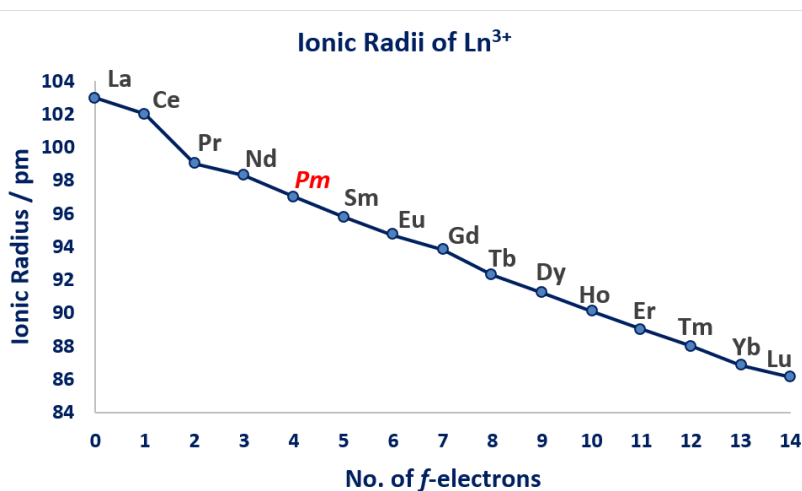


Figure 4.1 Ionic radii of the Ln^{3+} ions from lanthanum to lutetium showing the marked decrease leading to the lanthanide contraction. Promethium is highlighted in red since it is the only lanthanide with no stable isotopes.

One of the biggest manifestations of the poor shielding of the 4f-electrons is the limited radial extension of the 4f-orbitals – they effectively behave as core orbitals, and therefore do not interact with ligands. Any crystal field effects are negligible. Thus, bonding in lanthanide complexes is predominantly ionic, which makes the lanthanides hard Lewis acids, with the Lewis acidity increasing slightly across the series. In addition, the lanthanides are highly oxophilic, with water rapidly displacing other monodentate ligands under aqueous conditions unless multidentate or bulky ligands are employed. This makes the phosphonate ligand with its three oxygen atoms ideal candidates for coordination to lanthanides. Therefore, we opted to attempt coordination with (*S*)-**bpa** to all of the lanthanides (excluding promethium).

4.2 Coordination to Early Lanthanides, La – Sm, (*S*)-**54** – (*S*)-**58**

As we have seen in Chapter 1, the lanthanides react to phosphonic acids in a similar way to their transition metal counterparts, producing layered structures when reacted with non-bulky phosphonic acids such as phenylphosphonic acid and producing discrete clusters when reacted with sterically encumbered phosphonic acids in the presence of ancillary ligands.^{57,64,127} It seemed that a logical place to start would be with lanthanum, the first lanthanide. The lanthanide salts we opted to use for our crystallisations were the chloride hydrates, $\text{LnCl}_3 \cdot x\text{H}_2\text{O}$. As with the transition metals, the hydrate salts offered improved solubility in the solvent systems that we utilised when compared to the anhydrous counterparts.

When (*S*)-**bpa** and lanthanum(III) chloride hexahydrate were dissolved in pyridine and stirred for 24 hours, a white precipitate had formed. This also occurred when mixtures of ethanol/pyridine and acetonitrile/pyridine were used. Thus, we turned to our layering technique, and after a surprisingly short time of two hours, colourless rhombohedral crystals had formed. Single-crystal X-ray diffraction revealed these crystals to be of a highly regular pentametallic lanthanum phosphonate cluster, (*S*)-**54**. Interestingly, when the chloride hydrate salts of cerium, praseodymium, neodymium and samarium were reacted in the same manner, they all produced isostructural phosphonates to that of lanthanum ((*S*)-**55**, (*S*)-**56**, (*S*)-**57** and (*S*)-**58** respectively). This is not surprising, given the incredibly similar chemistry of the lanthanides. Indeed, a literature search reveals that other groups have prepared several isostructural lanthanide phosphonates.¹²⁸ Figure 4.2 shows the structure of the pentametallic cerium phosphonate, (*S*)-**55** and the same cluster with the binaphthyl groups omitted. Cerium was chosen in this instance as its crystal structure was the most refined out of the five isostructural lanthanide phosphonates.

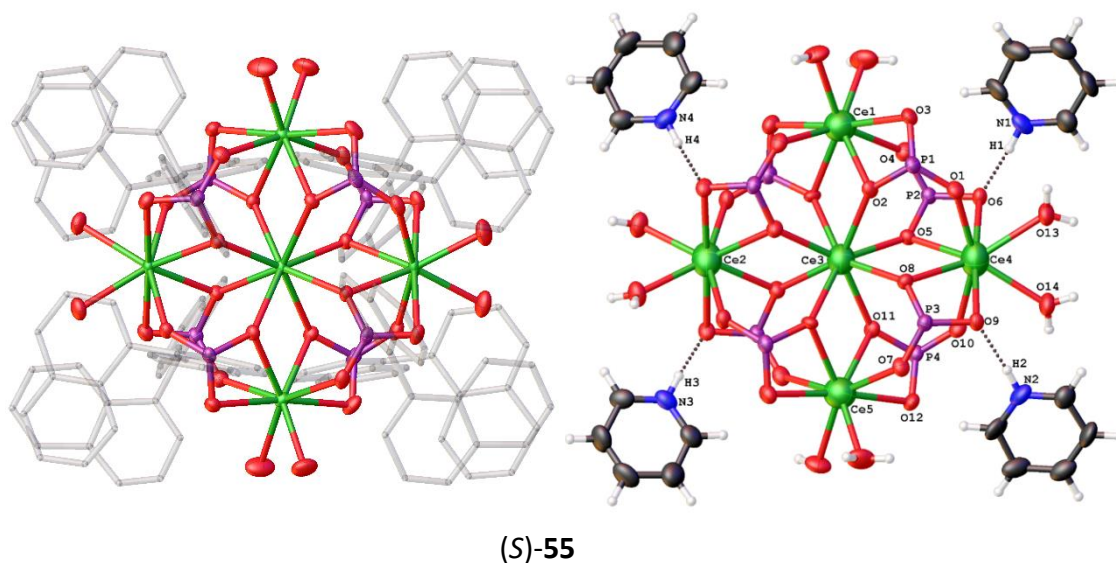


Figure 4.2 Left: Structure of (S)-55 in the crystal, with binaphthyl groups represented as translucent sticks and hydrogen atoms omitted. Not shown are the three chloride counter-anions which balances the charge of the cluster. Right: Structure of the (S)-55 core in the crystal with Ce ellipsoids increased in size for ease of viewing. Also shown are the four pyridinium cations that balance the charge of the cluster.

(S)-55 (and indeed (S)-54 – (S)-58) can be described as a highly regular, four-fold rotationally-symmetrical pentametallic cluster crystallising in the $I2$ space group. The cerium atoms form a cross-like arrangement with the periphery cerium atoms being capped by two aqua ligands. Each cerium is octahedrally coordinated with the central cerium (Ce1) adopting a square antiprismatic arrangement while the peripheral cerium atoms (Ce2 – Ce5) adopt a distorted square antiprismatic arrangement. Each of the eight phosphonate ligands are identical and bind in a $[3.1_21_21_3]$ manner where the subscript 1, 2 and 3 refer to any three different cerium centres. The overall charge of the cluster was deduced to be $1-$ ($15+$ from the five Ce^{3+} atoms and $16-$ from the eight doubly deprotonated phosphonate ligands). This charge of $1-$ is supplemented by four pyridinium molecules hydrogen bonding to the oxygens of four of the phosphonates and three Cl^- atoms which were found in the asymmetric unit. This overall charge of $1+$ balances the $1-$ charge of the cluster. The bond lengths are summarised in Table 10. While the bond lengths for the other four lanthanide phosphonates are not shown, these were also found to be consistent with similar lanthanide phosphonates in the literature.¹²⁹

Bond	Length / Å	Bond	Length / Å	Bond	Length / Å
Ce1-O2	2.520(5)	Ce4-O9	2.505(6)	P2-O5	1.535(6)
Ce1-O3	2.476(6)	Ce4-O10	2.467(6)	P2-O6	1.524(6)
Ce1-O4	2.453(6)	Ce4-O13	2.483(6)	P3-O7	1.505(7)
Ce3-O2	2.545(5)	Ce4-O14	2.483(6)	P3-O8	1.535(6)
Ce3-O5	2.432(6)	Ce5-O7	2.453(6)	P3-O9	1.524(6)
Ce3-O8	2.432(5)	Ce5-O11	2.520(5)	P4-O10	1.503(6)
Ce3-O11	2.545(5)	Ce5-O12	2.476(6)	P4-O11	1.545(5)
Ce4-O1	2.467(6)	P1-O1	1.503(6)	P4-O12	1.537(6)
Ce4-O5	2.524(5)	P1-O2	1.545(5)	O6...H1	1.736
Ce4-O6	2.505(6)	P1-O3	1.537(6)	O9...H2	1.730
Ce4-O8	2.524(5)	P2-O4	1.505(7)		

Table 10 Selected bond lengths in (*S*)-**47** between all atoms labelled in Figure 4.21.

As lanthanum is an f^0 element, it contains no unpaired electrons and we were therefore able to perform a $\{^1\text{H}\}^{31}\text{P}$ NMR experiment on (*S*)-**54**. Figure 4.3 shows the $\{^1\text{H}\}^{31}\text{P}$ NMR spectrum of (*S*)-**54**.

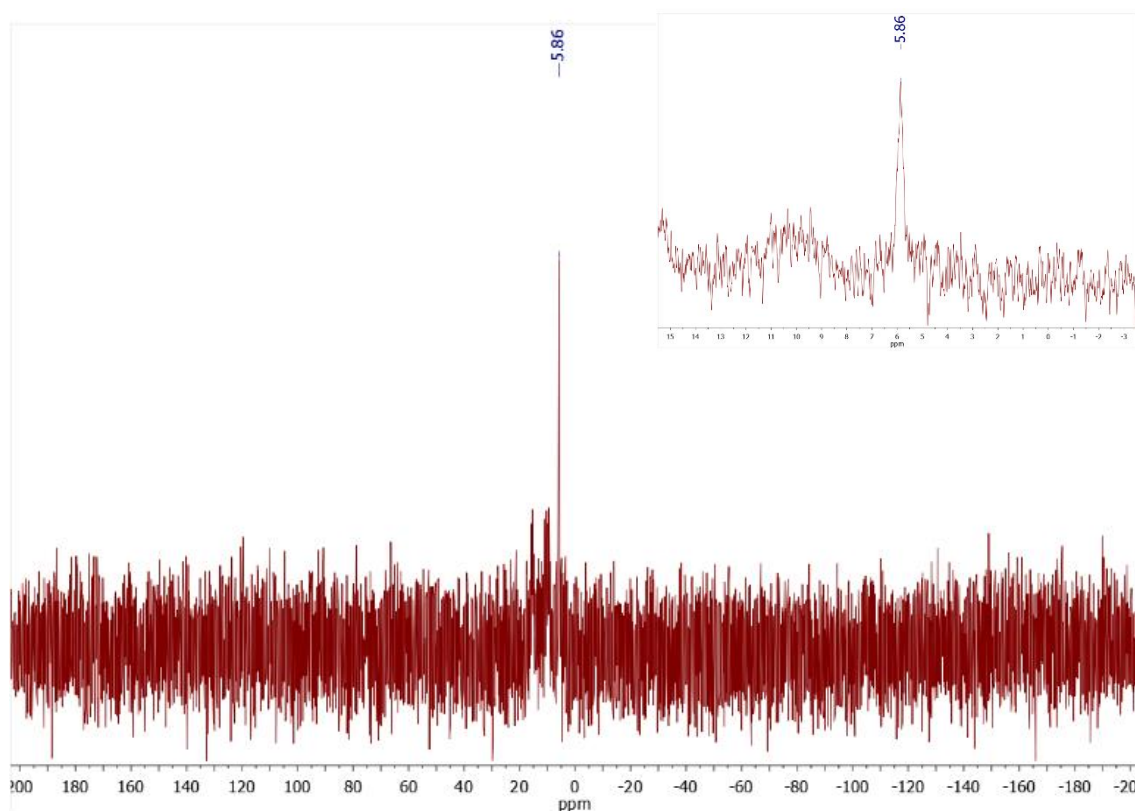


Figure 4.3 Main: $\{^1\text{H}\}^{31}\text{P}$ NMR spectrum of (*S*)-**54** (ran in non-deuterated DMSO). Peak is at 5.86 ppm. Inset: Expansion of the pertinent region. For reference, uncoordinated (*S*)-**bpa** has a chemical shift of 12.40 ppm in this solvent.

As can be seen, a single peak is present at 5.86 ppm. This correlates with the information provided by the crystal structure. There is one type of phosphonate present in (S)-**54** – (S)-**58** as previously mentioned, and thus it should follow that there would be one peak in the phosphorus NMR spectrum, which is what is seen. Furthermore, since (S)-**54** – (S)-**58** are completely isostructural with one another, the $\{^1\text{H}\}^{31}\text{P}$ NMR spectrum, and indeed other NMR experiments, of (S)-**54** can be used to probe NMR information of (S)-**55** – (S)-**58**, which themselves cannot be ran, since these species are paramagnetic.

Figure 4.4 shows the packing diagram of (S)-**55**. It can be seen that each cluster is oriented so that the binaphthyl groups of each layer have some interaction with one another. The minimum distance between one cluster and the other in the same layer is about 9.61 Å, with a multitude of solvent molecules occupying these void spaces (not shown).

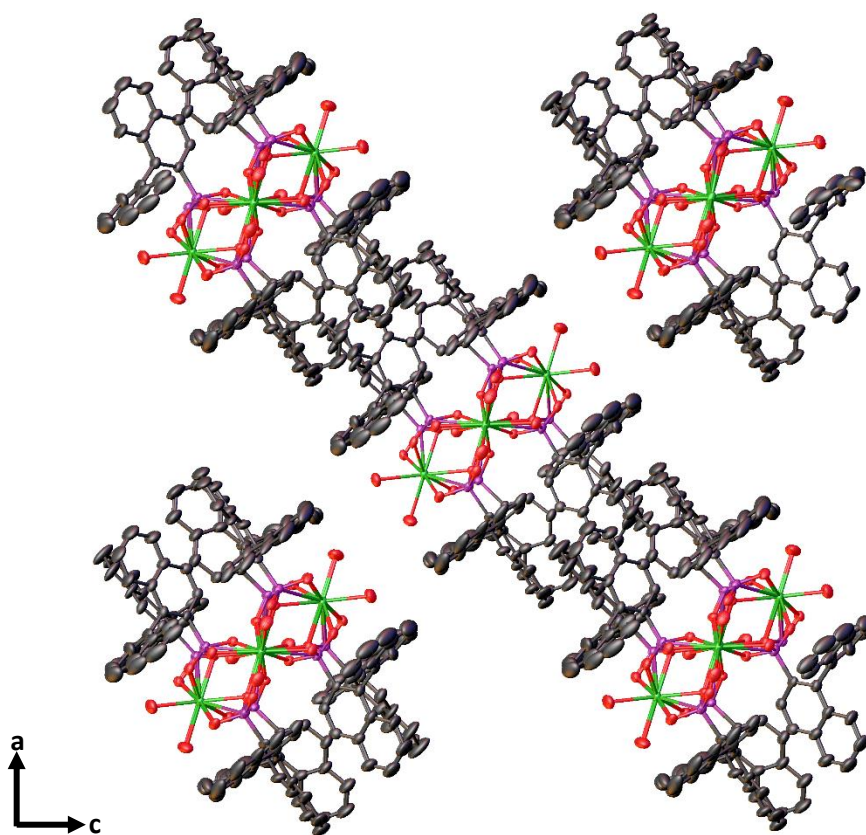


Figure 4.4 Packing diagram of (S)-**55** down the *b*-axis with hydrogen atoms omitted.

One interesting observation was that the Nd and Sm phosphonates crystallised in the orthorhombic space group $P2_12_12$, unlike the monoclinic space group $I2$ which the La – Pr phosphonates crystallised in. The structures of the individual clusters remained unchanged, however.

A literature search of the CCDC regarding the pentanuclear lanthanide architecture we had prepared revealed that no such other lanthanide phosphonate structure exists. These lanthanide phosphonate motifs are therefore completely novel. With the layering technique proving successful at preparing (*S*)-**bpa** phosphonate clusters of the first six lanthanides (excluding the radioactive promethium), we then proceeded to perform crystallisations on the remaining nine lanthanides (europium – lutetium).

4.3 Coordination to Later Lanthanides, Eu – Tm, (*S*)-**59** – (*S*)-**65**

After samarium, europium was the next lanthanide in the series and initially we believed that the layering technique which had served us well for the previous lanthanides would also be viable in this instance. However, it was found that layering a pyridine solution of (*S*)-**bpa** on top of the normal solution of europium(III) chloride hexahydrate resulted in the formation of an insoluble precipitate almost immediately.

Thus, after some solvent screenings, we found that mixing the lanthanide salt and (*S*)-**bpa** in ethanol and pyridine (3:1) for 24 hours before leaving the solution to slowly evaporate formed plate-like crystals after one week. All later lanthanides (Eu – Lu) were reacted in this manner. Single-crystal X-ray diffraction revealed that the lanthanide phosphonate clusters from europium to thulium were all hexametallic clusters which were isostructural with one another, similar to how the earlier lanthanide phosphonates (*S*)-**54** – (*S*)-**58** shared the same structure. The clusters (*S*)-**59** – (*S*)-**65** are shown in Figure 4.5, with the dysprosium phosphonate (*S*)-**62**, used as an example.

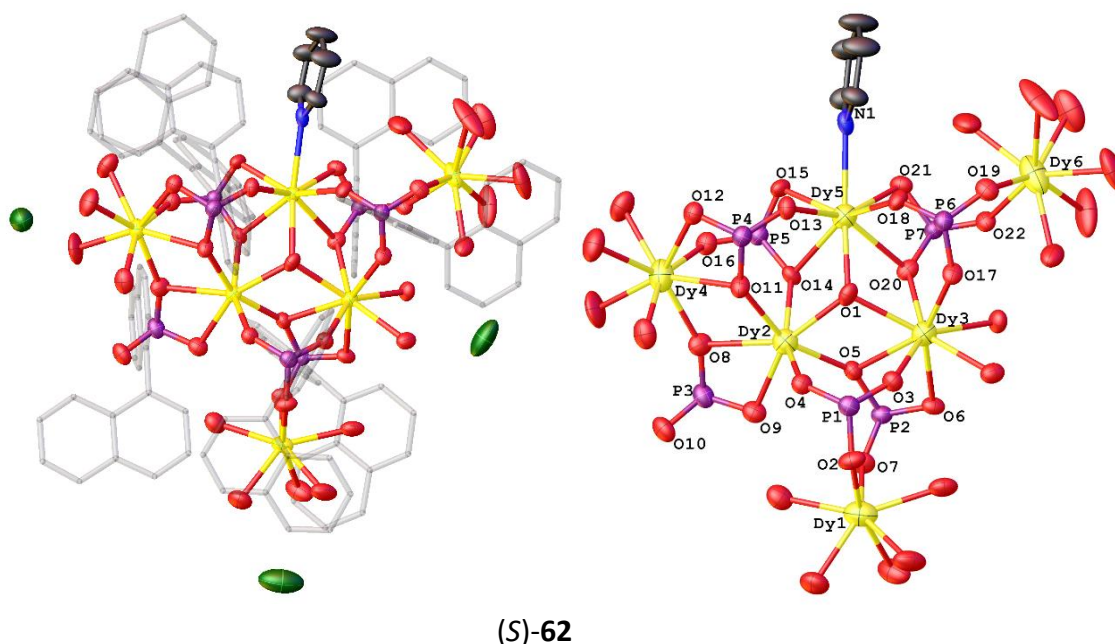


Figure 4.5 Left: Structure of (*S*)-**62** in the crystal, with binaphthyl groups represented as translucent sticks and hydrogen atoms omitted. Also shown are the three chloride counter-anions which balances the charge of the cluster. Right: Structure of the (*S*)-**62** core in the crystal with hydrogen atoms and chloride counter-anions omitted.

Not only do (S)-**59** – (S)-**65** share the same structure with each other, but they are also isostructural with the yttrium phosphonate, (S)-**52** (Chapter 3). This is perhaps to be expected, since yttrium itself behaves as a lanthanide – its dominant oxidation state is the +3 and it is often found in nature co-existing with other lanthanide ores. Much like (S)-**52**, (S)-**62** and its counterparts possess two main types of binding modes for their phosphonate ligands – two bind in a monodentate configuration while the other five are bidentate. They also all crystallise in the $P2_1$ space group, much like (S)-**52**. Table 11 lists the pertinent bond lengths of (S)-**62**. While the bond lengths for the other five lanthanide phosphonates are not shown, these were also found to be consistent with similar lanthanide phosphonates in the literature.¹³⁰

Bond	Length / Å	Bond	Length / Å	Bond	Length / Å
Dy1-O2	2.159(9)	Dy4-O12	2.374(9)	P2-O7	1.496(9)
Dy1-O7	2.244(8)	Dy4-O16	2.295(9)	P3-O8	1.531(10)
Dy2-O1	2.310(9)	Dy5-O1	2.397(8)	P3-O9	1.515(10)
Dy2-O4	2.276(8)	Dy5-O13	2.319(8)	P3-O10	1.497(9)
Dy2-O5	2.258(8)	Dy5-O14	2.472(8)	P4-O11	1.516(9)
Dy2-O8	2.469(9)	Dy5-O15	2.332(8)	P4-O12	1.532(9)
Dy2-O9	2.329(9)	Dy5-O18	2.206(8)	P4-O13	1.510(9)
Dy2-O11	2.305(8)	Dy5-O20	2.494(8)	P5-O14	1.542(9)
Dy2-O14	2.304(8)	Dy5-O21	2.416(8)	P5-O15	1.504(9)
Dy3-O1	2.420(8)	Dy5-N1	2.562(10)	P5-O16	1.500(9)
Dy3-O3	2.269(8)	Dy6-O19	2.265(8)	P6-O17	1.512(9)
Dy3-O5	2.526(8)	Dy6-O22	2.308(8)	P6-O18	1.523(9)
Dy3-O6	2.401(8)	P1-O2	1.508(9)	P6-O19	1.504(9)
Dy3-O17	2.279(8)	P1-O3	1.495(9)	P7-O20	1.518(9)
Dy3-O20	2.352(8)	P1-O4	1.533(9)	P7-O21	1.525(9)
Dy4-O8	2.333(9)	P2-O5	1.541(9)	P7-O22	1.527(9)
Dy4-O11	2.479(8)	P2-O6	1.506(9)		

Table 11 Selected bond lengths in (S)-**62** between all atoms labelled in Figure 4.31.

The packing diagram of (*S*)-**62** is shown in Figure 4.6. It can be seen that, like with (*S*)-**55**, layers of discrete clusters are present. The minimum distance between each cluster in one layer is about 3.37 Å, which is significantly shorter than the cluster-cluster distance in (*S*)-**55** (9.61 Å).

It was thought that the different methods of crystallisation were perhaps causing this change in structure. We therefore reacted (*S*)-**bpa** with CeCl₃·7H₂O and NdCl₃·6H₂O by dissolving both species in pyridine and stirring for 24 hours, before leaving to crystallise, as described above. Interestingly, in both cases, the pentametallic clusters formed again, which ruled out the possibility of reaction conditions dictating the resultant structure. Clearly this change was more intrinsic in origin.

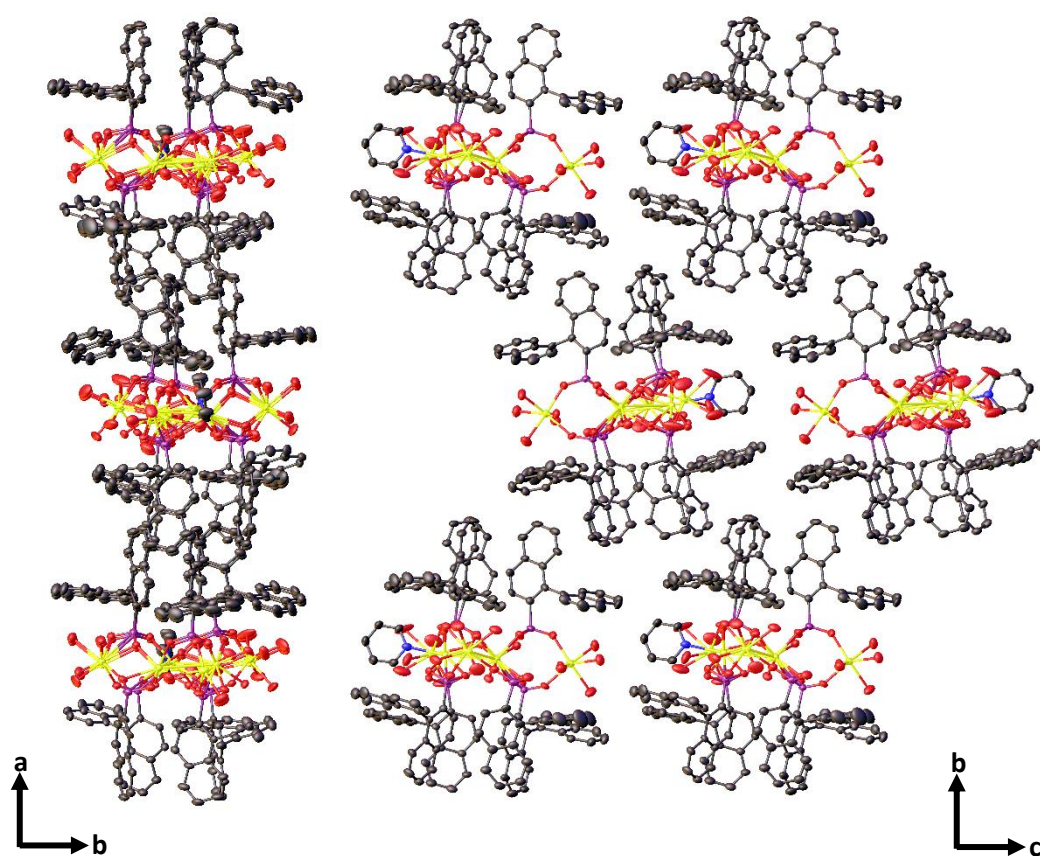


Figure 4.6 Left: Packing diagram of (*S*)-**62** down the *c*-axis. Right: Packing diagram of (*S*)-**62** down the *a*-axis. Hydrogen atoms have been omitted.

In the same manner as for the La – Sm lanthanides, (*S*)-**54** – (*S*)-**58**, a literature search was conducted to ascertain whether these phosphonates architectures were known. A search of the CCDC returned no results, which means the motifs for the Eu – Tm phosphonates shown above (and by extension, the yttrium phosphonate) are also novel. The final lanthanide phosphonates which we prepared were of ytterbium and lutetium, (*S*)-**66** and (*S*)-**67** respectively. These were expected to retain the same structure as (*S*)-**59** – (*S*)-**65**, but a final surprise awaited us when the crystal structures were elucidated.

4.4 Coordination to Final Lanthanides, Yb and Lu, (S)-**66** and (S)-**67**

The final lanthanide phosphonates we prepared were of the ytterbium and lutetium analogues, (S)-**66** and (S)-**67** respectively. These were prepared in the same manner as the later lanthanide phosphonates (Eu – Tm). However, single-crystal X-ray diffraction revealed these to be of a different structure to the aforementioned lanthanide phosphonates. For one, these phosphonates crystallised in the orthorhombic space group $P2_12_12$ (the same space group as the Nd and Sm phosphonates), as opposed to the monoclinic space group $P2_1$ that the Eu – Tm phosphonates crystallised in. Furthermore, inspection of the structure revealed some differences, although unlike the transition from the samarium to europium phosphonate, this change was more nuanced. Figure 4.7 shows the structure of the ytterbium phosphonate (S)-**66**, in the crystalline state and also the (S)-**66** core.

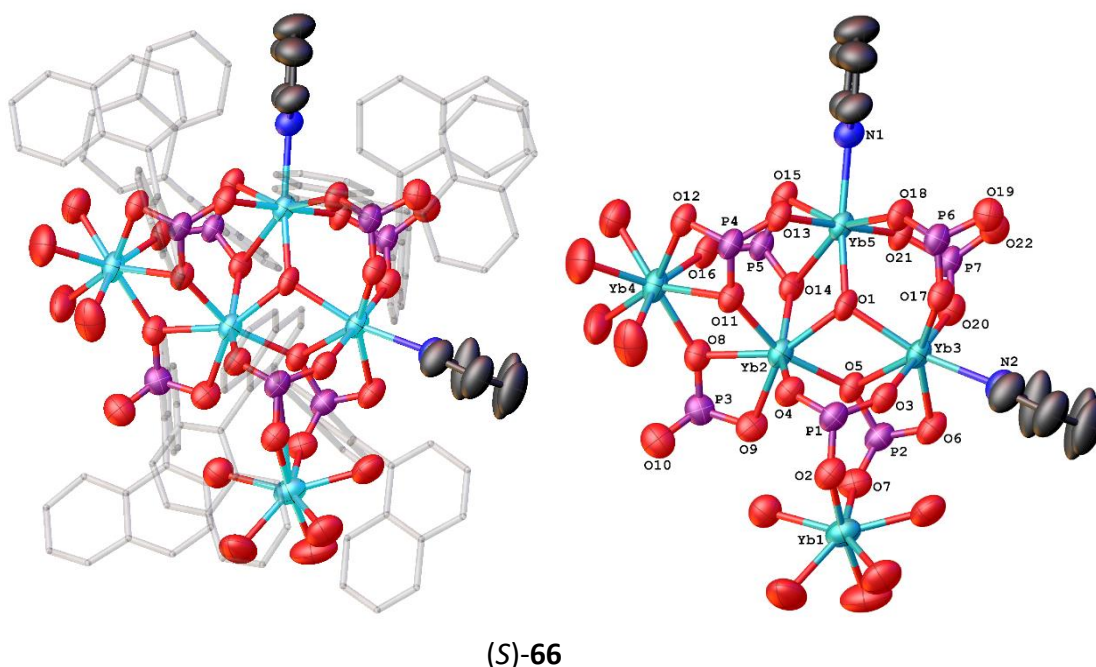


Figure 4.7 Left: Structure of (S)-**66** in the crystal, with binaphthyl groups represented as translucent sticks and hydrogen atoms omitted. Right: Structure of the (S)-**66** core in the crystal with hydrogen atoms and chloride counter-anions omitted.

As can be seen from Figure 4.7, (S)-**66** and (S)-**67** retain many characteristics as the Eu-Tm phosphonates – they still contain the μ_3 -OH⁻ bridge, as well as the seven doubly-deprotonated (S)-**bpa** ligands. However, the Ln6 ion which would normally bind to the O19 and O22 oxygen atoms is no longer present, making the Yb and Lu clusters pentametallic. This has significant implications on the overall charge of the cluster – for these lanthanide phosphonates, the charges balance exactly (15+ from Yb³⁺ x 5 versus 15– from the seven doubly-deprotonated phosphonate ligands plus the 1– from the μ_3 -OH⁻). Furthermore, the two aqua ligands which would normally bind to the Ln3 ion have been substituted for another pyridine ligand.

One final change concerns the binding configuration of the P7 phosphonate ligand. In the Eu-Tm phosphonates, there was a bond between the O20 and Ln5 centres which is no longer present here. This changes the binding configuration of the P7 phosphonate from [3.2₃₅1₅1₆] to [2.1₃1₅0], and as a consequence of no lanthanide ion present, the P6 phosphonate's Harris configuration also changes from [3.1₃1₅1₆] to [2.1₃1₅0]. The pertinent bond lengths in Figure 4.7 are listed in Table 12. Both the Yb and Lu phosphonate bond lengths were found to be consistent with similar lanthanide phosphonates in the literature.¹³¹

Bond	Length / Å	Bond	Length / Å	Bond	Length / Å
Yb1-O2	2.149(6)	Yb4-O8	2.278(6)	P2-O7	1.510(7)
Yb1-O7	2.241(6)	Yb4-O11	2.471(5)	P3-O8	1.529(7)
Yb2-O1	2.302(5)	Yb4-O12	2.339(6)	P3-O9	1.543(7)
Yb2-O4	2.240(5)	Yb4-O16	2.268(6)	P3-O10	1.465(8)
Yb2-O5	2.239(5)	Yb5-O1	2.311(5)	P4-O11	1.542(6)
Yb2-O8	2.416(6)	Yb5-O13	2.263(5)	P4-O12	1.535(6)
Yb2-O9	2.305(6)	Yb5-O14	2.466(6)	P4-O13	1.496(6)
Yb2-O11	2.267(5)	Yb5-O15	2.288(5)	P5-O14	1.537(6)
Yb2-O14	2.285(6)	Yb5-O18	2.202(5)	P5-O15	1.510(7)
Yb3-O1	2.342(5)	Yb5-O21	2.178(5)	P5-O16	1.506(6)
Yb3-O3	2.174(6)	Yb5-N1	2.475(7)	P6-O17	1.510(7)
Yb3-O5	2.434(6)	P1-O2	1.522(7)	P6-O18	1.517(5)
Yb3-O6	2.337(6)	P1-O3	1.519(7)	P6-O19	1.517(7)
Yb3-O17	2.267(6)	P1-O4	1.544(6)	P7-O20	1.522(6)
Yb3-O20	2.167(6)	P2-O5	1.550(6)	P7-O21	1.512(5)
Yb3-N2	2.478(8)	P2-O6	1.518(7)	P7-O22	1.511(7)

Table 12 Selected bond lengths in (S)-**66** between all atoms labelled in Figure 4.41.

Once again, a search of the CCDC returned no results for the motifs seen in (S)-**66** and (S)-**67**. Thus, all of the lanthanide phosphonate structures shown here are of a completely novel architecture. The packing diagram of (S)-**66** is shown in Figure 4.8.

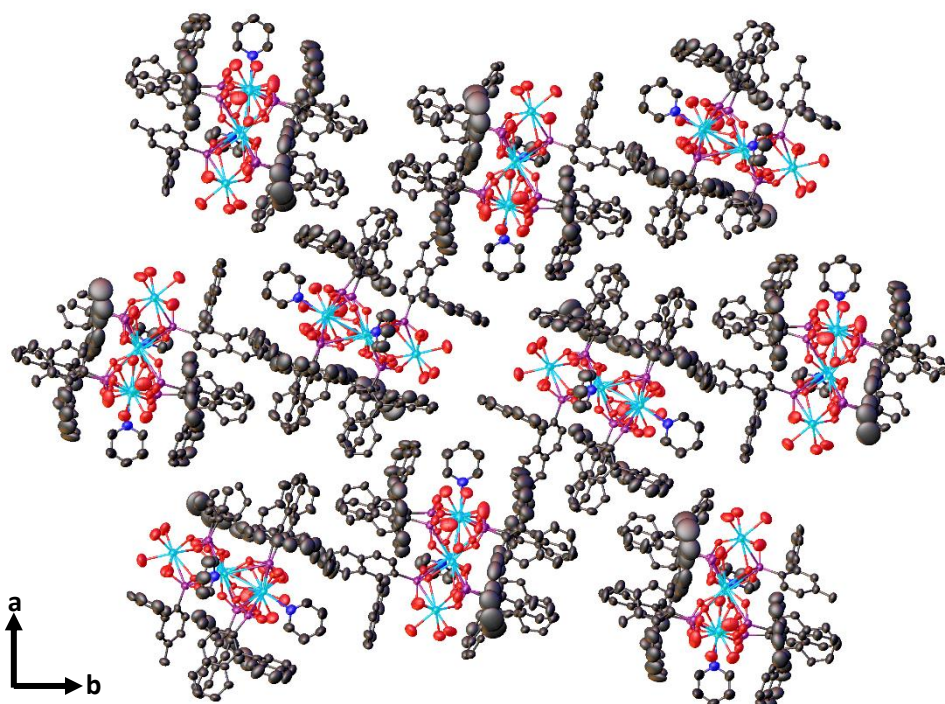


Figure 4.8 Packing diagram of (*S*)-**66** down the *c*-axis. Hydrogen atoms have been omitted.

To conclude, 14 new lanthanide phosphonates (the entire series excluding promethium) were successfully prepared and analysed by single-crystal X-ray diffraction. The phosphonates adopted a highly regular pentametallic arrangement from lanthanum to samarium (Figure 4.2). However, from europium to thulium, the structures switched to highly irregular hexametallic clusters (Figure 4.5). A final change in morphology was seen in ytterbium and lutetium, whose structures were almost identical to the europium – thulium structures, but with the loss of a peripheral lanthanide ion and the acquisition of an extra pyridine, as well as some binding configuration changes (Figure 4.7). These results have been summarised in Figure 4.9. This sudden change in morphology of lanthanide complexes is a known occurrence and can be attributed to the lanthanide contraction – the steadily decreasing ionic radius of the Ln^{3+} ions as one traverses across the series (see above). There have been numerous reports detailing this phenomenon in the literature.¹³²

In our case, one supporting piece of evidence regarding how ionic radius dictates the structure of the resultant lanthanide phosphonate lies in the structure of the yttrium phosphonate, (*S*)-**52**. This shares the same structure as the later lanthanide phosphonates (Eu – Tm). The experimentally derived ionic radii of these M^{3+} ions (see below) reveals that the effective ionic radius across the whole lanthanide series drops from 125.78 pm (La^{3+}) to 113.78 pm (Lu^{3+}) for our lanthanide phosphonates, with the first change in structure occurring somewhere between

121.59 and 119.72 pm (Sm^{3+} and Gd^{3+}) respectively. The effective ionic radius of Y^{3+} was found to be 117.54 pm. This places its ionic radius between holmium and erbium in the series, whose ionic radii are 117.94 and 117.01 pm respectively, and these have already been established as forming the hexametallic cluster. Therefore, it follows that yttrium should also form the same structure, which experimentally, it does. This is visualised in Figure 4.10.

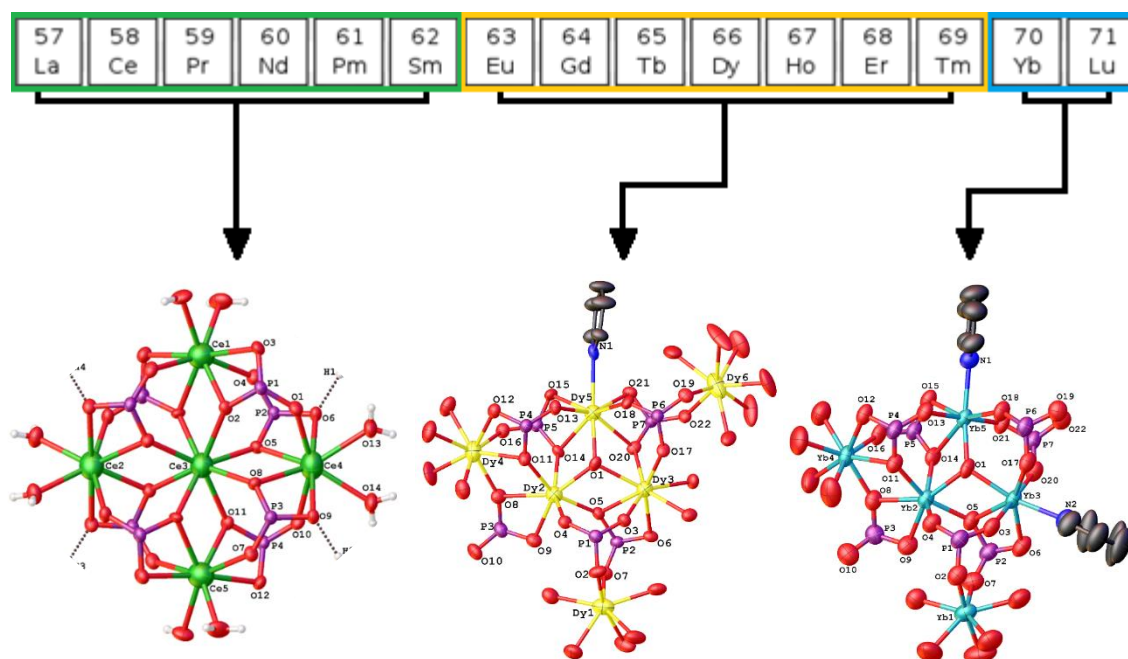


Figure 4.9 Summary of which Ln-(S)-bpa phosphonate is observed across the series.

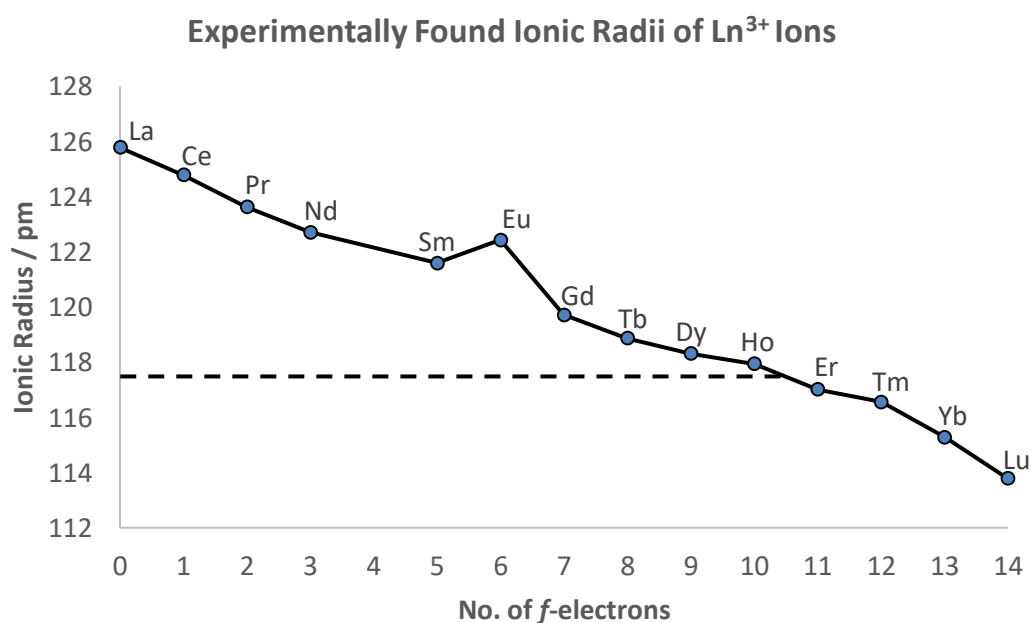


Figure 4.10 Experimentally found ionic radii of the Ln^{3+} ions from the lanthanum phosphonate to lutetium phosphonate. The dashed line at 117.54 pm is the ionic radius of the yttrium phosphonate.

The experimental ionic radii of the lanthanide phosphonates were found empirically, utilising the crystal structures we had obtained. These were determined by compiling all Ln-O bonds for a given Ln-(S)-**bpa** phosphonate (Ln-N and Ln-OH₂ bonds were disregarded) and averaging these values. Then, the mean value was divided by two to yield a length which represents ionic radial extension of the lanthanide ion. It should be noted that these values are not comparative with other ionic radii for lanthanide phosphonates in the literature, as the methodology used in these cases will differ. It is only sufficient for the purposes of comparing our lanthanide phosphonates.

From Figure 4.10, it can be seen that the ionic radius generally decreases from La – Lu, which was to be expected. However, for the europium phosphonate ((S)-**59**), the ionic radius increases before falling sharply again in the gadolinium phosphonate ((S)-**60**). This is almost certainly not representative of reality and can probably be attributed to the lower quality of refinement for (S)-**59** compared with the other lanthanide phosphonates. It was noted that when compiling the Eu-O bonds lengths, the bond lengths were given to three significant figures, as opposed to four significant figures for all other lanthanide phosphonates. A future chemist working on this project would be wise to remake (S)-**59** and have its X-ray data re-collected.

As an addendum, while the promethium-(S)-**bpa** phosphonate was never made, we can predict that its ionic radius should fall between 122.71 and 121.59 pm.

Dried and triturated samples of the Gd₆ and Dy₆ phosphonates ((S)-**60** and (S)-**62**) were sent to the National EPR Facility and Service at the University of Manchester for ac susceptibility studies. These were chosen since Gd and Dy are intrinsically the most anisotropic lanthanides. Unfortunately, these phosphonates were found to not exhibit any slow magnetic relaxation. This was attributed to the lack of communication between the lanthanide centres – a consequence of the contracted ionic radii of the Ln³⁺ ions. The majority of lanthanide SMMs consist of monometallic octahedral lanthanide complexes with a z-axis distortion which gives rise to high anisotropy.^{25,26} Future endeavours should include the attempted preparation of monomeric lanthanide phosphonates using (S)-**bpa**.

4.5 Photophysical Properties of Eu Phosphonate, (S)-51

We were eager to probe the photophysical properties of some of our lanthanide phosphonates, notably the europium phosphonate (S)-59 and the terbium phosphonate (S)-61, since Eu^{3+} and Tb^{3+} possess the most interesting photophysical properties. This is due to the emission properties of these two lanthanides – they emit in the visible region, producing a distinct red light for Eu^{3+} complexes and a green light for Tb^{3+} complexes. All of the other Ln^{3+} ions tend to emit in the infrared region.⁵⁷ A screening of solvents for our clusters led to the conclusion that only dimethyl sulfoxide was capable of dissolving a reasonable quantity of material, and therefore this was the solvent which was used for all photophysical experiments.

Unfortunately, the terbium phosphonate (S)-61 only produced very weak emission despite excitation at a number of wavelengths and concentrations. Even under simple illumination from a laboratory ultraviolet lamp, no characteristic green glow could be observed. We attributed this to the numerous aqua ligands which occupy the periphery of the cluster (Figure 4.5). It is known that unless complete encapsulation of the lanthanide ion is achieved, then significant quenching (in the form of non-radiative processes) will occur *via* the aqua ligands.²³ Despite this, our europium phosphonate (S)-59 produced a strong red glow when illuminated (254 nm) and an emission spectrum was recorded (Figure 4.11).

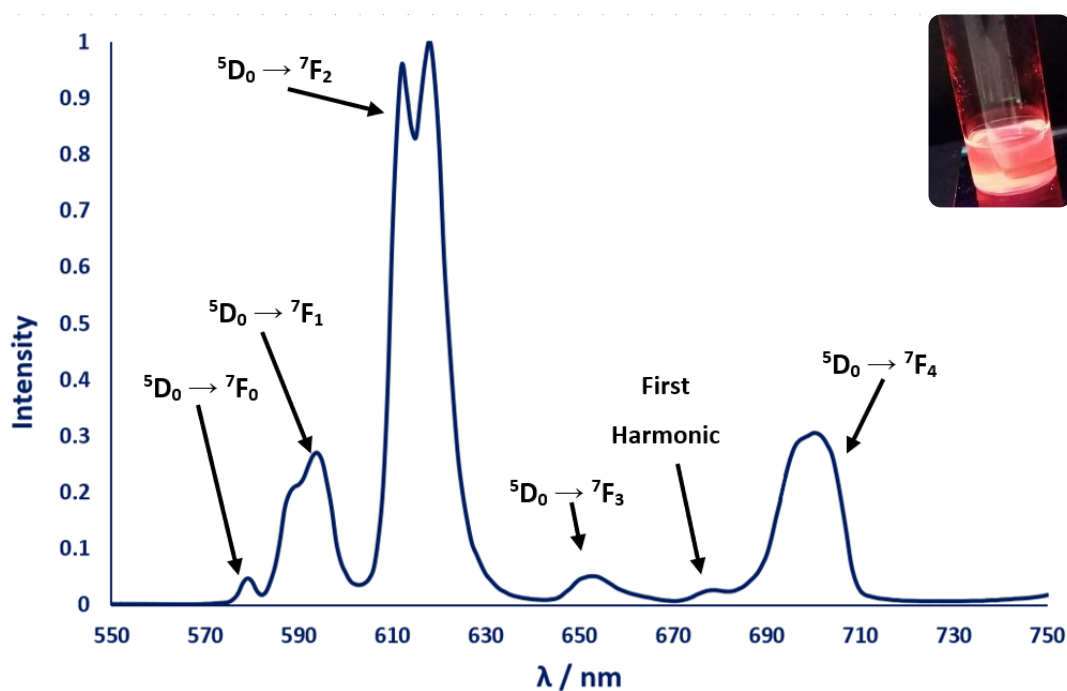


Figure 4.11 Main: Emission spectrum of (S)-59 ($\lambda_{\text{ex}} = 340 \text{ nm}$) with normalised intensity. Also shown are the main $f \rightarrow f$ transitions and first harmonic. Inset: A 1mM solution of (S)-59 in DMSO, being illuminated at 254 nm.

It was unclear as to why the europium phosphonate demonstrated strong fluorescence while the terbium phosphonate did not, despite the fact that the two clusters are isostructural with one another. Nevertheless, we had successfully prepared a chiral, fluorescent europium phosphonate. Each emission band in Figure 4.11 has been labelled with its corresponding transition. The small peak at 680 nm is the first harmonic, which occurs at values of $2n, 3n, 4n...$ where n is the wavelength of excitation, which in this case was 340 nm. The electronic dipole transition $^5D_0 \rightarrow ^7F_2$ – the most intense transition – is responsible for the characteristic red colour of most europium complexes. It is known that the intensity of this transition increases as the symmetry around the Eu(III) centre decreases, and if the Eu(III) atom lies on an inversion centre, this transition disappears completely.⁵⁷ The result of this is an orange colour when fluorescing, due to the $^5D_0 \rightarrow ^7F_0$ and $^5D_0 \rightarrow ^7F_1$ transitions now taking precedence. In the case of (*S*)-**59**, none of the europium atoms lie on an inversion centre, and thus the $^5D_0 \rightarrow ^7F_2$ dominates, leading to a red colour. These transitions are illustrated in the Eu^{3+} energy level diagram shown in Figure 4.12.

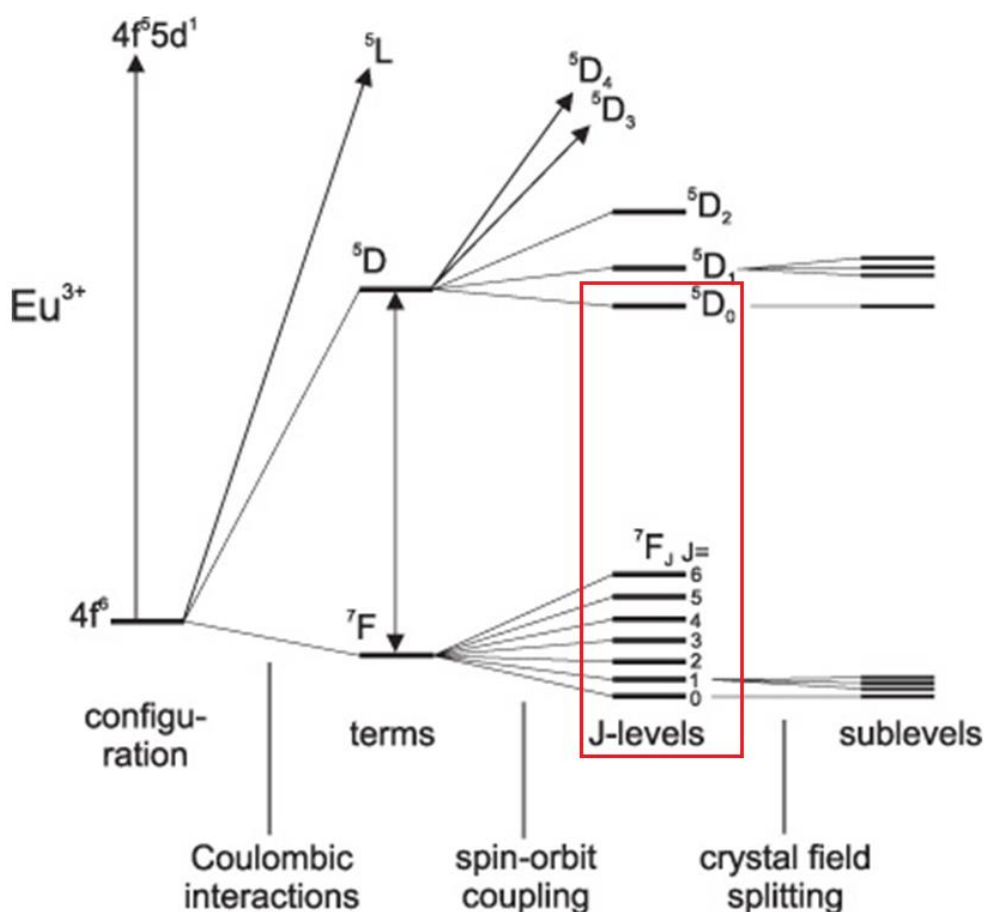


Figure 4.12 Energy level diagram for Eu^{3+} with pertinent transitions outlined in red. As can be seen, spin-orbit coupling dominates over crystal field effects, whereas in a transition metal complex, the opposite would be true.

As can be seen in Figure 4.12, the majority of electronic transitions in these complexes are the $f \rightarrow f$ transitions. One interesting manifestation of these transitions are their unusual sharp emission bands produced in emission spectra. This is due to the fact that these $f \rightarrow f$ transitions are symmetrically forbidden by Laporte's rules. Moreover, unlike in $d \rightarrow d$ transitions (such as those found in transition metal complexes), the 4f orbitals are essentially shielded – crystal field effects are virtually non-existent (represented by the negligible splitting of the J -levels in Figure 4.51). This means a particular transition will always have the same energy regardless of the ligand bound to the Ln(III) ion – only the relative intensities change. In conclusion, we have successfully prepared a chiral fluorescent Eu(III) cluster in (S)-**59**.

4.6 Conclusion

We have successfully prepared 14 new chiral lanthanide phosphonates using (S)-**bpa**. The ability to coordinate and crystallise to each lanthanide in the series in a facile manner is further testament to the impressive versatility of our sterically encumbered ligand. Although our layering technique only worked for lanthanum to samarium, it was found that both stirring and layering produced the exact same pentametallic clusters in both cases.

Coordination to all lanthanides (excluding promethium) in the series gave us insight into how the lanthanide contraction – more specifically, the decreasing ionic radii of the lanthanides from La to Lu – caused a change in morphology in our clusters. This was strongly supported by the fact that yttrium, whose ionic radius is akin to that of holmium, forms a cluster that is isostructural to that holmium (and indeed five other lanthanides) when reacted with (S)-**bpa** in the same manner. Furthermore, this phenomenon has been documented by other research groups (see above).

Future work involving coordination of (S)-**bpa** to lanthanides should focus on preparing monometallic complexes. For instance, a Ln-(S)-**bpa** complex isostructural to the monometallic TM-(S)-**bpa** complexes such as (S)-**37** would certainly be an interesting compound in terms of its SMM-like behaviour, since a single lanthanide ion would possess high intrinsic anisotropy. Furthermore, since it has been demonstrated that (S)-**bpa** is capable of forming mixed transition metal complexes in (S)-**43**, and as such, future work should focus on adopting these reaction conditions to potentially form mixed TM-Ln-(S)-**bpa** complexes. These types of compounds are known to possess interesting magnetic properties by virtue of 3d-4f interactions increasing the ground spin-state.¹³³

Conclusion and Future Work

To conclude, we have prepared a new sterically encumbered chiral phosphonic acid, (*S*)-**bpa** and used it to synthesise 27 new metal phosphonates – 13 transition metal and 14 lanthanide. To do this, we employed three synthetic methods – stirring the ligand and metal in solution, layering a solution of the ligand on top of a solution of the metal and the hydrothermal method. The latter two methods were used to prepare three cobalt phosphonates of three different dimensionalities. Further to this, we have demonstrated that it was possible to synthesise the analogous (*R*)-**bpa** and used it to prepare the corresponding (*R*)- cobalt phosphonates, (*R*)-**37**, (*R*)-**38** and (*R*)-**42**. With regards to the magnetic susceptibility, the measurements for the three cobalt phosphonates (*S*)-**37**, (*S*)-**38** and (*S*)-**42** are still pending. However, we discovered that a known mononuclear Co(II) complex, **36**, a by-product in the early crystallisation attempts of (*S*)-**37**, demonstrated slow magnetic relaxation. We have since published these results.

This change in phosphonate morphology by modification of the reaction conditions as seen in cobalt was also seen with manganese. Two manganese phosphonates, a mononuclear complex (*S*)-**45** and a hexanuclear cluster (*S*)-**48** were prepared by employing two different methods, layering and stirring following slow evaporation respectively.

The successful coordination and crystal structure determination of (*S*)-**bpa** with all of the lanthanides (excluding promethium) was a promising result and granted us insight into how the decreasing ionic radii of the Ln³⁺ ions across the series dictated the resultant structure of the phosphonate. Three different morphologies were observed, the first from La – Sm, the second from Eu – Tm and the final in Yb and Lu. Furthermore, photophysical tests were conducted on the fluorescent europium phosphonate (*S*)-**59** and an emission spectrum was recorded.

Future work in this project should firstly focus on the preparation of mixed TM-Ln, TM-TM or Ln-Ln clusters. This is certainly feasible in ambient conditions, as we have demonstrated with the mixed Co₃Sc₃ cluster (*S*)-**43**. However, all avenues of synthetic methods (stirring, layering and hydrothermal method) should certainly be explored. Mixed TM-Ln phosphonates are likely to possess interesting magnetic properties due to the 3d-4f interactions increasing the ground spin-state (high spin-ground state is an essential prerequisite for an effective SMM).¹³³

The 2-dimensional cobalt sheet, (*S*)-**42** was found to be ineffective at Baeyer-Villiger oxidations, although there are a plethora of other phosphonates which we have prepared that may demonstrate some other applications. For instance, a lanthanum-(*S*)-**bpa** phosphonate could be prepared *via* the hydrothermal method and it could be tested against the lanthanum

phosphonate prepared by Bein and co-workers which proved to possess high selectivity towards monovalent alkali cations.¹⁸ Another example is the iron phosphonate prepared by Bhaumik and co-workers which demonstrated effectiveness at catalysing the conversion cyclohexanone to adipic acid in air and water.^{15d} Perhaps our iron phosphonate (*S*)-**48** could prove to be just as effective.

Further crystallisation attempts on other first-row transition metals should also be attempted, namely in vanadium and chromium. While their potential applications are more limited when compared to cobalt, manganese and iron, it would nevertheless be interesting to see if the same $[M((S)\text{-bpa})_2(Py)_4]$ complexes form as with (*S*)-**37**, (*S*)-**45**, (*S*)-**49**, (*S*)-**50** and (*S*)-**53**, or if a different structure is observed. Moreover, further crystallisation attempts on second-row transition metals could be attempted, particularly silver, as a significant number of silver phosphonates exist in the literature (see Chapter 3).

It could be possible to prepare a number of potential derivatives of (*S*)-**bpa**. One such example is the 2'-hydroxy derivative, (*R*)-(2'-hydroxy-[1,1'-binaphthalen]-2-yl)phosphonic acid, (*R*)-**hbpa** (Figure 5.1). This could be prepared from (*R*)-binol in the same way that (*S*)-**bpa** is, with the only difference being there would be no reduction step – the phosphorylation would immediately follow the first mono-triflation. The additional hydroxyl group would certainly afford different architectures to (*S*)-**bpa** when coordinating this ligand to the same metals, and it would be interesting to see how the two differ.

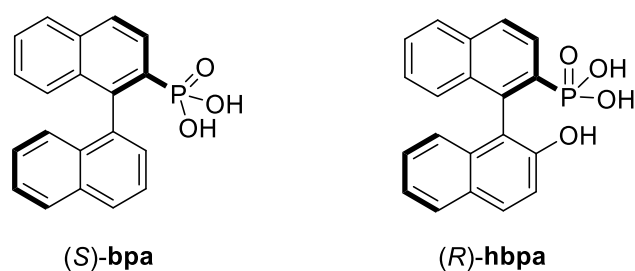


Figure 5.1 Structure of (*S*)-**bpa** and (*R*)-**hbpa**. Both are derived from (*R*)-binol with the latter retaining its absolute configuration due to the presence of the hydroxyl group on the lower naphthyl ring, as opposed to a hydrogen in (*S*)-**bpa**.

While it may seem like we have prepared many structures, we have only scratched the surface of metal phosphonate chemistry. By adapting the reaction conditions, employing different bases than pyridine and using combinations of two or more metal salts, a near infinite number of crystallisations could be set up. We hope that this thesis provides a solid foundation with which to build and develop the ideas presented here.

Experimental

General Procedure

Step (V) – the hydrolysis of (S)-**34** to (S)-**bpa** – was performed using standard Schlenk line techniques under an atmosphere of nitrogen with oven dried glassware. CH₂Cl₂ (CaH₂) was dried and distilled prior to use. All other ligand synthesis steps and coordination reactions were performed in air; solvents and reagents were of standard laboratory reagent grade and used without further purification.

Chromatographic purifications were performed using Geduran[®] silica gel purchased from Fluorochem (40 – 63 μ , 60 Å). All NMR spectra (¹H, ¹³C, ³¹P, ¹⁹F) were recorded on either a Bruker 300 MHz or a JEOL 400 MHz spectrometer. Infrared spectra were recorded on a Varian 800 FT-IR spectrometer. High resolution mass spectrometry analyses were performed at the National Mass Spectrometry Facility, Swansea using a Thermo Scientific LTQ Orbitrap XL apparatus. Thin layer chromatographic analyses were performed on Merck aluminium-backed plates (silica gel 60, F₂₅₄). UV illumination was provided by means of a UV light (λ = 254 nm) from UVP. Optical rotation values were determined with an Optical Activity Polaar 2001 device. Luminescence spectra were recorded on a Shimadzu RF-600 Spectro Fluorophotometer and data was processed on the Lab Solutions RF software. Hydrogenations were performed in glass reactors in a Buchi AG Miniclave system. EPR and SQUID analyses were performed at the EPSRC National Service for Electron Paramagnetic Resonance Spectroscopy at the University of Manchester.

All crystal structure data, except those for **36**, (S)-**42**, (R)-**42**, (S)-**44**, (S)-**52**, (S)-**56**, (S)-**57**, (S)-**58**, (S)-**59**, (S)-**61**, (S)-**62**, (S)-**64**, (S)-**66** and (S)-**67** were collected on an Xcalibur, Atlas, Gemini Ultra diffractometer equipped with an Oxford Cryosystems CryostreamPlus open-flow N₂ cooling device. Data for (S)-**45**, (S)-**49**, (S)-**50**, (S)-**53**, (S)-**54**, (S)-**60** and (S)-**63** were collected using molybdenum radiation ($\lambda_{\text{MoK}\alpha}$ = 0.71073 Å) and for (S)-**37**, (R)-**37**, (S)-**38**, (R)-**38**, (S)-**43**, (S)-**48**, (S)-**51**, (S)-**55** and (S)-**65** using copper radiation ($\lambda_{\text{CuK}\alpha}$ = 1.54184 Å). All structures apart from (S)-**37**, (R)-**37**, (S)-**54**, (S)-**65**, (S)-**45** and (S)-**51** had their intensities corrected for absorption empirically using spherical harmonics and for these structures by a multifaceted crystal model created by indexing the faces of the crystal for which data were collected.¹ Data were collected at 150 K except in the case of (S)-**50** and (S)-**53** for which data were collected at 120 K and 210 K respectively. Cell refinement, data collection and data reduction were undertaken *via* the software CrysAlisPro.²

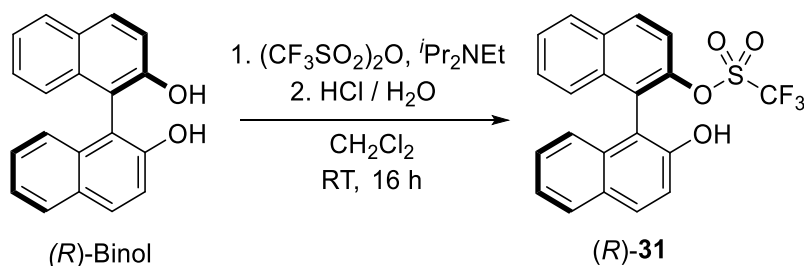
Data for **36**, (S)-**42**, (R)-**42**, (S)-**44**, (S)-**52**, (S)-**56**, (S)-**57**, (S)-**58**, (S)-**59**, (S)-**61**, (S)-**62**, (S)-**64**, (S)-**66**

and (*S*)-**67** were collected at 100 K on beamline I19 at Diamond Light Source using synchrotron radiation ($\lambda = 0.68890 \text{ \AA}$) and the data processed using the software APEX2.³ All structures were solved using XT⁴ and refined by XL⁵ using the Olex2 interface.⁶ All non-hydrogen atoms were refined anisotropically and hydrogen atoms were positioned with idealised geometry, with the exception of those bound to heteroatoms where the positions could be located using peaks in the Fourier difference map. The displacement parameters of the hydrogen atoms were constrained using a riding model with $U_{(H)}$ set to be an appropriate multiple of the U_{eq} value of the parent atom.

To prepare (*S*)-**bpa**, (*R*)-binol was used and vice versa. To wash and dry all metal phosphonate crystals for analysis, the crystals were separated from the mother liquor, triturated, washed three times with ethanol (3 mL) and dried under vacuum at room temperature for 3 h. Any metal phosphonate that does not have its corresponding optical rotation measurement was due to its insoluble nature.

-
- 1 R. C. Clark and J. S. Reid, *Acta Crystallogr., Sect. A*, 1995, **51**, 887–897.
 - 2 CrysAlisPro, Rigaku Oxford Diffraction, Tokyo, Japan.
 - 3 APEX2, Bruker AXS inc., Madison, Wisconsin, USA.
 - 4 G. M. Sheldrick, *Acta Crystallogr., Sect. A*, 2015, **71**, 3–8.
 - 5 G. M. Sheldrick, *Acta Crystallogr., Sect. A*, 2008, **64**, 112–122.
 - 6 O. V. Dolomanov, L. J. Bourhis, R. J. Gildea, J. A. K. Howard, H. J. Puschmann, *Appl. Cryst.*, 2009, **42**, 339–341.

Synthesis of (R)-31



(R)-binol (8.00 g, 27.9 mmol, 1 eq.) was dissolved in CH_2Cl_2 (500 mL) before $i\text{Pr}_2\text{NEt}$ (4.9 mL, 27.9 mmol, 1 eq.) was added. The solution was cooled to 0 °C for 10 min before $(\text{CF}_3\text{SO}_2)_2\text{O}$ (4.7 mL, 27.9 mmol, 1 eq.) was added dropwise, turning the clear solution pale purple. The solution was left stirring for 16 h at room temperature.

The solution was then concentrated to roughly half of its volume and washed with H_2O (100 mL), 1 M HCl (100 mL) and brine (100 mL) and the combined organic phases were dried over MgSO_4 before being reduced *in vacuo*. CH_2Cl_2 (50 mL) and Et_3N (20 mL) were added to the resultant oil. Dark yellow crystals formed after 24 h and were subsequently washed with H_2O (3 x 15 mL) and acetone (3 x 15 mL). Pale yellow crystals of the triethylamine salt were obtained. These were redissolved in CH_2Cl_2 (50 mL) and washed with H_2O (50 mL) and 1 M HCl (50 mL). The combined organics were dried over MgSO_4 , filtered and reduced *in vacuo*. This yielded the title product, a white solid (10.8 g, 25.8 mmol, 92 %).

$\alpha_D = +166.4$ (1.112 g/100 cm³, CH_2Cl_2 , 20 °C).

$R_f = 0.25$ (Toluene).

^1H NMR (300 MHz, CDCl_3): $\delta = 8.03$ (d, 1H, ArH), $\delta = 7.93$ (d, 1H, ArH), $\delta = 7.88$ (d, 1H, ArH), $\delta = 7.79$ (d, 1H, ArH), $\delta = 7.53 - 7.46$ (m, 2 H, ArH), $\delta = 7.39 - 7.31$ (m, 2H, ArH), $\delta = 7.29 - 7.16$ (m, 3H, ArH), $\delta = 6.91$ (d, 1H, ArH), $\delta = 4.81$ (broad s, 1H, OH) ppm.

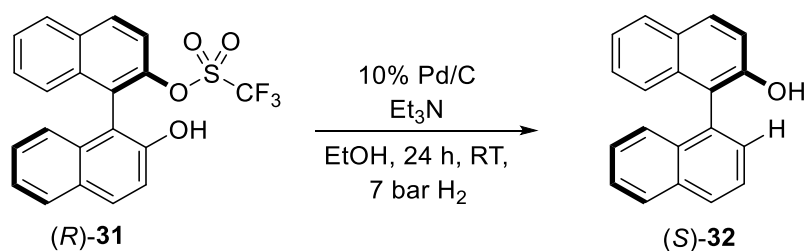
^{13}C NMR (75 MHz, CDCl_3): $\delta = 151.78$ (ArC), $\delta = 146.16$ (ArC), $\delta = 133.26$ (ArC), $\delta = 133.20$ (ArC), $\delta = 132.92$ (ArC), $\delta = 131.64$ (ArC), $\delta = 131.42$ (ArC), $\delta = 129.12$ (ArC), $\delta = 128.50$ (ArC), $\delta = 128.36$ (ArC), $\delta = 128.24$ (ArC), $\delta = 127.61$ (ArC), $\delta = 127.06$ (ArC), $\delta = 126.46$ (ArC), $\delta = 124.19$ (ArC), $\delta = 123.82$ (ArC), $\delta = 120.35$ (ArC), $\delta = 119.83$ (ArC), $\delta = 117.89$ (ArC), $\delta = 112.06$ (ArC) ppm.

^{19}F NMR (282 MHz, CDCl_3): $\delta = -74.45$ ppm.

HRMS (NSI Full, (CH₂Cl₂/MeOH, NH₄OAc): *m/z* [M + NH₄]⁺ calcd for C₂₀H₁₄F₃O₄S: 436.0825; found 436.0813.

IR (neat / cm⁻¹): 3300 (w), 1206 (s), 1138 (s).

Synthesis of (S)-32



(R)-**31** (2.7 g, 6.5 mmol, 1 eq.) was dissolved in EtOH (40 mL). The solution was transferred to a miniclave vessel along with Et₃N (8.2 mL, 58.8 mmol, 3 eq.) and 10% Pd/C (200 mg, 1.88 mmol, 0.01 eq.). The suspension was stirred at 7 bar H₂ for 48 h, after which TLC analysis indicated complete consumption of the starting material.

The black suspension was filtered twice to remove the Pd/C residues and the solvent removed *in vacuo*. CH₂Cl₂ (50 mL) was then added to the solution. The organic phase was washed with H₂O (50 mL), 1 M HCl (50 mL), 1 M NaHCO₃ (50 mL) and brine (50 mL), before being dried over MgSO₄. A pale yellow solid of the title product was obtained after concentrating the solution *in vacuo* (1.39 g, 5.16 mmol, 80 %).

$\alpha_D = -103.4$ (1.112 g/100 cm³, CH₂Cl₂, 20 °C)

R_f = 0.50 (Toluene).

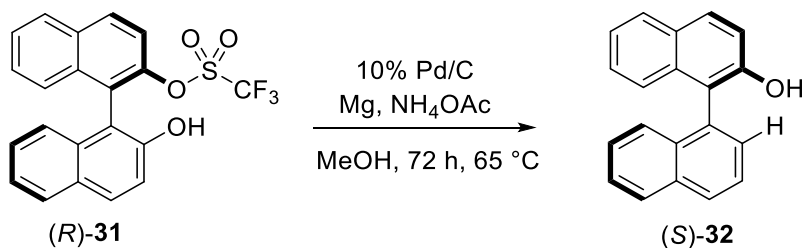
¹H NMR (300 MHz, CDCl₃): δ = 7.85 (t, 2H, ArH), δ = 7.75 (dd, 2H, ArH), δ = 7.52-7.47 (m, 1H, ArH), δ = 7.41 – 7.36 (m, 1H, ArH), δ = 7.29 – 7.17 (m, 4H, ArH), δ = 7.13 – 7.07 (m, 1H, ArH), δ = 6.98 (d, 1H, ArH), δ = 4.80 (s, 1H, OH) ppm.

¹³C NMR (75 MHz, CDCl₃): δ = 151.02 (ArC), δ = 134.25 (ArC), δ = 133.98 (ArC), δ = 132.90 (ArC), δ = 131.53 (ArC), δ = 129.94 (ArC), δ = 129.71 (ArC), δ = 129.28 (ArC), δ = 129.00 (ArC), δ = 128.53 (ArC), δ = 128.08 (ArC), δ = 126.93 (ArC), δ = 126.62 (ArC overlapping), δ = 126.62 (ArC overlapping), δ = 126.07 (ArC), δ = 125.86 (ArC), δ = 125.04 (ArC), δ = 123.43 (ArC), δ = 118.82 (ArC), δ = 117.53 (ArC) ppm.

HRMS (NSI Full, (CH₂Cl₂/MeOH, NH₄OAc): *m/z* [M + H]⁺ calcd for C₂₀H₁₄O: 271.1117; found 271.1121.

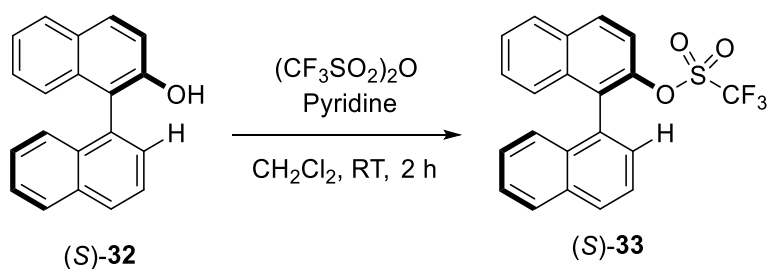
IR (neat / cm⁻¹): 3280 (br).

Alternative Synthesis of (S)-32



(R)-31 (1 g, 2.39 mmol, 1 eq.) was added to a Schlenk flask, followed by 10% Pd/C (100 mg, 0.94 mmol, 0.01 eq.), Mg turnings (55 mg, 2.3 mmol, 1.2 eq.) and NH₄OAc (148 mg, 1.9 mmol, 1 eq.). The solids were dissolved in anhydrous MeOH (13 mL) and the solution was degassed for 120 s. The reaction was heated at 65 °C under a nitrogen atmosphere for 72 h. TLC analysis indicated complete consumption of starting material. The suspension was cooled and filtered through Celite before being reduced *in vacuo*. This yielded the title compound – a white solid (0.54 g, 1.98 mmol, 83%).

Synthesis of (S)-33



(S)-32 (2.43 g, 8.99 mmol, 1 eq.) was dissolved in CH₂Cl₂ (35 mL) before pyridine (1.1 mL, 13.49 mmol, 1.5 eq.) was added. The solution was cooled to 0 °C for 10 min before (CF₃SO₂)₂O (2.3 mL, 13.67 mmol, 1.5 eq.) was added dropwise. The reaction was left stirring at room temperature for 2 h. The organic phase was washed with H₂O (50 mL), 1 M HCl (50 mL), 1 M NaHCO₃ (50 mL) and brine (50 mL) before being dried over MgSO₄ and concentrated *in vacuo* to yield a pale orange solid (2.89 g, 7.19 mmol, 80%).

R_f = 0.9 (Toluene)

$\alpha_D = -28.6$ (1.112 g/100 cm³, CH₂Cl₂, 20 °C)

¹H NMR (300 MHz, CDCl₃): δ = 8.04 (t, 2H, ArH), δ = 7.97 (t, 2H, ArH), δ = 7.67 – 7.62 (m, 1H, ArH), δ = 7.59 – 7.47 (m, 4H, ArH), 7.41-7.29 (m, 3H, ArH), 7.21 (d, 1H, ArH) ppm.

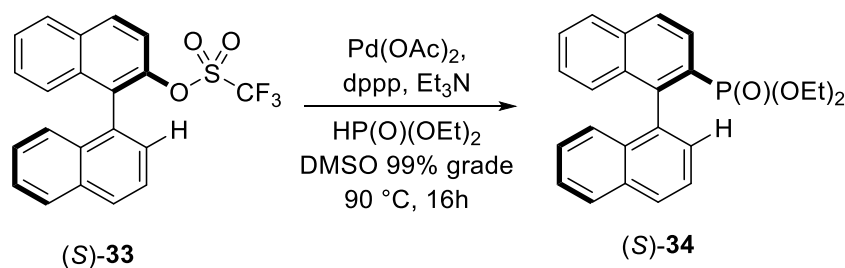
¹³C NMR (75 MHz, CDCl₃): δ = 144.95 (ArC), δ = 133.85 (ArC), δ = 133.61, δ = 132.49 (ArC), δ = 132.42 (ArC), δ = 130.84 (ArC), δ = 130.55 (ArC), δ = 130.43 (ArC), δ = 129.27 (ArC), δ = 129.12 (ArC), δ = 128.38 (ArC), δ = 128.12 (ArC), δ = 127.56 (ArC), δ = 127.07 (ArC), δ = 127.04 (ArC), δ = 126.46 (ArC), δ = 126.11 (ArC), δ = 125.59 (ArC), δ = 125.22 (ArC), δ = 119.49 (ArC) ppm.

¹⁹F NMR (282 MHz, CHCl₃): δ = -74.48 ppm.

HRMS (NSI Full, (CH₂Cl₂/MeOH, NH₄OAc): m/z [M + NH₄]⁺ calcd for C₂₀H₁₄F₃O₄S: 436.0825; found 436.0813.

IR (neat / cm⁻¹): 3300 (br), 1206 (s), 1138 (m).

Synthesis of (S)-34



(S)-**33** (3 g, 7.5 mmol, 1 eq.), Pd(OAc)₂ (84 mg, 0.37 mmol, 0.05 eq.) and Ph₂P(CH₂)₃PPh₂ (dppp) (231 mg, 0.56 mmol, 0.075 eq.) were dissolved in DMSO (30 mL) in a Schlenk flask. The reaction mixture was stirred for 10 min under a nitrogen atmosphere before Et₃N (1.6 mL, 21.78 mmol, 1.5 eq.) and HP(O)(OEt)₂ (2.5 g, 18.1 mmol, 1.2 eq.) were added. The solution was then heated to 90 °C and left stirring for 16 h.

H₂O (30 mL) was added to the mixture and a white suspension immediately formed. The suspension was extracted with CH₂Cl₂ (80 mL) and the organic layer was washed with brine (3 x 50 mL) before being dried over MgSO₄ and concentrated *in vacuo*. The resulting yellow oil was purified by column chromatography (EtOAc/petroleum ether 40-60 °C, 2:1). The combined

fractions were concentrated *in vacuo* and a yellow oil was formed. The oil was left to crystallise, yielding the title product – pale yellow crystals (2.1 g, 5.38 mmol, 72 %).

$R_f = 0.30$ (EtOAc/Petroleum ether 40-60 °C 2:1)

$\alpha_D = -28.6$ (1.112 g/100 cm³, CH₂Cl₂, 20 °C)

¹H NMR (300 MHz, CDCl₃): $\delta = 8.24$ (dd, 1H, ArH), 8.05 (dd, 1 H, ArH), 8.01 – 7.94 (m, 3H, ArH), 7.65 – 7.58 (m, 1H, ArH), 7.57 – 7.51 (m, 2H, ArH), 7.46 (dt, 1H, ArH), 7.32 – 7.19 (m, 4H, ArH), 7.11 (d, 1H, ArH), 3.86 – 3.52 (m, 4H, ArH), 1.01 (t, 3H, CH₂), 0.74 (t, 3H, CH₃) ppm.

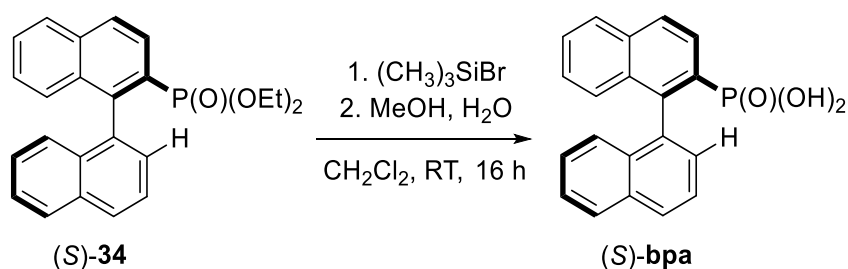
¹³C NMR (75 MHz, CDCl₃): $\delta = 135.92$ (ArC), $\delta = 135.85$ (ArC), $\delta = 134.94$ (ArC), $\delta = 134.90$ (ArC), $\delta = 133.36$ (ArC), $\delta = 133.12$ (ArC), $\delta = 128.75$ (ArC), $\delta = 128.70$ (ArC), $\delta = 128.61$ (ArC), $\delta = 128.25$ (ArC), $\delta = 128.01$ (ArC), $\delta = 127.92$ (ArC), $\delta = 127.83$ (ArC), $\delta = 127.77$ (ArC), $\delta = 127.58$ (ArC), $\delta = 127.45$ (ArC), $\delta = 126.70$ (ArC), $\delta = 125.87$ (ArC), $\delta = 125.60$ (ArC), $\delta = 124.94$ (ArC) ppm.

³¹P{¹H} NMR (121 MHz, CDCl₃): $\delta = 17.93$ ppm.

HRMS (NSI Full, (CH₂Cl₂/MeOH, NH₄OAc): m/z [M + H]⁺ calcd for C₂₄H₂₃O₃P: 391.1458; found 391.1454.

IR (neat / cm⁻¹): 1240 (s), 1019 (m).

Synthesis of (S)-bpa



(S)-**34** (1.00 g, 2.56 mmol, 1 eq.) was dissolved in anhydrous CH₂Cl₂ (5 mL) under a nitrogen atmosphere before (CH₃)₃SiBr (1.86 mL, 14.1 mmol, 5 eq.) was added dropwise. The solution was left to stir at room temperature for 16 h.

After 16 h, the solvent was evaporated in the Schlenk flask forming a yellow residue. The residue was redissolved in MeOH (2 mL) and stirred for 5 min until complete dissolution was achieved. H₂O (50 mL) was then added and a white precipitate formed. CH₂Cl₂ (50 mL) was added and the

organic layer was washed with brine (3 x 50 mL) before being concentrated *in vacuo*. This yielded (S)-**bpa** – a white solid (0.765 g, 2.29 mmol, 90 %).

$R_f = 0.12$ (EtOAc/MeOH 2:1) – solution had 3 drops of 2 M ethereal HCl added.

$\alpha_D = -28.6$ (1.112 g/100 cm³, CH₂Cl₂, 20 °C)

¹H NMR (300 MHz, CDCl₃): $\delta = 7.98$ (dd, 0.5 H, ArH), $\delta = 7.81$ (m, 3H, ArH), $\delta = 7.58$ (t, 1H, ArH), $\delta = 7.45$ (m, 2H, ArH), $\delta = 7.30$ (dt, 1H, ArH), $\delta = 7.15$ (m, 2H, ArH), $\delta = 7.05$ (dt, 1H, ArH), $\delta = 6.95$ (m, 1.5H, ArH), $\delta = 6.85$ (t, 0.5H, ArH), $\delta = 6.73$ (d, 0.5H, ArH), $\delta = 5.63$ (broad s, 1H, OH) ppm.

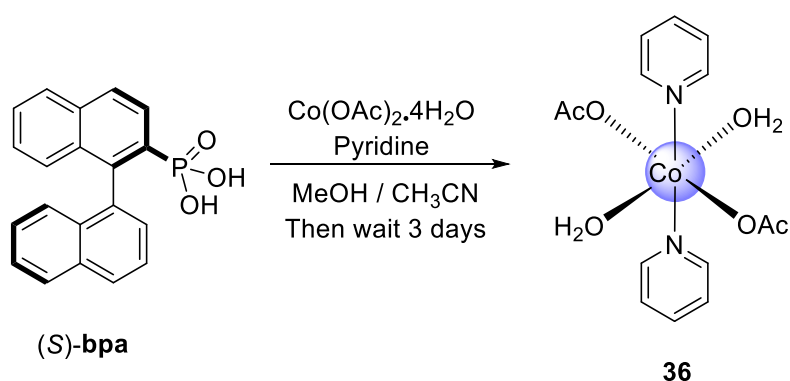
¹³C NMR (101 MHz, CDCl₃): $\delta = 128.93$ (ArC), $\delta = 127.92$ (ArC), $\delta = 127.88$ (ArC), $\delta = 127.84$ (ArC), $\delta = 127.80$ (ArC), $\delta = 127.73$ (ArC), $\delta = 127.64$ (ArC), $\delta = 127.58$ (ArC), $\delta = 127.36$ (ArC), $\delta = 127.30$ (ArC), $\delta = 127.22$ (ArC), $\delta = 126.67$ (ArC), $\delta = 126.29$ (ArC), $\delta = 125.87$ (ArC), $\delta = 125.86$ (ArC), $\delta = 125.69$ (ArC), $\delta = 125.39$ (ArC), $\delta = 125.34$ (ArC), $\delta = 125.27$ (ArC), $\delta = 125.11$ (ArC) ppm.

³¹P{¹H} NMR (121 MHz, CDCl₃): $\delta = 12.78$ ppm.

HRMS (NSI Full, (CH₂Cl₂/MeOH, NH₄OAc): m/z [M - H]⁻ calcd for C₂₀H₁₅O₃P: 333.0686; found 333.0682.

IR (neat / cm⁻¹): 2700 (br), 1254 (s).

Synthesis of **36**



$\text{Co}(\text{OAc})_2 \cdot 4\text{H}_2\text{O}$ (373 mg, 1.5 mmol, 1 eq.) was dissolved in MeOH (5 mL). This was stirred for 5 min before slowly being added to a solution of pyridine (0.5 mL, 6 mmol, 4 eq.) in CH_3CN (2.5 mL). The new solution was stirred for 5 min at room temperature and set aside to crystallise in open air. After 3 days, pink rhombohedral crystals of **36** were obtained.

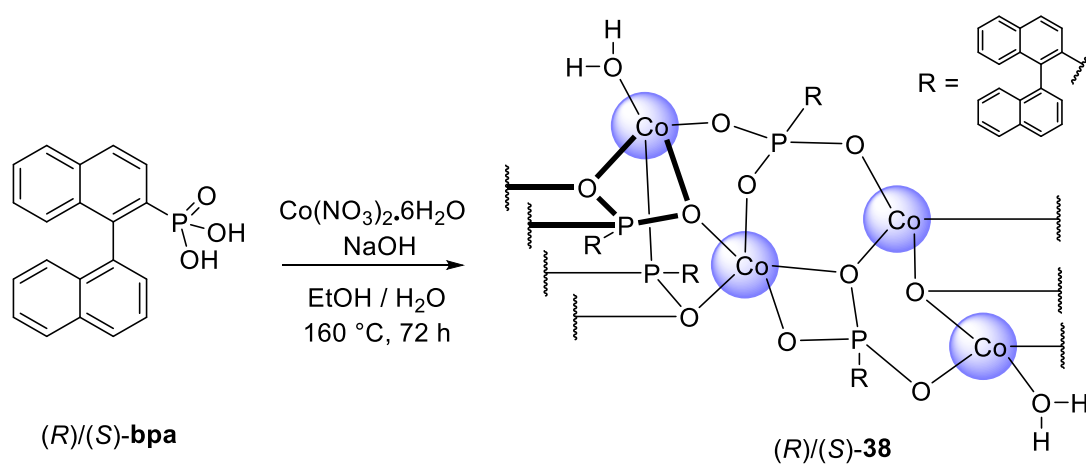
Yield: 289 mg, 0.8 mmol, 51%

HRMS (FTMS + p APCI corona Full, (MeOH): m/z $[\text{M} - \text{H}]^+$ calcd for $\text{C}_{20}\text{H}_{15}\text{O}_3\text{P}$: 371.2560; found 369.8336.

Anal. Calc. for $\text{C}_{14}\text{H}_{20}\text{N}_2\text{O}_6\text{Co}$ ($M_r = 371.26 \text{ g mol}^{-1}$): C, 45.29; H, 5.43; N, 7.55. Found: C, 46.75; H, 5.30; N, 7.81.

IR (neat / cm^{-1}): 3317 (w), 3082 (w), 1699 (s), 1609 (m), 1548 (m), 1419 (w), 1325 (s), 1241 (s), 1080 (w), 1045 (w), 1016 (w), 937 (m), 850 (m), 765 (S), 699 (m), 657 (w), 632 (m).

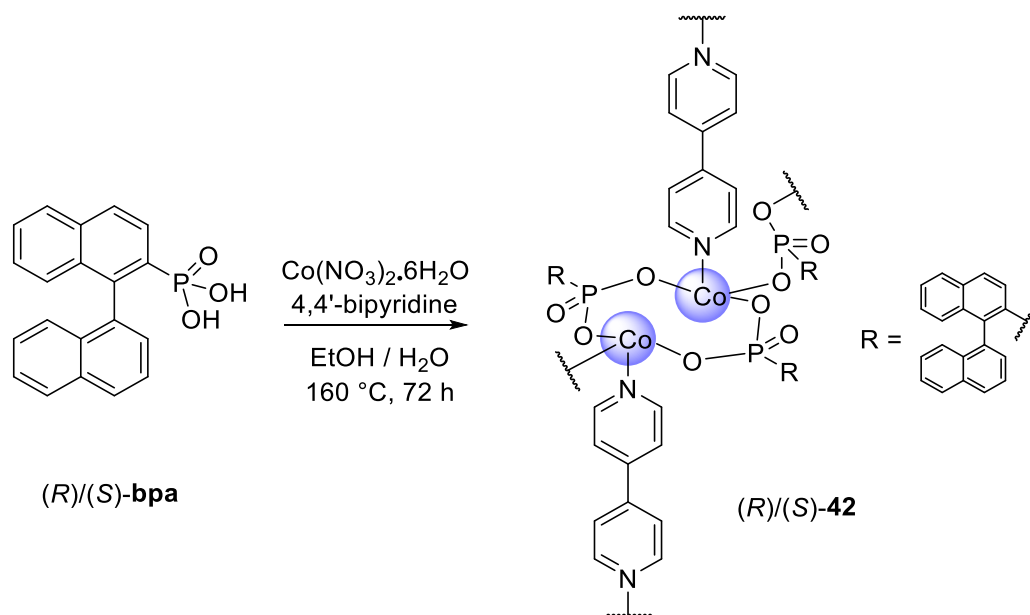
Synthesis of (*S*)/(*R*)-**38**



(*R*)/(*S*)-**bpa** (33 mg, 0.1 mmol, 1 eq.), $\text{Co(NO}_3)_2 \cdot 6\text{H}_2\text{O}$ (29 mg, 0.1 mmol, 1 eq.), NaOH (8 mg, 0.2 mmol, 2 eq.), EtOH (2 mL) and H_2O (2 mL) were loaded into a Teflon-lined stainless steel reactor. This was placed into an oven and heated to 160 °C for 72 h before being cooled at a rate of 0.1 °C/min. Blue needles of (*R*)/(*S*)-**38** were obtained.

IR (neat / cm^{-1}): 3054 (w), 1501 (s), 1367 (s), 1165 (w), 1103 (m), 1025 (m), 985 (m), 938 (s), 816 (w), 798 (s), 779 (m), 769 (m), 736 (w), 691 (w), 676 (s), 661 (m), 640 (m), 619 (m), 573 (w), 524 (m), 457 (m).

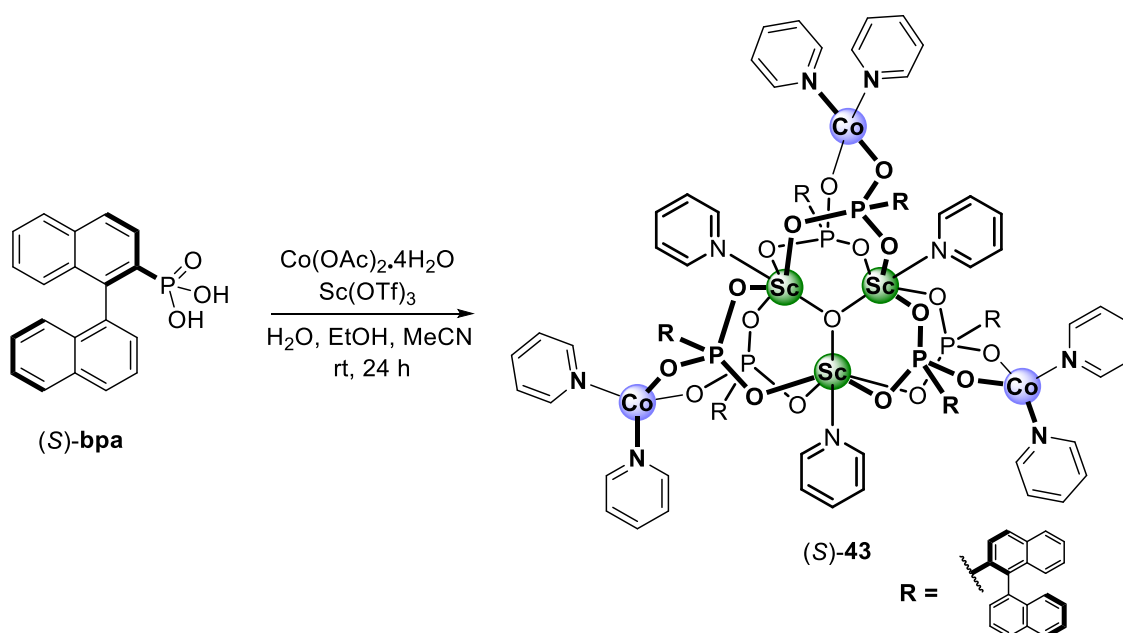
Synthesis of (*S*)/(*R*)-42



(*R*)/(*S*)-**bpa** (33 mg, 0.1 mmol, 1 eq.), $\text{Co(NO}_3)_2 \cdot 6\text{H}_2\text{O}$ (29 mg, 0.1 mmol, 1 eq.), 4,4'-bipyridine (8 mg, 0.05 mmol, 0.5 eq.), EtOH (2 mL) and H_2O (2 mL) were loaded into a Teflon-lined stainless steel reactor. This was placed into an oven and heated to 160 °C for 72 h before being cooled at a rate of 0.1 °C/min. Lustrous blue needles of were (*R*)/(*S*)-**42** were obtained.

IR (neat / cm^{-1}): 3044 (w), 1607 (s), 1534 (s), 1501 (m), 1414 (m), 1218 (s), 1118 (w), 1067 (w), 1044 (w), 998 (m), 943 (s), 865 (m), 810 (m), 772 (s), 741 (w), 691 (m), 661 (w), 639 (m), 564 (m), 525 (w), 459 (m), 435 (m).

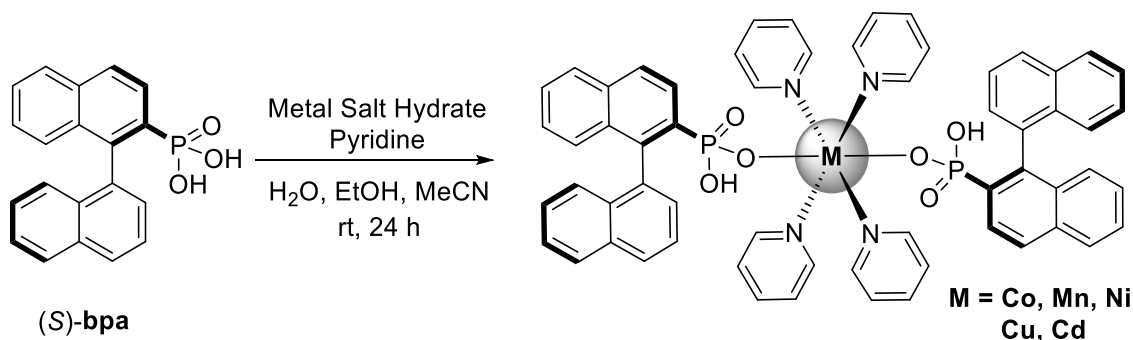
Synthesis of (S)-43



(S)-**bpa** (33 mg, 0.1 mmol, 1 eq.) was dissolved in pyridine in a medium-sized vial. In another medium sized vial, $\text{Co(OAc)}_2 \cdot 4\text{H}_2\text{O}$ (13 mg, 0.05 mmol, 0.5 eq.) and Sc(OTf)_3 (26 mg, 0.05 mmol, 0.5 eq.) were dissolved in a mixture of H_2O (1 mL), EtOH (1.5 mL) and MeCN (1.5 mL) and stirred for 5 min until complete dissolution was achieved. The pyridine solution containing the ligand was then carefully layered on top of the cobalt and scandium solution. Parafilm was placed over the vial and three holes were perforated. After 24 h, dark blue dendritic crystals of (S)-**43** formed.

IR (neat / cm^{-1}): 2981 (w), 1606 (s), 1447 (s), 1366 (m), 1257 (s), 1142 (w), 1093 (w), 1067 (m), 1003 (s), 944 (w), 861 (m), 783 (m), 748 (w), 693 (w), 638 (m), 523 (m), 406 (m).

Synthesis of Monometallic Co, Mn, Ni, Cu, Cd Phosphonates (*S*)-37, 45, 49, 50, 53 General Procedure



(*S*)-**bpa** (33 mg, 0.1 mmol, 1 eq.) was dissolved in pyridine (1 mL) in a medium-sized vial. In a separate vial, the appropriate metal diacetate hydrate (dichloride in the case of Mn and dinitrate in the case of Cd) (0.1 mmol, 1 eq.) was dissolved in a mixture of H₂O (0.5 mL), EtOH (1 mL) and MeCN (1 mL) and stirred for 5 min until complete dissolution was achieved. The pyridine solution containing the ligand was then carefully layered on top of the metal solution. Parafilm was placed over the vial and three holes were perforated. After 24 h, crystals of the desired monometallic phosphonate formed.

IR (neat / cm⁻¹) **Co**: 3056 (w), 2324 (w), 1725 (s), 1597 (s), 1442 (m), 1363 (w), 1216 (s), 1140 (m), 1098 (w), 1064 (m), 921 (s), 751 (m), 702 (m), 509 (m), 426 (w).

Co: $\alpha_D = -33.81$ (0.278 g/100 cm³, DMSO, 20 °C).

IR (neat / cm⁻¹) **Mn**: 2981 (w), 1596 (s), 1573 (m), 1489 (w), 1442 (s), 1364 (m), 1253 (s), 1232 (w), 1218 (w), 1147 (m), 1063 (m), 923 (w), 826 (m), 780 (w), 752 (m), 703 (m), 691 (w), 637 (s), 573 (m), 510 (w), 417 (m).

Mn: $\alpha_D = -10.07$ (0.278 g/100 cm³, DMSO, 20 °C).

IR (neat / cm⁻¹) **Ni**: 3056 (w), 2652 (w), 2324 (w), 1726 (s), 1599 (s), 1574 (m), 1557 (w), 1500 (w), 1486 (w), 1442 (m), 1362 (m), 1314 (w), 1254 (w), 1233 (s), 1215 (w), 1146 (w), 917 (m), 884 (m), 871 (m), 852 (w), 826 (w), 793 (m), 633 (m), 509 (m), 497 (m).

Ni: $\alpha_D = +25.2$ (0.5 g/100 cm³, DMSO, 20 °C).

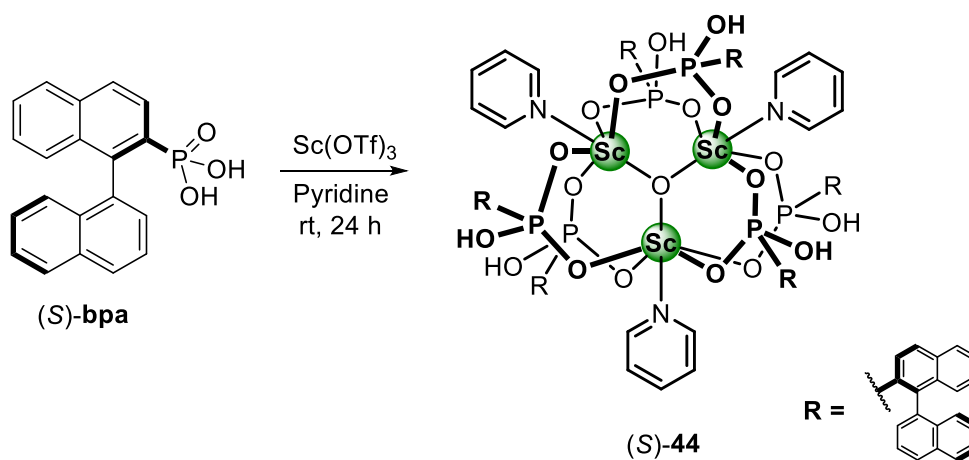
IR (neat / cm⁻¹) **Cu:** 3002 (w), 2946 (w), 2886 (w), 2631 (m), 2341 (w), 1823 (w), 1621 (s), 1598 (m), 1485 (m), 1446 (w), 1436 (w), 1352 (m), 1217 (s), 1070 (w), 1050 (w), 1037 (m), 1008 (s), 899 (m), 822 (s), 799 (m), 764 (m), 705 (m).

Cu: α_D = Unable to measure – insoluble.

IR (neat / cm⁻¹) **Cd:** 3060 (w), 3040 (w), 2361 (w), 1597 (s), 1574 (m), 1557 (w), 1506 (s), 1490 (m), 1445 (m), 1362 (w), 1314 (w), 1253 (s), 1233 (m), 1218 (m), 1149 (w), 1108 (w), 1066 (w), 1034 (s), 1006 (w), 953 (m), 922 (m), 871 (m), 825 (m), 793 (s), 780 (w), 752 (w), 703 (m), 693 (w).

Cd: $\alpha_D = -2.8$ (0.5 g/100 cm³, DMSO, 20 °C).

Synthesis of (S)-44



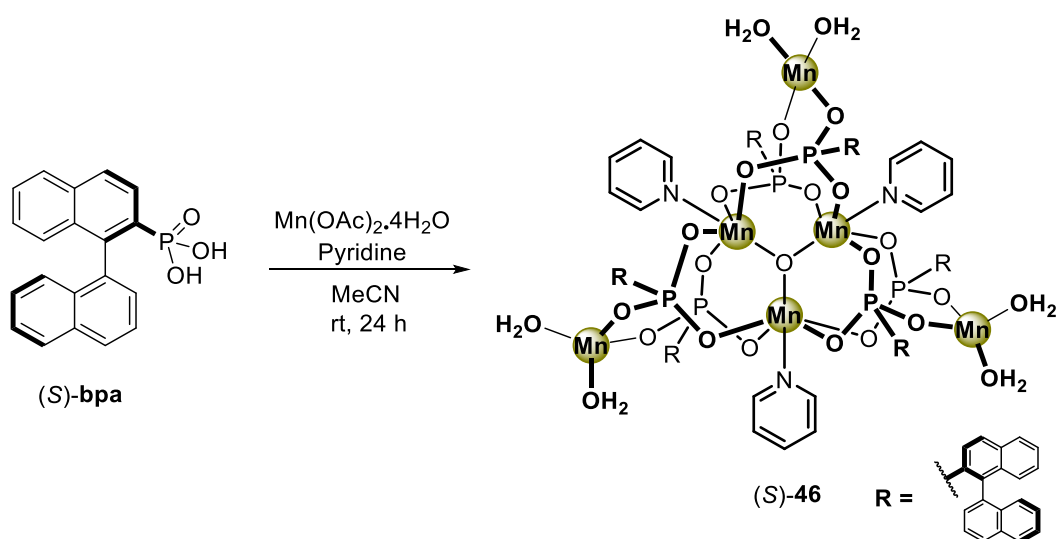
(*S*)-**bpa** (33 mg, 0.1 mmol, 1 eq.) and Sc(OTf)₃ (25 mg, 0.05 mmol, 0.5 eq.) were dissolved in pyridine (3 mL). This was stirred at room temperature for 24 h before being filtered. The filtrate was transferred to another vial. Parafilm was placed over the vial and three holes were perforated. After two weeks, colourless blocks of (*S*)-**44** were obtained.

³¹P{¹H} NMR (121 MHz, DMSO): δ = 7.21, 2.93, −3.95 ppm; δ = 11.66 ppm (after addition of 1 drop 2 M HCl to NMR tube).

IR (neat / cm^{−1}): 3058 (w), 1618 (s), 1489 (m), 1224 (s), 1166 (m), 1069 (m), 1026 (m), 824 (w), 804 (w), 784 (m), 774 (m), 748 (m), 679 (w), 662 (w), 637 (s), 617 (w), 518 (m), 573 (m).

α_D = −4.4 (0.5 g/100 cm³, DMSO, 20 °C)

Synthesis of (S)-46

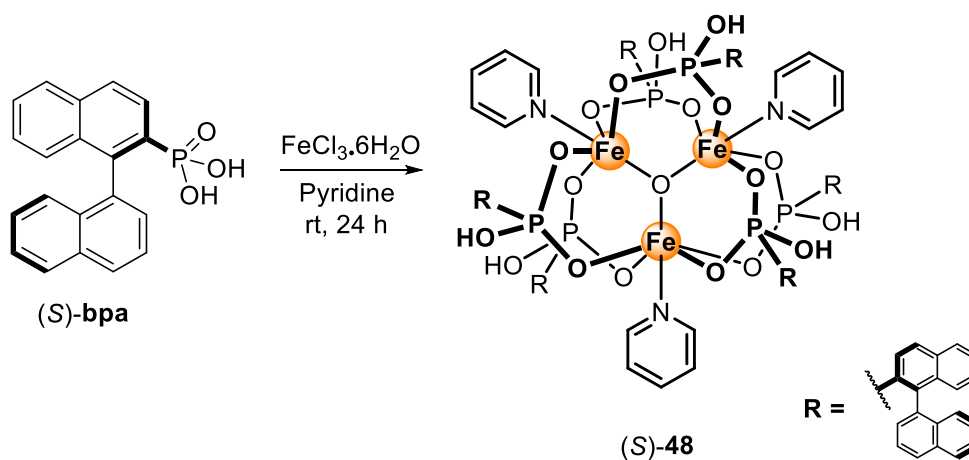


(S)-bpa (33 mg, 0.1 mmol, 1 eq.) and $\text{Mn}(\text{OAc})_2 \cdot 4\text{H}_2\text{O}$ (25 mg, 0.1 mmol, 1 eq.) were dissolved in acetonitrile (3 mL) before pyridine (1 mL) was added. This was stirred at room temperature for 24 h before being filtered. The filtrate was transferred to another vial. Parafilm was placed over the vial and three holes were perforated. After two weeks, dark brown blocks of (S)-46 were obtained.

IR (neat / cm^{-1}): 3053 (w), 2982 (w), 1558 (s), 1506 (w), 1446 (m), 1256 (s), 1121 (w), 1068 (m), 1012 (m), 968 (m), 940 (m), 869 (w), 824 (w), 782 (m), 747 (m), 692 (w), 638 (s), 615 (w).

$\alpha_D = +104$ (0.125 g/100 cm^3 , DMSO, 20 °C).

Synthesis of (S)-48

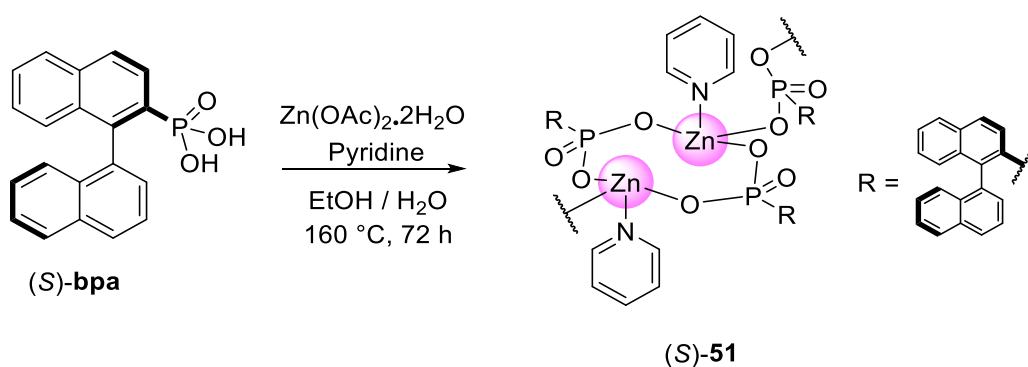


(*S*)-**bpa** (33 mg, 0.1 mmol, 1 eq.) and $\text{FeCl}_3 \cdot 6\text{H}_2\text{O}$ (27 mg, 0.1 mmol, 1 eq.) were dissolved in ethanol (3 mL) before pyridine (1 mL) was added. This was stirred at room temperature for 24 h before being filtered. The filtrate was transferred to another vial. Parafilm was placed over the vial and three holes were perforated. After two weeks, yellow blocks of (*S*)-**48** were obtained.

IR (neat / cm^{-1}): 3053 (w), 1605 (s), 1488 (s), 1446 (w), 1366 (s), 1069 (w), 996 (m), 826 (m), 801 (m), 781 (w), 772 (m), 747 (w), 691 (m), 679 (w), 661 (m), 638 (m), 616 (w), 568 (s), 534 (w), 515 (m), 435 (m).

$\alpha_D = +62.8$ (0.5 g/100 cm^3 , DMSO, 20 °C).

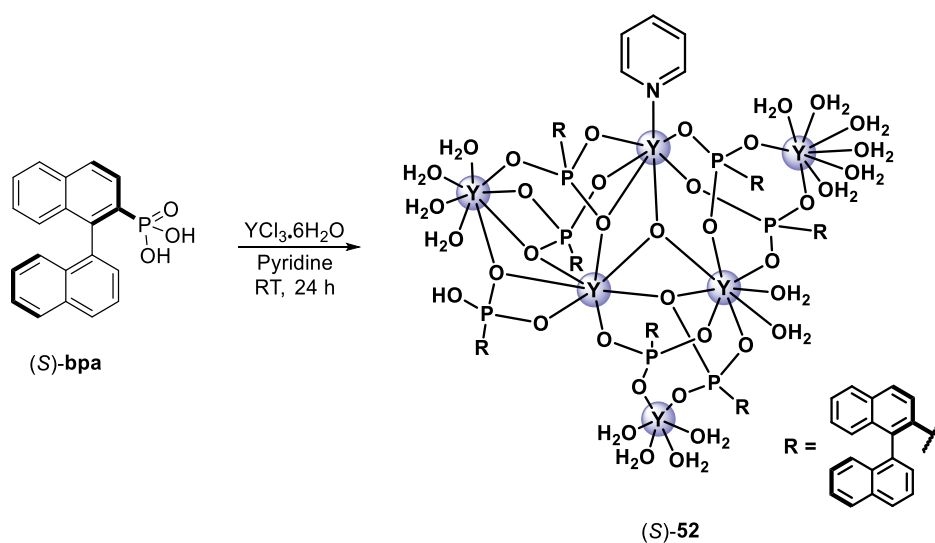
Synthesis of (S)-51



(S)-**bpa** (33 mg, 0.1 mmol, 1 eq.), Zn(OAc)₂·2H₂O (22 mg, 0.1 mmol, 1 eq.), pyridine (0.25 mL), EtOH (1 mL) and H₂O (1 mL) were loaded into a Teflon-lined stainless steel reactor. This was placed into an oven and heated to 160 °C for 72 h before being cooled at a rate of 0.1 °C/min. Colourless needles of (S)-**51** were obtained.

IR (neat / cm⁻¹): 3048 (w), 1610 (s), 1534 (m), 1413 (w), 1218 (s), 1121 (m), 1044 (w), 998 (m), 944 (w), 810 (m), 779 (m), 741 (w), 693 (m), 661 (w), 642 (m), 560 (w), 528 (m), 462 (w).

Synthesis of (S)-52

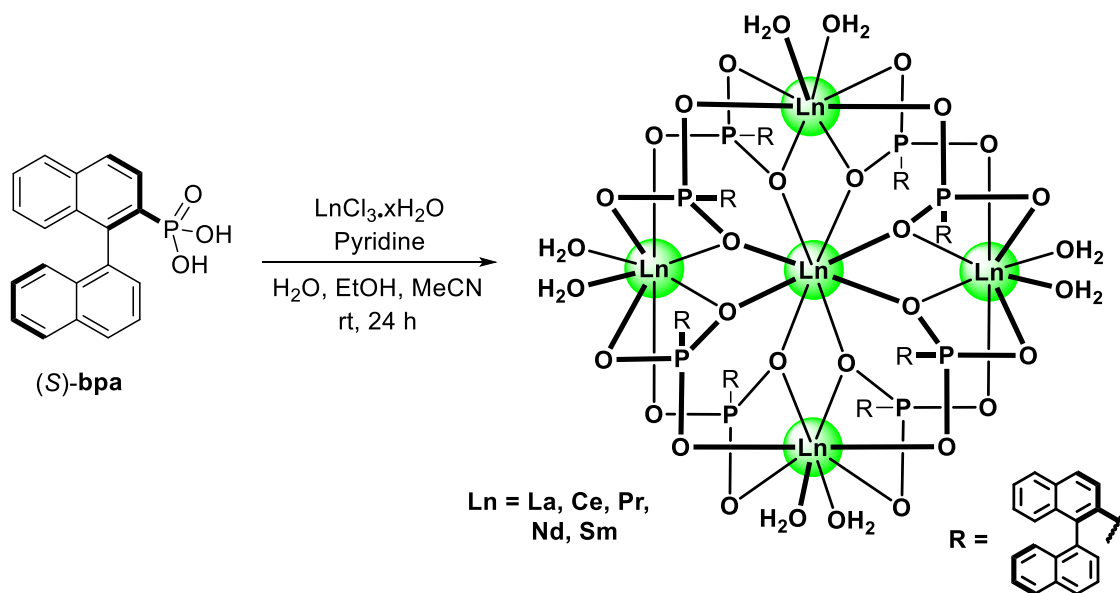


(S)-bpa (33 mg, 0.1 mmol, 1 eq.) and $\text{YCl}_3 \cdot 6\text{H}_2\text{O}$ (30 mg, 0.05 mmol, 0.5 eq.) were dissolved in pyridine (3 mL). This was stirred at room temperature for 24 h before being filtered. The filtrate was transferred to another vial. Parafilm was placed over the vial and three holes were perforated. After two weeks, colourless blocks of (S)-52 were obtained.

$^{31}\text{P}\{^1\text{H}\}$ NMR (121 MHz, DMSO): $\delta = 11.17, 3.76$ ppm.

IR (neat / cm^{-1}): 3051 (w), 1591 (s), 1442 (m), 1122 (s), 1045 (w), 989 (s), 941 (w), 803 (m), 783 (m), 746 (w), 691 (m), 679 (s), 663 (m), 641 (s), 618 (w), 577 (w), 525 (w), 451 (m).

Synthesis of La, Ce, Pr, Nd, Sm Phosphonates (*S*)-54, 55, 56, 57, 58, General Procedure



(*S*)-**bpa** (33 mg, 0.1 mmol, 1 eq.) was dissolved in pyridine (1 mL) in a medium-sized vial. In a separate vial, the appropriate lanthanide salt hydrate (0.1 mmol, 1 eq.) was dissolved in a mixture of H₂O (0.5 mL), EtOH (1 mL) and MeCN (1 mL) and stirred for 5 min until complete dissolution was achieved. The pyridine solution containing the ligand was then carefully layered on top of the lanthanide salt solution. Parafilm was placed over the vial and three holes were perforated. After 24 h, crystals of the desired lanthanide phosphonate formed.

La: $^{31}\text{P}\{^1\text{H}\}$ NMR (121 MHz, DMSO): $\delta = 5.85$ ppm.

IR (neat / cm^{-1}) **La**: 3055 (w), 1591 (s), 1489 (m), 1133 (s), 1015 (w), 975 (m), 936 (m), 867 (m), 826 (s), 803 (w), 783 (m), 774 (m), 747 (s), 681 (w), 663 (w), 639 (w), 617 (m), 575 (w), 555 (m), 536 (m), 523 (w), 491 (m), 447 (w), 411 (m).

La: $\alpha_D = +23.74$ (0.278 g/100 cm^3 , DMSO, 20 °C).

IR (neat / cm^{-1}) **Ce**: 3338 (w), 1618 (s), 1489 (w), 1364 (w), 1311 (w), 1135 (s), 1016 (w), 978 (s), 962 (m), 937 (s), 868 (m), 826 (w), 804 (w), 783 (w), 774 (m), 747 (s), 681 (m), 663 (m), 639 (m), 617 (w), 575 (w), 556 (s), 535 (w), 523 (m), 492 (m), 449 (w), 411 (m).

Ce: $\alpha_D = +50.36$ (0.278 g/100 cm^3 , DMSO, 20 °C).

IR (neat / cm^{-1}) **Pr**: 3315 (w), 1618 (s), 1489 (m), 1135 (s), 1016 (m), 978 (w), 962 (w), 937 (s), 827 (w), 804 (m), 783 (s), 748 (w), 681 (m), 663 (m), 639 (m), 617 (s), 575 (w), 557 (m), 535 (m), 523 (m), 493 (w), 450 (s), 412 (w).

Pr: $\alpha_D = +38.85$ (0.278 g/100 cm^3 , DMSO, 20 °C).

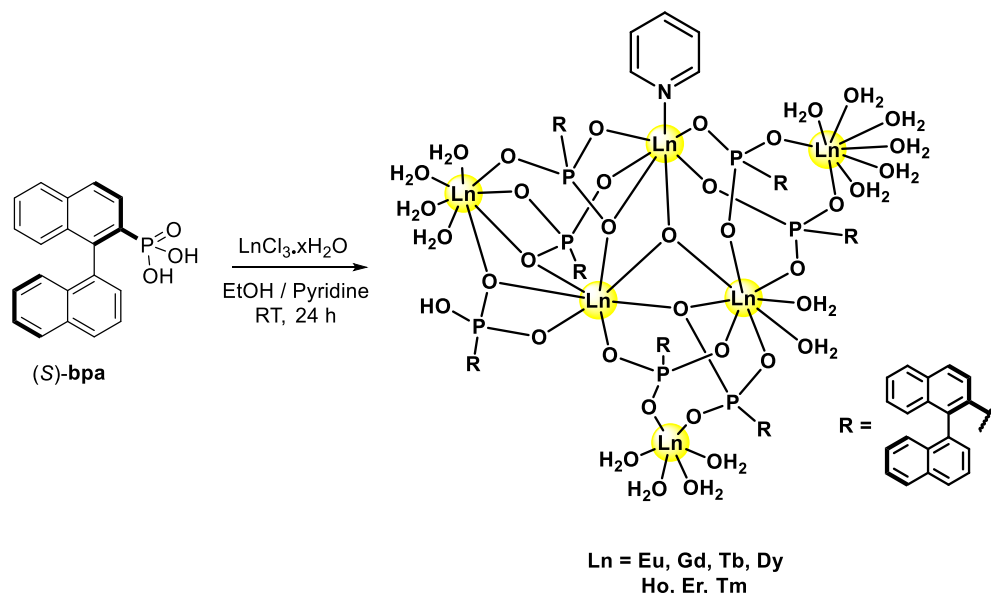
IR (neat / cm^{-1}) **Nd**: 3056 (w), 1591 (s), 1558 (w), 1490 (m), 1364 (w), 1312 (w), 1256 (w), 1135 (s), 1045 (m), 1014 (m), 978 (w), 961 (w), 936 (m), 867 (m), 774 (w), 747 (m), 690 (m), 680 (w), 663 (s), 639 (w), 617 (m).

Nd: $\alpha_D = +30.22$ (0.278 g/100 cm^3 , DMSO, 20 °C).

IR (neat / cm^{-1}) **Sm**: 3309 (w), 1591 (s), 1501 (w), 1070 (s), 1025 (w), 986 (m), 941 (w), 804 (m), 783 (m), 746 (m), 690 (m), 679 (s), 662 (w), 640 (s), 617 (w), 576 (m), 523 (m), 447 (w), 411 (m).

Sm: $\alpha_D = +4.32$ (0.278 g/100 cm^3 , DMSO, 20 °C).

Synthesis of Eu, Gd, Tb, Dy, Ho, Er, Tm Phosphonates (*S*)-59, 60, 61, 62, 63, 64, 65, General Procedure



(*S*)-**bpa** (33 mg, 0.1 mmol, 1 eq.) and the appropriate lanthanide (0.1 mmol, 1 eq.) were dissolved in ethanol (3 mL) and pyridine (1 mL). This was stirred at room temperature for 24 h before being filtered. The filtrate was transferred to another vial. Parafilm was placed over the vial and three holes were perforated. After two weeks, colourless blocks of the desired lanthanide phosphonate were obtained.

IR (neat / cm^{-1}) **Eu**: 2980 (w), 1044 (s), 984 (w), 941 (m), 783 (m), 746 (s), 640 (w), 618 (m), 577 (m), 524 (w).

Eu: $\alpha_D = -9.35$ (0.278 g/100 cm^3 , DMSO, 20 °C).

IR (neat / cm^{-1}) **Gd**: 3304 (w), 1591 (s), 1502 (w), 1072 (s), 1045 (m), 990 (m), 941 (m), 805 (w), 783 (s), 745 (w), 691 (m), 678 (m), 662 (m), 640 (m), 617 (m), 576 (s), 524 (m), 443 (m), 411 (w).

Gd: $\alpha_D = -3.60$ (0.278 g/100 cm^3 , DMSO, 20 °C).

IR (neat / cm^{-1}) **Tb**: 3308 (w), 1618 (s), 1502 (m), 1073 (s), 1045 (m), 992 (m), 942 (m), 805 (w), 784 (w), 774 (w), 745 (m), 691 (m), 678 (s), 662 (m), 640 (w), 618 (m), 576 (m), 524 (w), 450 (w).

Tb: $\alpha_D = -14.39$ (0.278 g/100 cm^3 , DMSO, 20 °C).

IR (neat / cm^{-1}) **Dy**: 3300 (w), 1618 (s), 1501 (w), 1364 (s), 1074 (w), 1045 (m), 993 (m), 942 (w), 868 (m), 805 (m), 784 (w), 774 (m), 746 (w), 691 (m), 679 (m), 663 (w), 640 (m), 618 (s), 577 (m), 524 (w), 450 (m).

Dy: $\alpha_D = -25.90$ ($0.278 \text{ g}/100 \text{ cm}^3$, DMSO, 20°C).

IR (neat / cm^{-1}) **Ho**: 3300 (w), 1591 (s), 1503 (m), 1365 (s), 1075 (w), 1045 (m), 993 (m), 942 (w), 868 (w), 805 (m), 784 (s), 774 (w), 745 (s), 691 (m), 678 (m), 663 (w), 640 (m), 618 (s), 576 (m), 524 (m), 449 (w), 411 (m).

Ho: $\alpha_D = -19.42$ ($0.278 \text{ g}/100 \text{ cm}^3$, DMSO, 20°C).

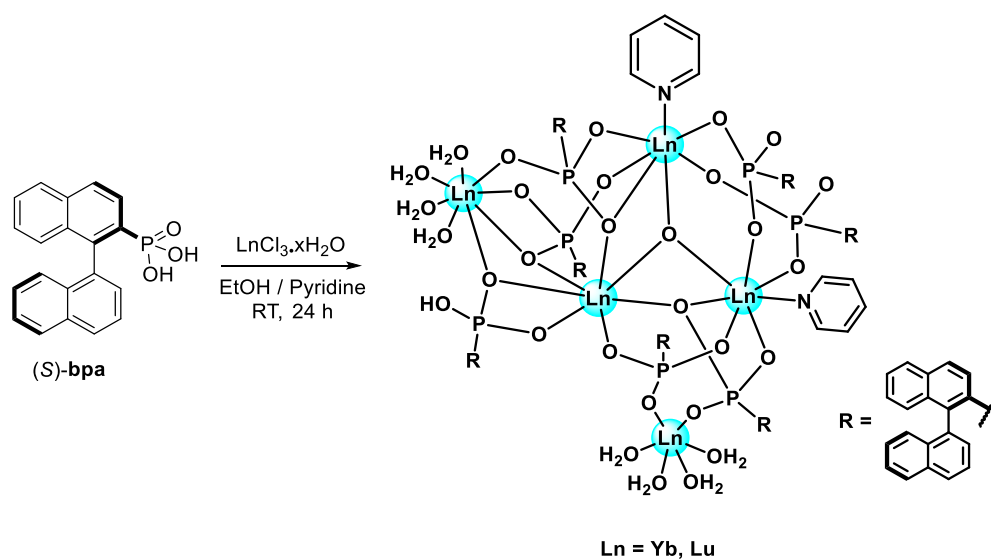
IR (neat / cm^{-1}) **Er**: 3308 (w), 1618 (s), 1080 (w), 1045 (s), 995 (m), 942 (m), 805 (m), 784 (w), 746 (m), 691 (w), 679 (m), 662 (s), 640 (w), 618 (m), 576 (m), 524 (w), 450 (m), 411 (w).

Er: $\alpha_D = -4.32$ ($0.278 \text{ g}/100 \text{ cm}^3$, DMSO, 20°C).

IR (neat / cm^{-1}) **Tm**: 3326 (w), 1630 (s), 1502 (w), 1489 (w), 1365 (m), 1314 (s), 1214 (m), 1167 (m), 1106 (s), 1073 (w), 1046 (w), 1007 (m), 977 (s), 943 (w), 818 (m), 804 (m), 784 (w), 774 (w), 746 (s), 690 (m), 678 (w), 662 (m), 640 (m), 618 (m), 575 (w), 523 (m), 450 (m).

Tm: $\alpha_D = +10.07$ ($0.278 \text{ g}/100 \text{ cm}^3$, DMSO, 20°C).

Synthesis of Yb and Lu Phosphonates (S)-66, 67, General Procedure



(S)-**bpa** (33 mg, 0.1 mmol, 1 eq.) and the appropriate lanthanide (0.1 mmol, 1 eq.) were dissolved in ethanol (3 mL) and pyridine (1 mL). This was stirred at room temperature for 24 h before being filtered. The filtrate was transferred to another vial. Parafilm was placed over the vial and three holes were perforated. After two weeks, colourless blocks of the desired lanthanide phosphonate were obtained.

IR (neat / cm^{-1}) **Yb**: 3338 (w), 1636 (s), 1543 (w), 1488 (m), 1365 (m), 1313 (w), 1124 (s), 1079 (m), 997 (m), 951 (m), 922 (w), 869 (m), 804 (m), 783 (w), 774 (m), 745 (s), 677 (w), 662 (m), 639 (w), 616, 573 (s), 519 (m), 443 (m).

Yb: $\alpha_D = +12.95$ (0.278 g/100 cm^3 , DMSO, 20 °C).

IR (neat / cm^{-1}) **Lu**: 3297 (w), 1618 (s), 1502 (w), 1365 (m), 1109 (s), 1075 (m), 1046 (w), 1010 (m), 943 (m), 868 (w), 805 (w), 784 (m), 774 (m), 746 (w), 691 (m), 679 (s), 662 (m), 640 (m), 618 (m), 576 (w), 524 (m), 450 (m).

Lu: $\alpha_D = -6.47$ (0.278 g/100 cm^3 , DMSO, 20 °C).

References

- 1 For instance, (a) T. O. Salami, X. Fan, P. Y. Zavalijb and S. R. J. Oliver, *Dalton Trans.*, 2006, **0**, 1574–1578; (b) F. Zhang, Y. Bao, S. Ma, L. Liua and X. Shi, *J. Mater. Chem. A*, 2017, **5**, 7474–7481; (c) D. M. Poojary, B. Zhang, P. Bellinghausen and A. Clearfield, *Inorg. Chem.*, 1996, **35**, 4942–4949; (d) D. E. J. Packiam and K. Vidyasagar, *Dalton Trans.*, 2017, **46**, 16102–16112; (e) I. L. V. Rosa, E. J. Nassar and O. A. Serra, *J. Alloys Compd.*, 1998, **275–277**, 315–317.
- 2 P. R. Meyer, W. Rutvisuttinunt, S. E. Matsuura, A. G. So and W. A. Scott, *J. Mol. Biol.*, 2007, **369**, 41–54.
- 3 S. B. Powles, *Pest Manag. Sci.*, 2008, **64**, 360–365.
- 4 (a) E. Gumienna-Kontecka, J. Jezierska, M. Lecouvey, Y. Leroux, H. Kozlowski, *J. Inorg. Biochem.*, 2002, **89**, 13–17; (b) E. Gumienna-Kontecka, R. Silvagni, R. Lipinski, M. Lecouvey, F. C. Marincola, G. Crisponi, V. M. Nurchi, Y. Leroux and H. Kozlowski, *Inorg. Chim. Acta*, 2002, **339**, 111–118; (c) E. Matczak-Jon, B. Kurzak, A. Kamecka, P. Kafarski, *Polyhedron*, 2002, **21**, 321–332.
- 5 K. Popov, H. Rönkkömäki and L. H. J. Lajunen, *Pure Appl. Chem.*, 2001, **73**, 1641–1677.
- 6 R. G. Pearson, *J. Am. Chem. Soc.*, 1963, **85**, 3533–3539.
- 7 For instance, (a) Z. Li, X. Liu, Y. Ling, Z. Chen and Y. Zhou, *Inorg. Chem. Commun.*, 2017, **84**, 59–62; (b) X. Houa and S.-F. Tang, *RSC Adv.*, 2016, **6**, 100158–100166; (c) M. Wilke, L. Batzdorf, F. Fischer, K. Rademann and F. Emmerling, *RSC Adv.*, 2016, **6**, 36011–36019.
- 8 The Cambridge Crystallographic Data Centre (CCDC) compiles and distributes the Cambridge Structural Database (CSD), the world's repository of experimentally determined organic and metal-organic crystal structures (www.ccdc.cam.ac.uk).
- 9 P. Gouzerh and M. Che, *l'actualité chimique*, 2006, **298**, 1–14.
- 10 S.-S. Wang, and G.-Y. Yang, *Chem. Rev.* 2015, **115**, 4893–4962.
- 11 (a) M. Wang, W. Zhong, S. Zhang, R. Liu, J. Xinga and G. Zhang, *J. Mater. Chem. A*, 2018, **6**, 9915–9921; (b) J. Fielden, J. M. Sumliner, N. Han, Y. V. Geletii, X. Xiang, D. G. Musaev, T. Lian and C. L. Hill, *Chem. Sci.*, 2015, **6**, 5531–5543.
- 12 J. T. Rhule, C. L. Hill, D. A. Judd and R. F. Schinazi, *Chem. Rev.*, 1998, **98**, 327–357.
- 13 (a) C. Venturello, R. D'Aloisio, J. C. J. Bart and M. J. Ricci, *Mol. Catal.*, 1985, **32**, 107–110; (b) R. Ishimoto, K. Kamata and N. Mizuno, *Angew. Chem. Int. Ed.*, 2012, **51**, 4662–4665; (c) Y. Yang, B. Zhang, Y. Wang, L. Yue, W. Li and L. Wu, *J. Am. Chem. Soc.*, 2013, **135**, 14500–14503.
- 14 J. D. Satterlee, *Concepts Magn. Reson.*, 1990, **2**, 119–129.
- 15 For instance, (a) J. Ai, X. Min, C.-Y. Gao, H.-R. Tian, S. Dang and Z.-M. Sun, *Dalton Trans.*, 2017, **46**, 6756–6761; (b) H. Rao, H. Fu, Y. Jiang and Y. Zhao, *J. Org. Chem.*, 2005, **70**, 8107–8109; (c) A. Dutta, A. K. Patra and A. Bhaumik, *Micro. Meso. Mater.*, 2012, **155**, 208–214; (d) P. Bhanja, K. Ghosh, S. S. Islam, A. K. Patra, S. M. Islam and A. Bhaumik, *ACS Sustainable Chem. Eng.*, 2016, **4**, 7147–7157.
- 16 S. Kirumakki, S. Samarajeewa, R. Harwell, A. Mukherjee, R. H. Herberb and A. Clearfield, *Chem. Commun.*, 2008, **0**, 5556–5558.
- 17 K. Maeda, *Micro. Meso. Mater.*, 2004, **73**, 47–55.
- 18 (a) M. Plabst, L. B. McCusker and T. Bein, *J. Am. Chem. Soc.*, 2009, **131**, 18112–18118; (b) M. Plabst and T. Bein, *Inorg. Chem.*, 2009, **48**, 4331–4341.
- 19 (a) P. G. Fournier, V. Stresing, F. H. Ebetino and P. Clézardin, *Neoplasia*, 2010, **12**, 571–578; (b) F. Daubiné, C. Le Gall, J. Gasser, J. Green and P. Clézardin, *J. Natl. Cancer. Inst.*, 2007, **99**, 322–330.

- 20 (a) Y.-Z. Zheng, M. Evangelisti, F. Tuna and R. E. P. Winpenny, *J. Am. Chem. Soc.*, 2012, **134**, 1057–1065; (b) P. Goddard, J. Liu, K. Gopa, J. Goura and V. Chandrasekhar, *Polyhedron*, 2014, **72**, 35–42.
- 21 O. A. Adebayo, K. A. Abboud and G. Christou, *Inorg. Chem.*, 2017, **56**, 11352–11364.
- 22 J. G. Mao, *Coord. Chem. Rev.*, 2007, **251**, 1493–1520.
- 23 S. J. Butler, M. Delbianco, L. Lamarque, B. K. McMahon, E. R. Neil, R. Pal, D. Parker, J. W. Walton and J. M. Zwier, *Dalton Trans.*, 2015, **44**, 4791–4803.
- 24 R. Sessoli, D. Gatteschi, A. Caneschi and M. A. Novak, *Nature*, 1993, **365**, 141–143.
- 25 D. N. Woodruff, R. E. P. Winpenny and R. A. Layfield, *Chem. Rev.*, 113, **7**, 5110–5148.
- 26 F.-S. Guo, B. M. Day, Y.-C. Chen, M.-L. Tong, A. Mansikkamäki and R. A. Layfield, *Angew. Chem. Int. Ed.*, 2017, **56**, 11445–11449.
- 27 D. A. Thompson and J. S. Best, *IBM J. Res. Develop.*, 2000, **44**, 311–322.
- 28 H. J. Richter, A. Lyberatos, U. Nowak, R. F. L. Evans and R. W. Chantrell, *J. Appl. Phys.*, 2012, **111**, 033909-1–033909-9.
- 29 M. Affronte, F. Troiani, A. Ghirri, A. Candini, M. Evangelisti, V. Corradini, S. Carretta, P. Santini, G. Amoretti, F. Tuna, G. Timco and R. E. P. Winpenny, *J. Phys. D: Appl. Phys.*, 2007, **40**, 2999–3004.
- 30 For instance, (a) S. Kyatskaya, J. R. G. Mascarós, L. Bogani, F. Hennrich, M. Kappes, W. Wernsdorfer and M. Ruben, *J. Am. Chem. Soc.*, 2009, **131**, 15143–15151; (b) S. Stepanow, J. Honolka, P. Gambardella, L. Vitali, N. Abdurakhmanova, T.-C. Tseng, S. Rauschenbach, S. L. Tait, V. Sessi, S. Klyatskaya, M. Ruben and K. Kern, *J. Am. Chem. Soc.*, 2010, **132**, 11900–11901; (c) M. Gonidec, R. Biagi, V. Corradini, F. Moro, V. de Renzi, U. del Pennino, D. Summa, L. Muccioli, C. Zannoni, D. B. Amabilino and J. Veciana, *J. Am. Chem. Soc.*, 2011, **133**, 6603–6612.
- 31 For instance, (a) J. T. Brockman, T. C. Stamatatos, W. Wernsdorfer, K. A. Abboud and G. Christou, *Inorg. Chem.*, 2007, **46**, 9160–9171; (b) S. J. Langley, M. Helliwell, R. Sessoli, P. Rosa, W. Wernsdorfer and R. E. P. Winpenny, *Chem. Commun.*, 2005, **0**, 5029–5031; (c) C. Benelli, J. Cano, Y. Journaux, R. Sessoli, G. A. Solan and R. E. P. Winpenny, *Inorg. Chem.*, 2001, **40**, 188–189; (d) I. Doroshenko, M. Babiak, A. Buchholz, J. Tucek, W. Plass and J. Pinkas, *New J. Chem.*, 2018, **42**, 1931–1938; (e) K. H. Zangana, E. Moreno Pineda and R. E. P. Winpenny, *Dalton Trans.*, 2015, **44**, 12522–12525. Also see references 21 and 32.
- 32 V. Baskar, K. Gopal, M. Helliwell, F. Tuna, W. Wernsdorfer and R. E. P. Winpenny, *Dalton Trans.*, 2010, **39**, 4747–4750.
- 33 See references 15a and 15b.
- 34 R. M. Park, J. F. Bena, L. T. Stayner, R. J. Smith, H. J. Gibb and P. S. J. Lees, *Risk Anal.*, 2004, **24**, 1099–1108; inspection of the hazard labels on any chromium(VI)-based reagent will reveal the H-phrase H350 (May cause cancer).
- 35 A. Corma, L. Nemeth, M. Renz and S. Valencia, *Nature*, 2001, **412**, 423–425.
- 36 G.-J. ten Brink, I. W. C. E. Arends and R. A. Sheldon, *Chem. Rev.*, 2004, **104**, 4105–4124.
- 37 (a) M. Jurado-Gonzalez, J. R. H. Wilson and A. C. Sullivan, *Tet. Lett.*, 2003, **44**, 4283–4286; (b) N. Al-Haq, J. R. H. Wilson and A. C. Sullivan, 2003, **44**, 769–771.
- 38 M. Jurado-Gonzalez, J. R. H. Wilson and A. C. Sullivan, *Tet. Lett.*, 2004, **45**, 4465–4468.
- 39 M. Al-Hashimi, E. Fisset, J. R. H. Wilson and A. C. Sullivan, *Tet. Lett.*, 2006, **47**, 8017–8019.
- 40 The VO(II), Mn(II), Co(II) and Ce(IV) analogues (product codes: 23-4380, 25-1200, 27-0900 and 58-5100 respectively) all retail at £248.00 = 5 g (www.strem.com), as of 26/07/2018.
- 41 Q. Yue, J. Yang, G.-H. Li, G.-D. Li and J.-S. Chen, *Inorg. Chem.*, 2006, **45**, 4431–4439.

- 42 For instance, (a) Y. Peng, T. Gong, K. Zhang, X. Lin, Y. Liu, J. Jiang and Y. Cui, *Nat. Commun.*, 2014, **5**:4406; (b) J. Zhang, Z. Li, W. Gong, X. Han, Y. Liu and Y. Cui, *Inorg. Chem.*, 2016, **55**, 7229–7232; (c) B. Liu, H.-F. Zhou, L. Hou, Z. Zhuc and Y.-Y. Wang, *Inorg. Chem. Front.*, 2016, **3**, 1326–1331.
- 43 G. F. de Sá, O. L. Malta, C. de Mello Donegá, A. M. Simas, R. L. Longo, P. A. Santa-Cruz, E. F. da Silva Jr., *Coord. Chem. Rev.* 2000, **196**, 165–195.
- 44 For instance, (a) S. Lis, Z. Piskula, K. Staninski, S. Tamaki, M. Inoue, Y. Hasegawa, *J. Rare Earths*, 2008, **26**, 185–191; (b) M. M. Nolasco, R. F. Mendes, P. P. Lima, F. A. Almeida Paz, L. D. Carlos and J. Rocha, *Eur. J. Inorg. Chem.* 2015, 1254–1260; (c) W. Yang, H.-R. Tian, J.-P. Li, Y.-F. Hui, X. He, J. Li, S. Dang, Z. Xie and Z.-M. Sun, *Chem. Eur. J.*, 2016, **22**, 15451–15457.
- 45 Metcalf and Eddy, *Wastewater Engineering: Collection, Treatment, Disposal*, McGraw-Hill Inc., US, 1972.
- 46 M. A. Reuter, K. Heiskanen, U. Boin, A. Van Schaik, E. Verhoef, Y. Yang and G. Georgalli, *The Metrics of Material and Metal Ecology Harmonizing the Resource, Technology and Environmental Cycles*, Elsevier, Amsterdam, 2005.
- 47 A. A. Zagorodni, *Ion Exchange Materials: Properties and Applications*, Elsevier, Amsterdam, 2006.
- 48 J. Hodgkinson and R. P. Tatam, *Meas. Sci. Technol.*, 2013, **24**, 012004.
- 49 (a) S Herrmann, L. de Matteis, J. M. de la Fuente, S. G. Mitchell and C. Streb, *Angew. Chem. Int. Ed.*, 2017, **56**, 1667–1670; (b) Z. Zhang, M. Sadakane, T. Murayama, N. Sakaguchi and W. Ueda, *Inorg. Chem.*, 2014, **53**, 7309–7318.
- 50 S. Kitagawa and M. Kondo, *Bull. Chem. Soc. Jpn.*, 1998, **71**, 1739–1753.
- 51 C. Serre, C. Mellot-Draznieks, S. Surble, N. Audebrand, Y. Filinchuk and G. Ferey, *Science*, 2007, **315**, 1828–1831.
- 52 (a) A. J. Fletcher, E. J. Cussen, T. J. Prior, M. J. Rosseinsky, C. J. Kepert and K. M. Thomas, *J. Am. Chem. Soc.*, 2001, **123**, 10001–10011; (b) K. Barthelet, J. Marrot, D. Riou and G. Ferey, *Angew. Chem. Int. Ed.*, 2002, **41**, 281–284; (c) R. Kitaura, K. Seki, G. Akiyama and S. Kitagawa, *Angew. Chem. Int. Ed.*, 2003, **42**, 428–431.
- 53 (a) S. Bourrelly, P. L. Llewellyn, C. Serre, F. Millange, T. Loiseau and G. Ferey, *J. Am. Chem. Soc.*, 2005, **127**, 13519–13521; (b) P. L. Llewellyn, S. Bourrelly, C. Serre, Y. Filinchuk and G. Ferey, *Angew. Chem. Int. Ed.*, 2006, **45**, 7751–7754.
- 54 R. S. Weinstein, P. K. Roberson and S.C. Manolagas, *N. Engl. J. Med.*, 2009, **360**, 53–62.
- 55 S. G. Harris, Ph.D. Thesis, The University of Edinburgh, 1999
- 56 S. K. Langley, M. Helliwell, S.J. Teat and R.E.P. Winpenny, *Dalton Trans.*, 2012, **41**, 12807–12817.
- 57 A. Clearfield and K. Demadis, *Metal Phosphonate Chemistry: From Synthesis to Applications*, RSC Publishing, Cambridge, 2011.
- 58 U. Costantino, S. Allulli, N. Tomassini and G. Alberti, *J. Inorg. Nuc. Chem.*, 1978, **40**, 1113–1117.
- 59 D. M. Poojary, H.-L. Hu, F. L. Campbell and A. Clearfield, *Acta Crystallogr. Sect. B*, 1993, **49**, 996–1001.
- 60 (a) A. Clearfield and G. D. Smith, *Inorg. Chem.*, 1969, **8**, 431–436; (b) J. M. Troup and A. Clearfield, *Inorg. Chem.*, 1977, **16**, 3311–3314.
- 61 B. Bujol, P. Palvadeau and J. Rouxel, *Chem. Mater.*, 1990, **2**, 582–589.
- 62 E. I. Tolis, M. Helliwell, S. Langley, J. Raftery and R. E. P. Winpenny, *Angew. Chem. Int. Ed.*, 2003, **42**, 3804–3808.
- 63 For instance, (a) M. Wang, D.-Q. Yuan, C.-B. Ma, M.-J. Yuan, M.-Q. Hu, N. Li, H. Chen, C.-N. Chen and Q.-T. Liu, *Dalton Trans.*, 2010, **39**, 7276–7285; (b) C. Köhler and E. Rentschler, *Dalton Trans.*, 2016, **45**, 12854–12861; (c) E. M. Pineda, F. Tuna, R. G.

- Pritchard, A. C. Regan, R. E. P. Winpenny and E. J. L. McInnes, *Chem. Commun.*, 2013, **49**, 3522–3524; also see reference 32.
- 64 R. C. Wang, Y. Zhang, H. Hu, R. R. Frausto and Abraham Clearfield, *Chem. Mater.*, 1992, **4**, 864–871.
- 65 R. A. Coxall, S. G. Harris, D. K. Henderson, S. Parsons, P. A. Tasker and R. E. P. Winpenny, *Dalton Trans.*, 2000, **0**, 2349–2356.
- 66 R. S. Cahn, C. Ingold and V. Prelog, *Angew. Chem. Int. Ed.*, 1966, **5**, 385–415.
- 67 (a) R. Murugavel and S. Shanmugam, *Dalton Trans.*, 2008, **0**, 5358–5367; (b) V. Chandrasekhar, L. Nagarajan, R. Clérac, S. Ghosh and S. Verma, *Inorg. Chem.*, 2008, **47**, 1067–1073; (c) V. Chandrasekhar and S. Kingsley, *Angew. Chem. Int. Ed.*, 2000, **39**, 2320–2322; (d) R. A. Laudise, *Chem. Eng. News*, 1987, **65**, 30–43.
- 68 V. Baskar, M. Shanmugam, E. C. Sañudo, M. Shanmugam, D. Collison, E. J. L. McInnes, Q. Weia and R. E. P. Winpenny, *Chem. Commun.*, 2007, **0**, 37–39.
- 69 See references 62 and 68.
- 70 V. Chandrasekhar, S. Kingsley, B. Rhatigan, M. K. Lam and A. L. Rheingold, *Inorg. Chem.*, 2002, **41**, 1030–1032.
- 71 For instance, (a) K. D. Demadis, Z. Anagnostou, A. Panera, G. Mezei, M. V. Kirillovac and A. M. Kirillov, *RSC Adv.*, 2017, **7**, 17788–17799; (b) J.-L. Song, H.-H. Zhao, J.-G. Mao and K. R. Dunbar, *Chem. Mater.*, 2004, **16**, 1884–1889.
- 72 For instance, (a) Y.-S. Ma, Y. Song, Y.-Z. Li and L.-M. Zheng, *Inorg. Chem.*, 2007, **46**, 5459–5461; (b) K. H. Zangana, E. M. Pineda and R. E. P. Winpenny, *Dalton Trans.*, 2014, **43**, 17101–17107.
- 73 R. Xu and Y. Xu, *Modern Inorganic Synthetic Chemistry 2nd Edition*, Elsevier, Amsterdam, 2017.
- 74 C. Liu, W. Yang, N. Qu, L.-J. Li, Q.-J. Pan and Z.-M. Sun, *Inorg. Chem.*, 2017, **56**, 1669–1678.
- 75 For instance, (a) D. Grohol, F. Gingl, and A. Clearfield, *Inorg. Chem.*, 1999, **38**, 751–756; (b) K. E. Knopea and C. L. Cahill, *Dalton Trans.*, 2010, **39**, 8319–8324; (c) D. Grohol, M. A. Subramanian, D. M. Poojary and A. Clearfield, *Inorg. Chem.*, 1996, **35**, 5264–5271.
- 76 W. Briner, *Int. J. Environ Res. Public Health*, 2010, **7**, 303–313.
- 77 Racemic, (*R*)- and (*S*)-binol retail on Sigma-Aldrich at 5 g = £20.20, £69.30 and £69.60 respectively, as of 30/07/18.
- 78 J. Clayden, N. Greeves and S. Warren, *Organic Chemistry, Second Edition*, Oxford University Press, Oxford, 2012.
- 79 R. M. Hiney, L. J. Higham, H. Müller-Bunz, D. G. Gilheany, *Angew. Chem. Int. Ed.*, 2006, **45**, 7248–7251.
- 80 A. Ficks, W. Clegg, R. W. Harrington and L. J. Higham, *Organometallics*, 2014, **33**, 6319–6329.
- 81 Dr Connor Sibbald and Dr Ana Cioran, who were previous members of the Higham group, successfully synthesised (*S*)-**bpa** and prepared cobalt, iron, dysprosium and gadolinium phosphonates. The work is unpublished.
- 82 C. I. Branden and J. Tooze, *Introduction to Protein Structure, Second Edition*, Garland Science, New York, 1998.
- 83 A. Mori, T. Mizusaki, T. Ikawa, T. Maegawa, Y. Monguchi and H. Sajiki, *Chem. Eur. J.*, 2007, **13**, 1432–1441.
- 84 M. T. Higa, N. H. Cheung, M.-C. McKenna and C. E. McKenna, *Tett. Lett.*, 1977, **18**, 155–158.
- 85 P. L. Coe, *Encyclopedia of Reagents for Organic Synthesis*, Wiley & Sons, New York, 2004.
- 86 K. Fink, C. Wang and V. Staemmler, *Inorg. Chem.*, 1999, **38**, 3847–3856.

- 87 M. Murrie, *Chem. Soc. Rev.*, 2010, **39**, 1986–1995.
- 88 A. Bailey, W. P. Griffith, D. W. C. Leung, A. J. P. White and D. J. Williams, *Polyhedron*, 2004, **23**, 2631–2636.
- 89 D. F. Shriver and P. W. Atkins, *Inorganic Chemistry 3rd Edition*, Oxford University Press, Oxford, 1999.
- 90 J. P. S. Walsh, G. W. Bowling, A.-M. Ariciu, N. F. M. Jailani, N. F. Chilton, P. G. Waddell, D. Collison, F. Tuna and L. J. Higham, *Magnetochemistry*, 2016, **23**.
- 91 O. Kahn, *Molecular Magnetism*, Wiley-Blackwell, New York, 1993.
- 92 S. K. Langley, M. Helliwell, R. Sessoli, S. J. Teat, and R. E. P. Winpenny, *Inorg. Chem.*, 2008, **47**, 497–507.
- 93 For instance, (a) K. van der Merwe, H. G. Visser and J. A. Venter, *Acta Crystallogr. Sect. E*, 2011, **67**, 1468–1469; (b) D. Heineke, S. J. Franklin and K. N. Raymond, *Inorg. Chem.*, 1994, **33**, 2413–2421; (c) D. Cao, Y. Li and L. Zheng, *Inorg. Chem.*, 2007, **46**, 7571–7578.
- 94 For instance, (a) F. Tong, Z.-G. Sun, K. Chen, Y.-Y. Zhu, W.-N. Wang, C.-Q. Jiao, C.-L. Wang and C. Li, *Dalton Trans.*, 2011, **40**, 5059–5065; (b) T. M. S. Pellizzaria, Y.-Z. Zhang, J. Gooch, A. Lau, S. McLeish, K. R. Dunbar and J. Zubieta, *Inorg. Chim. Acta*, 2017, **458**, 109–115.
- 95 D. Altermatt and I. D. Brown, *Acta. Crystallogr. Sect. B*, 1985, **41**, 240–244.
- 96 (a) D. Cao, S. Gao and L. Zheng, *J. Solid State Chem.*, 2004, **177**, 2311–2315; (b) P. Wang, D. Cao, S. Bao, H. Jin, Y. Li, T. Wang and L. Zheng, *Dalton Trans.*, 2011, **40**, 1307–1312.
- 97 W. Lu, Z. Wei, Z. Gu, T. Liu, J. Park, J. Park, J. Tian, M. Zhang, Q. Zhang, T. Gentle, M. Boscha and H. Zhou, *Chem. Soc. Rev.*, 2014, **43**, 5561–5593.
- 98 For instance, (a) S. Seth, G. Savitha, S. Jhulki and J. N. Moorthy, *Cryst. Growth. Des.*, 2016, **16**, 2024–2032; (b) J. Y. Song, I. Ahmed, P. W. Seo and S. H. Jung, *ACS Appl. Mater. Interfaces*, 2016, **8**, 27394–27402; (c) R. Luo, H. Xu, H. Gu, X. Wang, Y. Xu, X. Shen, W. Baoa and D. Zhu, *Cryst. Eng. Comm.*, 2014, **16**, 784–796.
- 99 For instance, (a) W. Li and S. Lee, *Chem. Phys. Lett.*, 2011, **506**, 57–60; (b) W. R. Lee, S. Y. Hwang, D. W. Ryu, K. S. Lim, S. S. Han, D. Moon, J. Choide and C. S. Hong, *Energy Environ. Sci.*, 2014, **7**, 744–751; (c) J. S. Yeon, W. R. Lee, N. W. Kim, H. Jo, H. Lee, J. H. Song, K. S. Lim, D. W. Kang, J. G. Seo, D. Moon, B. Wiers and C. S. Hong, *J. Mater. Chem. A*, 2015, **3**, 19177–19185.
- 100 M. Eddaoubi, D. F. Sava, J. F. Eubank, K. Adil and V. Guillerme, *Chem. Soc. Rev.*, 2015, **44**, 228–249.
- 101 K. Manna, T. Zhang, F. X. Greene and W. Lin, *J. Am. Chem. Soc.*, 2015, **137**, 2665–2673.
- 102 For instance, (a) H. Zhu, J. Huang, S. Bao, M. Ren and L. Zheng, *Dalton Trans.*, 2013, **42**, 14075–14080; (b) J. Feng, S. Bao, M. Ren, Z. Cai and L. Zheng, *Chem. Eur. J.*, 2015, **21**, 17336–17343.
- 103 Z. Shi, S. Feng, S. Gao, L. Zhang, G. Yang and J. Hua, *Angew. Chem. Int. Ed.*, 2000, **39**, 2325–2327.
- 104 Y. Su, D. Cao, Y. Duan, Y. Li and L. Zheng, *J. Solid State Chem.*, 2010, **183**, 1588–1594.
- 105 For instance, (a) L. Liu, J. Li, Z.-G. Sun, D.-P. Dong, N. Zhang, X. Lu, W.-N. Wang and F. Tong, *Z. Anorg. Allg. Chem.*, 2010, **636**, 247–252; (b) T. J. Greenfield, A. E. Hoffman, N. Marino, A. G. Goos, F. Lloret, M. Julve and R. P. Doyle, *Inorg. Chem.*, 2015, **54**, 6537–6546; (c) J.-S. Feng, Z.-S. Cai, M. Ren, S.-S. Bao and L.-M. Zheng, *Dalton Trans.*, 2015, **44**, 18122–18129.
- 106 M. Zhang, D. Zhou, J. Li, J. Yu, J. Xu, F. Deng, G. Li and R. Xu, *Inorg. Chem.*, 2007, **46**, 136–140.
- 107 L. R. Piquer and E. C. Sañudo, *Dalton Trans.*, 2015, **44**, 8771–8780.

- 108 M. A. St. Clair, B. D. Santarsiero and J. E. Bercaw, *Organometallics*, 1989, **8**, 17–22.
- 109 For instance, (a) J. T. Fleming, P. G. Waddell, M. R. Probert, W. Clegg and L. J. Higham, *Eur. J. Inorg. Chem.*, 2017, **2017**, 2837–2844; (b) M. Karakus, *Phosphorus Sulfur Silicon Relat. Elem.*, 2011, **186**, 1523–1530; (c) E. Colacio, A. Romerosa, J. Ruiz, P. Roman, J. M. Gutierrez-Zomilla, A. Vegas and M. Martinez-Ripoll, *Inorg. Chem.*, 1991, **30**, 3743–3749; (d) J.C. Lima and L. Rodriguez, *Anticancer Agents Med. Chem.*, 2011, **11**, 921–928.
- 110 H. Zhao, A. Pendri and R. B. Greenwald, *J. Org. Chem.*, 1998, **63**, 7559–7562.
- 111 For instance, (a) E. K. Brechin, R. A. Coxall, A. Parkin, S. Parsons, P. A. Tasker and R. E. P. Winpenny, *Angew. Chem. Int. Ed.*, 2001, **40**, 2700–2703; (b) S. Khanra, M. Kloth, H. Mansaray, C. A. Muryn, F. Tuna, E. C. Sañudo, M. Helliwell, E. J. L. McInnes and R. E. P. Winpenny, *Angew. Chem. Int. Ed.*, 2007, **46**, 5568–5571.
- 112 S. R. Miller, E. Lear, J. Gonzalez, A. M. Z. Slawin, P. A. Wright, N. Guilloub and G. Férey, *Dalton Trans.*, 2005, **0**, 3319–3325.
- 113 C. L. J. Aurora, *Chem. Educ.*, 1977, **54**, 302–303.
- 114 For instance, (a) N. Stock and T. Bein, *J. Mater. Chem.*, 2005, **15**, 1384–1391; (b) N. Burkovskaya, G. Aleksandrov, E. Ugolkova, N. Efimov, I. Evstifeev, M. Kiskin, Z. Dobrokhotova, V. Minin and I. Eremenko, *New J. Chem.*, 2014, **38**, 1587–1593; (c) T. M. Smith, D. Symester, K. Perrin, J. Vargas, M. Tichenor, C. J. O'Connor, J. Zubieta, *Inorg. Chim. Acta*, 2013, **402**, 46–59.
- 115 H. Aghabozorg, G. J. Palenik, R. C. Stouffer and J. Summers, *Inorg. Chem.*, 1982, **21**, 3903–3907.
- 116 W. M. Haynes, *CRC Handbook of Chemistry and Physics 97th edition*, CRC Press, USA, 2016.
- 117 For instance, (a) S. Konar, N. Bhuvanesh and A. Clearfield, *J. Am. Chem. Soc.*, 2006, **128**, 9604–9605; (b) S. Khanra, S. Konar, A. Clearfield, M. Helliwell, E. J. L. McInnes, E. Tolis, F. Tuna and R. E. P. Winpenny, *Inorg. Chem.*, 2009, **48**, 5338–5349; (c) X.-Y. Yi, L.-M. Zheng, W. Xu and J.-S. Chen, *Dalton Trans.*, 2003, **0**, 953–956.
- 118 For instance, (a) C. Cadiou, M. Murrie, C. Paulsen, V. Villar, W. Wernsdorfer and R. E. P. Winpenny, *Chem. Commun.*, 2001, **0**, 2666–2667; (b) S. T. Ochsenbein, M. Murrie, E. Rusanov, H. Stoeckli-Evans, C. Sekine and H. U. Güdel, *Inorg. Chem.*, 2002, **41**, 5133–5140; (c) B. Moubaraki, K. S. Murray, T. A. Hudson and R. Robson, *Eur. J. Inorg. Chem.*, 2008, **2008**, 4525–4529.
- 119 For instance, (a) M. Wilke, A. G. Buzanich, U. Reinholz, K. Rademann and F. Emmerling, *Dalton Trans.*, 2016, **45**, 9460–9467; (b) C. Bellitto, E. M. Bauer, S. A. Ibrahim, M. R. Mahmoud and G. Righini, *Chem. Eur. J.*, 2003, **9**, 1324–1331; (c) Z. Chen, L. Weng and D. Zhao, *Inorg. Chem. Commun.*, 2007, **10**, 447–450.
- 120 R. G. Pearson, *Chemical Hardness*, Wiley-VCH Verlag GmbH, Weinheim, 1997.
- 121 R. Janes and E. A. Moore, *Metal Ligand Bonding*, RSC Publishing, Cambridge, UK, 2004.
- 122 For instance, (a) D. I. Arnold, X. Ouyang and A. Clearfield, *Chem. Mater.*, 2002, **14**, 2020–2027; (b) H. A. Habib, B. Gil-Hernández, K. Abu-Shandi, J. Sanchiz and C. Janiak, *Polyhedron*, 2010, **29**, 2537–2545; (c) D. Gibson and R. Karaman, *Inorg. Chem.*, 1989, **28**, 1928–1932; (c) M. McCann, E. Murphy, C. Cardin and M. Convery, *Polyhedron*, 1992, **11**, 3101–3107.
- 123 For instance, (a) X. Hou and S.-F. Tang, *Dalton Trans.*, 2016, **45**, 7349–7359; (b) O. R. Evans, D. R. Manke and W. Lin, *Chem. Mater.*, 2002, **14**, 3866–3874.
- 124 For instance, (a) G. Huan, A. J. Jacobson, J. W. Johnson and E. W. Corcoran, *Chem. Mater.*, 1990, **2**, 91–93; (b) W. Ouellette, G. Wang, H. Liu, G. T. Yee, C. J. O'Connor and J. Zubieta, *Inorg. Chem.*, 2009, **48**, 953–963; (c) W. Ouellette, M.-H. Yu, C. J. O'Connor and J. Zubieta, *Inorg. Chem.*, 2006, **45**, 3224–3239.

- 125 For instance, (a) K. L. Nash, R. D. Rogers, J. Ferraro and J. Zhang, *Inorg. Chim. Acta.*, 1998, **269**, 211–223; (b) A. D. G. Firmino, R. F. Mendes, M. M. Antunes, P. C. Barbosa, S. M. F. Vilela, A. A. Valente, F. M. L. Figueiredo, J. P. C. Tomé and F. A. A. Paz, *Inorg. Chem.*, 2017, **56**, 1193–1208; (c) M. T. Wharmby, S. R. Miller, J. A. Groves, I. Margiolaki, S. E. Ashbrooka and P. A. Wright, *Dalton Trans.*, 2010, 39, 6389–6391.
- 126 For instance, (a) F. Tong, Z.-G. Sun, K. Chen, Y.-Y. Zhu, W.-N. Wang, C.-Q. Jiao, C.-L. Wang and Chao Li, *Dalton Trans.*, 2011, **40**, 5059–5065; (b) R. Chen, Y. Chen, X. Zeng, J. Li and X. Luo, *J. Coord. Chem.*, 2017, **70**, 949–959; (c) Y.-Y. Zhu, M.-L. Wang, M.-X. Ma, Z.-G. Sun, C.-Q. Jiao, C. Ma and H.-Y. Li, *New J. Chem.*, 2016, **40**, 578–588; (d) Y. Su, X. Cai, H. Sun, Z. Sun, D. Dong, Y. Zhu and T. Wang, *ChemistrySelect*, 2018, **3**, 6845–6851; (e) Z. Zhao, D. Yang, B. Xing, C. Ma, Z.-G. Sun, Y.-Y. Zhu, H.-Y. Li and J. Li, *RSC Adv.*, 2016, **6**, 92175–92185; (f) L.-L. Dai, Y.-Y. Zhu, C.-Q. Jiao, Z.-G. Sun, S.-P. Shi, W. Zhou, W.-Z. Li, T. Sun, H. Luo and M.-X. Ma, *Cryst. Eng. Comm.*, 2014, **16**, 5050–5061; (g) S.-P. Chen, Y. Guo, Q.-L. Chen, M. Li, L.-J. Yuan and J.-T. Sun, *J. Coord. Chem.*, 2008, **61**, 973–983; (h) S.-Z. Hou, D.-K. Cao, Y.-Z. Li and L.-M. Zheng, *Inorg. Chem.*, 2008, **47**, 10211–10213.
- 127 V Chandrasekhar and P. Sasikumara, *Dalton Trans.*, 2008, **0**, 6475–6480.
- 128 For instance, (a) K. Krekić, D. Klintucha and R. Pietschnig, *Chem. Commun.*, 2017, **53**, 11076–11079; (b) Y. Ma, Y.-S. Yang, Y.-H. Jiang, Y.-X. Li, M. Liu, Z.-F. Li, H.-L. Han, Y.-P. Yang, X.-L. Xin and Q.-H. Jin, *RSC Adv.*, 2017, **7**, 41651–41666; (c) M. Feyand, C. Näther, A. Rothkirch and N. Stock, *Inorg. Chem.*, 2010, **49**, 11158–11163; (d) X. Hu, W. Dou, C. Xu, X. Tang, J. Zhenga and W. Liu, *Dalton Trans.*, 2011, **40**, 3412–3418.
- 129 (a, La) M. Bazaga-García, G. K. Angeli, K. E. Papathanasiou, I. R. Salcedo, P. Olivera-Pastor, E. R. Losilla, D. Choquesillo-Lazarte, G. B. Hix, A. Cabeza and K. D. Demadis, *Inorg. Chem.*, 2016, **55**, 7414–7424; (b, Ce) Y.-Y. Zhu, Z.-G. Sun, F. Tong, Z.-M. Liu, C.-Y. Huang, W.-N. Wang, C.-Q. Jiao, C.-L. Wang, C. Lia and K. Chen, *Dalton Trans.*, 2011, **40**, 5584–5590; (c, Pr) Y.-F. Liu, G.-F. Hou, Y.-H. Yu, P.-F. Yan, G.-M. Lia and J.-S. Gao, *New J. Chem.*, 2014, **38**, 1328–1335; (d, Nd) M. Paula, C. Campello, S. Lacerda, I. C. Santos, G. A. Pereira, C. F. G. C. Geraldés, J. Kotek, P. Hermann, J. Vaněk, P. Lubal, V. Kubíček, É. Tóth and I. Santos, *Chem. Eur. J.*, 2010, **16**, 8446–8465; (e, Sm) J. Diwu, D. J. Grant, S. Wang, L. Gagliardi and T. E. Albrecht-Schmitt, *Inorg. Chem.*, 2012, **51**, 6906–6915.
- 130 (a, Eu) See reference 23; (b, Gd) O. R. Evans, H. L. Ngo and W. Lin, *J. Am. Chem. Soc.*, 2001, **123**, 10395–10396; (c, Tb) See reference 128a; (d, Dy) See reference 129d; (e, Ho) M. Le Fur, M. Beyler, N. Lepareur, O. Fougère, C. Platas-Iglesias, O. Rousseaux and R. Tripier, *Inorg. Chem.*, 2016, **55**, 8003–8012; (f, Er) Z.-Y. Du, H.-B. Zu and J.-G. Mao, *Inorg. Chem.*, 2006, **45**, 9780–9788; (g, Tm) Y.-S. Yang, M. Liu, Y.-P. Yang, Q.-H. Jin, Z.-F. Li, X.-N. Xue, Z.-J. Zhang and W.-J. Zheng, *Polyhedron*, 2015, **93**, 66–75.
- 131 (a, Yb) See references 129d and 130g; (b, Lu) See reference 130e.
- 132 For instance, (a) Q.-D. Liu, S. Gao, J.-R. Li, B.-Q. Ma, Q.-Z. Zhou and K.-B. Yu, *Polyhedron*, 2002, **21**, 1097–1103; (b) H.-L. Sun, C.-H. Ye, X.-Y. Wang, J.-R. Lia, S. Gao and K.-B. Yu, *J. Mol. Struct.*, 2004, **702**, 77–83; (c) Y. Wan, L. Jin, K. Wang, L. Zhang, X. Zheng and S. Lu, *New J. Chem.*, 2002, **26**, 1590–1596; (d) F. Benetollo, G. Bombieri, L. Calabi, S. Aime, and M. Botta, *Inorg. Chem.*, 2003, **42**, 148–157.
- 133 For instance, (a) S. Osa, T. Kido, N. Matsumoto, N. Re, A. Pochaba and J. Mrozinski, *J. Am. Chem. Soc.*, 2004, **126**, 420–421; (b) C. M. Zaleski, E. C. Depperman, J. W. Kampf, M. L. Kirk and V. L. Pecoraro, *Angew. Chem. Int. Ed.*, 2004, **116**, 4002–4004; (c) A. Mishra, W. Wernsdorfer, S. Parsons, G. Christou and E. K. Brechin, *Chem. Commun.*, 2005, **0**, 2086–2088.

Appendix

Table of Screenings for the Layering, Stirring and Hydrothermal Synthesis

Below is a comprehensive list of all solvent conditions as well as molar equivalent variations attempted in order to prepare suitable crystals for each of the three methods (stirring, layering and hydrothermal route) used to prepare (*S*)-**bpa** phosphonates. These were attempted for all metals mentioned in this thesis. Conditions highlighted in bold yielded good quality crystals.

Method	(<i>S</i>)-bpa mol. / mmol	Additional Reactants	Additional Reactants mol. / mmol	Solvents	Solvent Volume / mL
Stir / Hyd.	0.1	Pyrazine	0.1	EtOH	3
Stir / Hyd.	0.2	Pyrazine	0.1	EtOH	3
Stir / Hyd.	0.1	Pyrazine	0.2	EtOH	3
Stir / Hyd.	0.1	Pyrazine	0.1	EtOH Pyridine	3 1
Stir / Hyd.	0.2	Pyrazine	0.1	EtOH Pyridine	3 1
Stir / Hyd.	0.1	Pyrazine	0.2	MeCN Pyridine	3 1
Stir / Hyd.	0.2	Pyrazine	0.1	MeCN Pyridine	3 1
Stir / Hyd.	0.1	NaOH	0.1	EtOH	3
Stir / Hyd.	0.2	NaOH	0.1	EtOH	3
Stir / Hyd.	0.1	NaOH	0.2	EtOH	3
Stir / Hyd.	0.1	NaOH	0.1	EtOH Pyridine	3 1
Stir / Hyd.	0.2	NaOH	0.1	EtOH Pyridine	3 1
Stir / Hyd.	0.1	NaOH	0.2	MeCN Pyridine	3 1
Stir / Hyd.	0.2	NaOH	0.1	MeCN Pyridine	3 1

Method	(S)-bpa mol. / mmol	Additional Reactants	Additional Reactants mol. / mmol	Solvents	Solvent Volume / mL
Stir / Hyd.	0.1	NaOH	0.2	EtOH H₂O	1 1
Stir / Hyd.	0.1	2,2'-bipyridine	0.1	EtOH	3
Stir / Hyd.	0.2	2,2'-bipyridine	0.1	EtOH	3
Stir / Hyd.	0.1	2,2'-bipyridine	0.2	EtOH	3
Stir / Hyd.	0.1	2,2'-bipyridine	0.1	EtOH Pyridine	3 1
Stir / Hyd.	0.2	2,2'-bipyridine	0.1	EtOH Pyridine	3 1
Stir / Hyd.	0.1	2,2'-bipyridine	0.2	MeCN Pyridine	3 1
Stir / Hyd.	0.2	2,2'-bipyridine	0.1	MeCN Pyridine	3 1
Stir / Hyd.	0.1	4,4'-bipyridine	0.1	EtOH	3
Stir / Hyd.	0.2	4,4'-bipyridine	0.1	EtOH	3
Stir / Hyd.	0.1	4,4'-bipyridine	0.2	EtOH	3
Stir / Hyd.	0.1	4,4'-bipyridine	0.1	EtOH Pyridine	3 1
Stir / Hyd.	0.2	4,4'-bipyridine	0.1	EtOH Pyridine	3 1
Stir / Hyd.	0.1	4,4'-bipyridine	0.2	MeCN Pyridine	3 1
Stir / Hyd.	0.2	4,4'-bipyridine	0.1	MeCN Pyridine	3 1
Stir / Hyd.	0.1	4,4'-bipyridine	0.1	EtOH H₂O	1 1
Stir / Hyd.	0.1	None	-	Pyridine	3
Stir / Hyd.	0.1	None	-	H ₂ O EtOH Pyridine	1 1 1

Method	(S)-bpa mol. / mmol	Additional Reactants	Additional Reactants mol. / mmol	Solvents	Solvent Volume / mL
Layering	0.1	None	-	H ₂ O EtOH Pyridine	2 1 1
Layering	0.1	None	-	H ₂ O EtOH Pyridine	1 2 2
Layering	0.1	None	-	H ₂ O EtOH Pyridine	0.5 1 1
Layering	0.1	None	-	H ₂ O EtOH MeCN Pyridine	1 1 1 1
Layering	0.1	None	-	H₂O EtOH MeCN Pyridine	0.5 1 1 1

Bond Valence Sum Calculations

BVS analysis was conducted on the cobalt 1D chain, (S)-**38** and the Mn₆ Cluster, (S)-**46** using the following equations.

$$V = \sum (v_i)$$

$$v_i = \exp \left(\frac{R_0 - R_i}{b} \right)$$

V = Valence of an atom

v_i = Individual bond valence

R_0 = Tabulated parameter expressing the (ideal) bond length when an element i has a valence equal to exactly 1

R_i = Observed bond length

b = Empirical constant which varies depending on the bond being measured

Co 1-D Chain, (S)-**38**

Bond	R_i	R_0	b	v_i
Co1-O1	2.007	1.685	0.37	0.42
Co1-O2	2.262	1.685	0.37	0.21
Co1-O3	2.020	1.685	0.37	0.40
Co1-O5	2.095	1.685	0.37	0.33
Co1-O6	1.939	1.685	0.37	0.50

$$V = \sum (0.42 + 0.21 + 0.40 + 0.33 + 0.50)$$

$$V = 1.86 \approx 2$$

Bond	R_i	R_0	b	v_i
Co2-O4	1.994	1.685	0.37	0.43
Co2-O5	2.084	1.685	0.37	0.34
Co2-O7	1.975	1.685	0.37	0.46
Co2-O8	2.013	1.685	0.37	0.41
Co2-O9	2.380	1.685	0.37	0.15
Co2-O11	2.292	1.685	0.37	0.19

$$V = \sum (0.43 + 0.34 + 0.46 + 0.41 + 0.15 + 0.19)$$

$$V = 1.98 \approx 2$$

Bond	R_i	R_0	b	v_i
Co3-O10	2.011	1.685	0.37	0.41
Co3-O11	1.973	1.685	0.37	0.46
Co3-O13	2.016	1.685	0.37	0.41
Co3-O14	2.063	1.685	0.37	0.36

$$V = \sum (0.41 + 0.46 + 0.41 + 0.36)$$

$$V = 1.64 \approx 2$$

Bond	R_i	R_0	b	v_i
Co4-O12	1.937	1.685	0.37	0.51
Co4-O14	2.048	1.685	0.37	0.38
Co4-O15	1.959	1.685	0.37	0.48
Co4-O16	1.983	1.685	0.37	0.45

$$V = \sum (0.51 + 0.38 + 0.48 + 0.45)$$

$$V = 1.82 \approx 2$$

Mn₆ Cluster, (S)-**46**

The octahedral Mn atom Mn3 and the tetrahedral Mn atom Mn5 were measured.

Bond	R_i	R_0	b	v_i
Mn3-N3	2.176	1.837	0.37	0.40
Mn3-O1	1.996	1.732	0.37	0.49
Mn3-O4	1.894	1.732	0.37	0.65
Mn3-O7	1.921	1.732	0.37	0.60
Mn3-O10	2.018	1.732	0.37	0.46
Mn3-O11	2.158	1.732	0.37	0.32

$$V = \sum (0.40 + 0.49 + 0.65 + 0.60 + 0.46 + 0.32)$$

$$V = 2.91 \approx 3$$

Bond	R_i	R_0	b	v_i
Mn5-O3	2.189	1.790	0.37	0.34
Mn5-O6	2.145	1.790	0.37	0.38
Mn5-O8	2.029	1.790	0.37	0.52
Mn5-O9	2.027	1.790	0.37	0.53

$$V = \sum (0.34 + 0.38 + 0.52 + 0.53)$$

$$V = 1.77 \approx 2$$

Crystallographic Information Tables

The following tables are pertinent crystallographic information regarding all of the crystal structures elucidated. Note: The data for the Mn₆ phosphonate, (S)-**46** are missing since this structure could not be sufficiently refined.

	36 [Co(OAc) ₂] ₂ (Py) ₂ (OH ₂) ₂]	(S)- 37 [Co((S)-bpa) ₂ (Py) ₄]	(R)- 37 [Co((R)-bpa) ₂ (Py) ₄]
Empirical Formula	C ₁₄ H ₂₀ CoN ₂ O ₆	C ₆₀ H ₄₈ CoN ₄ O ₆ P ₂	C ₆₀ H ₄₈ CoN ₄ O ₆ P ₂
Formula Weight / g.mol⁻¹	371.25	1041.89	1041.89
Temperature / K	100(2)	150.0(2)	150.0(2)
Crystal System	Orthorhombic	Monoclinic	Monoclinic
Space Group	<i>Pbca</i>	<i>P2₁</i>	<i>P2₁</i>
a / Å	12.301(2)	10.6304(2)	10.63801(17)
b / Å	8.8423(18)	9.96011(18)	9.9582(2)
c / Å	14.888(3)	24.2053(4)	24.1949(6)
α / °	90	90	90
β / °	90	99.5065(18)	99.3899(19)
γ / °	90	90	90
Cell Volume / Å³	1619.4(5)	2527.66(8)	2528.76(9)
Z	4	2	2
ρ_{calc} g / cm³	1.523	1.369	1.368
μ / mm⁻¹	0.966	3.727	3.725
F(000)	772	1082.0	1082.0
Crystal Size / mm³	0.20 × 0.15 × 0.10	0.16 × 0.13 × 0.03	0.28 × 0.10 × 0.04
Radiation	Synchrotron (λ = 0.6889)	CuKα (λ = 1.54184)	CuKα (λ = 1.54184)
2θ range for data collection / °	3.1 to 27.5	7.406 to 133.71	7.406 to 133.904
Index Ranges	−15 ≤ h ≤ 16, −11 ≤ k ≤ 11, −19 ≤ l ≤ 17	−12 ≤ h ≤ 12, −11 ≤ k ≤ 11, −28 ≤ l ≤ 28	−12 ≤ h ≤ 12, −11 ≤ k ≤ 11, −28 ≤ l ≤ 28
Reflections Collected	15214	35965	36371
Independent Reflections	2027 [R _{int} = 0.0367]	8937 [R _{int} = 0.0505, R _{sigma} = 0.0402]	8934 [R _{int} = 0.0484, R _{sigma} = 0.0406]
Data / Restraints / Parameters	2027 / 0 / 116	8937 / 3 / 664	8934 / 3 / 664
Goodness-of-fit on F²	1.039	1.017	1.018
Final R Indices [I ≥ 2σ (I)]	R ₁ = 0.0234, wR ₂ = 0.0603	R ₁ = 0.0372, wR ₂ = 0.0912	R ₁ = 0.0396, wR ₂ = 0.0958
Final R Indices [all data]	R ₁ = 0.0261, wR ₂ = 0.0618	R ₁ = 0.0426, wR ₂ = 0.0957	R ₁ = 0.0457, wR ₂ = 0.1001
Largest diff. peak / hole / e Å⁻³	0.33 / −0.34	0.27 / −0.37	0.39 / −0.41
Flack Parameter		−0.041(4)	−0.033(3)

	(S)-38 (S)-Co 1-D Chain	(R)-38 (R)-Co 1-D Chain	(S)-42 (S)-Co 2-D Sheet
Empirical Formula	C ₈₀ H ₅₈ Co ₄ O ₁₅ P ₄	C ₈₀ H ₅₆ Co ₄ O ₁₅ P ₄	C ₅₂ H ₃₉ Co ₂ N ₂ O _{6.5} P ₂
Formula Weight / g.mol⁻¹	1618.86	1616.84	975.65
Temperature / K	150.0(2)	150.0(2)	100(2)
Crystal System	Monoclinic	Monoclinic	Triclinic
Space Group	<i>P</i> 2 ₁	<i>P</i> 2 ₁	<i>P</i> 1
a / Å	7.82942(10)	7.82168(16)	10.3565(16)
b / Å	27.4179(5)	27.4270(7)	13.603(2)
c / Å	16.3076(3)	16.2856(4)	17.736(3)
α / °	90	90	76.4689(16)
β / °	96.7915(15)	96.690(2)	75.8042(17)
γ / °	90	90	87.2599(18)
Cell Volume / Å³	3476.12(10)	3469.88(14)	2355.0(6)
Z	2	2	2
ρ_{calc} g / cm³	1.547	1.548	1.376
μ / mm⁻¹	8.798	8.813	0.726
F(000)	1652.0	1648.0	1002
Crystal Size / mm³	0.27 × 0.06 × 0.03	0.41 × 0.04 × 0.02	0.10 × 0.05 × 0.005
Radiation	CuKα (λ = 1.54184)	CuKα (λ = 1.54184)	Synchrotron (λ = 0.6889)
2θ range for data collection / °	8.45 to 133.556	8.454 to 133.842	2.0 to 29.7
Index Ranges	−9 ≤ h ≤ 8, −32 ≤ k ≤ 32, −19 ≤ l ≤ 18	−9 ≤ h ≤ 7, −32 ≤ k ≤ 32, −19 ≤ l ≤ 18	−10 ≤ h ≤ 14, −19 ≤ k ≤ 19, −25 ≤ l ≤ 25
Reflections Collected	25509	25674	28248
Independent Reflections	11077 [R _{int} = 0.0455, R _{sigma} = 0.0592]	11207 [R _{int} = 0.0903, R _{sigma} = 0.1137]	20074 [R _{int} = 0.0357]
Data / Restraints / Parameters	11077 / 6 / 953	11207 / 3 / 943	20074 / 51 / 1163
Goodness-of-fit on F²	1.021	1.055	1.066
Final R Indices [I ≥ 2σ (I)]	R ₁ = 0.0399, wR ₂ = 0.0795	R ₁ = 0.0531, wR ₂ = 0.1132	R ₁ = 0.0581, wR ₂ = 0.1520
Final R Indices [all data]	R ₁ = 0.0517, wR ₂ = 0.0847	R ₁ = 0.0812, wR ₂ = 0.1285	R ₁ = 0.0770, wR ₂ = 0.1631
Largest diff. peak / hole / e Å⁻³	0.32 / −0.36	0.48 / −0.46	1.25 / −0.80
Flack Parameter	−0.031(3)	−0.039(5)	

	(R)-42	(S)-43	(S)-44
	(R)-Co 2-D Sheet	Co ₃ Sc ₃ Mixed Cluster	Sc ₃ Cluster
Empirical Formula	C ₁₀₀ H ₇₀ Co ₄ N ₄ O _{13.5} P ₄	C ₁₆₆ H ₁₂₃ Co ₃ F ₃ N ₉ O ₂₂ P ₆ SSc ₃	C ₁₈₁ H ₁₄₄ F ₃ N ₁₂ O ₂₂ P ₆ SSc ₃
Formula Weight / g.mol⁻¹	1903.20	3182.31	3248.83
Temperature / K	100.0(2)	150.0(2)	100(2)
Crystal System	Triclinic	Cubic	Cubic
Space Group	<i>P</i> 1	<i>P</i> ₂ ₁ 3	<i>P</i> ₂ ₁ 3
a / Å	10.44450(10)	26.14318(15)	26.3793(11)
b / Å	13.65000(10)	26.14318(15)	26.3793(11)
c / Å	17.64280(10)	26.14318(15)	26.3793(11)
α / °	76.392	90	90
β / °	76.644	90	90
γ / °	87.582	90	90
Cell Volume / Å³	2378.36(3)	17868.0(3)	18356(2)
Z	1	3.99996	4
ρ_{calc} g / cm³	1.329	1.183	1.176
μ / mm⁻¹	0.811	4.202	0.222
F(000)	974.0	6540.0	6744
Crystal Size / mm³	0.097 × 0.061 × 0.017	0.30 × 0.22 × 0.15	0.090 × 0.080 × 0.040
Radiation	Synchrotron (λ = 0.6889)	CuKα (λ = 1.54184)	Synchrotron (λ = 0.6889)
2θ range for data collection / °	2.976 to 53.146	7.562 to 133.94	1.1 to 24.1
Index Ranges	-13 ≤ h ≤ 13, -17 ≤ k ≤ 17, -22 ≤ l ≤ 22	-29 ≤ h ≤ 26, -31 ≤ k ≤ 25, -22 ≤ l ≤ 30	-31 ≤ h ≤ 31, -31 ≤ k ≤ 31, -31 ≤ l ≤ 31
Reflections Collected	33726	43514	205231
Independent Reflections	19848 [R _{int} = 0.0255, R _{sigma} = 0.0446]	10514 [R _{int} = 0.0483, R _{sigma} = 0.0422]	10690 [R _{int} = 0.1247]
Data / Restraints / Parameters	19848 / 1164 / 1153	10514 / 822 / 685	10690 / 2201 / 868
Goodness-of-fit on F²	1.075	1.033	1.280
Final R Indices [I ≥ 2σ (I)]	R ₁ = 0.0276, wR ₂ = 0.0786	R ₁ = 0.0677, wR ₂ = 0.1750	R ₁ = 0.1207, wR ₂ = 0.3059
Final R Indices [all data]	R ₁ = 0.0290, wR ₂ = 0.0792	R ₁ = 0.0834, wR ₂ = 0.1893	R ₁ = 0.1475, wR ₂ = 0.3294
Largest diff. peak / hole / e Å⁻³	0.35 / -0.42	0.45 / -0.55	0.92 / -0.65
Flack Parameter	0.047(4)	-0.013(4)	

	(S)-45 [Mn((S)-bpa) ₂ (Py) ₄]	(S)-48 Fe ₃ Cluster	(S)-49 [Ni((S)-bpa) ₂ (Py) ₄]
Empirical Formula	C ₆₀ H ₄₈ MnN ₄ O ₆ P ₂	C ₁₈₅ H ₁₄₉ O _{22.5} P ₆ Fe ₃ N ₁₃ Cl	C ₆₀ H ₄₈ N ₄ NiO ₆ P ₂
Formula Weight / g.mol⁻¹	1037.90	3302.98	1041.67
Temperature / K	150.0(2)	150.01(10)	150.0(2)
Crystal System	Monoclinic	Trigonal	Monoclinic
Space Group	<i>P</i> 2 ₁	<i>P</i> 3 ₁ 21	<i>P</i> 2 ₁
a / Å	10.64402(19)	18.1588(5)	10.6630(3)
b / Å	9.99094(18)	18.1588(5)	9.9357(2)
c / Å	24.4347(5)	42.1318(16)	24.0443(6)
α / °	90	90	90
β / °	24.4347(5)	90	99.489(2)
γ / °	90	120	90
Cell Volume / Å³	2562.75(8)	12031.3(8)	2512.50(11)
Z	2	3	2
ρ_{calc} g / cm³	1.345	1.368	1.377
μ / mm⁻¹	0.377	3.474	0.508
F(000)	1078.0	5145.0	1084.0
Crystal Size / mm³	0.28 x 0.15 x 0.11	0.271 x 0.127 x 0.039	0.24 x 0.22 x 0.08
Radiation	MoKα (λ = 0.71073)	CuKα (λ = 1.54184)	MoKα (λ = 0.71073)
2θ range for data collection / °	6.508 to 59.044	5.62 to 133.844	5.64 to 55.98
Index Ranges	-14 ≤ h ≤ 14, -13 ≤ k ≤ 13, -33 ≤ l ≤ 33	-17 ≤ h ≤ 16, -21 ≤ k ≤ 21, -41 ≤ l ≤ 49	-13 ≤ h ≤ 14, -13 ≤ k ≤ 13, -31 ≤ l ≤ 31
Reflections Collected	83689	43818	16901
Independent Reflections	12788 [R _{int} = 0.0471, R _{sigma} = 0.0396]	13689 [R _{int} = 0.1055, R _{sigma} = 0.1133]	16901 [R _{int} = ?, R _{sigma} = 0.0432]
Data / Restraints / Parameters	12788 / 1 / 664	13689 / 918 / 1060	16901 / 3 / 665
Goodness-of-fit on F²	1.025	0.994	1.018
Final R Indices [I ≥ 2σ (I)]	R ₁ = 0.0366, wR ₂ = 0.0719	R ₁ = 0.0573, wR ₂ = 0.1121	R ₁ = 0.0311, wR ₂ = 0.0769
Final R Indices [all data]	R ₁ = 0.0536, wR ₂ = 0.0785	R ₁ = 0.0985, wR ₂ = 0.1273	R ₁ = 0.0365, wR ₂ = 0.0782
Largest diff. peak / hole / e Å⁻³	0.24 / -0.40	0.46 / -0.38	0.41 / -0.26
Flack Parameter	-0.013(6)	-0.007(5)	-0.006(8)

	(S)-50 [Cu((S)-bpa) ₂ (Py) ₄]	(S)-51 Zn Polymer	(S)-52 Y ₆ Cluster
Empirical Formula	C ₇₀ H ₅₈ N ₆ O ₆ P ₂ Cu	C ₁₀₀ H ₇₂ N ₄ O _{12.41} P ₄ Zn ₄	C ₁₈₀ H ₂₁₁ Cl ₃ N ₈ O ₅₈ P ₇ Y ₆
Formula Weight / g.mol⁻¹	1204.70	1913.61	4271.16
Temperature / K	120.0	150.0(2)	100(2)
Crystal System	Triclinic	Monoclinic	Monoclinic
Space Group	<i>P</i> 1	<i>P</i> 2 ₁	<i>P</i> 2 ₁
a / Å	9.7755(5)	10.6720(2)	17.713(3)
b / Å	10.6386(5)	16.4176(3)	32.465(5)
c / Å	15.6962(8)	24.9107(4)	18.724(3)
α / °	94.1568(16)	90	90
β / °	94.9182(15)	92.552(2)	108.9852(16)
γ / °	116.5843(15)	90	90
Cell Volume / Å³	1443.11(13)	4360.24(13)	10182(3)
Z	1	2	2
ρ_{calc} g / cm³	1.386	1.458	1.393
μ / mm⁻¹	0.496	2.485	1.702
F(000)	627.0	1959.0	4402
Crystal Size / mm³	0.215 × 0.152 × 0.074	0.35 × 0.07 × 0.05	0.20 × 0.20 × 0.050
Radiation	MoKα (λ = 0.71073)	CuKα (λ = 1.54184)	Synchrotron (λ = 0.6889)
2θ range for data collection / °	4.314 to 60.1	7.104 to 133.74	1.3 to 24.3
Index Ranges	−13 ≤ h ≤ 13, −14 ≤ k ≤ 14, −22 ≤ l ≤ 22	−11 ≤ h ≤ 12, −19 ≤ k ≤ 19, −29 ≤ l ≤ 29	−21 ≤ h ≤ 21, −38 ≤ k ≤ 32, −22 ≤ l ≤ 22
Reflections Collected	24442	12957	79632
Independent Reflections	16275 [R _{int} = 0.0270, R _{sigma} = 0.0642]	12957 [R _{int} = ?, R _{sigma} = 0.0258]	30811 [R _{int} = 0.0457]
Data / Restraints / Parameters	16275 / 3 / 774	12957 / 3130 / 1541	30811 / 3567 / 2360
Goodness-of-fit on F²	0.999	1.032	1.043
Final R Indices [I ≥ 2σ (I)]	R ₁ = 0.0413, wR ₂ = 0.0897	R ₁ = 0.0334, wR ₂ = 0.0836	R ₁ = 0.0576, wR ₂ = 0.1527
Final R Indices [all data]	R ₁ = 0.0542, wR ₂ = 0.0946	R ₁ = 0.0381, wR ₂ = 0.0862	R ₁ = 0.0778, wR ₂ = 0.1644
Largest diff. peak / hole / e Å⁻³	0.87 / −0.32	0.46 / −0.58	1.31 / −1.17
Flack Parameter	0.041(5)	0.327(16)	

	(S)-53 [Cd((S)-bpa) ₂ (Py) ₄]	(S)-54 La ₅ Cluster	(S)-55 Ce ₅ Cluster
Empirical Formula	C ₆₀ H ₄₈ CdN ₄ O ₆ P ₂	C ₁₈₀ H ₁₄₄ Cl ₃ La ₅ N ₄ O _{42.5} P ₈	C ₁₈₀ H ₁₄₄ Ce ₅ Cl ₃ N ₄ O ₃₂ P ₈
Formula Weight / g.mol⁻¹	1095.36	4091.64	3929.69
Temperature / K	210.0(2)	150.0(2)	150.0(2)
Crystal System	Triclinic	Monoclinic	Monoclinic
Space Group	<i>P</i> 1	<i>I</i> 2	<i>I</i> 2
a / Å	10.0187(2)	22.3278(5)	21.88211(17)
b / Å	10.5982(3)	21.4956(4)	21.52244(16)
c / Å	24.8854(6)	22.8071(6)	23.22975(17)
α / °	82.028(2)	90	90
β / °	89.0579(19)	90.141(2)	90.2855(6)
γ / °	86.902(2)	90	90
Cell Volume / Å³	2612.88(12)	10946.2(4)	10940.07(14)
Z	2	2	2
ρ_{calc} g / cm³	1.392	1.241	1.193
μ / mm⁻¹	0.535	1.113	9.231
F(000)	1124.0	4096.0	3938.0
Crystal Size / mm³	0.20 × 0.15 × 0.10	0.32 × 0.21 × 0.06	0.18 × 0.16 × 0.14
Radiation	MoKα (λ = 0.71073)	MoKα (λ = 0.71073)	CuKα (λ = 1.54184)
2θ range for data collection / °	5.864 to 54.97	5.792 to 58.998	5.598 to 133.962
Index Ranges	−13 ≤ h ≤ 12, −13 ≤ k ≤ 13, −31 ≤ l ≤ 31	−30 ≤ h ≤ 30, −28 ≤ k ≤ 27, −30 ≤ l ≤ 28	−24 ≤ h ≤ 25, −25 ≤ k ≤ 26, −27 ≤ l ≤ 27
Reflections Collected	83270	99189	18863
Independent Reflections	22905 [R _{int} = 0.0423, R _{sigma} = 0.0473]	25533 [R _{int} = 0.0625, R _{sigma} = 0.0720]	18863 [R _{int} = ?, R _{sigma} = 0.0392]
Data / Restraints / Parameters	22905 / 1287 / 1328	25533 / 3112 / 1361	18863 / 689 / 1172
Goodness-of-fit on F²	1.021	1.019	1.053
Final R Indices [I ≥ 2σ (I)]	R ₁ = 0.0346, wR ₂ = 0.0613	R ₁ = 0.0504, wR ₂ = 0.1128	R ₁ = 0.0428, wR ₂ = 0.1131
Final R Indices [all data]	R ₁ = 0.0539, wR ₂ = 0.0671	R ₁ = 0.0831, wR ₂ = 0.1291	R ₁ = 0.0462, wR ₂ = 0.1162
Largest diff. peak / hole / e Å⁻³	0.42 / −0.35	2.75 / −0.96	1.29 / −1.91
Flack Parameter	−0.028(10)	0.112(7)	−0.012(2)

	(S)-56 Pr ₅ Cluster	(S)-57 Nd ₅ Cluster	(S)-58 Sm ₅ Cluster
Empirical Formula	C ₁₈₀ H ₁₇₂ Cl ₃ N ₄ O ₄₆ P ₈ Pr ₅	C ₂₀₀ H ₁₇₈ Cl ₃ N ₈ Nd ₅ O ₃₉ P ₈	C ₂₀₀ H ₁₇₈ Cl ₃ N ₈ O ₃₉ P ₈ Sm ₅
Formula Weight / g.mol⁻¹	4185.87	4392.80	4423.35
Temperature / K	100(2)	100(2)	100(2)
Crystal System	Monoclinic	Orthorhombic	Orthorhombic
Space Group	<i>I</i> 2	<i>P</i> 2 ₁ 2 ₁ 2	<i>P</i> 2 ₁ 2 ₁ 2
a / Å	22.283(7)	18.712(4)	18.698(5)
b / Å	21.572(4)	32.092(7)	32.042(9)
c / Å	22.556(4)	15.673(4)	15.658(4)
α / °	90	90	90
β / °	90.3830(10)	90	90
γ / °	90	90	90
Cell Volume / Å³	10842(4)	9412(4)	9381(4)
Z	2	2	2
ρ_{calc} g / cm³	1.282	1.550	1.566
μ / mm⁻¹	1.170	1.361	1.605
F(000)	4228	4434	4454
Crystal Size / mm³	0.150 x 0.080 x 0.030	0.080 x 0.040 x 0.020	0.050 x 0.050 x 0.040
Radiation	(Synchrotron, λ = 0.6889)	(Synchrotron, λ = 0.6889)	(Synchrotron, λ = 0.6889)
2θ range for data collection / °	1.8 to 27.5	1.3 to 24.4	1.6 to 24.3
Index Ranges	-22 ≤ h ≤ 29, -28 ≤ k ≤ 28, -30 ≤ l ≤ 30	-22 ≤ h ≤ 21, -38 ≤ k ≤ 38, -15 ≤ l ≤ 18	-22 ≤ h ≤ 17, -37 ≤ k ≤ 38, -18 ≤ l ≤ 16
Reflections Collected	56436	60663	58115
Independent Reflections	25861 [R _{int} = 0.0342]	16874 [R _{int} = 0.0566]	15751 [R _{int} = 0.0593]
Data / Restraints / Parameters	25861 / 1423 / 1124	16874 / 374 / 1251	15751 / 368 / 1250
Goodness-of-fit on F²	1.029	1.070	1.042
Final R Indices [I ≥ 2σ (I)]	R ₁ = 0.0395, wR ₂ = 0.1078	R ₁ = 0.0738, wR ₂ = 0.1918	R ₁ = 0.0547, wR ₂ = 0.1334
Final R Indices [all data]	R ₁ = 0.0506, wR ₂ = 0.1145	R ₁ = 0.0933, wR ₂ = 0.2059	R ₁ = 0.0768, wR ₂ = 0.1476
Largest diff. peak / hole / e Å⁻³	2.00 / -0.91	4.35 / -3.62	3.07 / -2.70
Flack Parameter			

	(S)-59 Eu ₆ Cluster	(S)-60 Gd ₆ Cluster	(S)-61 Tb ₆ Cluster
Empirical Formula	C ₁₈₀ H ₂₁₁ Cl ₃ Eu ₆ N ₈ O ₅₈ P ₇	C ₁₆₀ H ₁₄₄ Cl ₃ Gd ₆ N ₄ O ₃₈ P ₇	C ₁₈₀ H ₂₁₁ Cl ₃ N ₈ O ₅₈ P ₇ Tb ₆
Formula Weight / g.mol⁻¹	4649.46	3997.42	4691.22
Temperature / K	100(2)	150.0(2)	100(2)
Crystal System	Monoclinic	Monoclinic	Monoclinic
Space Group	<i>P</i> 2 ₁	<i>P</i> 2 ₁	<i>P</i> 2 ₁
a / Å	18.0663(11)	17.9637(3)	17.876(3)
b / Å	32.4619(19)	32.2351(4)	32.600(5)
c / Å	19.5931(12)	19.5313(4)	18.826(3)
α / °	90	90	90
β / °	111.445(3)	111.270(2)	110.1822(18)
γ / °	90	90	90
Cell Volume / Å³	10695.2(11)	10539.4(3)	10297(3)
Z	2	2	2
ρ_{calc} g / cm³	1.444	1.260	1.513
μ / mm⁻¹	1.753	2.011	2.038
F(000)	4690	3952.0	4714
Crystal Size / mm³	0.110 x 0.100 x 0.070	0.31 x 0.29 x 0.19	0.120 x 0.090 x 0.030
Radiation	Synchrotron (λ = 0.6889)	MoKα (λ = 0.71073)	Synchrotron (λ = 0.6889)
2θ range for data collection / °	1.1 to 24.4	5.858 to 58.78	1.1 to 27.4
Index Ranges	−21 ≤ h ≤ 21, −38 ≤ k ≤ 38, −23 ≤ l ≤ 23	−23 ≤ h ≤ 24, −43 ≤ k ≤ 41, −26 ≤ l ≤ 26	−23 ≤ h ≤ 23, −36 ≤ k ≤ 43, −25 ≤ l ≤ 25
Reflections Collected	95045	203313	103285
Independent Reflections	36951 [R _{int} = 0.1217]	49532 [R _{int} = 0.0571, R _{sigma} = 0.0578]	44578 [R _{int} = 0.0288]
Data / Restraints / Parameters	36951 / 4340 / 2053	49532 / 2516 / 1979	44578 / 4395 / 2207
Goodness-of-fit on F²	1.024	1.023	1.107
Final R Indices [I ≥ 2σ (I)]	R ₁ = 0.1187, wR ₂ = 0.3032	R ₁ = 0.0632, wR ₂ = 0.1498	R ₁ = 0.0535, wR ₂ = 0.1130
Final R Indices [all data]	R ₁ = 0.1799, wR ₂ = 0.3508	R ₁ = 0.0875, wR ₂ = 0.1686	R ₁ = 0.0738, wR ₂ = 0.1260
Largest diff. peak / hole / e Å⁻³	4.57 / −1.87	3.47 / −1.51	3.37 / −2.45
Flack Parameter		0.134(4)	

	(S)-62 Dy ₆ Cluster	(S)-63 Ho ₆ Cluster	(S)-64 Er ₆ Cluster
Empirical Formula	C ₁₈₀ H ₂₁₁ Cl ₃ Dy ₆ N ₈ O ₅₈ P ₇	C ₁₆₅ H ₁₁₆ Cl ₄ Ho ₆ N ₅ O ₃₉ P ₇	C ₁₈₅ H ₂₁₆ Cl ₄ Er ₆ N ₉ O ₅₈ P ₇
Formula Weight / g.mol⁻¹	4712.70	4140.97	4855.81
Temperature / K	100(2)	150.0(2)	100(2)
Crystal System	Monoclinic	Monoclinic	Monoclinic
Space Group	<i>P</i> 2 ₁	<i>P</i> 2 ₁	<i>P</i> 2 ₁
a / Å	17.727(3)	17.9088(6)	17.798(6)
b / Å	32.613(5)	32.6170(7)	32.684(10)
c / Å	18.760(3)	18.8573(6)	18.783(6)
α / °	90	90	90
β / °	108.8166(15)	108.940(4)	108.814(3)
γ / °	90	90	90
Cell Volume / Å³	10266(2)	10418.8(6)	10342(6)
Z	2	2	2
ρ_{calc} g / cm³	1.525	1.320	1.559
μ / mm⁻¹	2.039	2.417	2.272
F(000)	4726	4056.0	4868
Crystal Size / mm³	0.150 x 0.150 x 0.100	0.25 × 0.22 × 0.13	0.450 x 0.300 x 0.200
Radiation	Synchrotron (λ = 0.6889)	MoKα (λ = 0.71073)	Synchrotron (λ = 0.6889)
2θ range for data collection / °	1.1 to 23.3	5.494 to 60.45	1.1 to 27.5
Index Ranges	−20 ≤ h ≤ 20, −37 ≤ k ≤ 36, −21 ≤ l ≤ 21	−24 ≤ h ≤ 24, −45 ≤ k ≤ 44, −24 ≤ l ≤ 26	−23 ≤ h ≤ 23, −43 ≤ k ≤ 37, −25 ≤ l ≤ 24
Reflections Collected	76055	182304	96878
Independent Reflections	31593 [R _{int} = 0.0411]	51587 [R _{int} = 0.1257, R _{sigma} = 0.1514]	46246 [R _{int} = 0.0402]
Data / Restraints / Parameters	31593 / 3279 / 2359	51587 / 3912 / 2056	46246 / 3318 / 2405
Goodness-of-fit on F²	1.043	1.015	1.181
Final R Indices [I ≥ 2σ (I)]	R ₁ = 0.0437, wR ₂ = 0.1023	R ₁ = 0.0696, wR ₂ = 0.1413	R ₁ = 0.0530, wR ₂ = 0.1350
Final R Indices [all data]	R ₁ = 0.0538, wR ₂ = 0.1065	R ₁ = 0.1238, wR ₂ = 0.1737	R ₁ = 0.0551, wR ₂ = 0.1383
Largest diff. peak / hole / e Å⁻³	1.78 / −1.77	2.92 / −2.48	6.97 / −7.08
Flack Parameter		−0.017(6)	

	(S)-65 Tm ₆ Cluster	(S)-66 Yb ₅ Cluster	(S)-67 Lu ₅ Cluster
Empirical Formula	C ₁₆₀ H ₁₄₇ Cl ₄ N ₄ O ₄₂ P ₇ Tm ₆	C ₁₇₅ H ₁₅₂ Cl ₃ N ₇ O ₃₃ P ₇ Yb ₅	C ₁₇₅ H ₁₅₂ Cl ₃ Lu ₅ N ₇ O ₃₃ P ₇
Formula Weight / g.mol⁻¹	4169.98	4069.37	4079.02
Temperature / K	150.0(2)	100(2)	100(2)
Crystal System	Monoclinic	Orthorhombic	Orthorhombic
Space Group	<i>P</i> 2 ₁	<i>P</i> 2 ₁ 2 ₁ 2	<i>P</i> 2 ₁ 2 ₁ 2
a / Å	17.9916(3)	31.306(7)	31.104(4)
b / Å	32.6532(4)	35.386(8)	35.179(5)
c / Å	18.8284(3)	22.039(5)	22.045(3)
α / °	90	90	90
β / °	109.154(2)	90	90
γ / °	90	90	90
Cell Volume / Å³	10449.0(3)	24415(10)	24122(6)
Z	2	4	4
ρ_{calc} g / cm³	1.325	1.107	1.123
μ / mm⁻¹	6.046	1.841	1.964
F(000)	4116.0	8084	8104
Crystal Size / mm³	0.17 × 0.14 × 0.05	0.073 × 0.042 × 0.030	0.065 × 0.040 × 0.014
Radiation	CuKα (λ = 1.54184)	Synchrotron (λ = 0.6889)	Synchrotron (λ = 0.6889)
2θ range for data collection / °	7.35 to 133.8	1.1 to 25.5	0.8 to 24.3
Index Ranges	−20 ≤ h ≤ 21, −38 ≤ k ≤ 38, −22 ≤ l ≤ 22	−39 ≤ h ≤ 39, −44 ≤ k ≤ 44, −27 ≤ l ≤ 27	−37 ≤ h ≤ 37, −41 ≤ k ≤ 41, −26 ≤ l ≤ 26
Reflections Collected	78983	237510	243177
Independent Reflections	31770 [R _{int} = 0.0630, R _{sigma} = 0.0754]	49665 [R _{int} = 0.0724]	42710 [R _{int} = 0.1108]
Data / Restraints / Parameters	31770 / 2470 / 2035	49665 / 4346 / 2101	42710 / 4664 / 2147
Goodness-of-fit on F²	1.006	0.958	1.069
Final R Indices [I ≥ 2σ (I)]	R ₁ = 0.0519, wR ₂ = 0.1262	R ₁ = 0.0454, wR ₂ = 0.1144	R ₁ = 0.0851, wR ₂ = 0.2359
Final R Indices [all data]	R ₁ = 0.0664, wR ₂ = 0.1376	R ₁ = 0.0553, wR ₂ = 0.1184	R ₁ = 0.1206, wR ₂ = 0.2666
Largest diff. peak / hole / e Å⁻³	1.66 / −0.94	2.41 / −1.08	5.70 / −1.78
Flack Parameter	0.075(7)		

(S)-bpa (Uncoordinated)	
Empirical Formula	C _{20.50} H ₁₈ ClO ₄ P
Formula Weight / g.mol ⁻¹	394.77
Temperature / K	150(2)
Crystal System	Monoclinic
Space Group	<i>P</i> 12 ₁ 1
a / Å	13.6254(4)
b / Å	8.1533(3)
c / Å	16.8480(6)
α / °	90
β / °	95.322(3)
γ / °	90
Cell Volume / Å ³	1863.61(11)
Z	4
ρ _{calc} g / cm ³	1.407
μ / mm ⁻¹	0.314
F(000)	820
Crystal Size / mm ³	0.20 × 0.10 × 0.10
Radiation	MoKα (λ = 0.71073)
2θ range for data collection / °	2.9 to 28.6
Index Ranges	−16 ≤ h ≤ 18, −10 ≤ k ≤ 10, −21 ≤ l ≤ 22
Reflections Collected	18161
Independent Reflections	7854 [R _{int} = 0.0369]
Data / Restraints / Parameters	7854 / 9 / 511
Goodness-of-fit on F ²	1.055
Final R Indices [I ≥ 2σ (I)]	R ₁ = 0.0439, wR ₂ = 0.0733
Final R Indices [all data]	R ₁ = 0.0594, wR ₂ = 0.0794
Largest diff. peak / hole / e Å ⁻³	0.33 / −0.29
Flack Parameter	